Laser Induced Nitrogen Doping of Zinc Oxide

Jodie M. West

A thesis submitted in partial fulfilment of the requirements of Nottingham Trent University for the degree of Doctor of Philosophy.

School of Science and Technology

Nottingham Trent University

May 2023

Copyright Statement

Abstract

The p-n junction is the fundamental building block of many electronic and optoelectronic devices, including diodes, transistors, light emitting diodes (LEDs), solar cells, integrated circuits and many more. Of the many devices, UV LEDs based on wide bandgap semiconductor p-n homojunctions promise a plethora of widescale functionalities for use in a variety of important medical, environmental, and industrial applications. However, the development of low-cost, highly efficient materials for use in UV LEDs with emissions spanning across the UV spectrum is essential if such widescale applications are to be realised. Zinc oxide (ZnO) is a promising candidate for a low cost, non-toxic alternative material to Gallium Nitride (GaN) for use in UV LEDs. Yet, the desirable ZnO p-n homojunction remains elusive due to the current research bottleneck in achieving stable, reproducible, and high-quality p-type ZnO. Various research groups have investigated routes to achieving p-type doping in ZnO, but most of the materials developed exhibit poor crystalline quality with unstable and unreproducible p-type conductivity with high native point defect densities and in-active dopants. As such, several major research challenges must be addressed if the full potential and advantages of ZnO as a UV LED material are to be harnessed in real devices. These challenges include improving dopant solubility, minimising hole compensation by native defects or background impurities, and the production of shallow acceptor states with low ionisation energies for the realisation of high quality and stable p-type ZnO. To address these challenges, this work is devoted to the development of a robust and repeatable doping strategy to achieve high quality, stable, and controllable p-type ZnO material. A disruptive progression towards the realisation of such p-type conductivity in ZnO is demonstrated through the development of a Controlled Environment Excimer Laser Doping (CEELD) process conducted in a pressurised nitrogen (N) containing environment to induce high-level, stable and reproducible N acceptor doping in Atomic Layer Deposition (ALD) ZnO. It is revealed that CEELD can incorporate and promote N into preferential lattice sites in the film through co-doping with the high level of background impurity hydrogen (H) present in the as grown ALD films. Once the N is incorporated, the high laser energy density simultaneously breaks the $N-H$ bond and provides enough thermal energy for the out-diffusion of the otherwise passivating H from the film, in turn activating N as an acceptor type dopant. Extensive characterisation of the electrical, optical, and compositional properties of the films is performed to further verify the achievement of CEELD induced p-type ZnO. The development of Ohmic contacts to the seed n- and p-type materials are investigated, and the seed materials implemented into simple p-n junction and thin film transistor (TFT) devices to further demonstrate the achievement of p-type ZnO. The CEELD process is then presented as a one-step, ultra-fast, low thermal budget, and highly selective doping strategy for the achievement of ultra-shallow p-n junctions for both lateral and laterally printed vertical p-n homojunction devices in ZnO.

Covid-19 Impact Statement

The 2020 coronavirus pandemic occurred during the second year of this Ph.D. study, and the lockdowns and further restrictions were not without effect on the research undertaken. Namely, lab closures and subsequent limited access to the laboratory facilities, alongside stunted and extended timelines for planned external collaborative research all impacted the studies. Despite the many challenges brought about by the Covid-19 pandemic, the pause from lab-based activities allowed for other avenues of research to be explored. A change of research direction was made to adapt to the situation of the lab closure by shifting the research to focus on modelling and analysing ellipsometry data that had already been acquired, with an aim to investigate further the optical properties of the thin films under development. In particular, the extensive analysis of IRSE data collected prior to the pandemic revealed interesting IR phononic and plasmonic properties of the ZnO materials which led to a large study into new fields of research including strong coupling phenomena and exotic polaritonic behaviours such as hyperbolic dispersion. Ultimately, this led to a vast body of work that was aside from the main aims of the Ph.D. research but allowed for valuable expansion of knowledge and experience into different fields, which has ultimately led to publishable results and the writing and development of a research paper. The body of work regarding the IR optical properties of ZnO features as a stand-alone chapter in this thesis (Chapter 6) and starts from an introduction to the topic to the experiment and results.

Acknowledgements

Firstly, I would like the thank my Director of Studies, Professor Mary O'Neil, and my supervisors Dr. Demosthenes Koutsogeorgis and Dr. Nikolaos Kalfagiannis, for allowing me to carry out this research. Whose guidance, insights, time, and generosity throughout this PhD program have not only greatly contributed to the accomplishments in this work but have had profound impact in my development as a researcher throughout my time at NTU.

I also extend my sincere thanks to collaborators across the world. In particular I would like to thank Dr Long Jiang at the University of Nottingham for his efforts into performing the ToF-SIMS measurements, Professor Wayne Cranton for providing training and unlimited access to the use of the Hall Effect system at Sheffield Hallam University, Professor Panos Patsalas and Dr. Dimitrios Karfaridis at the Aristotle University of Thessaloniki for their contribution of Valence Band XPS measurements and their insights for analysis, Professor Thomas Anthopoulos and Dr. Hendrik Faber at the King Abdullah University of Science and Technology for performing Kelvin Force Probe Microscopy, and finally thank you to Dr. Elefterios Lidorikis and Ioannis Vangelidis at the University of Ioannina for their efforts into performing FDTD simulations.

To my friends and colleagues, past and present in iSMART and at NTU, Dr Jake Spear for all of your help and advice at the very start, with the ever-true wisdom of 'you need PhD friends', Mike Brown my iSMART The Musical cofounder, Dr GaRRy Mudd and his lentil soup, and to Dr Magda Patel, Ryan Toms, and Elena Abeywikrama for your support and friendship. A big thank you goes to Matthew Spink and Thomas Howe for being the weird metalhead physicists in the corner with me, and to Christina Koutsiaki and Josh Barkby for sharing in the highs and lows of a Ph.D. journey - thank you to you all for your friendship, interesting conversations, insights, and support along the way. To my partner in crime, Luke Blythe, thank you for all the laughter and goodness your brought to the lab, alongside many cry-laughing moments, 'tacky matt' will always be a highlight. To Luke Butler, my long-suffering friend, I feel privileged to have been able to go through an entire NTU undergraduate-postgraduate journey with you, and of course Dr James Hillier whose stickiness I tolerated for pleasure of your friendship, thank you for taking me under your wing during my master’s project, I'm certain without your 'good example' I wouldn't have been writing this today.

I also extend my deepest thanks to John Lewis Nottingham and all the friends and colleagues I have had the pleasure of working with over my last 9+ years as a partner, whose friendship, support, and grounding from the crazy physics world has been invaluable throughout this journey. I am immensely grateful for the opportunity of working in the partnership during the entirety of my studies and for the immeasurable contribution it has had to the growth of the person I am today. I would like to also thank my now lifelong JL friend and Literary Ph.D. genius Thomas Lockwood-Moran and his husband Josh

for their never-ending friendship throughout the many years and all the joy and happiness they have brought to this journey and beyond.

To those we have loved and lost, my grandad Geoff and Nanna Vera, who I know have been with me every step of the way. To my grandad Dennis, who we sadly lost midway through this PhD journey and who was so much looking forward to seeing me complete it. To lovely Lynz, who we lost far too soon, I promise my future research efforts will be devoted to help others in your memory. Thank you to you all, we love and miss you every day. Thank you also to the rest of my family and friends and to my Mama, Mavis, thank you for the love and support you have given me throughout my studies and for the creativity you have inspired.

A special thank you, of course, goes to my partner Rich. Thank you for being by my side throughout this journey, for your safe and calming presence, unwavering support, and for all the light and love you bring to my life every day. The next chapter is ours to create.

Finally, to my biggest supporters of all, my Mum and Dad, to whom this work is dedicated to. Thank you to you both for your endless love, your support and guidance and the precious friendship we share, all of this has been made possible because of you. You are loved more than you know, and I am so grateful to you for everything.

So, to you,

Mum and Dad,

with love,

always.

List of Publications

Journal Articles

Peer reviewed, under revision:

- **J.M.West,** I. Vangelidis, M. O'Neill, D. C. Koutsogeorgis, E. Lidorikis, N. Kalfagiannis. "*Natural Hyperbolic Materials: Phonon-plasmon Coupling Enables Extreme Anisotropy in* ZnO" In preparation for submission to 'Nanomaterials (MDPI)' Summer 2024

Under preparation:

- **J.M.West,** M. O'Neill, N. Kalfagiannis, D. C. Koutsogeorgis. "Signed CEELD Delivered: Controlled Environment Excimer Laser Doping (CEELD) Induced Nitrogen Acceptor-Type Doping in Atomic Layer Deposition ZnO" Under preparation for submission in 2024, journal to be confirmed
- **J.M.West,** M. O'Neill, N. Kalfagiannis, D. C. Koutsogeorgis. "Controlled Environment Excimer Laser Doping (CEELD) for Ultra-shallow P-N Homojunction Formation in ZnO" Under preparation for submission in 2024, journal to be confirmed

List of Conference Presentations

Contributed Talks

- *"P-type ZnO: Fairy-tale or Reality?"* **J. M. West**, Regional Heat of the Institute of Physics Three Minute Wonder Science Communication Competition, Leicester, UK (16th March 2022)
- *"P-type ZnO: Fairy-tale or Reality?"* **J. M. West**, Final of the Institute of Physics Three Minute Wonder Science Communication Competition, The Royal Institution, London, UK (17th May 2022)
- *"P-Type ZnO: Excimer Laser Annealing Induced Nitrogen Doping of Atomic Layer Deposition ZnO Thin Films"*, **J.M.West,** M. O'Neill, N. Kalfagiannis, D. C. Koutsogeorgis, E-MRS Spring Meeting 2022, Virtual Conference, (30th May – 3rd June 2022)
- "*P-Type ZnO: Excimer Laser Annealing Induced Nitrogen Doping of ALD ZnO Thin Films*", **J.M.West,** M. O'Neill, N. Kalfagiannis, D. C. Koutsogeorgis, 8th International Symposium on Transparent Conductive Materials & 12th International Symposium on Transparent Oxides and Related Materials for Electronics and Optics 2022, Crete, Greece (16th – 21st October 2022)

Poster Contributions

- "*Natural Hyperbolic Materials: Phonon-plasmon Coupling Enables Extreme Anisotropy in* ZnO" **J.M.West,** M. O'Neill, D. C. Koutsogeorgis, N. Kalfagiannis, 8th International Symposium on Transparent Conductive Materials & 12th International Symposium on Transparent Oxides and Related Materials for Electronics and Optics 2022, Crete, Greece (16th – 21st October 2022)

Table of Contents

List of Symbols

E	(Photon) energy	r_p	Fresnel Reflection Coefficient p-Polarisation
E_0	Peak position	r_s	Fresnel Reflction Coefficient s-Polarisation
$\tilde{\varepsilon}$	Complex dielectric function or permittivity	ρ_f	Ratio of Fresnel Reflection Coefficients
ε'	Real part of the complex permittivity	Ψ	Psi Ellipsometric Angle
ε''	Imaginary part of the complex permittivity	Δ	Delta Ellipsometric Angle
ε_∞	High-frequency permittivity	$< \tilde{\varepsilon}(E) >$	Complex *pseudo*- permittivity
$\tilde{n}$	Complex refractive index	d_B	Film Thickness
n	(Real) refractive index	d_l	Layer/Film Thickness
κ	Extinction coefficient	E_G	Band gap
ε_0	Permittivity of free space	Φ_m	Work Function of Metal
μ_0	Permeability of free space	Φ_s	Work Function of Semiconductor
c	Speed of light	χ_{sc}	Semiconductor Electron Affinity
k_b	Boltzmann constant	Φ_B	Barrier Height
T	Temperature	E_C	Energy Position of the Conduction Band
ε_r	Relative permittivity of a material	E_V	Energy Position of the Valence Band
t	Time	$E_{f,n}$	Fermi Level of n-type semiconductor
q	Charge density	$E_{f,p}$	Fermi Level of p-type semiconductor
j	Current density	L	Length
ω	(Photon) angular frequency	V_{bulk}	Voltage through semiconductor bulk
λ	Wavelength	$V_{contact}$	Voltage at contact
v	Phase velocity	R_{bulk}	Resistance in the bulk semiconductor
α	absorption coefficient	$R_{contact}$	Contact Resistance
δ_p	Penetration depth	ρ_c	Specific Contact Resistivity
ω_0	Resonant frequency	A	Contact Area
γ	Damping coefficient	N_A	Acceptor Concentration
m^*	Effective mass ratio	N_D	Donor Concentration
m_e	Mass of the electron	V_0	Built-in Potential
e	Charge of the electron	n	Electron concentration
$\hbar$	Reduced Planck's constant	p	Hole concentration
n	Principle quantum number/ counting term	n_c	Intrinsic Carrier Concentration in Conduction Band
ω_p	Plasma frequency	p_v	Intrinsic Carrier Concentration in Valence Band
γ_p	Drude damping coefficient	n_i	Intrinsic Carrier Concentration
μ	Carrier mobility	W_0	Depletion Region Width
ρ	Resistivity	V_f	Forward Bias Voltage
σ	Conductivity	I_0	Saturation Current
N	Free carrier concentration	n	Diode ideality factor
ρ_{VdP}	Van der Pauw Resistivity	V_r	Reverse Bias Voltage

List of Symbols

N_{Hall}	Hall carrier concentration	V_{Th}	Threshold Voltage
E_G	Band gap	V_{ON}	Turn On Voltage
T	Transmissivity	I_D	Drain Current
D_h	Thermal diffusivity	S	Subthreshold Swing
ρ_M	Material density	μ_{FE}	Field Effect Mobility
K_T	Thermal conductivity	t	time of flight
C_V	Specific heat capacity	D	Distance
L_h	Heat diffusion length	m_x	Secondary Ion Mass
t_d	Dwell time	υ_x	Secondary Ion Velocity
t_p	Laser pulse duration.	z_x	Number of charges of an ion, x
θ	Angle	I_s^x	Secondary Ion Current
d	Distance, thickness or spacing	I_p	Primary Partical Flux
E_K	Kinetic energy of electron	γ_x	Sputter yield
ϕ	Work function	η_i	Instrument Transmission
R_{sh}	Sheet resistance	$\alpha^{\pm}$	Ionisation Probabiltiy
V	Voltage	θ_x	Fractional concentration of species x
I	Current	E_B	Binding Enegry of Electron
w	Width	E_k	Kinetic energy of electron
B	Magnetic field strength	Φ_{spec}	Work function of Spectrometer
F_L	Lorentz force	V_{CPD}	Contact Potential Difference
F_e	Electrostatic force	Φ_{tip}	Work function of tip
V_H	Hall voltage	$R(E)$	Frequency Dependent Reflectance
A	Area	$\tilde{n}$	Complex refractive index
R_H	Hall coefficient	n	refractive index
R_S	Sheet resistance	k	extinction coefficient
A_G	Gaussian Amplitude	ε'	Real permittivity
γ_G	Gaussian Broadening	ε''	Imaginary permittivity
E_G	Gaussian Energy	I_l	Intensity of reflected light from lamp
δ_p	Penetration depth	I_s	Intensity of reflected light from sample
Φ_{sample}	Work function of sample	I_d	Dark Intensity
v_d	drift velocity	α	absorption coefficient
F_L	Lorentz force	ε_∞	High frequency permittivity
F_{EL}	Electrostatic force	ω_p	Plasma frequency/energy
E_y	Electric Field Strength	γ_p	Plasma damping
R_{Al}	Aluminium Reference Mirror Reflectivity	ω_{LO}	LO Phonon Energy
S	Diode Sensitivity	ω_{TO}	TO Phonon Energy
I_{Ph}	Photocurrent	$\omega_{LPP^{+/-}}$	Phonon-Plasmon Coupled Mode Energies
I_{dark}	Dark Current	$\gamma_{LPP^{+/-}}$	Broadening of the Phonon-Plasmon Coupled Modes
I_{light}	Light Current	γ_{TO}	TO Mode Broadening

List of Abbreviations

LED	Light Emitting Diode	Au	Gold
TFT	Thin Film Transistor	Al	Aluminium
CEELD	Control envirionment excimer laser annealing	Pt	Platinum
WLED	White Light Emitting Diode	Ag	Silver
UV	Ultraviolet	Ti	Titanium
NUV	Near Ulraviolet	Ni	Nickel
DUV	Deep Ultraviolet	In	Indium
I	Current	Mg	Magnesium
V	Voltage	H	Hydrogen
IRSE	Infrared Spectroscopic Ellipsometry	Zn	Zinc
HE	Hall Effect	O	Oxygen
VdP	Van der Pauw	C	Carbon
ToF-SIMS	Time-of-Flight Secondary Ion Mass Spectroscopy	Si	Silicon
ALD	Atomic Layer Deposition	Kr	Krypton
DEZ	Diethylzinc	Ar	Argon
ORS	Optical Reflectance Spectroscopy	N	Nitrogen
KPFM	Kelvin Probe Force Microscopy	Li	Lithium
VB XPS	Valence Band X-ray Photoelectron Spectroscopy	Na	Sodium
EBD	Energy Band Diagram	Ar	Arsenic
VBM	Valence Band Maximum	Sb	Antimony
CBM	Conduction Band Minimum	P	Phosphorus
A-D-A	Acceptor-Donor-Acceptor	B	Boron
M-S	Metal-Semiconductor	Ga	Gallium
SCL	Space Charge Layer	Cs	Ceasium
WCD	Wet Chemical Deposition	Bi	Bismuth
PVD	Physical Vapour Deposition	K	Potassium
CVD	Chemical Vapour Deposition	KrF	Krypton Fluoride
ELA	Excimer Laser Annealing	ZnO	Zinc oxide
XPS	X-ray Photoelectron Spectroscopy	Al_2O_3	Aluminium oxide
UHV	Ultra-High Vacuum	SiO_2	Silicon dioxide
AFM	Atomic Force Microscopy	GaN	Gallium nitride
IR	Infrared	DEZ	Diethylzinc
NIR	Near Infrared	H2O	Water
VIS	Visible	SiC	Silicon Carbide
LO	Longitudinal Optical	GaAs	Gallium Arsenide
TO	Transverse Optical	h-BN	Hexagonal Boron Nitride
LPP	Longitudinal Phonon-Plasmon Coupled Mode	BeO	Berillium Oxide
IQE	Internal Quantum Efficiency	CdO	Cadmium Oxide
LEE	Light Extraction Efficiency	MgO	Magnesium Oxide
KK	Kramers Kronig	HOPG	Highly Ordered Pyrolytic Graphite

List of Figures

Figure 4.03 Average Hall Effect results for the $150\ ^{o}\mathrm{C}$ ALD ZnO film laser processed in high pressure N_2 environment treated with $1-5$ laser pulses at various laser energy density of (a) $150\ \mathrm{mJcm^{-2}}$, (b) $200\ \mathrm{mJcm^{-2}}$ and (c) $250\ \mathrm{mJcm^{-2}}$. Carrier type is indicated by closed data symbols for electrons (n-type) and open data symbols for holes (p-type), whilst the half-filled symbols indicate samples that returned mixed carrier type over consecutive, HE measurements. The as grown sample is identified as the sample treated with zero pulses. The stability of the electrical behaviour of the $200\ \mathrm{mJcm^{-2}}$ samples over a period of 6 months is presented in figure (d), where measurements of the 1 and 2 pulse sample measured 18 months from the first measurement in (b) are indicated by the open star symbols.

Figure 4.04. Average Hall Effect results for the full $150-200\ ^{o}\mathrm{C}$ temperature range ALD ZnO films laser processed in high pressure N_2 environment treated with (a) 1 pulse and (b) 2 pulses at a laser energy density of $200\ \mathrm{mJcm^{-2}}$. Carrier type is indicated by closed data symbols for electrons (n-type) and open data symbols for holes (p-type), whilst the half-filled symbols indicate samples that returned mixed carrier type over consecutive HE measurements. The as grown sample is identified as the sample treated with zero pulses.

Figure 4.05 Electrical results of the (a) Hall Carrier Concentration, (b) Van der Pauw resistivity and (c) Hall mobility for the as grown, and 1 and 2 pulse CEELD samples processed in Ar, N_2, and NH_3 environment. Carrier type is indicated by closed data symbols for electrons (n-type) and open data symbols for holes (p-type), The as grown sample is identified as the sample treated with zero pulses. The shaded region is added to guide the eye to the conversion between n- and p-type samples.

Figure 4.06 ToF-SIMS results of the normalised intensity of $\mathrm{ZnO^{2-}}$ and $\mathrm{AlO^{2-}}$ ions as a function of sputter time throughout the 80 nm ZnO thin films, where 0 s is taken as the ZnO surface. Results are shown for the 7-sample set including the as grown film (magenta line), and the 6 samples laser processed with 1 and 2 pulses $200\mathrm{mJcm^{-2}}$ in various high-pressure environments: Ar (blue lines), N_2 (green lines) and NH_3 (red lines), where the 1 and 2 pulses samples are indicated by the light and dark line colours respectively.

Figure 4.07 ToF-SIMS results of the normalised intensity of (a) $\mathrm{CN^-}$, (b) $\mathrm{CNO^-}$, (c) $\mathrm{NO_2^-}$ and (d) $\mathrm{NO^-}$ ions as a function of depth throughout the 80 nm ZnO thin films, where 0 nm is taken as the ZnO surface. Results are shown for the 7-sample set including the as grown film (magenta line), and the 6 samples laser processed with 1 and 2 pulses $200\mathrm{mJcm^{-2}}$ in various high-pressure environments: Ar (blue lines), N_2 (green lines) and NH_3 (red lines), where the 1 and 2 pulses samples are indicated by the light and dark line colours respectively.

Figure 4.08 3D representation of the ToF-SIMS measurement area results of the normalised intensity of $\mathrm{CN^-}$, $\mathrm{CNO^-}$) $\mathrm{NO_2^-}$ and $\mathrm{NO^-}$ ions as a function of depth throughout the 80 nm ZnO thin films. Results are shown for the 7-sample set including the as grown film (taken as the 0-pulse sample), and

List of Tables

1. Introduction

1.1. Introduction, Motivation and Challenges

The p-n junction is the fundamental building block of many electronic and optoelectronic devices, including diodes, transistors, light emitting diodes (LEDs), solar cells, integrated circuits and many more.[1] The advancement of such devices is often owed to the research and development into new material systems that promise superior qualities compared to their predecessors. One such developing material system is ZnO, which has received heightened interest in the past two decades as a promising low cost, non-toxic and environmentally friendly alternative to the leading material for short wavelength devices, gallium nitride (GaN).[2–5] Indeed, the commercial and widespread success of GaN based optoelectronic and electronic devices[6–9] has spurred interest into the potential of ZnO based devices since both GaN and ZnO have many comparable properties due to their similarly wide energy band gap, making ZnO an attractive alternate material.[10] Of the many potential applications that would be made possible by a p-n homojunction based on ZnO is the Ultraviolet Light Emitting Diode (UV LED).[5] The current main market for UV LEDs is for white light generation.[11–13] White LEDS (WLEDs) are considered as one of the most important solid-state sources in the lighting industry, owed to their superior qualities such as high brightness, low power consumption, long operational lifetime and environmental friendliness. Conventional WLEDs are achieved by encapsulating a blue LED chip with YAG:Ce^{2+} yellow phosphors. This partial conversion WLED system is limited by high thermal quenching leading to unstable chromaticity, low colour rendering index (CRI) due to minimal red fluorescence from the phosphor and a high intensity blue emission peak which has a damaging photochemical effect on the eye.[14] Such limitations could be avoided with the use of NUV LEDs for UV pumped white light emission from tricolour phosphors for improved CRI, chromatic stability and elimination of the blue light hazard. [12] Another major market for UV light sources is as an alternative to chlorination and ozonation processes in water sterilisation.[15] Conventional UV light sources are dominated by unsustainable, expensive, bulky and toxic mercury tube technology. The use of such technology causes the anthropogenic release of toxic mercury which is detrimental to the environment and human health. [16] There is therefore great focus on developing UV LEDs as an environmentally friendly, tuneable, low-cost, compact, robust and energy efficient alternative. Such compact solid-state UV LEDs go far beyond just replacing traditional UV sources but promise a variety of different applications such as: water, air and food sterilisation and decontamination; disinfection in surface, food and medical industries; fluorescence or Raman detection and identification of biological and chemical agents; forensics; biomedical and analytical instrumentation; epoxy curing and photopolymerization for odontology and various industrial applications; counterfeit detection; phototherapy and photochemotherapy for the treatment of dermatological diseases; diagnostic and therapeutic applications; fluorescent light sources for lighting and display screens; free space non-line-of-sight

(NLOS) communication; UV pumped WLEDs; and as an alternative to antibiotics in treatment of localised infections. Furthermore, it is expected that further research and improved performance of UV LEDs will unlock even more UV irradiation applications.[17][18] The full range of potential applications of UV LEDs is also dependent upon achieving UV LEDs with a broad spectrum of wavelengths across the full UV range from the NUV (UVA) to DUV (UVC).[19,20] Once optimal performance of UV LEDs has been achieved the market for such LEDs could explode. Therefore, the development of low-cost highly efficient materials for use in UV LEDs with emissions spanning across the UV spectrum is essential if such widescale applications are to be realised. The revolutionary development of blue light emission from GaN based LEDs in the early 1990s and the combination with phosphors to generate white light emission, caused the LED market to boom with widescale use in display screen technologies, space and illumination applications.[21,22] However fundamental material limitations significantly lower the efficiency and therefore applicability of GaN in LEDs for applications in the UV.[23] The natural efficacy of ZnO as a material for UV LED applications is owed to its many superior qualities compared to GaN when considering optoelectronic devices.[10] Unlike Ga, Zn is earth abundant, offers non-toxic material systems, and requires no special handling. As such, ZnO is a much more sustainable and environmentally friendly solution to the growing demands of the optoelectronic and electronics industries compared to GaN. Furthermore, ZnO is also inexpensive, offers easy fabrication and large area growth by a large variety of deposition techniques, alongside the availability of high-quality single crystals as native substrates for growth to avoid the lattice mismatch complications faced by GaN, making the fabrication of ZnO based devices an attractive prospect. Another superior attribute of ZnO is its larger exciton binding energy of $60\,meV$, compared to the $25\,meV$ of GaN, providing a fundamental advantage of ZnO based devices for the realisation of highly efficient excitonic UV emissions and stable optoelectronic devices at room temperature and above.[10,24–26] The application of ZnO for UV LED applications is further cemented by the availability to realise band gap engineering by alloying with MgO ($E_g = 7.8eV$), BeO ($E_g = 10.6eV$) or CdO ($E_g = 2.2eV$) which is a crucial step for the development of UV LEDs in a broad range of emission wavelengths across the UV spectrum to target the various applications promised by UV LEDs.[27–31] The intrinsic material advantages and advanced tunability of ZnO material systems could unlock the plethora of applications promised by UV LEDs and many other devices based on ZnO p-n homojunctions. Therefore, significant research and development of high quality ZnO materials is critical if the promise of ZnO UV LEDs is to be met.

Owing to its many attractive properties, the naturally n-type ZnO is already a well-established multifunctional material.[2,25] Typically, as deposited ZnO materials exhibit n-type behaviour, although the origin of this behaviour is still under debate, it is most often assigned to intrinsic defects such as V_OOand Zn_i, or to background impurity hydrogen that may be readily incorporated into the ZnO material during growth.[32] Moreover, this n-type behaviour can be readily tuned *via* careful modification of these defects and impurities or by extrinsic doping with group III transition metals such

as Al, Ga, In and B to produce the well-known transparent conductive oxides.[33] Typically, n-type materials have been employed in p-n heterojunctions with p-type GaN.[4,5] The relative ease of fabrication of these devices make them an attractive option, but several disadvantages arise from the chemical and crystallographic variations between the different materials in the heterojunction such as dislocations from lattice mismatch, surface quenching of carriers as well as thermal stressing from unmatched thermal expansion coefficients.[34] Therefore, the most desirable solution would be to develop a UV LED based purely on a ZnO homojunction to eliminate the detrimental effects observed in heterojunction LEDs. Despite such promise, the development of ZnO p-n homojunctions has been slow due to the difficulty in achieving stable and reproducible p-type ZnO with high hole concentration, good carrier mobility, high stability, with good reproducibility. The essential but elusive p-type material has proved far more difficult to realise due to the huge doping asymmetry associated with wide band gap semiconductor materials and remains a huge research bottleneck in the development of ZnO based devices.[2,29,35,36] The main difficulties in achieving p-type ZnO arise from a low solubility of acceptor dopants, formation of deep acceptor levels associated with high ionisation energies and the compensation of p-type character by intrinsic donor-like defects or background donor impurities which act as hole-killers.[28,37] Nevertheless, a huge research effort has been devoted to the study of p-type doping in ZnO, with reports of advancements in achieving p-type material and the observation of electroluminescence from ZnO homojunction based LED devices.[5,29,37–41] In general, group I and V elements have been identified as suitable acceptor type dopants in ZnO, with N often cited as the most promising candidate due to its comparable atomic radius to O that would induce only minor strain to the lattice and thus is a more energetically favourable substitutional dopant.[38] Additionally, N has both a similar electronegativity to O and energy values of the valence $2p$ states. Despite this, the solubility of N in ZnO is still low and despite some experimental evidence of N doping, theory suggests substitutional N cannot behave as a shallow acceptor in ZnO.[42] Aside from substitution, the formation of acceptor$-V_{Zn}$ complexes or complexes with other background impurities such as carbon or hydrogen may produce shallow acceptors for p-type conduction.[32,37] To address the acceptor solubility issues, another potential route to achieving p-type conductivity was proposed termed co-doping, which consists of the simultaneous doping of both donors and acceptors to increase the acceptor solubility.[43–46] Various reports of both mono- and co-doping have suggested the achievement of p-type ZnO, however the choice of dopant, optimal growth technique and the very existence of p-type ZnO remains controversial, with the stability, reliability, reproducibility, and quality of the materials still under question.[5,37,38,45,47] Despite the considerable progress made, the various materials developed so far have suffered from a lack of reproducibility, low achievable hole concentration and instability in the p-type character over time. As such, several major research challenges must be addressed for the realisation of high quality and stable p-type ZnO including improving dopant solubility, minimising donor like defects and background electron concentration to reduce hole compensation and the production of shallow acceptor states with low ionisation energies. To address these challenges, the development of

a robust and repeatable doping method to achieve high quality and stable p-type material is essential if the full potential and many advantages of ZnO are to be harnessed in real, ubiquitous devices.

1.2. Research Aim

The predominant aim of this research was to investigate the potential of performing excimer laser annealing in a controlled environment to induce N acceptor doping in ALD ZnO for the achievement of a tuneable, stable, and reproducible p-type doping strategy in ZnO for implementation into simple devices including an ultra-shallow p-n homojunction.

1.3. Research Objectives

The research aim was realised through the following objectives:

- Development and optimisation of the seed (starting) as deposited ZnO materials for processing. Seed material development using atomic layer deposition (ALD), and a process for optimising the electrical properties of the as deposited materials by variations in the deposition parameters such as the deposition temperature and purge process parameters.

- Investigation into the potential of controlled environment excimer laser doping (CEELD), as a method to induce p-type doping and develop understanding of the underlying doping mechanism in ALD ZnO. Processing of the seed materials with the CEELD process technique in a variety of gaseous environments and the optimisation of the CEELD processing parameters and their effect on the electrical and compositional properties of the laser processed materials. Investigations into the depth of the induced N concentration for further insights into the N doping induced by CEELD. Input of these insights to the successful development of CEELD processing as a post growth doping method to induce N acceptor doping in ALD ZnO and the mechanisms governing the doping.

- Further verification of CEELD achieved p-type doping in ZnO beyond Hall Effect measurements. Development of Infrared Spectroscopic ellipsometry (IRSE), as an indicative method for carrier type determination in ZnO by assessing the broadening behaviour of coupled phonon-plasmon modes based on the differences between electron and hole free carrier plasmons. Reconstruction of simple energy band diagrams for the seed n- and p-type materials to observe shifts in the Fermi level as an indication of acceptor type doping.

- Development of Ohmic contacts to both n-type and p-type materials. Utilising the key seed materials to investigate Ohmic contact metallisation schemes to achieve good Ohmic contact to both materials for implementation into devices and verifying the contact Ohmic behaviour by I-V characterisation.

- Implementation of seed n- and p-type materials into simple devices. Utilising seed materials and Ohmic contact metallisation scheme to fabricate a host of simple devices: lateral p-n homojunctions, vertical p-n homojunctions, and thin film transistors. I-V characterisation of the devices to observe fundamental device physics for further verification of achieving p-type conductivity in the laser processed samples. Further implication of this work in the development of CEELD as an ultrafast, highly selective, low thermal budget, ultra-shallow p-n homojunction fabrication technique for lateral and laterally patterned vertical p-n homojunction devices based on ZnO.
- Investigate the influence of a broad range of laser processing and deposition parameters on the infrared optical properties of the ZnO materials. Work building upon the IRSE Kukharskii model analysis for the identification of carrier type in ZnO. Understand the phononic and plasmonic properties of the films developed in this work and their potential for polaritonic applications.

1.4. Overview of Research Methodology

This work involves the use of ALD to deposit ZnO thin films that are then post processed by Controlled Environment Excimer Laser Doping (CEELD) to induce N acceptor doping in the seed ZnO materials and reviews the potential of the CEELD approach as a one-step ultra-shallow p-n homojunction fabrication for both lateral and laterally patterned vertical devices. ALD is widely regarded as one of the most attractive thin film deposition techniques due to its superior control over composition and thickness and its production of highly conformal thin film coatings applicable to more complex substrate geometries. The ALD growth process for development of the as deposited seed ZnO thin film material was achieved by the sequential pulsing of zinc (diethylzinc, DEZ) and O (water, H_2O) precursors, followed by a purge process after each pulse, performed in a cyclic process. Monolayer growth of ZnO material is achieved by the individual surface reactions of the precursors with the substrate per ALD cycle. The thickness of the ZnO produced is therefore controlled by the number of ALD cycles, whilst the electrical properties of the ZnO films produced are tuned by varying several ALD parameters including the deposition temperature and purge process parameters which are proposed to control the defect composition in the deposited material

A variety of techniques exist to induce extrinsic doping in semiconductor materials, however most result in inefficient dopant activation that requires an additional processing step of thermal annealing to activate the dopants into electrically active sites for effective doping. Conventional annealing techniques such as rapid thermal annealing and furnace annealing have high thermal budgets making them unsuitable for use in devices with temperature sensitive substrates. Additionally, these conventional techniques are cumbersome, involving the entire sample stack and require long dwell times for the desired annealing effect. Another key challenge associated with conventional doping

methods is their inability to dope selective areas of a material, which is highly desirable for micropatterning of more complex electronic devices. Moreover, the ever miniaturisation of devices requires ultra-shallow p-n homojunctions of less than $100\ nm$, which is difficult to efficiently achieve with conventional doping methods. To combat all three of the above outlined challenges in the field, in this work CEELD is investigated as an ultrafast, low thermal budget, highly controllable and selective doping technique to induce effective incorporation of N acceptors in ZnO into non-passivated, electrically active, shallow acceptor sites. Furthermore, the controllable laser doping area and the nature of CEELD as a surface processing method, provides a route to highly selective ultra-shallow doping for ultra-shallow ($< 100\ nm$) p-n homojunction fabrication capable of lateral patterning. Investigations into carrier type were delivered *via* electrical characterisation by Van der Pauw (VdP) resistivity and Hall Effect (HE) measurements. Time-of-Flight Secondary Ion Mass Spectrometry (ToF-SIMS) was used to investigate N ion incorporation into the ZnO films before and after laser processing. Further verification of carrier type was sought through investigating shifts in the Fermi level *via* construction of simple electronic energy band structure diagrams, which was achieved using a variety of techniques including Optical Reflectance Spectroscopy (ORS), Kelvin Probe Force Microscopy (KPFM) and valence band X-ray Photoelectron Spectroscopy (XPS). Meanwhile, IRSE was investigated as a potential contactless method for carrier type determination by investigations into coupled phonon-plasmon modes in the ZnO materials and observing changes in the broadening behaviour between the electron or hole based free carrier plasmons. The seed n- and p-type materials are also implemented into simple devices with verified Ohmic contacts and device outputs characterised by current-voltage investigations.

1.5. Novelty and contribution to the field of ZnO based Materials Science

This research study has investigated the development of a CEELD process for the doping and defect engineering of ALD ZnO to achieve stable and reproducible N acceptor-type doping in ZnO for use in various p-n junction device applications. During this research, multiple substantial contributions to the field of material science and engineering, ZnO research, device physics and fabrication and IR photonics have been made:

1. The electrical properties of as grown ZnO materials were collated by HE and VdP resistivity measurements to determine the effect of the ALD deposition variables on the free carrier concentration, resistivity, and carrier mobility of ZnO materials deposited by ALD. The role of the deposition variables on the ALD surface chemistry and stoichiometry of the film was evaluated.

2. The use of CEELD to induce dopants from the laser annealing environment and the resultant effect on the electrical and compositional properties was presented. The underlying physical mechanisms for the CEELD induced N doping in ALD ZnO were revealed.

3. CEELD in a N containing environment is therefore presented as an ultrafast, low thermal budget, industry viable, and highly controllable process to produce stable and reproducible p-type doping in ALD ZnO.

4. CEELD induced changes to the optoelectronic, compositional, and structural properties of ZnO were uncovered. Producing an extensive understanding of the role of the laser processing parameters (fluence, number of pulses, and environment composition) on the ZnO material properties.

5. The depth of N diffusion and acceptor doping achieved by the CEELD process was investigated by depth profile ToF-SIMS and depth profile valence band XPS measurements to aid further understanding into the CEELD doping process. CEELD was revealed to produce ultra-shallow doped regions $(20 - 40\,nm)$ which is highly desirable for the ever miniaturisation of the electronics industry.

6. The potential of IRSE as a non-destructive, indicative method for carrier type determination in the ZnO films developed in this work was presented. Whereby, examination of the phonon and plasmon properties of the materials was found to be able to distinguish between holes and electrons according to changes in the broadening parameters of both the plasmon and coupled phonon-plasmon modes in the materials.

7. The impact of inducing variations in the carrier concentration on the real part of the dielectric permittivity of ZnO was revealed. The presence of phonon-plasmon coupling in ZnO was identified, and the effect of the phonon-plasmon coupling on the bandwidth of hyperbolic dispersion modes was presented and a perspective for ZnO as a low cost, tuneable, natural hyperbolic material for mid-IR hyperbolic applications was delivered.

8. Implementation of the seed materials into simple devices revealed the potential of using device physics for carrier type determination beyond the Hall effect. Fundamental devices physics proved the p-type nature of the N CEELD ZnO materials.

9. The unique ability of laser annealing to harness and exploit light-matter interactions for the precise energy high energy delivery to the material surface and control the physiochemical processes on the nanoscale enabled the development of the CEELD process as an ultra-shallow p-n homojunction fabrication method. The CEELD process is therefore presented as an industry viable, ultrafast, low thermal budget, and highly controllable one-step method to print both lateral and laterally printed vertical p-n junction devices, amenable to high volume production with potential to facilitate flexible or plastic substrates.

1.6. Structure of Thesis

The thesis is composed of seven chapters, organised as follows:

1. **Chapter 1** presents the research aims and objectives alongside the motivation, research methodology and novelty of the present work.

2. **Chapter 2** explores the background literature and fundamental physics associated with the work undertaken and results presented in this work. The fundamentals of ZnO as a semiconductor is explored, and the difficulties in achieving p-type doping in ZnO is outlined. Attention is also given to the fundamentals of the ALD, previous studies into the development of ZnO materials, and different doping strategies. Lastly a brief overview is given of the fundamental physics behind metallic contacts, p-n junction devices and thin film transistor technology.

3. **Chapter 3** details the experimental methods and characterisation techniques employed in this work and relevant supporting information.

4. **Chapter 4** presents the work undertaken for the development of the seed n-type ZnO materials and the investigations into the development of the controlled environment laser doping technique to achieve p-type electrical character in ZnO *via* N acceptor doping. The chapter involves electrical characterisation and results as well as investigations into the compositional changes upon laser doping, whilst further experimental support of p-type doping is explored *via* investigating simple energy band diagrams and the potential of Infrared Spectroscopic Ellipsometry to determine carrier type in the ZnO thin films.

5. **Chapter 5** reports the results of the metallic contacts, p-n junctions and thin film transistor device investigations based on the seed materials developed in Chapter 4. The chapter explores how implementation of the materials into simple devices can provide further experimental support for the achievement of p-type doping in ALD ZnO *via* controlled environment laser doping. The chapter also presents the potential of CEELD as a one-step p-n homojunction fabrication method.

6. **Chapter 6** continues the investigation into the results and analysis of the infrared optical properties of ZnO that is introduced in Chapter 4. The chapter investigates the potential of ZnO as a Natural Hyperbolic Material and the potential of the phonon-plasmon coupling phenomena to engineer the hyperbolic response. The hyperbolic behaviour of the ZnO materials investigated in this work are compared to a literature case.

7. **Chapter 7** remarks on the conclusions and key outcomes of this work alongside suggestions on future perspectives and suggested work to develop further the ideas presented in this thesis.

2. Background and Literature Review

This chapter provides the background and literature information on the fundamentals of various aspects of this research, initially the fundamentals of ZnO deposition *via* ALD and the associated ALD material properties are explored. The chapter then discusses the fundamentals of doping ZnO materials, the grand research challenge in achieving p-type ZnO materials, and the various research efforts employed so far to induce acceptor type doping. The chapter also provides an overview of the current state-of-the-art doping techniques employed in the field. Finally, the chapter introduces the fundamentals and operation of various semiconductor devices, including metal-semiconductor interfaces for metallic contacts, the p-n junction, photodiodes, and lastly thin film transistor devices.

2.1. Atomic Layer Deposition

ALD is a form of chemical vapour deposition technique based on sequential, self-limiting reactions, that can produce extremely uniform and conformal thin films, boasting sub-nanometre layer thickness control and excellent tunability of the material properties *via* a variety of deposition variables.[48] Moreover, ALD is a relatively low-cost deposition technique that can be used to grow high quality materials at low temperatures on a wide variety of substrates and geometries, including planar surfaces and more complex topography surfaces such as high aspect ratio 3D geometries.[49] Many different materials can be deposited from the vapour phase using the ALD technique including metals[50,51], oxides[52,53], nitrides[54], sulphides[55], dichalcogenides[56], phosphates[57], including doped, ternary, and quaternary materials, and multilayer structures[58]. Therefore, since the development of the ALD technique began in the 1970s[59], it has become a powerful tool used in both research and industry and has been used to develop materials for a plethora of applications across a wide field of technologies such as microelectronics, photovoltaics, energy harvesting and storage and many more. Some applications of ALD thin films in these industries include: high-k dielectrics for various devices[55], transistors[60], dynamic random access memory (DRAM)[61], LEDs and solar cells[62–64], fuel cells[65], batteries[66–68], supercapacitors[69,70], and catalysts[71]. The use of ALD has thus become ubiquitous in many manufacturing and research technologies, as such the material value of ALD in industry is projected to reach $3.01 billion by 2025.[72]

The primary advantages of the ALD technique are all derived from the highly controllable, sequential, and self-saturating gas surface reactions that govern the deposition process. Typically, ALD is performed using two or more precursors that are sequentially pulsed and allowed to react individually with the surface. These individual gas-surface reactions are termed ‘half-cycles', and the entire combination of half cycles to achieve a single monolayer growth of the desired material is called an ALD cycle.[48] A simplified version of the four typical steps involved in one ALD cycling process is shown below:

1. First gas-surface reaction, typically the chemisorption reaction of the metallic precursor and subsequent ligand exchange
2. Purge process whereby any unreached precursors of gaseous by-products are evacuated from the deposition chamber
3. The second gas-surface reaction involving the counter reactant precursor to form the first monolayer of material
4. Purge process to remove precursor and reaction by-products.

The above process is then repeated in a cyclic manner until the desired thickness of material is achieved.[73] The resultant monolayer and self-saturating growth process promotes the efficacy of the ALD technique for the development of thin film materials on a variety of substrates and structures with complicated topographies. Monolayer growth also offers advanced control of the film thickness and the broad range of deposition parameters available provide excellent control over the type and individual properties of the thin film materials produced. Moreover, the option to perform 'super cycles' composed of multiple ALD processes offers the potential to perform extrinsic doping of materials and the fabrication of ternary and quaternary materials alongside multilayer structures.[58] Further to this, the ALD technique provides a route to tailor made material compositions that would be much harder to achieve using other deposition techniques.[72]

The necessity of the ALD process to deposit materials in a self-saturating regime imposes a series of requirements for the precursors and reactants used in a process including:

- Precursors and reactants must have effective reaction pathways
- Precursors and reactants should be volatile enough to be in the gaseous phase at either room temperature or upon moderate heating
- Whilst in the gaseous phase, the precursors and reactants should not decompose until they have reached and reacted with the sample surface
- Fast and irreversible reactions with the surface groups
- Once reacted, neither the precursor or by-product should etch, dissolve or in any way damage the substrate, growing films or the ALD reactor
- Reactants and precursors should be small enough to avoid reduced surface coverage due to steric hindrance effects

Other considerations include the economic and safety of the materials.[72] For each new material system developed according to the conditions above, careful optimisation of the ALD deposition variables must

be performed to ensure the desired self-saturating ALD process occurs and to achieve the desired material properties. The key deposition parameters that can be varied aside from the precursor and reactant materials include the deposition temperature and factors relating to the purge process. For a given material deposition, the optimal ALD temperature window must be identified to achieve the ideal growth reaction, which is often monitored by the achieved growth per cycle. At temperatures below the ALD window, precursors may condense, leading to non-saturating reactions or an incomplete reaction due to insufficient thermal energy of the precursors. At temperatures above the ALD window, decomposition of precursors prior to the desired reaction or desorption of surface groups may occur (such as $-OH$ species), leading to incomplete surface coverage or saturation.[48,72,74,75] However, even within the ALD window of a given reaction, the deposition temperature has been shown to drastically tune the material properties due to the effect of temperature on the ALD surface reactions.[76] Another important deposition parameter that is often overlooked is the purge times of the precursors and reactants. The ALD purge process must be carefully selected to ensure complete reactions and the full removal of by-products, otherwise gas phase reactions may result, leading to a CVD contribution to the deposition, yielding non-uniform films with limited reproducibility.[63] As a chemical process, inappropriate purge times may also lead to the incorporation of impurities and the growth of poor-quality films.[74] Purge times also dictate the deposition time which ideally should be as short as possible to meet the needs of quick manufacturing processes. The thin film material properties can therefore be largely tuned through variations in the growth parameters. Indeed, one of the most interesting advantages of the ALD process for the deposition of thin films is the ability to vastly change the electronic properties of materials without any external doping, through modification of the intrinsic defect composition by controlling the ALD surface reactions with the deposition parameters.[76] This therefore promotes ALD to the forefront of thin film deposition as it offers ultimate control over the composition and thickness of thin films at the nanoscale.[49]

2.1.1. ALD of ZnO

An attractive quality of using ZnO materials for widescale applications is its ease of large-scale fabrication using a variety of techniques. As such, the deposition of ZnO has been widely researched using all applicable thin film deposition methods from physical vapour deposition techniques such as sputtering, molecular beam epitaxy, and pulsed laser deposition, to wet chemical processes such as sol-gel and spin-coating as well as chemical vapour deposition methods.[10,28,40,77–79] In recent years, with the ever-growing need for smaller and more complicated material topographies, ALD has become one of the most attractive methods to deposit ZnO thin films due to its high conformality, uniformity, and applicability to relatively low temperature growth for polycrystalline films, and superior control over the thickness, composition and thus properties of the ZnO materials.[48,58,72,76,80–82] As mentioned above, the many advantages of ALD arise due to the nature of the self-saturating, sequential chemical reaction processes that occur at the surface of a sample during the ALD process. Sequential pulses of precursor

and reactant gases lead to the self-saturating chemisorption from the gaseous phase onto the surface, resulting in the monolayer growth of thin film materials. Moreover, ALD growth can be achieved using two or more gaseous precursors or reactants to grow a material by separate surface reactions[48] leading to the growth of multiple materials including doped, ternary, and quaternary materials.[58] For ZnO, the most documented ALD reactions used in research and applications is the highly exothermic diethylzinc (DEZ) and water (H_2O) reaction, which therefore requires lower deposition temperatures for ideal growth compared to other ALD ZnO reactions.[83] Other ZnO reactions requiring higher temperatures for ideal growth involve zinc acetate, dimethylzinc, or zinc chloride used as the Zn precursors alongside oxygen, ozone, or nitrous oxide for the O reactants.[82] Aside from the choice of materials used for the ALD process, careful optimisation of the ALD deposition parameters must also be performed to achieve the ideal self-limiting ALD growth. Moreover, even within the ideal growth temperature window for a given ALD reaction, broad tuning of the compositional, structural, and optoelectronic properties of ZnO have been established *via* variations of the deposition parameters due to their effect on the surface chemical reaction processes that control the monolayer growth of the material.[72,76,84,85] Therefore, careful control of the deposition parameters facilitates the production of a broad range of ZnO materials applicable to various applications including LEDs[86–88], solar cells[89–92], thin film transistors[93,94], gas sensors[95–98] and many other thin film and nanostructure based devices.[82,99] The ALD deposition temperature is often researched as having the most impact on the ALD material deposition, and it has been shown that a four order of magnitude variation in electron concentration can be achieved simply by varying the deposition temperature for ZnO.[76] Other parameters that play a significant role in defining the deposited materials properties are variables relating to the purge process which are often overlooked in the literature compared to the deposition temperature.[84,85,100]

2.1.2. Diethylzinc and H_2O ALD Process and Reaction

The deposition of ZnO and relevant surface reactions related to the diethylzinc and water reaction in a conventional thermal ALD system are outlined below. A diagram of a general ALD cycling process is shown in ***Figure 2.1***. Diethylzinc and water readily react as shown below:

$$C_2H_5 - Zn - C_2H_5 + H_2O \rightarrow ZnO + 2C_2H_6 \quad (1)$$

During the typical ALD growth process, sequential and alternating pulses of the gaseous chemical precursors (DEZ and H_2O) that react with the substrate occur, as such the process is divided into two individual reactions known as 'half cycles'. The individual reactions pertaining to the DEZ, and H_2O pulse phases of their individual half cycle are as follows:

$$DeZn\ pulse: -OH + C_2H_5 - Zn - C_2H_5 \rightarrow -O - Zn - C_2H_5 + C_2H_6 \quad (2)$$

$$H_2O\ pulse: -O - Zn - C_2H_5 + H_2O \rightarrow -O - Zn - OH + C_2H_6 \quad (3)$$

For the deposition, a substrate (of suitable surface with readily available $-OH$ dangling surface bonds for the oxide deposition in this case) is loaded into the ALD reaction chamber, which is heated to the desired deposition temperature and is held at vacuum under continuous flow of an inert carrier or purge gas such as N_2 or Ar resulting in a dynamic gas flow regime.

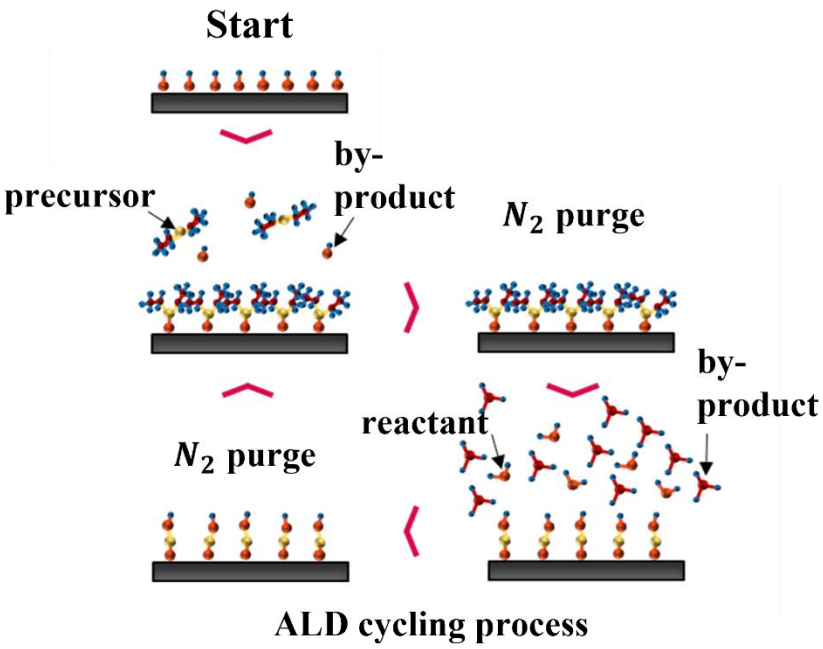

Figure 2.1 *ALD cycling process for a generic reaction.*

The sample is kept in the chamber for a given pre-process purge time to allow for purging of the sample surface and for the temperature of the substrate and reaction chamber to reach equilibrium to ensure uniform deposition. Once equilibrium is reached, the first DEZ pulse is released *via* a heated dose valve that is opened for a certain dose fill time, whereby a careful interplay between appropriate precursor release for full surface saturation and precursor wastage must be considered. For DEZ and H_2O, typical dose fill times are $< 0.5\ s$. The gaseous DEZ molecules are then carried to the deposition chamber *via* the inert carrier gas. Upon reaching the chamber, the DEZ reacts with the substrate surface through the half reaction (2), outlined above, whereby the DEZ molecules form O bonds by fully reacting with all available surface groups such as$-OH$ species (excluding those blocked by steric hinderance). Once the self-limiting and irreversible reaction takes place, the by-product ethane is released and a surface coating of no more than a single monolayer of $-O-Zn-C_2H_5$ species remains. Subsequently, the deposition chamber is purged with the inert gas to remove any unreacted precursor and reaction by-products, after which the first ALD half cycle is completed. The second half cycle then begins, and the H_2O counter reactant is pulsed to the chamber and reacts with the surface $-Zn-C_2H_5$ through mechanism (3). Once the reaction is complete, $-Zn-O-H$ surface groups are formed and C_2H_6 released. A subsequent purge process follows to remove any un-reacted precursor and by-products. The

above process is classed as an ALD cycle and can be repeated until the desired film thickness is achieved. Typical layers of 0.18 $nm/cycle$ are achieved for the DEZ and H_2O reaction.[76,82,83]

2.1.3. ALD ZnO Material Properties

ALD ZnO crystallises in the hexagonal wurtzite structure as shown in ***Figure 2.2***.

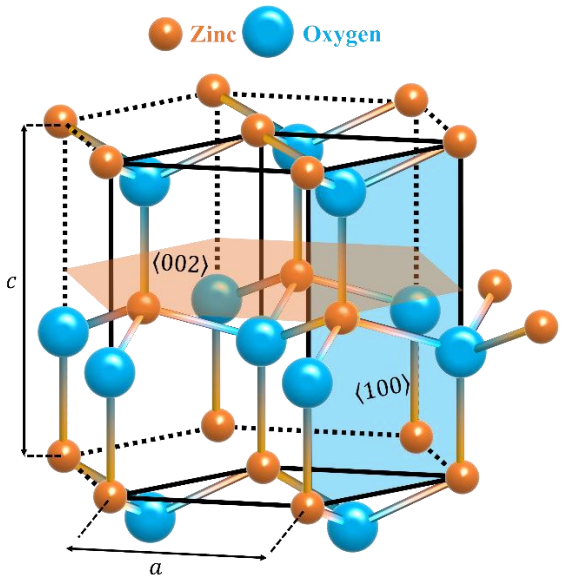

Figure 2.2 *The hexagonal wurtzite structure of ZnO*[101]*, where Zn atoms are represented by the orange spheres, and O atoms represented by the blue spheres. The crystallographic planes* ⟨002⟩ *and* ⟨100⟩ *are indicated by the orange and blue shaded regions respectively, and the c and α axis are identified.*

Typically, films deposited in the ALD growth temperature window between $100 - 200$ ℃ are polycrystalline with two primary growth directions. These prominent crystallographic orientations can be tuned according to the growth temperature, alongside some dependence on the precursor purge time and film thickness. At the lower temperature range of the growth window approaching 100 ℃, ALD ZnO films have preferred orientation in the ⟨002⟩ plane (indicated by the orange shaded region in Figure 2.2) with the surface parallel to the c-axis. The ⟨002⟩ plane is a charged, polar surface due to alternating layers of Zn^{2+} and O^{2-} along the c-axis. Conversely, ALD ZnO films deposited at temperatures in the upper half of ALD growth window have preferential growth with the surface perpendicular to the c-axis, in the ⟨100⟩ plane (indicated by the blue shaded region in Figure 2.2) along the α-axis. The ⟨100⟩ plane is a neutrally charged surface that consists of alternate rows of Zn^{2+} and O^{2-}. For deposition temperatures > 220 ℃, the preferred orientation reverts back to the ⟨002⟩ plane.[72,76,82] However, some variations in the reports of the deposition temperature influence on the preferred crystallographic orientation suggests other deposition parameters also play a role in determining the crystal structure of ALD ZnO.[85] Moreover, the polycrystalline ZnO films deposited by ALD have columnar growth with a granular surface structure that may also be varied according to

the film thickness and growth temperature. Larger crystallises and wider columns are typically obtained for larger film thicknesses and higher growth temperatures.[76]

The origin of the intrinsic electron concentration in nominally undoped ZnO is still under debate and is explored further in Section 2.2.1 but is generally assigned to the presence of intrinsic defects or impurities in the ZnO crystal. In polycrystalline films produced by ALD, the n-type free carrier concentration can be varied between $10^{16} - 10^{19}\ cm^{-3}$ within the ALD temperature window of $100 - 200\ ℃$. Thus, the electron concentration in ALD ZnO is heavily dependent on the deposition temperature.[72,76] This can be understood since the temperature will directly influence the reactivity of precursors on the film surface which has a profound effect on the stoichiometry of the ZnO films. Deviations from stoichiometry have been found to directly impact the electrical properties of ZnO due to the presence native defects and unintentional impurities in the crystal. For ALD ZnO, the ratio of $O{:}\,Zn$ has been found to vary with deposition temperature, namely, at the lower temperature range of the growth window close to $100\ ℃$, ALD growth is O-rich, whereas Zn-rich conditions are obtained for the higher deposition temperatures. Furthermore, the formation energy of intrinsic defects has been found to vary according to O-rich or Zn-rich conditions. Under O-rich growth, the formation energy of intrinsic defects such as V_{Zn} and O_i is reduced and so these defects can readily form. Conversely, Zn-rich conditions reduces the formation energy of Zn_i and V_O defects which can therefore easily form during growth.[76,102] Moreover, high levels of impurity H and C are expected during ALD growth and the incorporation of such impurities in a variety of different defect states and complexes have been found to vary with the ALD growth temperature.[76,103–105] Thus, the deposition temperature can directly tune the type of defects and impurities which play a key role in the electrical activity of ZnO. The effect of precursor pulse and purge times have also been shown to influence the electrical properties through stoichiometric changes, albeit with lower effect.

The optical band gap of ALD ZnO has generally been found to be lower than the expected value of $3.37\ eV$ of ZnO, with reduced E_g values in the range of $3 - 3.32\ eV$ depending on the deposition parameters and film thickness.[76,106,107]

2.2. Doping in ZnO

One of the many advantages of semiconductor materials is the ability to tailor the electrical properties and behaviour towards a plethora of applications either by modifying their intrinsic defect density or *via* the addition of impurity atoms to the crystal lattice of the material through extrinsic doping. These impurity atoms can either be classed as donor or acceptor type extrinsic dopants depending on whether they provide additional electrons or introduce holes to the material lattice which can be explained by the interaction of the dopant atom electronic energy levels with the conduction or valence bands of the crystal. The electronic energy band structure is related to the fundamental crystal structure and defect

composition of a material and can be represented in energy band diagrams (EBD) as a plot of the electronic energy against the electron wave vector. The EBDs of a material can be constructed from first principles density functional calculations and provide details on the electronic configurations in a material. Complex energy band diagrams have been developed for ZnO[108–110], but the core properties of the electronic band structure in ZnO can be represented by assuming isotropic parabolic energy bands for a simpler representation of the core levels. For simplified doping considerations, the main electronic bands of interest are the conduction and valence bands, alongside any defect or dopant states, and the position of the Fermi level energy. During the formation of metal oxides such as ZnO, borderline ionic/covalent bonding occurs due to the electronic charge transfer between the metal atoms (of lower ionisation energy) and the O atoms (with higher electron affinity). In ZnO, the valence band maximum consists of occupied $O2p^6$, $Zn3d^{10}$ and $O2s^2$ states, whilst the conduction band comprises of unoccupied $Zn4s^1$ states. Between the valence and conduction bands, there exists a wide energy band gap resulting from the high strength of the $Zn-O$ bonds.[28,111] The addition of dopant atoms introduces new electronic states to the EBD. Upon addition of donor atoms (atoms that have extra valence electrons compared to the host ZnO atoms), localised electronic states are introduced at the donor site because the extra electron(s) are bound and have localised wavefunctions. The energy band of these donor states, E_d, are introduced at a given energy below the conduction band, E_{CBM}, whereby the energy gap between E_d and E_{CBM} is equivalent to the minimum energy required by an electron to be excited to the conduction band. For shallow donors, this energy gap is small, and the electrons can be readily excited to the conduction band *via* thermal excitation from the lattice vibrations at room temperature. Upon excitation, the electrons exist as free charges in the conduction band that contribute to n-type conductivity, which is increased upon the addition of more and more free electrons. In order to achieve p-type doping, an atom with fewer valence electrons than the host Zn or O atoms is required and is classed as an acceptor type dopant due to its electron accepting behaviour. Doping with an acceptor dopant introduces an acceptor electronic energy level, which for shallow acceptors is introduced at a certain energy above, but close to, the valence band. The acceptor dopant, having a missing electron compared to the host atoms, generates a hole. Providing the acceptor level is shallow, a nearby electron in the valence band can tunnel into the hole position and displaces the existing hole further away from its bound acceptor atom.[112,113] The binding energy of this hole to the acceptor is typically very weak and so, at room temperature, the thermal lattice vibration energy can easily free the hole away from the acceptor and is released into the valence band where it then exists as a free hole and can contribute to p-type conduction. Thus, the semiconductor electrical properties can be readily tuned upon the introduction of donor or acceptor impurity atoms. The technological importance of ZnO based electronic and optoelectronic devices is dependent on the ability to achieve high quality and stable n-type and p-type doped materials. The n-type doping can be readily achieved through intrinsic or extrinsic doping and is explored in Section 2.2.1 and 2.2.2. However, the development of the essential

p-type counterpart remains a huge research challenge within the field. The main challenges associated with achieving p-type doping and the research progress in addressing these challenges are detailed in Section 2.2.3.

2.2.1. n-Type Doping in ZnO: Intrinsic Defects and Impurities

As with many other II-VI semiconductors, ZnO is naturally an n-type material. [10] The origin of this n-type conductivity has been widely debated but is proposed to arise from either intrinsic defects or unintentional impurity atoms.[114] Native point or intrinsic defects arise due to a deviation from the stoichiometry of ZnO caused by imperfections in the crystal lattice, and only involve the constituent elements of the material i.e., Zn and O.[102]

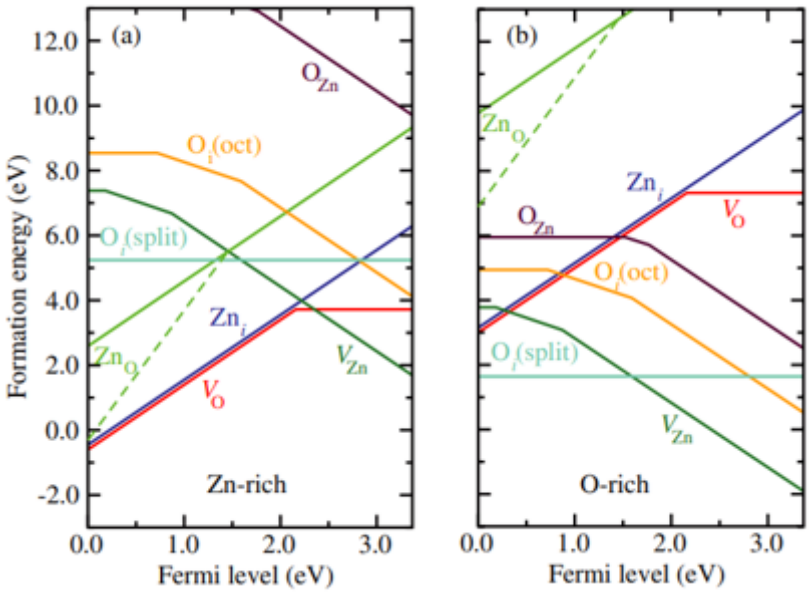

Figure 2.3 *Native point defect formation energies as a function of Fermi-level position in ZnO for (a) Zn-rich and (b) O-rich conditions. The zero of Fermi level corresponds to the valence-band maximum. Only segments corresponding to the lowest energy charge states are shown where the slope of these segments indicates the charge state. Kinks in the curves indicate transitions between different charge states. (Figure reproduced from A. Janotti and C G Van de Walle.*[32,115] *Permission to reproduce this figure was granted by IOP Publishing, Ltd.)*

Traditionally the Zn and O atoms in ZnO are tetrahedrally bound in the hexagonal wurtzite ZnO structure. A variety of different native point defects can form including interstitials (O_i and Zn_i - extra atoms occupying interstitial lattice sites in between the regular tetrahedral bonds in ZnO), vacancies (V_O and V_{Zn} - missing atoms at the regular expected lattice site) and antisites (O_{Zn} and Zn_O - opposite atom occupying the counterpart lattice site). These intrinsic defects may strongly influence the electrical and optical properties of ZnO and play an important role in the doping process and mechanisms. The results of first-principles calculations using density functional theory (DFT) for the formation energy

of different native point defects in ZnO as a function of Fermi level position are shown in Figure 2.3 for both (a) Zn-rich and (b) O-rich conditions. The figure is reproduced from pioneering works by Janotti and Van de Walle in refs [33] and [116] which provide comprehensive insights into the role of native point defects in ZnO and its fundamentals as a semiconductor for the interested reader.

In ZnO, the intrinsic defects most often reported to attribute to the intrinsic n-type conductivity are V_O and Zn_i. However, the limited experimental evidence of these claims are undermined by first principles calculations that reveal that both defects cannot be present as shallow donors in ZnO at high enough concentrations to contribute to the observed n-type conductivity behaviour.[32] Of the two defects, the V_O is the most mentioned defect in the ZnO literature that has been invoked as the source of unintentional high electron concentrations in ZnO[116], but despite having the lowest formation energy among the intrinsic donor defects, DFT revealed that V_O actually form deep level donor states that would require high ionisation energies before contributing electrons to the conduction band and consequently cannot contribute to the n-type conductivity in ZnO.[32] On the other hand, Zn_i, which may act as shallow donors in ZnO and contribute two electrons to the conduction band[102] have been proposed to have a high energy of formation and so are also unlikely to be the origin of high levels of n-type conductivity in ZnO.[32] Therefore, although often ascribed as the origin of the native n-type behaviour in ZnO, it is unlikely that defects such as V_O and Zn_i are the main source of n-type doping in unintentionally doped ZnO. Other potential defects such as O_i, O_{Zn} and Zn_O all have much higher formation energies and so are also discounted from governing the n-type character of ZnO at equilibrium.[102,117] A more probable source of n-type conductivity is from background impurity hydrogen, that may be unintentionally incorporated into the film in high concentrations due to its high mobility and small atomic radius.[118–121] Strong evidence that hydrogen interstitials (H_i) behave as shallow donors that can be present in high concentrations was provided by first principles calculations based on DFT. Such hydrogen interstitials have been revealed to prefer interstitial lattice sites where they can bond to O to form $O - H_i$ complexes.[32] Moreover, H_i have been found to have ionisation energies around $35 - 47\ meV$ and so can behave as shallow donors in ZnO that can be incorporated in high concentrations, leading it to be a promising candidate as the main source of unintentional n-type doping in ZnO.[118,122,123] The behaviour of hydrogen in ZnO is highly irregular, since in most semiconducting materials H_i impurities are found to be amphoteric, only acting as compensating centres that counteract the prevailing conductivity of the material, i.e., in p-type materials H_i exists in the positively charged state whereas in n-type materials H_i exists in the negatively charged state and as such H_i cannot act as a source of conductivity in other materials.[124] In contrast, in ZnO, H_i exclusively exists in the positively charged state and therefore has donor behaviour. Aside from H_i, hydrogen may also be incorporated as the O antisite, H_O, and has also been shown to be a shallow donor in ZnO existing in the positively charged state. The existence of H_O may also help to explain the electron concentration dependence on the presence of O during growth or annealing that is often incorrectly

attributed to V_O, which as explained previously, form deep donor states in ZnO.[32,102,125] Thus, both interstitial and substitutional hydrogen impurities form shallow donors in ZnO that may be readily incorporated in high concentrations during ZnO growth and as such are the most promising candidates to explain the high level of n-type conductivity exhibited by unintentionally doped ZnO.[103,126–128]

1.6.1. Extrinsic n-type Doping in ZnO

The extrinsic doping of ZnO can also be readily achieved to elevate the free electron concentration in ZnO for various applications.[129] Typically, extrinsic doping is achieved by incorporating group III transition metal elements such as Al, Ga, In and B, that are electrically active as donors when substitutionally occupying Zn sites in the lattice.[130–138] Substitutional group-III elements such as Al and Ga have a high solubility in ZnO due to their comparable atomic radius with Zn and induce shallow donor levels leading to the generation of a high density of free electrons in the material. Degenerate doping, defined as inducing free carrier concentrations in the order of $10^{20} - 10^{21}\ cm^{-3}$, can be readily achieved leading to well-known high quality transparent conducting oxides (TCOs) such as aluminium doped ZnO (AZO) and gallium doped ZnO (GZO) that have already been incorporated in a wide variety of TCO applications.[139–143] More recent efforts to improve the mobility of the TCO materials has been proposed by co-doping the group III transition metals with fluorine.[144] Hence, n-type doping in ZnO can be readily achieved and tuned across a broad range of free carrier concentrations by modification of intrinsic defects, background impurities and extrinsic dopants.

2.2.3. p-type Doping in ZnO: Research Bottleneck

ZnO, like many other wide band gap semiconducting materials suffers from a huge doping asymmetry between n- and p-type materials.[36,145] Unlike the n-type material, the achievement of a high level, stable, reproducible, and high-quality p-type ZnO material remains one of the most challenging research bottlenecks in the field.[29,38,41,145–147] Difficulties in producing the ever-elusive p-type ZnO arise due to a variety of reasons including the self-compensation of intrinsic defects that act as hole killers, low solubility of acceptor-type dopants, deep acceptor levels with high ionisation energies, alongside stability issues of the material. Chiefly, the self-compensation in II-V semiconductors has been widely documented.[35,148] The origin of the self-compensation during p-type doping in ZnO may arise from the spontaneous formation of native defects induced during doping, by background impurities such as $O - H$ groups, or by unintentional defects such as acceptor related antisites or interstitials that may all counteract the acceptor induced hole concentration. Spontaneous formation of intrinsic donor like defects upon acceptor type doping occurs because of Fermi statistics, which requires the energy barrier between the Fermi level and valence band to be as small as possible for p-type doping. However, as the Fermi level energy decreases, the formation of native donor defects decreases and so it becomes energetically favourable for the system to spontaneously form intrinsic donor defects that act as hole

killers by annihilating any holes generated by the acceptor impurity.[148] Therefore, during the fabrication of p-type ZnO materials, native donor defects such as V_O and Zn_i can be readily created. Despite the claims that V_O and Zn_i do not lead to the high level of residual n-type conductivity in unintentionally doped ZnO, the spontaneously formed V_O and Zn_i defects upon acceptor-type doping do act as compensating centres, always counteracting the prevailing conductivity and reducing the achievable hole concentration and stability.[32] Moreover, compensation or passivation of acceptor dopants by extrinsic impurities such as hydrogen is also a key issue to be addressed.[149] As such, careful attention should be paid to try to reduce the number of potential compensating centres and background electron concentration in ZnO starting materials for effective acceptor doping.[150] The ability to dope a semiconductor is also limited by the dopant atom solubility in the host lattice. Dopant solubility is related to the energy of formation of the dopant defect it forms, which is dictated by the chemical potential of the dopant and the constituent elements forming the lattice.[151,152] In many cases, acceptor dopants in ZnO have a low solubility into the host lattice particularly into electrically active sites to contribute to p-type conduction. However, even if an acceptor dopant does have a good solubility in ZnO, it is more likely to form a deep level defect state that cannot be readily ionised at room temperature and therefore cannot be activated to contribute p-type conducting holes. Nevertheless, assuming shallow doping is achieved at high levels, the complications associated with the self-compensation of different defects arise, and any free hole carriers are likely to be compensated by the oppositely charged defects and complexes formed during the acceptor doping process.[150] Therefore, several major challenges must be addressed for the realisation of high quality and stable p-type ZnO including improving dopant solubility, minimising donor like defects and background electron concentration to reduce hole compensation, and the production of shallow acceptor states with low ionisation energies. Various research efforts and methods have been attempted to achieve p-type doping in ZnO, these include: the mono-doping of a single group 1 element (Li, Na, K) for substitution of the Zn ion, the substitution of O ions with group V elements (N, P, As, Sb) through mono-doping, the incorporation of highly active groups to form stable acceptor−defect complexes, or by co-doping with both donor and acceptor dopants to enhance acceptor solubility.[38,153] These routes to p-type conduction and research progress so far will be addressed in the following sections.

1.2.4. Mono-Doping for p-Type ZnO

Typically, mono-doping of group I (Li, Na, K) and group V (N, P, As, Sb) has been attempted for substitutional doping on the Zn and O lattice sites respectively to try and achieve p-type conductivity.[29,37,41,154] In early works, Li and Na were investigated for Zn substitution, however the p-type doping efficiency of these elements was found to be limited by the formation of compensating interstitials of the dopants. For example, Li_{Zn} and Na_{Zn} are proposed to induce both shallow and deep acceptor levels in ZnO, however, during deposition the Na or Li may be incorporated at other non-preferential lattice sites such as interstitials where they are expected to introduce donor levels in ZnO

and therefore both group I elements act as amphoteric impurities. The substitutional and interstitial forms of the group I elements may therefore coexist at equivalent levels in ZnO, whereby any acceptor levels induced by the substitutional sites would be compensated by the hole-killing interstitials and consequently p-type conductivity cannot prevail. Research focus for acceptor doping in ZnO by group I elements therefore needs to focus on the activation of the interstitial dopant elements into preferential substitutional lattice sites for effective doping.[32] Among the group V elements, P and As are proposed to form deep acceptor states, and Sb is suggested to result in even deeper acceptor levels, and therefore should not contribute to p-type conductivity upon substitution of the O site. Despite this, p-type doping with P, As, and Sb have all been reported, including through complexes with V_{Zn} which may lead to shallower acceptor states.[155] The formation of such complexes are, however, not considered to be energetically favourable, raising questions as to the reliability of the p-type doping and lack of understanding of the induced acceptors.[32] Of the group V elements, N has the most comparable atomic radius to O and therefore would induce minor strain to the lattice and so is a more energetically favourable substitutional dopant. Additionally, N has similar energy values of the valence $2p$ states and an electronegativity akin to that of O. Therefore, N has been identified as the most promising candidate for acceptor doping in ZnO.[38] Despite this, the $Zn-N$ bonding energy is suggested to be relatively weak, limiting the stability of the doping and making it challenging to incorporate large amounts of N dopants that have good thermal stability in the material. Several groups have reported on N doping in ZnO, with claims of achieving the desired N_O substitutional site.[29,32,37,38] However, reports of the p-type conductivity induced by N doping, as with the other acceptor candidates mentioned previously, are generally considered controversial, since many of the reports are not substantiated by further experiments or research, indicating a lack of reproducibility, fuelling scepticism in the field. Moreover, the shallow or deep nature of the N_O acceptor is not well established, although reports that the N_O substitution is a deep level acceptor raises further questions to the efficacy of the N_O as a relevant acceptor dopant for p-type conduction in ZnO.[42,156]

1.6.2. Intrinsic Acceptor-like Defects and Complexes

The predicted most prominent acceptor-like intrinsic defects in ZnO is the, V_{Zn} point defect. The removal of a Zn atom from its regular position of the lattice induces three partially filled degenerate energy states in the bandgap just above the valence band maximum. These states can accept up to two additional electrons from the valence band, where upon excitation of the electrons to the V_{Zn} states, holes are produced in the valence band that may contribute to p-type conduction, thus V_{Zn} is an acceptor like defect in ZnO.[32] In n-type ZnO, V_{Zn} can form more easily due to the decrease in formation energy of acceptor like defects as the Fermi level energy increases towards the conduction band in n-type materials. Moreover, V_{Zn} have been identified as the most dominant compensating defect centre in n-type ZnO materials. [157,158] Contrastingly, in p-type materials, V_{Zn} have high formation energies and

therefore cannot exist in high enough concentrations to induce dominant p-type behaviour. Moreover, the V_{Zn} has a high energy of formation and is proposed to exist as a deep level acceptor in ZnO and so is unlikely to contribute to p-type conductivity.[102] However, complexes involving V_{Zn} and other intrinsic and extrinsic defects have been suggested to be hole providers in ZnO, including $V_{Zn}, V_{Zn} - V_{Zn}, V_{Zn} - V_O - V_{Zn}$clusters,$V_{Zn} - N_O, V_{Zn} - N_O - H, 3V_{Zn} - N_i$, and $As/Sb_{Zn} - 2V_{Zn}$.[153,155,159–165]

1.6.3. Co-doping

To overcome the low solubility of acceptor dopants, the co-doping of both acceptors and donors has been proposed as a potential route to achieve high level and stable p-type conduction in ZnO. The intentional simultaneous introduction of hole producing acceptors alongside donors is proposed to increase the solubility of the acceptor dopant by lowering both the lattice energy and the acceptor defect formation energy.[43,45,46] This is achieved by choosing acceptors and donors that form bonds with increased strength versus the host lattice element-acceptor dopant bond, minimising the ionic potentials and lowering the Madelung energy (which is related to the electrostatic potential energy of single point charges in an ionic crystal).[44] The doping of donors and acceptors to achieve p-type conductivity seems counterintuitive since the donor dopant should act to compensate the acceptor induced holes. During growth, compensation effects may be beneficial, since the donor doping would shift the Fermi level energy away from the valence band towards the centre of the gap. This increase in Fermi level energy leads to both an increased formation energy of intrinsic compensating defects such as V_O and Zn_i, whilst lowering the formation energy of acceptors, thereby increasing the acceptor solubility whilst minimising the compensation from intrinsic donor-like defects.[32] However, the compensation effect of the intentionally induced donor may persist after growth, inhibiting the acceptor induced p-type conduction. Overcoming the donor compensation may be addressed by incorporating complexes consisting of two acceptors and one donor, or by using donor impurities that may be weakly bound to the acceptor dopant and have high enough diffusivity that they can be readily removed from the acceptor by annealing, inducing the subsequent activation of the acceptor dopant for effective p-type conduction. The co-doping method involving the incorporation of two acceptors and one donor was proposed by Yamamoto to increase acceptor solubility by introducing acceptor-donor-acceptor (A-D-A) complexes on nearest neighbour substitutional lattice sites within the host crystal.[43] The strong interaction between the co-dopants lowers the acceptor and raises the donor energy levels in the band gap. This energy band adjustment combined with the enhanced acceptor solubility allows the acceptor orbitals to overlap sufficiently, introducing broader and shallower acceptor states near to the valence band and reducing the acceptor ionisation energy. The abundance of acceptors can therefore be easily ionised to form delocalised holes for effective p-type conduction.[43,46] Aluminium and N have been identified from the literature as promising co-dopants in ZnO.[166–172] The Aluminium donor dopant can be readily substituted into nearest neighbour sites, and since the affinity between Al and N is much higher than that of $Zn - N$, the two N acceptors may much more readily bond to the aluminium to form $N - Al -$

N trimer complexes. Therefore, enhancing the solubility of N to incorporate larger quantities of the now shallow N acceptors to induce high level and stable p-type conductivity. A similar increase in acceptor solubility is expected by another co-doping method involving the incorporation of acceptor dopants alongside donor dopants that weakly bind to the acceptor dopant and have high enough diffusivity that they can be readily removed from the acceptor by annealing. This may be achieved by the introduction of hydrogen into the material, which is often readily incorporated into films through growth process due to its high mobility and small ionic radius. The hydrogenation of acceptor dopants such as N allows for better dopant incorporation in ZnO since the hydrogen may readily bond to the N by donating an extra valence electron to the N acceptor in the $N-H$ bond to form an 'O-like' defect complex. However, in the $N-H$ bond, the hydrogen passivates the acceptor-like properties of the N atoms, rendering them inactive as acceptors.[149] Moreover, hydrogen has been demonstrated to increase the N concentration in ZnO but with the expected passivation effect limiting the resultant p-type behaviour.[149,173–176] To overcome this passivation effect, the weakly bound $N-H$ bond could be broken by the application of a suitable heat treatment that can simultaneously break the $N-H$ bond and provide enough energy for the highly mobile passivating hydrogen to diffuse out of the film, thereby activating the N dopant as a shallow acceptor. Relatively few works report on such defect engineering in ZnO[173–180], however a route to p-type GaN was only realised upon the removal of passivating hydrogen impurities and so is an interesting avenue of research for the development of p-type ZnO. Such an approach is, however, dependent on the binding energy and dissociation of the acceptor-hydrogen complexes, the barriers for hydrogen removal and the identification of a suitable post growth annealing method for efficient and effective hydrogen removal without inducing other donor-like defects.

Whilst some promising strategies for achieving acceptor doping in ZnO have been presented, scepticism still exists in the field arising from a lack of stability in the p-type conduction induced and a lack of reproducibility of the results. However, amongst the literature, p-n junction diode-like behaviour has been reported including photoconductivity behaviour and electroluminescence from ZnO p-n homojunction devices, which when considering the fundamentals of device physics[112], proves the existence of p-type ZnO materials developed in these works.[4,5,10,23,28,39,41,167,181–195] However, whilst the reported devices are of interest to study the physics and technology of ZnO based p-n junctions, most of the reported devices are far from being optimised for commercial use due to poor performance arising from the low quality of the p-type materials and limited lifetimes of the devices.[5] Moreover, a failure to reproduce the results reported for further work by most research groups suggests a lack of reproducibility, which raises further concerns regarding the reliability of the methods used so far to achieve p-type conductivity in ZnO. Thus, further research efforts are necessary for the development of high quality, stable and reproducible p-type ZnO materials for implementation and development of efficient p-n homojunction based devices with long lifetimes for commercial use.

2.3. Doping Techniques

The introduction of dopants to a semiconductor crystal lattice may be achieved by a variety of conventional methods including the introduction of dopant atoms during epitaxial growth to form uniformly doped layers, alloying, thermal diffusion of dopant impurities, or ion implantation.[196–198] Diffusion and ion implantation also offer the benefit of performing selective area doping which is desirable for fabrication of many micro-patterned devices. In thermal diffusion doping, atoms from either the solid, liquid, or gaseous phase diffuse throughout a material due to thermal motion through various mechanisms along a concentration gradient. In this process, atom incorporation is limited by the solid solubility limit. Alternatively, ion implantation utilises accelerated ions hitting and penetrating a material typically to a depth in the range of hundreds of nanometres. The process does however require high implantation energies that can often cause damage to the material. Compared to doping *via* diffusion processes, ion implantation is attractive due to its superior control over the doping profile and reproducibility, but the damage to the material by the high energy ions often requires an ultra-high temperature annealing process to reverse the damage and remove any defects that were formed.[199] However, in most of the above processes, the dopant atoms typically are not introduced into preferential lattice sites and are more often introduced into electrically inactive interstitial lattice sites. A post deposition annealing step is therefore often required to activate the dopants into the desired substitutional lattice sites for effective doping. Conventionally this annealing is achieved by methods such as rapid thermal annealing or furnace heating, however both methods require extremely high temperatures to be effective and as such are associated with an undesirable high thermal budget.[200] Moreover, these thermal methods induce transient enhanced diffusion and too low conductivity due to ineffective activation of dopants which therefore cannot lead to desirable dopant profiles.[201] With the ever-growing emerging need for low thermal budget processes, laser annealing (LA) presents itself as a rapid, large scale, low thermal budget (minimising damage to the film and substrate due to the selective absorption capability of the laser) alternative post processing method to conventional thermal annealing to produce high-quality materials.[202] During the LA process, the laser irradiates the surface of a material with high energy photons, where they are then absorbed by the material. The photon energy is then rapidly converted into thermal energy, generating a highly localised heating of the material with a thermal gradient from the material surface to the underlying layers. The LA can therefore induce a highly localised and controlled thermally assisted modification of the film's microstructure, defect density, crystallite size, internal strain and film stress and crucially the efficient activation of dopants into preferential lattice sites for the associated modulation of the optical and electrical properties of thin films.[203] LA is therefore an attractive alternative to conventional annealing process for the activation of dopants, and as such is rapidly becoming one of the only practical solutions to reduce thermal budget during fabrication of materials such as metal oxides.[201]

More recently, the concept of using the LA process to actively incorporate dopant atoms from either a solid, liquid, or gaseous dopant phase into a material have been investigated.[204–218] Laser doping from the three state phases is achieved either by depositing dopants in a solid form above the material surface, submerging the material surface in a dopant containing liquid or solution or by placing the material in a gaseous environment containing the dopant atoms prior to or during the laser annealing process. Of the three routes, laser doping induced from the solid or liquid dopant phases have been the most documented, whereas at the time of writing, only few reports seemingly exist for the gas immersed laser doping method for materials such as Si, SiC, and GaAs and remains lacking for alternate material systems such as metal oxides.[206,207,213,214,217,219] The gas immersion laser doping is based on the ability of the laser to both melt a controlled thickness of a material placed in a dopant environment and to photo-dissociate the gaseous dopant molecules before their chemisorption into the material surface where they then diffuse to a certain depth of the film depending on the material being processed and wavelength of the laser.[216] The dopant impurities are incorporated into electrically active sites by the laser induced thermal energy (negating the need for subsequent annealing as with other doping processes) and at concentrations exceeding the solid solubility limit due to the melt process. Moreover, the incident laser energy is converted to thermal energy at the sample surface, and as such the process of melting and recrystallisation is localised at the uppermost layer of the material ($< 100\ nm$ depth) occurring in less than $100\ ns$ due to the ultra-short laser pulse.[220]

This leads to another one of the most striking advantages of the laser doping technique, particularly when performed with short wavelength UV lasers, whereby the localised surface heating and shallow penetration depth of the UV photons enables shallow diffusion of dopants in each thickness of material. The depth of which can be modified by varying the laser processing parameters such as number of pulses and laser energy density. Ultra-shallow doping is essential to meet the needs of sub $100\ nm$ devices, where vertical depth of the p-n junction region incorporated in the devices must scale to maintain predictable performance.[201] Currently, shallow junction scaling has been achieved *via* ion implantation performed at ever decreasing acceleration voltages. However, the ion implantation scaling approach has increasing complexity to meet the needs of new technologies, leading to the necessity to develop alternate shallow doping strategies more suitable to the fabrication of shallow junctions below $100\ nm$.[220] Therefore, laser induced doping can be classed as an ultra-fast, low thermal budget technique capable of highly localised ultra-shallow doping, which is highly desirable for the modern semiconductor industry, leading it to be one of the most promising approaches being evaluated as an alternative to conventional high thermal budget doping techniques. Moreover, the technological gain is further accompanied by a reduction in manufacturing costs by eliminating many of the fabrication steps associated with ion implantation.[220]

Further to this, one of the other technological challenges faced in the semiconductor device industry is the ability to fabricate both lateral and laterally printed vertical p-n junctions which are the building

blocks for various advanced devices.[202] Traditionally, this may be achieved by spatially resolved selective doping by either selective diffusion or ion implantation methods or by selective area epitaxial regrowth methods - all of which require excessive fabrication steps, increasing both cost and complexity.[202] Alongside this, despite decades of development in mature Si based technology[220–222], it remains a huge bottleneck in the development alternate material based lateral devices, particularly for one of the leading potential alternate material candidates for high power devices, GaN, which suffers severe damage upon ion implantation and requires ultra-high temperature annealing to recover the damage.[202] The high temperature annealing may also introduce unwanted defects within the material which may contribute to undesirable material properties and device failure. Thus, the development of new techniques is vital if alternate material technology seeks to replace the current Si dominated market. Laser doping therefore lends itself as an attractive candidate to achieve laterally patterned devices due to its finer spatial resolution and control of the doping area and the potential for ultrafast scanning and patterning at near sub-micron scales.[204,208,216,223–229] Thus, laser doping may be used to achieve ultra-shallow doping to produce nano-dimension p-n junction devices that can be both lateral (upon optimisation of laser processing parameters and device dimensions) or laterally patterned vertical p-n junction devices for new advances in alternate material technology which had been previously overlooked, particularly for metal oxide-based material systems.

2.4. Metal Contacts

A prerequisite for optoelectronic and electronic device fabrication is the development of metal-semiconductor (M-S) contacts which are one of the most essential building blocks for virtually all semiconductor devices and are crucially important for both optimal device performance and accurate characterisation of the devices and their constituent materials. When a metal and a semiconductor are brought into intimate contact, electron transfer between the two materials occurs until equilibrium is reached. The nature of the interface formed between the metal and semiconductor is dependent upon a range of factors, however for the ideal case, the main factors dictating the type of contact formed are the metal work function, Φ_m, the semiconductor work function, Φ_s, the semiconductor electron affinity, χ_{sc}, and the type of semiconductor material (either n-type or p-type).[230,231] In practice, surface states at the interface also have significant impact on the formation of the junction by introducing different paths of conduction, in turn modifying the barrier height formed between the two materials.[232] The two main types of M-S junctions are categorised as either Schottky or Ohmic contacts.[233] Schottky contacts exhibit rectifying behaviour and produce asymmetric current-voltage characteristics due to a large potential barrier formed at the interface between M-S. Conversely, Ohmic contacts are non-rectifying and allow an unimpeded transfer of majority charge carriers across the interface independent of the polarity of applied voltage, thus exhibiting linear I-V characteristics according to Ohm's law.[231] Most high-performance devices and a variety of measurement techniques require good Ohmic metal contacts with negligible contact resistance for unimpeded device performance and accurate characterisation. The

development of Ohmic contacts to both n- and p-type materials is therefore the focus of the contact investigations in this work. The next few sub sections look further into Ohmic contact behaviour and the materials used to form Ohmic contacts to ZnO.

2.4.1. Ohmic Contacts

An Ohmic contact is a junction that forms between a metal and semiconductor that does not limit the current flow. The current flowing across the junction is therefore essentially only limited by the bulk resistance of the semiconductor material away from the contact region, rather than due to the thermal emission rate of carriers across a potential barrier as in Schottky contacts.[113] Ideally, a metal-semiconductor interface results in Ohmic contact if the barrier height, Φ_B, is 0, whereby the carriers are free to flow to and from the semiconductor with minimal resistance at the contact.

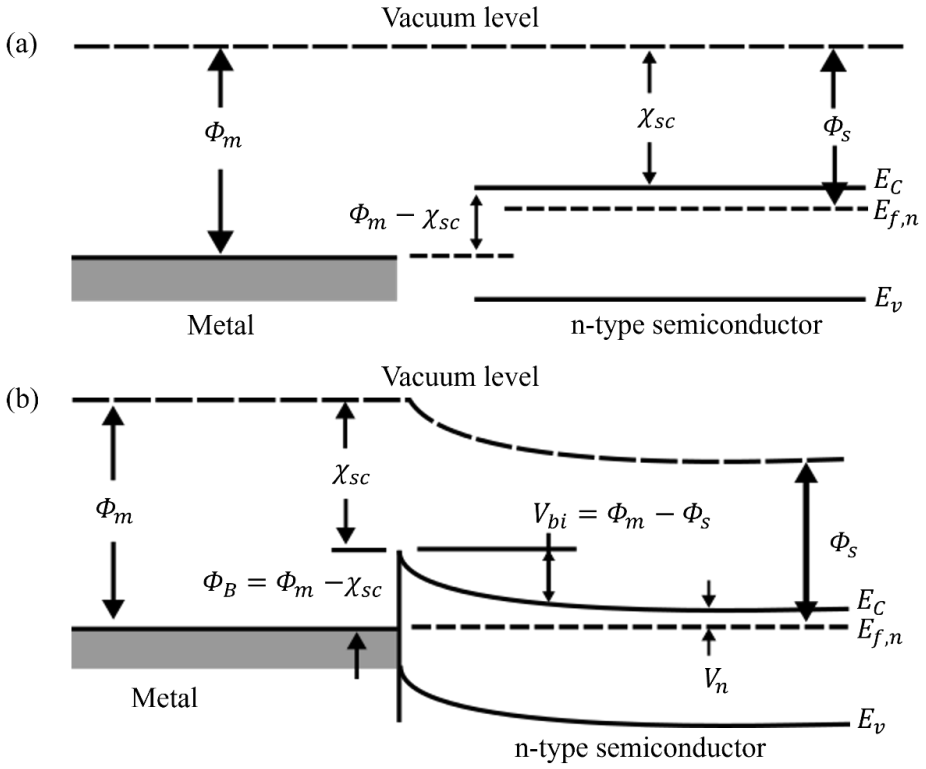

Figure 2.4 *Example simple energy band diagrams for metal-semiconductor junction (a) before and (b) after contact to an n-type semiconductor material of work function, Φ_s.*

For sufficiently high doping levels, the dominant carrier transport mechanism in Ohmic contact is tunnelling according to field emission, whereby the depletion region that forms between the metal and semiconductor is so narrow, and the doping sufficiently high, that carriers can tunnel through the full barrier width. Thus, the formation of Ohmic contacts to a semiconductor material can be achieved by either reducing the barrier height to increase thermionic emission or by increasing the surface carrier concentration of the semiconductor so that the barrier width narrows enough for carriers to tunnel through due to field emission.[234] The typical material requirements for formation of Ohmic contact to

an n-type semiconductor is that the work function of the metal, Φ_m, must be close to or smaller than the electron affinity, χ_{sc} of the semiconductor, i.e., $\Phi_m \leq \chi_{sc}$. Conversely Ohmic contact formation to a p-type semiconductor requires $\Phi_m \geq \chi_{sc} + E_g$, where E_g is the band gap energy of the semiconductor material. Therefore, careful consideration must be taken when selecting materials to form Ohmic contacts according to the semiconductor properties and the metal work function. **Figure 2.4** shows example simple energy band diagrams for metal-semiconductor junction (a) before and (b) after contact to an n-type semiconductor material of work function, Φ_s. When bought into contact and under thermal and chemical equilibrium, the Fermi level of the materials must align, leading to a band bending and the formation of a built-in potential barrier of certain height and width caused by the different work functions of the metal and semiconductor. The potential barrier between the semiconductor conduction band and metal Fermi level includes a difference between the semiconductor conduction band energy and the Fermi level. For Ohmic contacts, a small potential difference and a negligible depletion region is induced, and this small Ohmic barrier allows ease of charge flow with small applied bias.[113,230,231] Any contact between metal and semiconductor results in linear I-V characteristics regardless of bias polarity. Contact resistance is the measure of ease with which a current can flow across a metal-semiconductor interface. In a length L of uniformly heavily doped semiconductor with Ohmic contacts at either end of the material, an applied voltage, V, introduces a spatially uniform current, I, through the semiconductor bulk and the Ohmic contacts of cross-sectional area, A, with resistance, R. Under the low current assumption, the I-V relation becomes,

$$V = V_{bulk} + 2V_{contact} = (R_{bulk} + 2R_{contact})I \tag{2.01}$$

where,

$$R_{bulk} = \frac{dV_{bulk}}{dI} = \frac{\rho L}{A} \tag{2.02}$$

$$R_{contact} = \frac{dV_{contact}}{dI} = \frac{\rho_c}{A} \tag{2.03}$$

Where ρ is the resistivity of the bulk material, and ρ_c is the specific contact resistivity which is the important electrical characteristic property of Ohmic contacts and can therefore be defined as:

$$\rho_c = \frac{1}{2}\left(\left(\frac{AV}{I}\right) - \rho L\right) \tag{2.04}$$

2.4.2. Ohmic Contacts to ZnO

The achievement of acceptable ZnO device characterization and realisation of practical devices relies heavily upon developing good Ohmic contacts with low specific contact resistance for both n- and p-type materials. ZnO as a material resides at the border between covalent and ionic semiconductors, and

therefore the formation of Ohmic contacts to ZnO with low contact resistance can be achieved by either reducing the barrier height according to the material work function and electron affinity as in ionic semiconductors or by increasing the surface carrier density so that the barrier width becomes sufficiently narrow for carriers to tunnel through as is the case for many covalent semiconductors.[233,234]. As previously mentioned, Ohmic contact formation to n- and p-type materials is dependent on the metal work function and the semiconductor electron affinity. ZnO is typically reported to have an electron affinity of around 4.35 eV, but has been shown to be tuneable between $3.5 - 4.7\ eV$.[235–237] For the case of n-ZnO, metals such as $Al, Ti, Au, In, Pt,$ and Ag have been used in either single element contacts or as alloys in systems such as Ti/Au or Al/Pt to achieve Ohmic contact. As such, lots of progress has been made in the development of metallisation schemes for Ohmic contacts to n-ZnO with contact resistivities between $10^{-1} - 10^{-8}\ \Omega cm^2$ being reported in the literature.[233,234,238] Advances have also been made in the development of Ohmic contacts to p-ZnO, with efforts into Au, Pt, Ni, and Ni/Au, Ti/Au and Ni/Pt metallisation schemes being reported in the literature with contact resistivities as low as $10^{-6}\ \Omega cm^2$ achieved.[233,239–243] However, as well as achieving stable and high hole carrier concentration, further research into the development of low contact resistance Ohmic contact to p-ZnO is still required and remains a challenge in the field. In this work Al, Au and Pt metallisation schemes are investigated for Ohmic contact formation to the n- and p-type material.

2.5.P-N Junctions

The p-n junction is the fundamental building block of many electrical and optoelectronic devices. Developments in p-n junction technology have led to enormous advances in applications such as LEDs, semiconductor lasers, photodetectors, solar cells, and transistors which are all based on p-n junction principles.[10] The formation of a p-n junction is achieved when an n-type and p-type semiconductor material are brought into contact.[244] Upon contact, holes from the p-side diffuse to the n-side of the junction, whilst electrons diffuse from the n-side to the p-side, revealing immobile ionised negatively charged acceptor atoms and positively charged donor atoms on the p and n side of the junction respectively. Upon diffusion, the mobile holes and electrons recombine forming a depletion region or space charge layer which acts as a barrier for further diffusion of mobile carriers from both sides of the junction.[113] The built-in potential at the p-n junction allows for the rectification of current, whereby there is an asymmetric current flow across the junction, i.e., current can flow easily in one direction but is limited in the other. This rectifying behaviour is the basic function of a diode that can be exploited for various applications. The basics of p-n junction operation under different bias conditions is explored further below.

2.5.1. P-N Junction Basic Operation

For a p-n junction under zero bias and at equilibrium, there is no net current since the diffusion current of electrons and holes is balanced by the drift current of the carriers driven by the built-in field. However, if an external bias is applied across the p-n junction, it will no longer be in an equilibrium state and current starts to flow through the junction. This current is dependent on the polarity of the applied external bias: forward or reverse. Studying the energy band diagram for the case of p- and n-type materials can be used to understand the ideal p-n junction operation. **Figure 2.5 (a)** shows the energy band diagrams for an n- and p-type semiconductor of the same material when the semiconductors are isolated from each other.

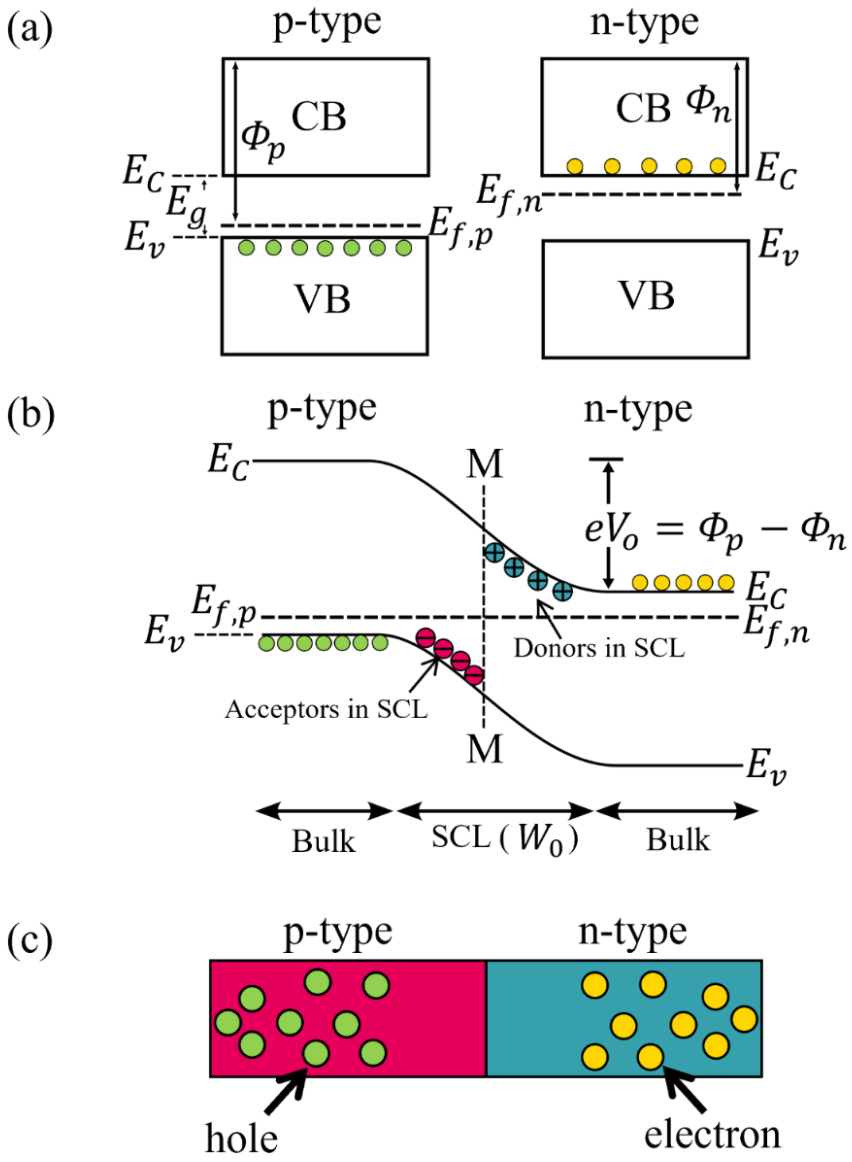

Figure 2.5 *Simple energy band diagrams of (a) n- and p-type semiconductor materials and (b) a p-n junction at equilibrium under zero bias. A simplified schematic of a p-n junction under zero bias is shown in (c).*

The p-type material contains mobile holes in the valence band and the Fermi level, $E_{f,p}$ is Φ_p below the vacuum level and close to the valence band, E_v. Conversely the n-type material contains mobile electrons in the conduction band, and the Fermi level, $E_{f,n}$ is Φ_n below vacuum and lies close to the conduction band, E_c. As such, the Fermi energy is dependent on the carrier concentration and the two are related for n- and p-type materials through:

$$n = n_c e^{\left(\frac{E_f - E_c}{k_B T}\right)} (n-type) \tag{2.05}$$

$$p = p_v e^{\left(\frac{E_v - E_f}{k_B T}\right)} (p-type) \tag{2.06}$$

Where n and p are the electron and hole carrier concentrations, n_c and p_v are the intrinsic carrier concentrations in the conduction and valence bands respectively.[112,113,230,231] If the two semiconductors were brought into contact to form a p-n junction, at zero applied bias, there would be an abrupt discontinuity between the n- and p- regions and a charge carrier concentration gradient would exist across the junction from majority holes in the p-region to minority holes in the n-region, and majority electrons in the n-region to minority electrons in the p-region. As a result of this concentration gradient, upon contact under zero bias, the two materials must equilibrate, and so majority holes in the p-region and majority electrons in the n-region diffuse across the p-n junction. When these mobile charges meet at the interface, they recombine near the junction. As a result of recombination, the junction region becomes depleted of free charge carriers compared with the bulk n- and p-regions away from the junction. The migration of holes from the p-side leaves behind negatively charged acceptor ions, N_A, and the diffusion of electrons exposes positively charged donor ions, N_D, around the junction. There is therefore a depletion region or space charge layer (SCL) formed by these exposed charged ions either side of the metallurgical junction. The immobile charged donor and acceptor ions induce an electric field or potential difference across the junction known as the diffusion voltage or built-in potential, V_0, which is the energy potential a charge carrier now requires to surmount the energy barrier and diffuse across the depletion region of the junction and is defined as:

$$V_0 = \frac{k_B T}{q} ln\left(\frac{N_A N_D}{n_i^2}\right), \tag{2.07}$$

$$n_i^2 = (N_A N_D) e^{\left(-\frac{eV_g}{k_B T}\right)}, \tag{2.08}$$

Where, k_B is the Boltzmann constant, T is temperature, q is the electric charge, n_i is the intrinsic carrier concentration, and V_g is the bandgap energy expressed in volts (i.e., $V_g = E_g/q$).

This built-in potential imposes an electric field on the junction inducing a ‘drift current’ of charge carriers in the exact opposite direction to the diffusion current therefore acting to oppose the diffusion

current. At zero bias, the drift and diffusion currents will continue until the two opposing fields become equal and the system reaches a thermal equilibrium. For a p-n junction system at equilibrium, the Fermi energy across the entire junction must be consistent, i.e., the fermi level of the two semiconductors, once brought together, must be uniform across the p-n junction. The energy band diagram of a p-n junction at equilibrium is shown in Figure 2.5 (b). This Fermi level equilibrium condition leads to band bending of the conduction and valence bands of the separate semiconductors around the junction due to the difference in E_f between the two materials. This band bending not only accounts for the carrier concentration gradient in this region, but also for the effect of the built-in potential. The significant implication of Equations 2.07 and 2.08 reflects the dependence of the built-in voltage, and hence I-V characteristics, of a p-n junction on the bandgap of the constituent materials (*via* V_0).

Once the built-in potential V_0, is known, the width of the depletion region, W_0, can also be determined:

$$W_0 = \left[\frac{2\varepsilon V_0}{q}\left(\frac{1}{N_A}+\frac{1}{N_D}\right)\right]^{\frac{1}{2}}, \tag{2.09}$$

Where ε is the permittivity. From Eq. 2.09, it can be deduced that the depletion width is mostly dependent upon the lighter doped side of the p-n junction and thus most of the depletion region will be in the light doped material. This can have a significant impact on the device performance and operation.[112,113,230,244]

2.5.2. Forward Bias

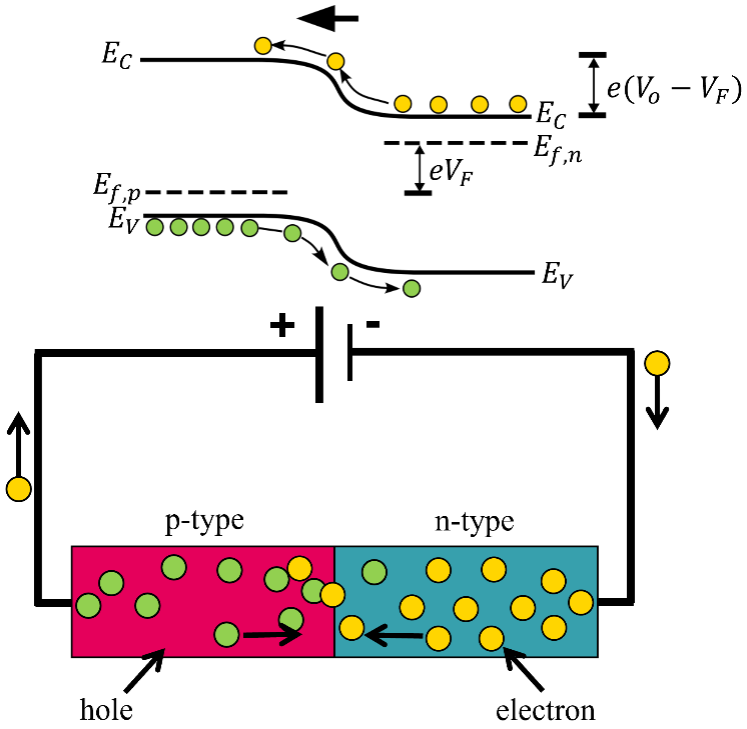

Figure 2.6 *Energy band diagram and simple circuit of a p-n junction under forward bias.*

Figure 2.6 shows the energy band diagram and simplified schematic for a p-n junction under forward applied bias, V. Under forward bias conditions, most of the applied voltage drops across the space charge layer, since the SCL region has been depleted of carriers when compared to the bulk semiconductor materials away from the junction. Thus, the applied voltage, V_F, is in the opposite direction to the built-in electric field, and consequently the potential barrier, V_0, is reduced by V_F ($V_0 - V_F$). The electrons on the n-side and holes on the p-side, can now readily overcome the lowered potential barrier to diffuse cross the depletion region to the other side of the junction – i.e., there is an injection of minority carriers across the junction. As the minority carriers diffuse across the junction, there is some possibility of recombination events, however the diffusing carriers are readily replenished by the terminal of the battery connected to the devices, maintaining the carrier injection across the junction.[113] Therefore, a current can readily flow and be maintained throughout the p-n junction under forward bias conditions. There is, however, some drift current due to majority carriers being affected by the new field, so the net current under forward bias is a combination of both drift and diffusion currents. The current flow through a forward bias p-n junction diode can be described by the ideal diode or Shockley diode equation:

$$I = I_0 \left[exp\left(\frac{qV}{nk_BT}\right) - 1 \right] \tag{2.10}$$

Where n is the ideality factor of the diode and is unity for a perfect diode.

2.5.3. Reverse Bias

When a reverse bias is applied across the junction, the voltage applied once again drops mainly across the depletion region. However, in this case, the applied voltage, V_r, now adds to the built-in voltage and so increases the built-in potential to $V_0 + V_r$. **Figure 2.7** shows the energy band diagram and circuit schematic for a p-n junction under reverse bias, V_r. Under reverse bias conditions, the charge carriers either side of the junction will be attracted towards the terminal on their respective sides, moving them further away from the SCL, exposing more immobile charged donor and acceptor ions, in turn widening the depletion region and increasing the built-in voltage/ internal electric field. The current flow across the SCL therefore becomes very small, and only a few carriers will be thermally excited across the junction, resulting in a small leakage current in reverse bias. Under sufficiently high reverse bias, a junction breakdown will occur *via* either avalanche or Zener mechanisms. Avalanche breakdowns tend to occur in moderately doped p-n junctions, whereby impact ionisation due to sufficiently high electric field generates electron-hole pairs, exciting the electron from the valence to the conduction band, in turn increasing the current flow through the avalanche effect. Conversely, Zener breakdown occurs in heavily doped junctions, where the depletion region can be narrow enough for electrons to tunnel through the junction under sufficiently high reverse bias inducing current.[113,230,245]

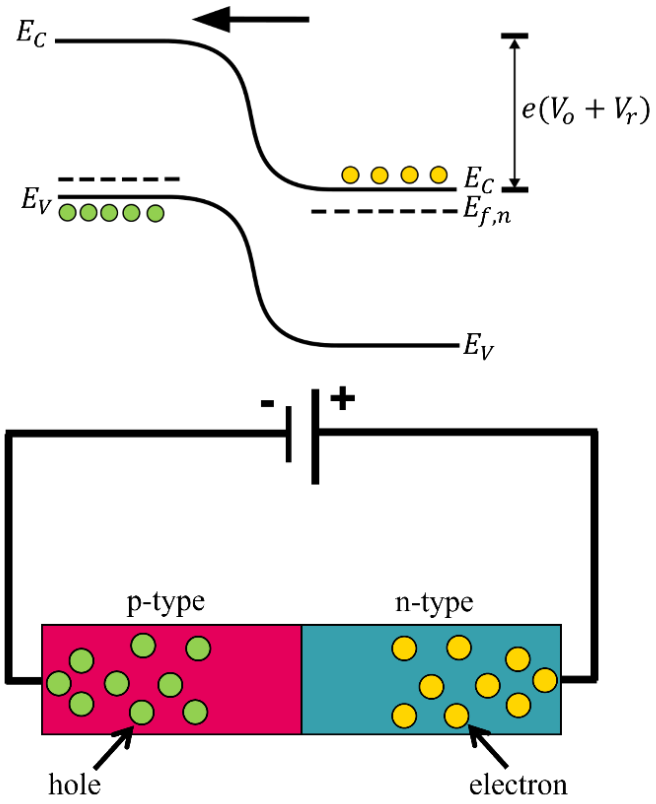

Figure 2.7 *Energy band diagram and circuit schematic for a p-n junction under reverse bias, V_r.*

2.5.4. Light Emitting Diode

The LED is a type of p-n junction that can emit light when a forward bias is applied across the junction *via* electroluminescence. For a p-n junction made up of a direct band gap semiconducting material, the application of a positive electric field causes the free electrons in the conduction band of the n-type region to recombine to with the holes in the valence band of the p-type region of the device *via* a radiative process. In doing so, the electron moves from a high energy potential in the conduction band to a lower energy in the valence band and the residual energy from this transition is emitted in the form of a photon, with energy proportional to the bandgap of the materials forming the p-n junction. For p-n junctions consisting of indirect bandgap materials, under forward bias, electrons recombine with holes *via* non-radiative processes and the excess energy dissipates as heat within the device and thus does not produce any optical emission. ZnO, however, is a direct gap semiconducting material with a wide bandgap of $\sim$3.37 eV, and thus, ZnO based p-n homojunctions should be able to act as an LED with NUV light emission. As mentioned previously, UV LEDs promise a plethora of technologically important applications in the UV across a broad range of fields including medicine, environment, and industry. Therefore, the UV emission promised by a ZnO based p-n homojunction is highly desirable and is a large driving force for research efforts into p-type ZnO.[113]

2.5.5. Photodiode

Photodiodes are another form of p-n junction, operated under reverse bias, for the purpose of light detection. When an optical signal is incident on a photodiode surface, the incoming photons of energy greater than the band gap of the material are absorbed in the depletion layer, exciting electrons from the valence to conduction band, generating electron-hole pairs (EHPs). The electric field across the depletion region then acts to separate the photogenerated EHPs. Under reverse bias, the newly generated charge carriers are then collected by the external contacts and so an electric current, called a photocurrent is generated and flows throughout the circuit. Thus, under illumination, the I-V characteristics of a photodiode are significantly different compared to the dark measurements of the p-n junction, since the absorption of photons generates additional EHPs which induces a large negative photocurrent under reverse bias. The magnitude of the photocurrent depends on the number of photogenerated EHPs and the drift velocities of the carriers.[112,113,231]

2.6. Thin Film Transistors

Thin film transistors (TFTs) are a class of field effect transistor consisting of three terminals, whose working principle is based on current modulation flowing in a thin film of semiconductor material (the active layer) placed between two metal electrodes: the source and drain. An insulating dielectric layer is placed between the semiconductor material and the third electrode called the gate, and an applied potential between the gate and source causes a modification in the semiconducting active layer conductivity. The semiconducting film and gate electrode are capacitively coupled whereby any change in applied bias on the gate induces the current modulation in the semiconducting film. The capacitive injection of charge carriers at the semiconductor insulator interface forms an accumulation layer and the current flow is obtained between the source and drain. This TFT behaviour originates from the field effect in which current flowing in a conductive channel between two electrodes is controlled by the applied field between the third electrode and one of the other terminals. TFTs functionally can be described as voltage controlled current sources.[246–249] The next few subsections explore the basics of TFTs and their operation.

2.6.1. TFT Structures and Classification

There are four basic TFT configurations that are classified based on the architecture of the TFT layers and electrode positions. Staggered TFT structures have the source and drain electrodes on one side of the semiconductor and the gate electrode on the opposing side, whilst coplanar structures have all three electrodes on the same side of the semiconducting active layer. These configurations are further classified depending on the gate electrode location with respect to the active layer. Top-gate TFTs have the gate above the active layer, whereas bottom-gated TFTs have the gate electrode underneath the active layer. Each arrangement offers its own merits and disadvantages dictated by the active material in TFT fabrication process.[246,248–250] In this research, for the purpose of ease of fabrication and to

mitigate other material uncertainties associated with laser processing, the staggered bottom gate structure was used. A further TFT classification can be made depending on the dominant charge carrier type in the semiconducting active layer. Thin film transistors where the semiconducting material is n-type doped can be classified as n-channel TFTs where the dominant charge carriers in the accumulation layer are electrons. Conversely TFTs with a p-type active layer are known as p-channel TFTs where the dominant charge carriers in the active layer are holes.

2.6.2. Basic TFT Operation

The ideal TFT operation can be explained by studying the energy band diagram for a semiconductor-insulator-metal stack upon applying different voltages to the metal. The origin of the gate induced charging (field effects) is classified in the simplified energy band diagrams in **Figure 2.8.**

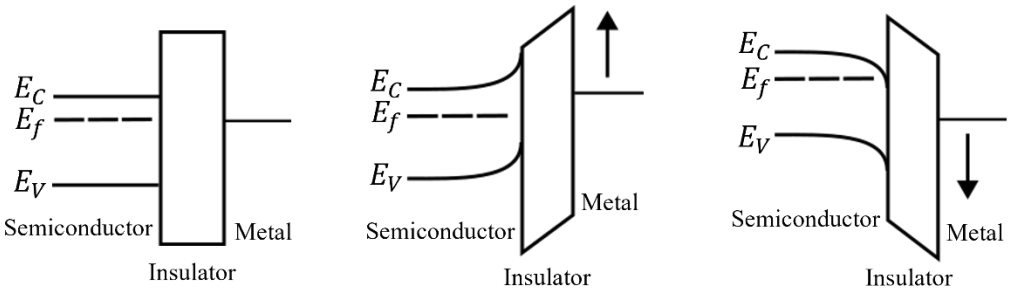

(a) $V_G = 0\ V$ (b) $V_G < 0\ V$ (c) $V_G > 0\ V$

Figure 2.8 *Energy band diagram for a n-type semiconductor-insulator-metal stack representing the origin of the field effect in TFTs. Energy band diagrams are shown under (a) zero bias ($V_g = 0$),, (b) reverse bias ($V_g < 0$), and (c) forward bias ($V_g > 0$).*

For the case of a TFT with an n-type active layer, assuming the Fermi level of the semiconductor and metal are well matched in energy at zero gate bias, when zero gate voltage is applied there should be little to no conduction in the semiconductor layer because there should be no mobile carriers at the semiconductor-insulator interface. Here the device is said to be off, and the energy bands are in equilibrium state as show in Figure 2.8 (a). Equally, applying a negative gate voltage to an n-channel TFT would repel electrons away from the semiconductor-insulator interface creating a depletion layer. This negative gate bias causes an upward positive band bending with the corresponding upward shift of the metal Fermi level with respect to the semiconductor (Figure 2.8 (b)). Thus, the TFT is switched 'off' for both equilibrium and depletion states. However, when a positive gate voltage is applied, mobile charges are induced and are attracted to the semiconductor-insulator interface forming a conductive channel (accumulation layer). This large electric field at the interface causes a negative band bending as shown in Figure 2.8 (c). The mobile electrons induced in the accumulation layer allow for an electric current between the source and drain upon application of a drain voltage bias, where electrons are injected from the grounded source to the accumulation layer and transported to the drain. The TFT

device is now considered to be switched 'on'. Since the accumulation layer is capacitively coupled to the gate voltage, the drain current can be modulated by varying the gate voltage.[230,231,246,248–250] The minimum gate voltage bias required to induce an electric field across the dielectric insulator that is strong enough to form the conductive channel at the semiconductor insulator interface is called the threshold voltage, V_{Th}. Once the TFT is switched on, there are two different operation regimes that can be identified depending on the drain voltage:

- Linear region: When the applied electric potential between the source and drain electrodes is less than the gate voltage minus threshold voltage, the current flow increases linearly with the gate voltage i.e., there is a linear gradient in charge concentration.
- Saturation region: As the drain voltage increases and the potential difference between the drain and gate decreases to zero, the accumulation layer region near the drain electrode becomes completely devoid of free carriers, resulting in a pinch-off of the channel. The gradual increase in drain voltage results in a quadratic I-V character until the pinch-off region whereby no further increase in drain current can be achieved when applying greater bias to the drain and the drain current becomes saturated in this region.[248]

2.6.3. TFT Electrical Characterisation

TFT performance is typically assessed by two standard methods of characterization namely either by holding the gate voltage constant and sweeping the drain voltage (output characteristic curves, where the drain current is recorded as a function of the drain voltage) or by holding the drain voltage constant and instead recording the drain current whilst sweeping the gate voltage (transfer characteristic curve). The output curves allow different TFT operation regimes to be distinguished, whilst most important TFT parameters are extracted from the transfer characteristic curves. Typically, the most important TFT static characteristics are the turn on voltage, V_{ON}, drain current I_D on/off ratio, subthreshold swing, S, and field effect mobility, μ_{FE} in the active layer.[251] However, for the case of this research into the development of n- and p-type ZnO materials, the TFT characteristics could be used to extract vital and elusive carrier type information. As described above, the polarity of the gate voltage required to induce accumulation of electrons in an n-channel TFT is positive. Conversely, the accumulation of holes in a p-channel TFT requires negative polarity gate voltage. Therefore, by examining both TFT output and transfer characteristics, the majority carrier type in the semiconducting layer can be deduced.[252] The main bulk of TFT investigations presented in this thesis will focus on using TFT behaviour as a method for further verification of carrier type in the ZnO thin films produced in this work.

3. Experimental Techniques and Methodology

This chapter outlines the key experimental methods and techniques used in this research from material deposition to characterisation and analysis.

3.1. Thin Film Deposition

Thin film materials are adopted for a vast range of applications and are an essential component of modern electronics and optoelectronics and beyond. The development of new, novel and high quality thin film materials of differing properties has therefore been at the core of research and industry for many decades.[253–256] As such, a wide variety of well-established thin fabrication techniques have been developed that can be broadly classified into three groups: wet chemical deposition (WCD)[257–261], physical vapour deposition (PVD)[255,262–266] and chemical vapour deposition (CVD)[80,259,267,268]. Ultimately, the deposition technique, conditions and parameters define the physical properties of the thin films produced. Each thin film deposition method has its own merits and advantages, and the decision of which deposition technique to use is often based on a complex trade-off between the desired material properties and quality needed for a given application, and the cost, reproducibility, scalability, safety, and environmental impact of the technique.[253,254,267,269,270] However, the need for the miniaturisation of devices and the ever-increasing device topography and dimension complexity alongside the need for superior control over the material properties has introduced further considerations for the most appropriate thin film deposition technique for a given application.[271] Such increasingly stringent requirements of the electronics industry, among other reasons, has led to the increased prominence of ALD technique for various thin film applications.[48,49,80,81,268,272,273] Further details into the fundamentals of ALD can be found in Section 2.1 in Chapter 1: Background and Literature. The experimental details for the thin film deposition methods used in this work are outlined below.

3.1.1. ALD Experimental Details

In this research, ALD of ZnO thin films and Al_2O_3 substrates was performed using an Anric Technologies $AT-400$ tabletop ALD system. Trimethylaluminium (TMA) and water were used as the Al and O precursor and reaction for the deposition of $\sim 40\ nm$ Al_2O_3 dielectric spacer layers onto (100) oriented n-type Si wafers ($1-10\ \Omega cm$). The standard Al_2O_3 recipe was as advised and developed by the manufacturer at Anric Technologies. During the deposition, 2 pulses of each precursor were sequentially delivered to the deposition chamber and subsequently purged for $6\ s$ (TMA)$-7\ s$ (H_2O) using a high purity N_2 gas as the purge gas which was set to a pressure of 200 mTorr above base vacuum. During the deposition the system was set to $150\ ^oC$ and put under a constant flow of the N_2 purge/carrier gas to facilitate dynamic flow of precursors and reactants and reaction by-products. Generally longer purge times are required for the O reactants. The Al_2O_3 dielectric spacer layer was introduced to

facilitate electrical characterisation and to provide an appropriate starting material ($-OH$ surface bonds) for the ideal ALD ZnO surface reactions to take place during the growth of the ZnO material. Diethylzinc and water were mainly used as the Zn precursor and O reactant, and the standard recipe was taken and modified from the Al_2O_3 recipe.

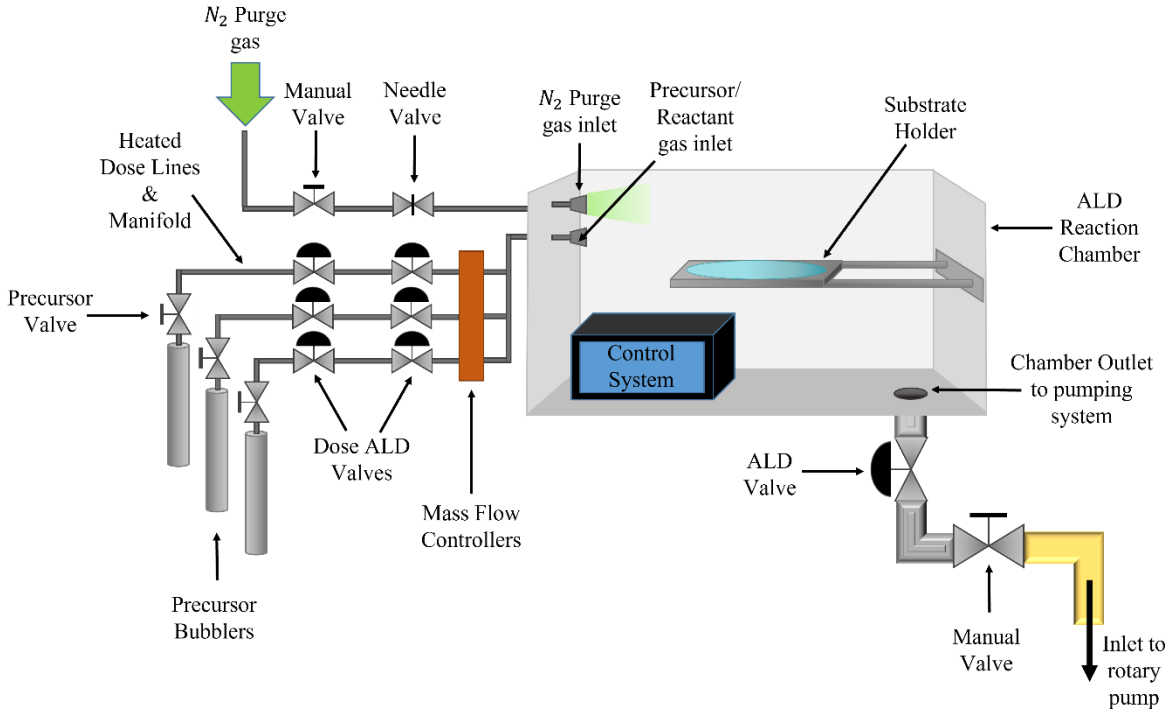

Figure 3.1 *Simplified schematic of the ALD system used in this work showing the reaction chamber, series of vacuum lines making up the manifold and dose lines and the dose valve system, precursor bubblers, and both precursor and purge gas inlets.*

Experiments including multi-layer deposition involving ZnO and zinc nitride (with NH_3 used as the N reactant) were attempted, alongside the use of O_2 and O_3 as O reactants. During the DEZ-H_2O reaction ZnO deposition, 2 pulses of DEZ were delivered to the chamber, followed by a purge process where the purge time was varied from $3-24\ s$, after purging, 2 pulses of H_2O were supplied followed by a purge process between $4-28\ s$. The flow of high purity N_2 through the system was set to a pressure between $100-200\ mTorr$ from base vacuum. Deposition temperature was varied between $150-200\ ^oC$. The ALD system used in this work is illustrated in **Figure 3.1** and consists of:

- A small reaction chamber that is kept under vacuum during the deposition and can be heated up to $350\ ^oC$. The pressure in the system is monitored *via* a pressure gauge situated between the chamber and vacuum pump.
- A transferrable substrate holder connected to the reaction chamber door seal that can support a 4" circular wafer that enables the introduction and removal of the samples to and from the deposition chamber. The process of sample loading and removal requires the chamber to be

vented using the purge gas, and once the sample is loaded the chamber is pumped down to base vacuum. The sample remains stationary throughout the deposition.

- A pumping system comprising of a rotary pump connected in series that can evacuate the reaction chamber to $\sim 10^{-2}\ mbar$.
- Liquid organometallic precursors (TMA and DEZ) and counter reactant (H_2O) bubblers/ cannisters connected to the system.
- System of semiconductor grade metal gas lines, manifold and valves that deliver the precursors to the chamber and are heated to facilitate gas product from the liquid precursors and prevent CVD in the lines.
- A gas inlet for the purge/carrier gas (N_2). The flow of the purge gas is controlled by a needle valve and set according to pressure increases in the main chamber from base vacuum.
- Electronic control system that allows for the setting of deposition parameters and variables including but not limited to the precursors and reactants to be used and the number of pulses of each for the reaction, dose fill and purge times for each precursors and reactants, temperature of the deposition, dose lines, manifold and the precursors, and the type of ALD process to occur between a single cycle process or a multi-cycle process for the deposition of doped, ternary and quaternary materials or multilayer structures.

3.2. Fabrication of Ohmic Contacts

Ohmic contacts were formed by two metallisation schemes, namely sputter coating and thermal evaporation of metals through a shadow mask, followed by a vacuum thermal anneal at various temperatures and annealing times in the ALD system. The two metal deposition techniques are outlined briefly below.

3.2.1. Sputter Coating

In the basic sputtering process, an inert gas such as argon is leaked into a pressurised sputtering chamber and is utilised alongside an applied electric field to excite and ionise the Ar atoms to create a glow discharge plasma above a target material that is to be sputtered. The highly energetic ions within the plasma are then accelerated towards the negatively charged target resulting in ion bombardment and a momentum transfer to the target atoms and leading to their subsequent ejection from the target surface. The vapour of the target atoms then condenses and sputters onto the substrate surface to be coated, in turn depositing a thin film of the target material on the substrate.[269] In this work, sputter coating was performed in a bench top sputter coater system. Ar was used as the inert sputtering gas, and targets of platinum (Pt) and gold (Au) were used to deposit the metal contacts onto the ZnO thin films through a shadow mask.

3.2.2. Thermal Evaporation

Thermal evaporation is performed under ultra-high vacuum, where vapours of the metal of choice are produced in an evaporation chamber *via* the thermal energy induced by an applied current. Prior to deposition, the material to be evaporated is placed inside a thermal basket and placed under ultra-high vacuum. A large AC electric field is then applied to the basket and consequently heated to very high temperatures to melt and vaporise the evaporation metal of choice. The metal vapours then condense onto the substrate to be coated where a thin film of the metal forms.[269]

In this work, an UHV thermal evaporation system was used to deposit aluminium (Al) contacts onto the ZnO thin films through a shadow mask. Al wire was used as the evaporation material and was housed in tungsten baskets (Kurt J. Lesker) inside the evaporation chamber. The Al wire was cleaned using acetone to aid the evaporation process before placing under UHV to avoid any undesirable reactions between the basket and evaporation material. Al evaporation was then performed, at a deposition rate of around $16\ \text{Å/s}$ to deposit roughly $100\ nm$ Al contacts.

3.3. Post Processing

The properties of room temperature sputter deposited thin films seldom meet the desired requirements for specific applications, therefore post processing techniques such as annealing can be employed to modify the structure and morphology of the film and thus significantly improve and tune the electrical and optical properties for the desired purpose.[274] One such post processing method is Excimer Laser Annealing and will be discussed in the following section.

3.3.1. Excimer Laser Annealing (ELA)

Conventionally, laser annealing (LA) is used as an alternative to thermal annealing methods for the improvement of structural, compositional, and thus optoelectronic properties of the materials after the deposition process which may not immediately have produced materials with the desired physical properties. Less favourable material properties typically occur due to low temperature growth where atoms have less kinetic energy for ideal atomic rearrangement.[274] Annealing processes involve elevating the temperature of the thin films to be processed to a desired temperature, T, and maintaining it at this temperature for a specific dwell time, t_d, before the film is allowed to slowly or rapidly cool back down to room temperature. The elevated temperature for the specific t_d provides thermal energy to the film, enabling atomic rearrangement and inducing alterations to the film microstructure, stoichiometry, and the density and/or distribution of defects including the activation of dopants into preferential lattice sites for efficient doping.[203] For example, it has been shown that manipulation of the annealing environment can directly probe the intrinsic defects of a material, in particular the O related defects for oxide materials.[275] Conventional annealing of thin films is carried out by indirect annealing techniques such as rapid thermal annealing or typical furnace heating. These indirect

annealing methods are so called as the thermal energy is generated externally to the thin film where it is then delivered by either conduction, convection, or radiation.[276] Laser annealing on the other hand is classed as a direct annealing technique and has been explored as a method to improve the optoelectronic properties of materials in recent decades.[200,275,277] The direct nature of laser annealing arises since the thermal processing energy is generated within the film itself as a result of the direct absorption of the highly energetic laser photons. Specifically, lasers with high energy photons, such as excimer lasers, are capable of inducing an ultra-fast nanosecond annealing process delivered to the surface of the thin film, which is highly preferential for the use of heat sensitive substrates as used in the flexible electronics industry.[200] In particular, the high energy of the UV photons are preferential for the processing of compounds such as metal oxides, who's high energy demands arise due to their wide bandgaps, that cannot undergo the required phonon emission for laser induced annealing by photon excitation wavelengths below their bandgap energy in the UV range. Moreover, the thermal dose delivered to the sample is spatially localised and therefore allows for a selective annealing process desirable for micro-patterning and printing. Developments into the processing of materials has established laser annealing as an excellent processing technique for the optimisation of the optoelectronic properties that may be tailored to a variety of different device applications such as light emitting diodes[278], thin film transistors[200], sensors[279], renewable energy[280], and photovoltaics[281]. As mentioned, recently, it has been shown that the laser annealing environment can directly probe the defect composition of transparent conducting oxides.[275] However, research into the capability of performing excimer laser annealing in a controlled environment to actively dope metal oxide materials with the environment atoms is currently lacking. As such, this research focusses on both the effective dopant incorporation and activation from the annealing environment and modification of the intrinsic defect density in ZnO to minimise self-compensation effects that inhibits efficient doping.

Excimer laser annealing is a direct annealing process that allows ultra-fast, localised energy delivery to a material surface via light-matter interactions. The UV photons of the excimer laser (with energy larger than the optical bandgap, E_g, of the material to be processed) induce an intense photon absorption by the thin film surface.[203] During the process, sufficient energy is transferred to the material that promotes the onset of multiple interband and intraband electron transition processes within the film. Upon de-excitation, the electrons perform a multi-phonon cascade emission by transferring their energy to phonons. These quantised lattice vibrations transport the laser energy as thermal energy throughout the film, inducing an instantaneous heating and thus producing the annealing effect in the irradiated material. Due to the nanosecond profile of the laser pulse and the picosecond de-excitation time, the laser annealing process is ultra-fast. Absorption of the UV photons during the laser process is governed by the optical absorption properties of the material being irradiated at the specific laser photon energy/wavelength, whereby the absorption coefficient, $\alpha(E)$, of the material dictates the strength of absorption and resultant penetration depth, δ_p, of the laser photons by the relationship in Equation 2.00

below. If the penetration depth of the laser photons is much shorter than the thickness of the thin film material, then most of the direct laser induced heating described will only affect the upper part of the film.

$$\delta_p = \frac{1}{\alpha_{\lambda_{laser}}} \tag{2.00}$$

As such, the remaining portion of the film will receive indirect thermal treatment by the diffusion of heat from the upper film that then dissipates deeper into the material producing a temperature gradient. This process of heat diffusion is defined by the thermal diffusivity, D_h, of the material[282]:

$$D_h(T) = \frac{K_T(T)}{\rho_M(T) C_V(T)} \tag{2.01}$$

where $K_T(T)$ is the thermal conductivity of the material, $\rho_M(T)$ the material density and $C_V(T)$ the specific heat capacity of the material which are all temperature dependent. The thermal diffusivity is then used to estimate the heat diffusion length, $L_h(T)$, (Eq. 2.02), which defines the distance at which the laser-generated heat can propagate throughout the annealed material.

$$L_h(T) \approx \sqrt{D_h t_p} \tag{2.02}$$

where t_p is the laser pulse duration. The temperature gradient induced by the two-fold heating process upon laser photon absorption results in a higher temperature surface irradiated layer which decreases to lower temperatures underneath, and as such there is an inherent depth dependence to the laser annealing process.[275,277]

Table 3.1 *The absorption coefficient and penetration depth for the seed as deposited ALD ZnO thin film at the wavelength of the KrF laser (*$248\ nm$*)*

ZnO Sample	$\boldsymbol{\alpha_{\lambda=248\ nm}\ (cm^{-1})}$	$\boldsymbol{\delta_p\ (nm)}$
As deposited ($150\ ^oC$)	1.69×10^5	59

For ZnO, the average optical bandgap is around $3.37\ eV$.[32] Using Planck's energy equation (Eq. 2.03), it can be calculated that the required photon wavelength for efficient laser annealing of ZnO must be smaller than $\sim 369\ nm$, which is achieved by the $248\ nm$ Krypton Fluoride (KrF) laser, with photon energy of $\sim 5eV$ used in this research. [133]

$$E_g = \frac{hc}{\lambda} \tag{2.03}$$

Where E_g is the optical band gap, h is Planck's constant, c is the speed of light and λ is the required wavelength. Table 3.1 below illustrates the absorption coefficient and associated penetration depth (as calculated from Eq. 2.00) for the as deposited $150\ ^oC$ ALD ZnO material developed in this work at the used KrF excimer laser processing wavelength of $248\ nm$. From the results, it can be shown that the direct laser photon absorption will occur in the top $\sim 59\ nm$ of ZnO material only, and any thickness of material beyond that will receive indirect thermal processing.

3.3.2. Excimer Laser System

The ELA system used in this research is illustrated in **Figure 3.2**. The three core components of the ELA system used in this work are: the laser source, the beam delivery system, and the sample stage. The laser source used in this research was a Krypton Fluoride (KrF) excimer laser (Lambda Physik LPX $305i$), capable of delivering $\sim 25\ ns$ pulses of unpolarised light at a wavelength of $248\ nm$ with an average energy per pulse of up to $1.5\ J$. The non-uniform raw beam is delivered from the laser to the sample *via* a complex beam delivery system comprising of:

- Variable attenuator to adjust the laser energy per pulse from between $10 - 90\%$ of the original beam *via* the use of a two-plate system, one reflecting and the other compensating for the displacement of the reflected beam,
- Beam homogenizer (Exitech Ltd., type EX‑HS‑700D) that utilises two lens arrays to split the raw beam into a series of 'beamlets', that are then overlapped in the focal plane *via* a condenser lens to generate a focussed rectangular (top-hat profiles on both the X and Y axes) homogenised laser spot,
- Series of optics, including a field lens, a mask stage that can equip different sizes and shape masks to shape the beam, and a projection lens with variable magnification. Additional mirrors are used to guide the laser beam through the system to the sample,
- Computer controlled *xyz* translation stage that houses and manipulates the position of the sample with micro-precision.

This laser delivery system allows for various annealing parameters to be changed including the laser fluence (which is defined as the energy density delivered to the sample to be processed, calculated from the energy and spot size of the laser, expressed in $mJcm^{-2}$) and number of pulses delivered to the sample. To examine the laser energy delivery, an energy monitor is positioned between the mask and projection lens between pulses. Of particular importance to the research in this work, is the ability to control the laser processing environment with the target of achieving laser induced doping. Consequently, a pressure cell with a UV transparent window is incorporated into the set-up. The

pressure cell is attached to the sample stage which encloses the sample and allows the annealing to occur under different environments and pressures to achieve the desired material properties. Various gases (Ar, O_2, N_2, NH_3, and 5% H_2 in N_2) can be delivered to the pressure cell up to a maximum pressure of 150 $psig$ (monitored by a pressure gauge) *via* secure pipelines, which can then be safely removed from the cell *via* exhaust lines fitted to the sample stage.[133,283] Prior to processing, the pressure cell is tested for leaks, and vented a minimum of 3 times using the desired gas to ensure purity of the environment.

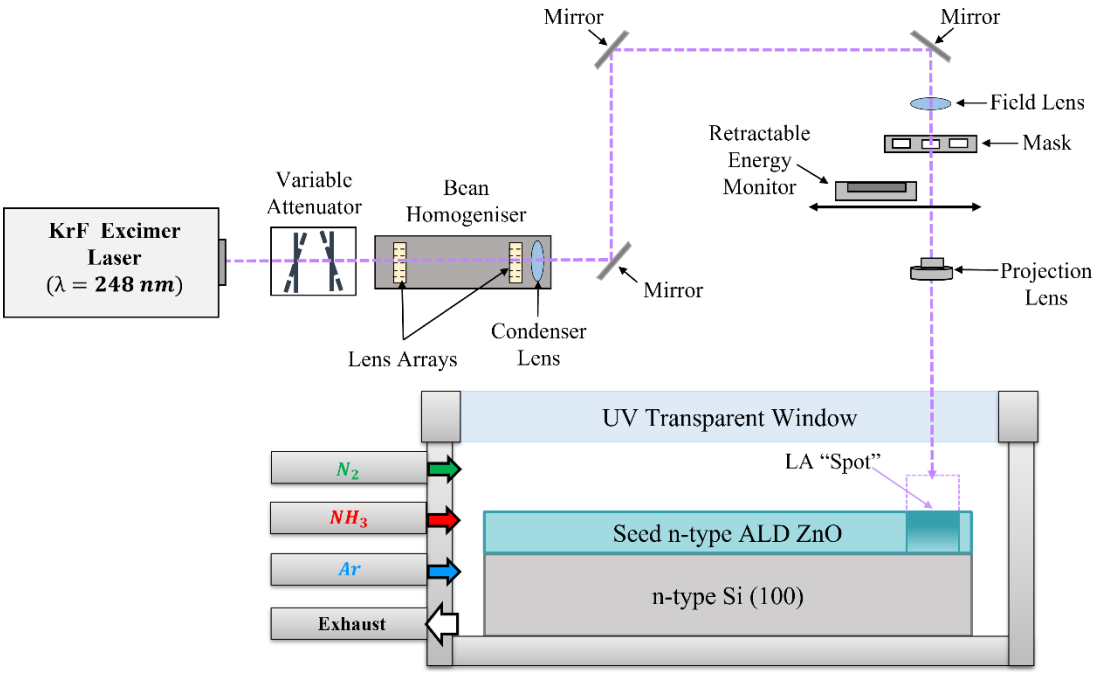

Figure 3.2 *Controlled environment excimer laser system used in this work showing the laser source, beam delivery system, and the sample stage (which is mounted on an xyz translation stage) contained with a pressure cell with UV transparent window and gas inlets for N_2, NH_3, Ar, and an exhaust. The laser processed area is defined by both the lens magnification and the mask and is indicated by the purple rectangle with a dashed outline. The processed region is indicated by the deep blue colour with colour gradient from the top surface of the film to highlight the gradient induced during the laser process, whereby the upper layer increases rapidly in temperature due to the direct absorption of the KrF laser photons, and a thermal gradient exists in the film layers beneath due to heat diffusion.*

3.3.3. Controlled Environment Excimer Laser Doping (CEELD) Experiment

Laser processing of the ZnO samples was conducted in a variety of high pressure ($100\ psig$) environments, including Argon (used as the control environment) and two N-based environments: high purity N_2 and NH_3 with the aim of introducing N related species into the ZnO lattice and induce acceptor-type doping. The laser fluence was varied between $150 - 200\ mJcm^{-2}$ in steps of $50\ mJcm^{-2}$ and the number of pulses varied from $0 - 5$, where 0 is taken to be the unprocessed as

deposited sample. A processing area (laser spot size) of $8 \times 8\ mm$ was set by a combination of a $13 \times 13\ mm$ square mask and a projection lens set-up with 1.8 × magnification, and the laser energy was varied to achieve the desired fluences based on the processing area. The focus and laser spot size were checked and monitored using burn paper at the sample position to confirm the desired $8 \times 8\ mm$ square laser mark with well defined, sharp edges.

3.4. Electrical Characterisation

Knowledge of the electrical properties of materials is crucial to determine how the material reacts to an applied electric field, its electrical conductivity, and how it stores electrical energy. Characterisation of the electrical properties is particularly important for the design and selection of suitable materials for a given desired electronic device application. In semiconducting materials, electrical characterisation can provide a means to assess the quality and reliability of the material, providing important information on parameters such as carrier doping type, concentration and mobility, the interface quality, trap density, bulk semiconductor defect density, contact and other parasitic resistances and semiconductor electrical integrity. A variety of techniques can be employed to examine the electrical character of thin film materials and devices, those used in this work are outlined below.

3.4.1. Van der Pauw Resistivity

The van der Pauw technique is a popular configuration used to determine the resistivity of thin film materials by obtaining the sheet resistance, R_s, of the film by I-V measurements.

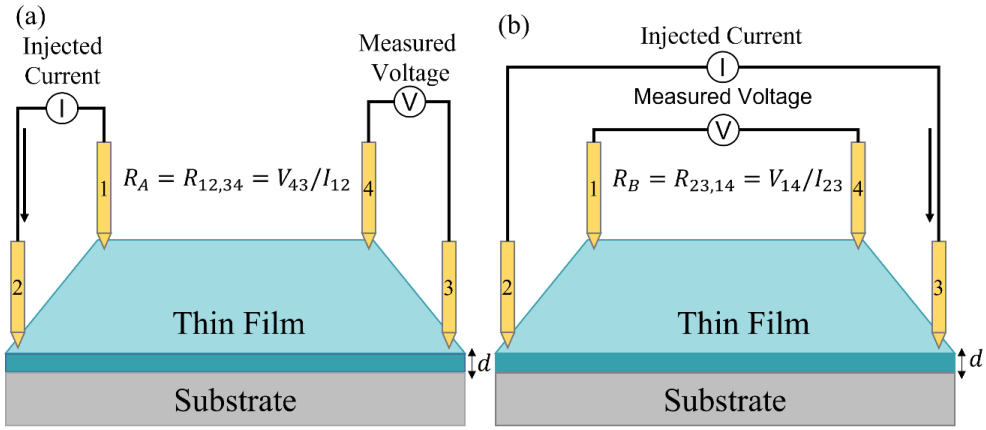

Figure 3.3 *Van der Pauw measurement process. The four collinear probes are placed at the outer periphery of the sample, preferably at the corners of a sample stack comprising of a thin film with thickness, d_{film}, on top of a non-conducting substrate. Current, I, is supplied, and the voltage measured across both the x and y planes of the sample as shown in (a) I_{12}, V_{43} and (b) I_{23}, V_{14}, to measure the two characteristic sheet resistances of the sample, R_A and R_B, respectively.*

In the vdP arrangement, electrical contact is made at four contacts placed at the outer periphery on a sample surface. According to van der Pauw, technically any arbitrary sample shape may be measured using this technique providing the contacts are placed at the edge of the sample and that the sample is of uniform thickness and free from macroscopic defects.[284] Despite this, symmetrical configurations are preferred with contact made across four 'corner' points of a sample.[285–290] A schematic of a standard rectangular vdP configuration is shown in **Figure 3.3**, with the four contacts labelled clockwise around the sample as 1, 2, 3 and 4. Van der Pauw established the existence of two characteristic sheet resistances, R_A and R_B, that are related to the directionality of the electrical terminals. These characteristic resistances are obtained according to Ohm's law, by applying a dc current, I, in and out of a pair of opposite contacts, and measuring the resulting voltage, V, across the other pair of contacts, as shown in Figure 3.3 (a) and (b) respectively. During the measurement process, current reversal, and geometry averages (repeated measurements on all sides of the sample) are performed to reduce inhomogeneous effects arising from sample geometry irregularities, imperfections at the contacts, or any inhomogeneity/ anisotropy within the films.

As such, a total of eight I-V measurements are taken and used to calculate R_A and R_B according to:

$$R_A = \frac{R_{12,43} + R_{21,34} + R_{34,21} + R_{43,12}}{4} \tag{2.04}$$

$$R_B = \frac{R_{23,14} + R_{32,41} + R_{41,32} + R_{14,23}}{4} \tag{2.05}$$

Where R_A and R_B are related to the total sheet resistance, R_S, through Eq. 2.06, which can then be numerically solved for R_S.

$$\exp\left(-\pi \cdot \frac{R_A}{R_S}\right) + \exp\left(\pi \cdot \frac{R_B}{R_S}\right) = 1 \tag{2.06}$$

The vdP resistivity can then be obtained according to Eq. 2.07:

$$\rho = R_S t \tag{2.07}$$

where t is the film thickness.

3.4.2. Hall Effect

The Hall Effect was discovered in 1879 by Dr Edwin Hall and may be utilised as an electrical characterisation tool of semiconductor materials.[291] This powerful technique can directly determine the type, density, and mobility of charge carriers within a semiconductor. The physical principle governing the Hall Effect shown in **Figure 3.4** is based upon the Lorentz force, F_L, and considers

electric and magnetic forces acting perpendicularly upon charge carriers within a semiconducting or conducting material and the resultant measurable potential difference across the semiconductor.

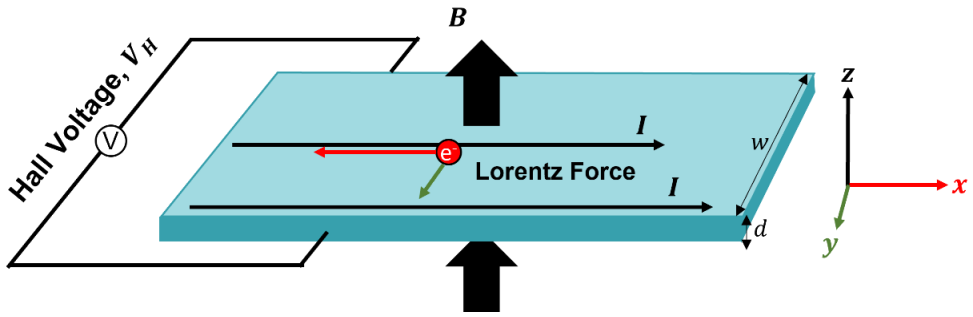

Figure 3.4 *Physical principle behind the Hall Effect based on the Lorentz force, where an electron (e-) moves in response to an electric field induced by an applied current, I. Upon imposing a magnetic field of strength, B, on the sample, the carriers are deflected by the Lorentz force and charge therefore builds on one side of the sample, resulting in a measurable potential difference, the Hall voltage,* V_H.

A charge carrier moving with drift velocity, v_d, along an applied electric field in the x direction is considered. If an external magnetic field is applied perpendicularly to this electric field (along the z axis), the charge carrier, q, will experience a magnetic force acting normal to both directions, which is the Lorentz force, F_L, defined in Eq. 3.08. The charge carriers will subsequently be deflected in the $+/-y$ direction by this F_L toward one of the sample edges, generating a build-up of charge (negative charge for majority electrons, positive charge for majority holes), which produces a potential difference in a transverse direction to the current flow.

$$F_L = q(v_d \times B) \tag{3.08}$$

The build-up of charges thus induces an electric field perpendicular to the current and magnetic field, of electrostatic force, F_{EL}, and strength, E_y, such that

$$F_{EL} = qE_y \tag{3.09}$$

At equilibrium, the electric field force, F_{EL}, will equal the opposing Lorentz force, F_L, and a measurable potential difference known as the Hall voltage, V_H, is created between the two sides, separated by width, w, of the sample and is equal to Eq. 3.10. At equilibrium, when $F_{EL} = F_L$, the relation between the generated electric field, E_y, and applied magnetic field, B_x, can be derived to give Eq. 3.12. The velocity, v_d, can be related to the current, I, which is described as the total charge passing through a cross sectional area, $A = wt$, to give Eq. 3.13.

$$V_H = \frac{E_y}{w} \tag{3.10}$$

$$qv_dB_x = qE_y \tag{3.11}$$

$$v_d B_x = E_y \tag{3.12}$$

$$v_d = \frac{I_x}{N_i q w t} \tag{3.13}$$

Where N_i is the free carrier concentration, and t is the thickness of the thin film.

Equation 3.13 can then be inserted in Eq. 3.12 to give:

$$E_y = \frac{I_x B_x}{pqwt} \tag{3.14}$$

Substitution of Eq. 3.14 into Eq. 3.10 yields:

$$V_H = \frac{I_x B_x}{Nqt} \tag{3.15}$$

Which is then used to extract the Hall coefficient, R_H:

$$R_H = \frac{V_H t}{I_x B_x} = \frac{1}{Nq} \tag{3.16}$$

Thus, the Hall coefficient is dependent on the sign of the charge, q, which is dependent on the type of charge carrier within the film. For n-type thin films with electrons as the majority carrier, $q = -e$ and so the Hall coefficient would be negative. Conversely, for p-type films, where holes are the majority charge carrier, $q = +h$ and so the Hall coefficient would be positive. Therefore, examination of the Hall coefficient can provide useful information on the type of majority charge carrier within the film.

Moreover, if the film thickness, t, is known, the carrier concentration, N_{Hall}, can be determined *via* Hall Effect measurements using:

$$N_{Hall} = \frac{1}{e|R_H|} = \frac{|I|B}{et|V_H|} \tag{3.17}$$

Hall effect measurement systems typically employ the van der Pauw configuration, where the current is injected across two diagonal contacts, and the voltage is measured across the other two diagonal contacts, with magnetic field perpendicular to the sample surface as presented in **Figure 3.5**. The Hall measurement is repeated for both axes of contacts and for reverse current polarity, such that the average of the eight measurements taken can be used to calculate R_H, V_H and N_{Hall}.[292,293]

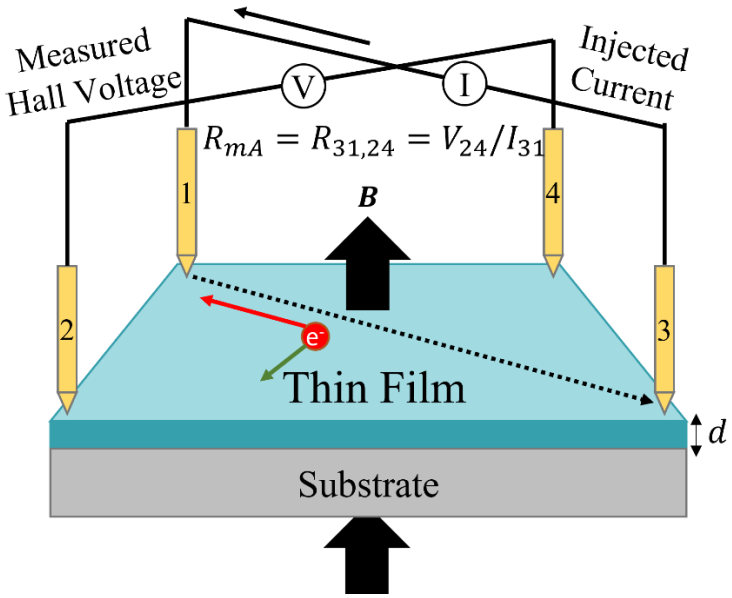

Figure 3.5 *Hall Effect measurement process in the Van der Pauw geometry. The sample is placed under a reversible magnetic field, with field strength, B, as indicated by the black arrows. The supply of current, I, and measurement of the voltage, V, occurs across both diagonals of the sample in order to measure the Hall voltage, V_H.*

The Hall mobility of the charge carriers, μ_{Hall}, can then be calculated in combination with the van der Pauw resistivity measurement of ρ using:

$$\mu_{Hall} = \frac{|R_H|}{\rho} \tag{3.18}$$

3.4.3. Van der Pauw resistivity and Hall Effect Measurements

Van der Pauw resistivity and Hall effect measurements were carried out using the Van der Pauw Ecopia HMS-3000 Hall Measurement system provided to Nottingham Trent University by Sheffield Hallam University to determine the electrical resistivity, carrier type, concentration, and mobility of the as deposited and laser annealed ZnO thin film samples. Room temperature resistivity measurements are performed using the Van der Pauw technique, followed by Hall Effect measurements with a magnetic field strength of $B = 0.553\ T$. Contact was made to the outer corners of the square $8 \times 8\ mm$ samples and electrical contact was verified through simple I-V curves before each measurement. The measurements were consecutively repeated three times on each sample without repositioning the contacts to calculate and report the mean value and corresponding standard error.

3.4.4. Electrical Characterisation of Devices

Electrical characterisation of the metallic contacts, p-n junctions and thin film transistor devices produced in this work were performed using a setup including a Kiethley 4200-SCS Parameter Analyser to perform the characterisation facilitated by a Semiprobe device measuring system. The experimental equipment involved in the device characterisation setup includes:

- The Keithley 4200 – SCS Parameter Analyser used to perform current-voltage characterisation of the devices. The system can be used to design custom measurements depending on the requirements of the electrical characterisation.
- A series of four Kiethley 4200 Source Measure Units (SMUs), including two high power SMUs, that offer advanced measurement versatility, and can precisely source current or voltage whilst simultaneously measuring the voltage and/or current with high accuracy. The setup also includes a 4200A-CVIV Multi-switch consisting of four channels connected to the SMUs, that allows for the automatic switching between the SMUs and to facilitate a variety of measurements without the need for re-probing.
- A Semiprobe SMU probing table, that allows for the accurate probing of a device loaded onto the table which includes a vacuum chuck to keep the sample in place and avoid sample movement during the measurement. The sample is probed using Tungsten tips coupled to the ends of two probing arms that are located above the device measurement area. These probing arms are connected to the Keithley 4200 SMUs to deliver and measure the current and voltage to and from the device.
- An xyz position control setup in conjunction with the probing table for sample positioning.
- A microscope used to ensure accurate device probing.
- A monitoring screen that may be used in addition to or as an alternative to the microscope.

3.5. Composition and Surface Characterisation

The study of the surface and compositional properties of a semiconductor material is of importance to help aid the understanding of the underlying mechanisms governing its electrical and optical properties. Such characterisation techniques are sensitive to elemental composition and associated states which is of particular importance for doping investigations, as well as insights into the band structure of the material. Below details the techniques used in this research to explore the composition and surface properties of the developed ZnO materials.

3.5.1. Time-of-Flight Secondary Ion Mass Spectrometry

Time-of-Flight Secondary Ion Mass Spectrometry (ToF-SIMS) is a powerful, ultra-high vacuum (UHV), surface sensitive analytical tool used to investigate the chemical and molecular properties of surfaces and thin films and is widely used in a broad range of fields including material science, semiconductors and nanotechnology[294], pharmaceutical and biomedical research[295,296], and environmental and space science[297]. Moreover, ToF-SIMS provides highly sensitive and spatially resolved information on the elemental, chemical and structural composition of a samples surface and may also provide information throughout the entire depth of a sample when performed during depth profiling. The technique involves the bombardment of a sample surface with a highly focussed, pulsed primary ion beam (typically Cs^+, Ga+, Ar^+, Bi^+), to remove chemical species from the atomic monolayers at the sample surface, liberating various secondary ions which can be positively or negatively charged. These secondary ions are then accelerated into a flight path towards a detector in a static electric field *via* an electric potential difference, V, where all ions obtain the same kinetic energy. The ions are then analysed by a time-of-flight mass spectrometer that can determine the mass of the ions by measuring the exact time at which they reach the detector – hence time-of-flight SIMS. The time of flight, t, for ions travelling a field free distance, D, towards to detector is given by:

$$t_x = \frac{D}{v_x} = D\sqrt{\frac{m_x}{2z_x eV}} \tag{3.19}$$

Where m_x and v_x are the secondary ion mass and velocity of species x respectively, z_x is the number of charges of the ion and e is the electron charge. The time may then be converted to m_x/z_x according to:

$$\frac{m_x}{z_x} = 2eV\left(\frac{t_x}{D}\right)^2 \tag{3.20}$$

In practice, calibration of the mass spectrum must be performed by using known reference ions, and is achieved by determining the constants a and b in:

$$\frac{m_x}{z_x} = at^2 + b \tag{3.21}$$

Since the time of flight of the particles from primary ion beam bombardment to the detector is in the order of nanoseconds, a very high mass resolution can be obtained, which, when combined with the high surface sensitivity associated with ToF-SIMS renders it a far more preferential method for analysing light element composition compared to other analysis techniques such as X-Ray Photoelectron Spectroscopy (XPS). Typically, ToF-SIMS offers three operational modes: surface spectroscopy by obtaining the mass spectrum of all secondary ions, XY surface maps and imaging of any masses of interest by raster-scanning the primary ion beam, and depth profile (Z-axis) spectrums of a sample by removing surface layers *via* sputtering using a secondary ion beam source.

The fundamental SIMS equation details the parameters involved in generating the mass spectrum:

$$I_s^x = I_p \gamma_x \alpha^{\pm} \theta_x \eta_i \tag{3.22}$$

Where I_s^x is the secondary ion current of species x, I_p is the primary particle flux, γ_x is the sputter yield (number of atomic and polyatomic particles emitted per primary ion impact), $\alpha^{\pm}$ is the ionisation probability to positive or negative ions, θ_x is the fractional concentration of species x in the surface layer, and η_i is the instrument transmission which is essential to the ability of the technique to detect and analyse the generated ions with good sensitivity. Whereby γ_m and $\alpha^{\pm}$ are the two main measurement parameters of interest.[294,298,299]

ToF-SIMS measurements were performed at the University of Nottingham using a ToF-SIMS V instrument (ION-TOF GmbH., Münster, Germany). Measurements are performed under UHV to increase the mean free path of ions released into the flight path. The system is equipped with a bismuth liquid metal ion gun used as the primary ion beam (Bi^+) run at $30\ kV$ with a pulsed target current of $\sim 0.6\ pA$. A caesium (Cs) gas cluster ion beam operated at 1keV was used to sputter the sample surface to perform depth profile measurements. The analysis was carried out by performing $200\ \mu m \times 200\ \mu m$ raster scans with 256×256 pixel resolution, whilst $500\ \mu m \times 500\ \mu m$ sputtered regions were produced, and 1 frame of analysis followed by 5 frames of sputtering were performed and analysed to produce the depth profile mass spectra. Data acquisition was undertaken using the SurfaceLab7 software (IONTOF GmbH.).

3.5.2. Valence Band X-Ray Photoelectron Spectroscopy (VB XPS)

X-ray Photoelectron Spectroscopy (XPS) is one of the most widely used surface sensitive techniques to analyse the composition and chemistry of materials at their surface. XPS is not only a useful technique for detecting the elemental abundance in materials but has a further advantage over other techniques due to both its surface sensitivity and ability to determine the chemical fingerprints of atoms in a sample.

The working principle of XPS is based on the photoelectric effect, whereby electrons can be emitted from a sample surface when irradiated with light. In XPS, X-ray photons bombard the surface of a material and transfer their energy to bound core electrons in the atoms of the sample. These electrons are then ejected from the core level and emitted from the sample as a photoelectron. The kinetic energy, E_k , of the emitted photoelectron is then analysed by an electron spectrometer. The E_k of the electron is the measured experimental parameter obtained *via* XPS but is dependent on the X-ray source and therefore not an intrinsic material property. However, the binding energy of an electron, E_B, is an intrinsic material property that determines how tightly bound the electron is to an atom or orbital and can be estimated according to Eq. 3.23.

$$E_B = hv - E_k - \Phi_{spec} \tag{3.23}$$

Where hv is the X-ray photon energy, E_k is the kinetic energy of the emitted electron, and Φ_{spec} is the 'work function' of the spectrometer.[300,301] The binding energy of the photoelectron is heavily affected by various factors including the electronegativity of nearest neighbour atoms and the oxidation state of the element, therefore providing useful information on the chemical environment of each element. As such, the photoelectron spectrum obtained *via* XPS can reproduce well the electronic structure of elements in a sample, and processing of the spectra allows for peak assignment to determine composition and chemistry for qualitative analysis, whilst the relative area underneath each peak is representative of the number of atoms present in each environment and therefore quantitative analysis can also be obtained from XPS measurements.

The emitted photoelectrons are collected by a detector which uses a combination of extraction lenses and energy analysers to measure the E_k of emitted electrons. The sample and measuring system are all kept under ultra-high vacuum (UHV) ($10^{-9} - 10^{-10}\ mbar$) to prevent electrons from scattering off any air molecules whilst travelling to the analyser. This UHV also ensures surface contamination of the sample in the chamber is kept to a minimum, which could otherwise drastically alter the sample chemistry and thus experimental results. XPS is a surface sensitive technique since it is only electrons able to escape the sample surface that can contribute to the characteristic photoelectron XPS peaks for analysis. Photoelectrons created deeper in the sample undergo inelastic collisions causing scattering events before they can reach the surface of the sample, and as such these photoelectrons only contribute to the background signal in the spectrum.[300–302] XPS information throughout the entire depth of a sample may be obtained *via* depth profiling whereby in-situ argon ion sputtering is performed to remove a certain depth material before acquiring XPS data. A similar process is also performed to remove any surface contaminants before performing XPS measurements on a sample surface. This depth profiling process can then be repeated until the entire depth of interest has been analysed.[303]

Wide XPS scans across a broad range of X-ray photon energies can be performed to capture information on both core and valence level electrons for analysis. For valence band analysis, the low energy part of

the XPS system is of interest since valence electrons are more loosely bound than core electrons and therefore need considerably less energy to be excited.[302] The valence spectra consists of many energy states in the same energy range and as such typically has few to no defined peaks, unlike the core electron spectra. From the VB spectrum, the VB maximum (VBM) can be obtained and is typically in the $0-5\ eV$ region. The VBM can be extracted from the spectra by performing a linear extrapolation from the onset of the valence band edge to the zero-intensity line. If the sample and instrument are brought into electrical contact during the measurement, the $0\ eV$ binding energy is taken to be the Fermi level, E_f, and thus the VBM position with respect to the E_f can be determined.

XPS measurements were performed at the Aristotle University of Thessaloniki using a Kratos Analytical Limited Axis Ultra XPS system. The system comprises of a UHV chamber ($10^{-9}\ mbar$), a monochromated $Al-K_{\alpha1}$ x-ray beam excitation source, a hemispherical energy analyser and a 128-channel detector. The samples were first etched with argon ions to remove any surface contamination and an initial low-resolution wide scan over a range of binding energies ($0-1200\ eV$) was collected to identify the set of XPS peaks of interest. Subsequent high-resolution scans were then performed to obtain narrow-range scans across the E_B regions of interest as identified by the wide scan XPS Spectra. The resulting XPS data then underwent background removal and calibration of peak energies to a known standard peak before analysis.

3.5.3. Kelvin Probe Force Microscopy (KPFM)

Kelvin Probe Force Microscopy (KPFM) is a non-contact variant of AFM, that can be used to indirectly measure the near surface properties of semiconductor and metal surfaces.[304] In particular, KPFM is used to measure the near surface work function of a material, Φ, which defines the minimum work required to move an electron from the material surface to the immediate vacuum space outside of the surface and is directly related to the Fermi level of a material. The basic working principle of KPFM relies on measuring the contact potential difference (CPD) between a conducting, oscillating AFM tip (Kelvin probe) and the sample surface. An AC voltage applied to the AFM cantilever tip generates an oscillating electrical force between the tip and sample surface and thus the two are electrically connected as in the standard non-contact mode AFM. When the probe is brought into close proximity to the sample surface, a potential difference, (V_{CPD}) forms between them due to the difference in work function between the two materials. The V_{CPD} is related to the work function of the KP tip, Φ_{tip}, and the work function of the sample, Φ_{sample}, through Eq. 3.24.

$$V_{CPD} = \frac{\Phi_{tip} - \Phi_{sample}}{-e} \tag{3.24}$$

As a result of the CPD, an electrical force is generated at the contact area due to the differences in the materials Fermi energy. Upon electrical contact, the Fermi levels of the two materials align through the

applied electron flow, and the system reaches an equilibrium state. The electrons therefore induce a charge at the tip and a resultant electrical force acts on the contact area. The KPFM technique is dependent on the detection of this electric field, which can be nullified *via* the application of an additional external DC voltage (V_{DC}), which is varied until the oscillations caused by V_{AC} are void and therefore the space in between the tip and sample is field free. The amount of external bias required to quash the AC field and reduce the contact area charge is equal to the work function difference between the sample and KP tip, and so Φ_{sample} can be calculated provided Φ_{tip} is known. Moreover, when the applied V_{DC} is the same magnitude as V_{CPD} but in the opposite polarity, the applied DC field eliminates the surface charges at the contact area. A lock in amplifier is employed in the experimental set-up to measure this V_{CPD}, which can then be used to calculate Φ_{sample} of the material, through Eq. 3.24.[305] Calibration of the measuring system must be performed using a sample of known work function to accurately determine the work function of the KP tip, which eliminates the potential for electrical offsets that may occur during the KPFM measurement itself.[306]

In this work, a freshly exfoliated highly ordered pyrolytic graphite (HOPG) was used as the reference sample, which is often favoured due to the inertness of its surface.[306] Measurements were performed using the Janis ST-500 Probe Station at the King Abdullah University of Science and Technology (KAUST), inside an N_2 filled glove box. Measurements on the as fabricated samples were performed, followed by repeat measurements after a mild thermal anneal at $80\ ^oC$ overnight inside a glove box to reduce surface contamination. In reality, the V_{CPD} depends not only on the surface work function but is also affected by a variety of other parameters including any adsorbate layer, oxide layers, dopant concentration within the semiconductor or any temperature changes within a sample.[305] Therefore, careful consideration must be made concerning sample handling and storage to minimise uncertainties in the KPFM measurement.

3.6. Optical Characterisation

The optical properties of a material describes how the material interacts with the electromagnetic (EM) field of light, which spans a wide range of wavelengths from radio waves, through infrared, visible, UV all the way to x-rays. The optical response of a material is often measured in terms of transmission, reflection, or absorption. Exploring the optical properties of a semiconductor material provides a useful tool to explore its energy band structure and impurity and defect levels, as well as the excitonic, phononic and plasmonic properties of the material. The EM spectrum of light spans a wide range of wavelengths from radio waves, through infrared to visible and UV, all the way to x-rays, all of which can probe different material responses. In this research, the optical properties from the near-UV to Mid-IR are explored and the methods are described in the following few subsections.

3.6.1. Optical Reflectance Spectroscopy (ORS)

Optical Reflectance Spectroscopy (ORS) was used to determine the optical band gap, E_g, of the ZnO films under study in this work, which is an essential energy range required to reconstruct the band diagram. ORS is an optical characterisation technique that can be used to determine the dielectric function of thin film materials in the NIR-VIS-UV spectral range as an alternate to NIR-VIS-UV spectroscopic ellipsometry. During an ORS measurement, the reflectance of thin film materials is determined by irradiating the film at normal incidence with a spectrometer light source and measuring the reflected intensity from the sample for each distinct wavelength. The resultant frequency dependent reflection spectrum can then be modelled using both optical dispersion relation and geometric models to describe the optical properties of the material.

The complex refractive index, $\tilde{n}$, can be determined from the dispersion *via* the simplified Fresnel reflection equations at normal incidence whereby the frequency dependent reflectance $R(E)$ is identical for s and p polarisations of light and so the simplified $R(E)$ is given by Eq. 3.25.

$$R(E) = \left|\frac{\tilde{n} - 1}{\tilde{n} + 1}\right|^2 \tag{3.25}$$

Where $\tilde{n} = n + ik$ is the complex refractive index of the material being measured with a real refractive index, n, and extinction coefficient, k.

Complex fitting of the Kramers-Kronig relations can then be performed to determine the real part of the refractive index and extinction coefficient since:

$$R(E) = \left|\frac{(n-1)^2 + k^2}{(n+1)^2 + k^2}\right|^2 \tag{3.26}$$

Thus, the real, ε', and imaginary, ε'', parts of the complex dielectric permittivity ($\tilde{\varepsilon} = \varepsilon' + i\varepsilon''$) can be calculated since $n = \sqrt{\varepsilon' + k^2}$ and $k = \frac{\varepsilon''}{2n}$, and an oscillator model can then be applied to describe the dielectric function.[307,308]

In this work, the VIS-UV optical properties of normal incidence optical reflectance spectra were measured from $350 - 900\ nm$ $(1.4 - 5.0\ eV)$ with the Ocean Optics Spectrasuite software using a VIS-UV (Ocean Optics USB4000) spectrometer, a balanced deuterium halogen light source (Ocean Optics DH2000BDL) and VIS-UV transparent optical fibres. The experimental setup is presented schematically in **Figure 3.6**. The spacing between the sample surface and optical fibre head was optimised to acquire the maximum reflection intensity. The spectral light intensity of the lamp , I_l, was recordedusing a highly reflective Aluminium reference mirror whilst the dark intensity, I_d, was recorded by closing off the light source to remove noise and background light intensity. The source was then reopened, and sample placed under the probe and the reflected light intensity from the sample, I_s,

was recorded for the broad spectrum of wavelengths. The frequency dependent reflectance of the thin film is then calculated from the measured intensities *via*

$$R(E) = \frac{I_s - I_d}{I_l - I_d} R_{Al} \tag{3.27}$$

where R_{Al} is the theoretical reflectivity of the Al reference mirror.

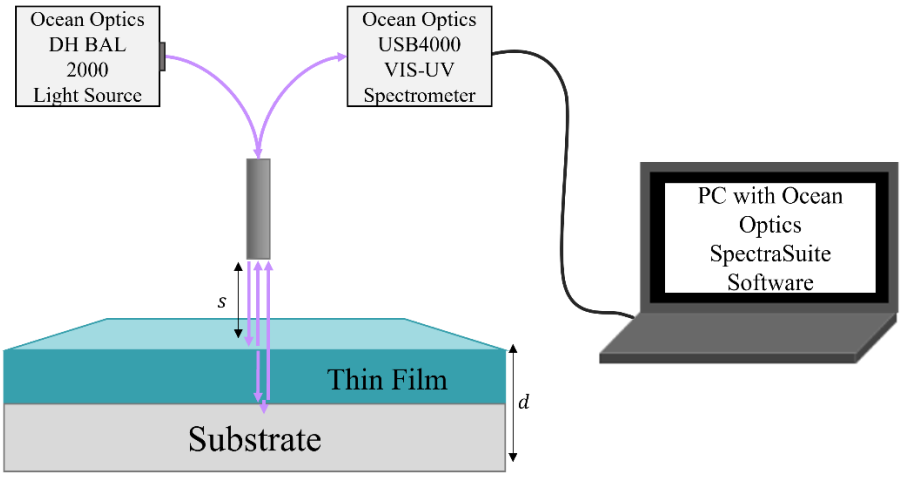

Figure 3.6 *Optical Reflectance Spectroscopy measurement set-up used in this work. The light from a balanced deuterium light source is directed from the source to a distance, s, above the thin film sample surface by optical fibres and probe head. The reflected light from the sample surface and sample/substrate interface is reflected back through the optical probe and collected by a spectrometer which records the intensity of reflected light as a function of the photon energy.*

The J.A.Woollam software, CompleteEase™ was then used to determine the optical constants of the material using the calculated reflectance. A geometric model describing the sample stack and individual layer optical constants was built. An oscillator model was then generated to describe the optical properties of the unknown ZnO film layer using a contribution of PSEMI-MO and Gaussian oscillators to describe the lineshape and extract the optical constants which are described further in Section 3.6.2.3.

From the optical constants n and k, the absorption coefficient, α, can be calculated using Eq. 3.28 to describe the absorption of the film.

$$\alpha = \frac{4\pi k}{\lambda} \tag{3.28}$$

In the VIS-UV spectral range, the main feature dominating the ZnO absorption spectrum is the optical band gap transition energy, E_g, around 3.3 eV. The E_g of a material may be related to the absorption

coefficient through the Tauc model in Eq. 3.29, since E_g details the threshold energy of the photons at which the material starts absorbing light through the interband transitions.

$$\alpha(hv) = C(hv - E_g)^n \tag{3.29}$$

Where h is the Planck constant, v is the photon frequency, C is a proportionality constant, and the exponent n has discrete values that are dependent on the type of carrier transitions across the bandgap. For indirect bandgap materials, $n = 2$, whereas for direct bandgap materials such as the ZnO explored in this work, $n = 1/2$ and so Eq. 2.29 becomes.

$$\alpha(hv) = C(hv - E_g)^{1/2} \tag{3.30}$$

Through the Tauc relation, the optical bandgap of thin film materials can be estimated by producing a Tauc plot, whereby a linear extrapolation of $(\alpha hv)^2$ versus hv plot is performed to the intercept of the energy (hv) axis, since $E_g = hv$ when $(\alpha hv)^2$ is zero, i.e., at $\alpha = 0$.[309,310]

3.6.2. IR Spectroscopic Ellipsometry (IRSE)

Spectroscopic Ellipsometry (SE) is used to determine the thickness and frequency dependant complex dielectric function of both single- and multi-layer thin film materials. SE measures the change in polarisation of light that is reflected or transmitted from a sample by measuring the ellipsometric angles that describe an amplitude ratio, $\Psi(\omega)$, and a phase difference, $\Delta(\omega)$, between light polarised parallel (p), and perpendicular (s) to the plane of incidence. From these measured angles, the optical response of isotropic or anisotropic films and substrates can be quantified through the ratio, $\rho_f(\omega)$, of the complex valued Fresnel reflection coefficients $\mathrm{r_p}(\omega)$ and $\mathrm{r_s}(\omega)$ for p- and s- polarisations which can be determined through Eq. 3.31[311]

$$\rho_f(\omega) = \frac{\mathrm{r_p}(\omega)}{\mathrm{r_s}(\omega)} = \tan\Psi(\omega) \cdot \mathrm{e}^{(\mathrm{i}\Delta(\omega))} \tag{3.31}$$

The 'pseudo-permittivity', which details the contribution to the real and imaginary parts of the permittivity from the entire sample stack (including the thin film and substrate etc), can be calculated from the measured value of $\rho(E)$ at each measurement angle, θ, according to:[311]

$$< \tilde{\varepsilon}(\omega,\theta) > = < \varepsilon'(\omega,\theta) > + i < \varepsilon''(\omega,\theta) > = \sin^2(\theta)\left(1 + \tan^2(\theta)\left[\frac{1-\rho(\omega)}{1+\rho(\omega)}\right]^2\right) \tag{3.32}$$

To transform $< \tilde{\varepsilon}(\omega,\theta) >$ into the optical constants, $\tilde{\varepsilon}(\omega)$, of an individual unknown layer, both a geometric model (detailing the layer thickness and sequence in the sample) and an optical parametric model (describing the permittivity of each layer) must be employed.[312,313]

The ellipsometry data in this work was analysed by using a layer-stack model inclusive of the ZnO film of unknown dielectric function alongside the Si substrate, the native SiO_2 and an Al_2O_3 dielectric layer

(where appropriate). Whereby the permittivity of the Si and native oxide layer are well known. The samples that were fabricated to include an Al_2O_3 dielectric layer were measured with SE prior to the ZnO deposition. As such the Al_2O_3 layer thickness and permittivity could be fitted using a summation of individual oscillators, and then fixed during the analysis of the full ZnO sample stack to reduce the number of free parameters when fitting the ZnO layer. This then enables the fitting of the permittivity and thickness of the ZnO layer defined by a parametric oscillator model to account for the optical phonon and free carrier properties of the ZnO thin films.

The parameters of the oscillator model dielectric function are fit using an iterative, nonlinear regression method (Levenberg-Marquardt algorithm) which operates on 90% confidence intervals to achieve the best match between the model and experiment.[314] One means of assessing the overall 'goodness' of the fit is by observing the resulting root mean squared error (MSE) of the fit given by Eq. 3.33, which quantifies the difference between the measured and fitted curves. During fitting the unknown parameters are allowed to vary until the minimum MSE is reached.

$$MSE = \sqrt{\frac{10^6}{3n-m}\sum_{n=1}^{m}\left[\left(N_{meas_i} - N_{fit_i}\right)^2 + \left(C_{meas_i} - C_{fit_i}\right)^2 + \left(S_{meas_i} - S_{fit_i}\right)^2\right]} \qquad (3.33)$$

where n is the number of data points acquired at individual photon energies, and m being the number of fitting parameters in the oscillator model. To simplify the MSE, the ellipsometry angles Ψ and Δ are replaced by the parameters $N = \cos(2\Psi)$, $C = \sin(2\Psi)\cos(\Delta)$, and $S = \sin(2\Psi)\sin(\Delta)$ to bind the resultant values between -1 and 1. The abbreviations 'meas' and 'fit' correspond to the measured and fitted data respectively.

3.6.2.2. Experimental Details

The near to far-infrared optical characterisation was performed using a J.A. Woollam Mark II IR Variable Angle Spectroscopic Ellipsometry (VASE) and data was obtained for the spectral range $1.6 - 40\ \mu m$. A schematic of the Mark *II IR-VASE* system used in this work is presented in **Figure 3.7.** The system comprises of three main parts: an IR source (featuring a SiC Globar with a Michelson style FTIR Spectrometer), the sample manipulator, and the detector. The source delivers linearly polarised light to the sample surface, which is vertically mounted on a sample stage and held in place *via* a small vacuum pump. The sample stage is then moved to the desired measurement angle, θ, normal to the sample surface. Meanwhile, the detector unit is rotated at an angle of 2θ. Typically, data was collected at three angles for each sample in the range of $65^o - 70^o$ by 5^o increments. The software WVASE was used to acquire the data whilst analysis was performed using the CompleteEase software. The backside of the Si substrates were roughened using a Dremel tool to reduce the effect of backside reflections on the measurement.

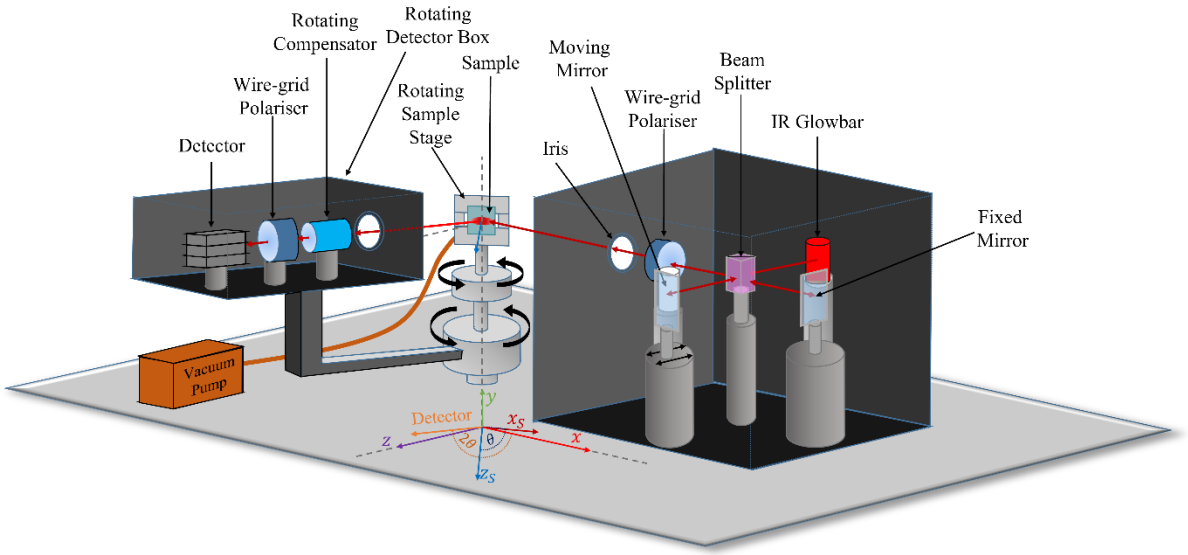

Figure 3.7 *Schematic of the Mark II IR-VASE system. The system comprises of three main parts: an IR source, the sample manipulator, and the detector. The source delivers linearly polarised light to the sample surface, which is rotated by the sample stage to the desired measurement angle, θ, normal to the sample surface. The sample is vertically mounted and held in place with a vacuum pump. The detector unit is rotated at an angle of 2θ.*

3.6.2.3. Oscillator Models

The frequency dependant dielectric function of an individual layer can be described by some addition or factorisation of the high frequency permittivity, ε_∞, and various individual oscillators. In the UV-VIS spectral range, the main dominating spectral feature for semiconducting materials is typically the optical bandgap transition, which can be described by a variety of different oscillator functions. In this work, an oscillator model based on the Herzinger-Johs Parametised Semiconductor oscillator function (PSEMI) was employed to reproduce the dielectric function of the complicated structure of the ZnO whilst maintaining Kramers-Kronig (KK) consistency. The PSEMI functions were generated to describe the optical properties of semiconductors with complicated critical point structures, providing a highly flexible lineshape comprising of four polynomial spline functions to describe the spectral features using KK consistent parameters. A PSEMI-M0 model was used in the UV-VIS spectral region, which models the shape of an M_0 critical point observed in direct bandgap semiconductors such as ZnO at its bandgap energy. The PSemi-M0 function contains seven fit parameters corresponding to the amplitude (Amp), broadening (Br), the width of the right and left side of the absorption (WR and WL), the control point position for the right and left side (PR and PL), the relative magnitude of the control points (AR and AL), and the coefficient for the second order polynomial terms for the left side of the polynomial ($O2L$). Of the parameters, those that are fixed at specific values during the modelling for the PSEMI-M0 are $WL = 0$, $PL = AL = 0.5$, and $O2L = 0$, whilst all other parameters are allowed to fit freely to describe the lineshape. In the UV-VIS region, an additional Gaussian oscillator is added to

account for additional features in the lineshape. The Gaussian is a complex function which describes the imaginary part of the permittivity by a Gaussian absorption, and the real part is its KK transform. The Gaussian description of the permittivity is given in Eq. 3.34:

$$\varepsilon_{Gauss} = \varepsilon' + i\varepsilon'' \tag{3.34}$$

Where,

$$\varepsilon'' = A_n e^{-\left(\frac{E-E_n}{\sigma}\right)^2} - A_n e^{-\left(\frac{E+E_n}{\sigma}\right)^2} \tag{3.35}$$

$$\sigma = \frac{Br_n}{2\sqrt{\ln(2)}} \tag{3.36}$$

Where the fit parameters are amplitude (A_n), energy (E_n), and broadening (Br_n) which is defined by the $\frac{1}{2}\sqrt{\ln(2)}$ function for the FWHM.

In the IR spectral region, for polar semiconducting materials such as the ZnO studied in this work, the contribution of free carriers and the optical polar phonon modes to the dielectric function must be considered.

The free carrier contribution can be described using a Drude term. The spectral dependence of the Drude dielectric function ($\tilde{\varepsilon}_{Drude}(\omega)$) is given by Eq. 3.37:

$$\tilde{\varepsilon}_{Drude}(\omega) = \varepsilon_\infty \left[1 - \frac{(\hbar\omega_p)^2}{(\omega^2 - i\gamma_p\omega)}\right] \tag{3.37}$$

$$\omega_p = \sqrt{\frac{Nq^2}{m^*\varepsilon_0\varepsilon_\infty}} \tag{3.38}$$

Where ħ is the reduced Planck's constant, γ_p is the plasma or Drude damping, and ω_p is the free carrier plasma energy which can be related to the free carrier concentration (N) and effective mass (m^*) of the free carriers through Eq. 3.38, where q is the charge of the free carriers and ε_0 is the vacuum permittivity.

For polar semiconductors such as ZnO, there is a charge separation causing a splitting of the Transverse Optical (TO) and Longitudinal Optical (LO) phonon modes, whereby the LO mode is shifted through a Coulomb interaction to a higher frequency. This splitting results in a forbidden spectral band between the two optical phonon energies referred to as the Reststrahlen band. The phonon contribution to the dielectric function of polar materials can be described by a factorised 'TOLO' oscillator model, which accounts for the anharmonic coupling effects seen in polar semiconductors.

The spectral dependence of the TOLO oscillator is given by Eq. (3.39):

$$\tilde{\varepsilon}_{TOLO}(\omega) = \varepsilon_{\infty}\left(\frac{\omega_{LO}^2 - \omega_{TO}^2}{\omega_{TO}^2 - \omega^2 - i\gamma\omega}\right) \tag{3.39}$$

Where ω_{LO} and ω_{TO} correspond to the LO and TO phonon frequencies respectively.

Traditionally, the effect of a system containing both free carriers and phonons on the dielectric function is described by a summation of the two oscillators summarised above in the form of Eq. 3.340.

$$\tilde{\varepsilon}(\omega) = \tilde{\varepsilon}_{Drude}(\omega) + \tilde{\varepsilon}_{TOLO}(\omega) \tag{3.40}$$

$$\tilde{\varepsilon}(\omega) = \tilde{\varepsilon}_{Drude}(\omega) \times \tilde{\varepsilon}_{TOLO}(\omega) \tag{3.41}$$

However, this summation does not consider any interaction between the two oscillators. In a system containing both plasmons and phonons there is a possibility for the two oscillators to couple as ω_p approaches ω_{LO}. In this frequency range, the two modes hybridise to form Longitudinal Phonon Plasmon (LPP) modes that a split into upper and lower branches. A factorised form of the multiplicative expression in Eq. 3.41 of the Drude and TOLO oscillators was developed in 1963 known as the 'Kukharskii model' (Eq. 3.42)[315–318] to account for the anharmonic coupling effects between plasmon excitations and LO phonon modes in polar semiconductor materials. A further exploration of phonon-plasmon coupling in ZnO can be found in **Chapter 6**.

A uniaxial form of the Kukharskii model[315] Eq. 3.42 with independently described ordinary, $\varepsilon_{||}$, and extraordinary, $\varepsilon_{\perp}$, principal axes dielectric functions was employed to describe the anisotropy in the Mid-IR in ZnO materials due to the uniaxial asymmetry of the hexagonal wurtzite structure and the effects of phonon-plasmon coupling on the frequency dependant dielectric function.

$$\varepsilon_{||,\perp}(\omega) = \varepsilon_{||,\perp;\infty}\frac{\left(\omega^2+i\gamma_{LPP^-_{:||,\perp}}\omega-\omega^2_{LPP^-_{:||,\perp}}\right)\cdot\left(\omega^2+i\gamma_{LPP^+_{:||,\perp}}\omega-\omega^2_{LPP^+_{:||,\perp}}\right)}{\omega\left(\omega+i\gamma_{p;||,\perp}\right)\cdot\left(\omega^2+i\gamma_{TO;||,\perp}\omega-\omega^2_{TO;||,\perp}\right)} \tag{3.42}$$

$$\omega_{LPP^{+/-}} = \sqrt{\frac{1}{2}\left[\omega_p^2 + \omega_{LO}^2 \pm \sqrt{(\omega_p^2 + \omega_{LO}^2)^2 - 4\omega_p^2\omega_{TO}^2}\right]} \tag{3.43}$$

where $\omega_{LPP^{+/-}}$ are the frequencies of the $LPP^{+/-}$ mode branches (extracted from Eq. 3.43) with associated broadening, $\gamma_{LPP^{+/-}}$, ω_p is the plasma energy with broadening, γ_p , ω_{TO} is the frequency of the IRSE active transverse optical phonon mode with broadening, γ_{TO} , and ω_{LO} is the LO phonon mode frequency.

The complex modelling of ellipsometry data to extract the dielectric functions of the ZnO investigated in this work will be explored in further detail in **Chapter 4**.

4. n-Type and p-Type Seed Materials

This chapter firstly presents investigations into the development of the as deposited ALD ZnO materials. This investigation revealed the potential of the ALD parameters to dramatically tune the electrical properties of the ZnO materials from very conducting n-type material to more highly resistive intrinsic material. From this investigation, the optimal deposition parameters were identified to produce highly n-type ZnO thin films that are utilised as the seed materials for further processing throughout further investigations. The rest of the chapter focuses on the development of the controlled excimer laser doping technique proposed in this work to induce p-type doping in ALD ZnO *via* laser induced N incorporation into the films. Verification of conductivity type is extensively sought and the underlying physical mechanisms governing the electrical behaviour are explored through Van der Pauw resistivity and Hall Effect measurements, Time-of-Flight Secondary Ion Mass Spectroscopy for N ion identification, reconstruction of simple energy band diagrams through a combination of results from Optical Reflectance Spectroscopy, Valence Band X-Ray Photoelectron Spectra and Kelvin Force Probe Microscopy, and the potential of infrared spectroscopic ellipsometry as an indicative method for carrier type determination is also investigated.

4.1 Seed n-Type Material Development

A prerequisite before conducting the CEELD investigation to induce N acceptor Doping in ZnO is the development of a good quality seed ZnO material fabricated by ALD. The next section therefore presents the work conducted to develop the seed ZnO materials, focusing on the effect of the ALD deposition parameters on the electrical properties of the ZnO material.

4.1.1 Effect of ALD Temperature on As Deposited ZnO Material

A variety of ALD deposition parameters need to be optimised and controlled to ensure the true, self-saturating ALD process occurs.[85] One of the most important ALD parameters that has significant impact on the deposited materials properties is the deposition temperature. The ALD process is based upon sequential self-limiting reactions and these surface reactions are heavily dependent on the deposition temperature since it determines the balance between the physical adsorption and desorption processes and the chemical reaction rate and reactivity of the precursor at the sample surface.[76] Therefore, the deposition temperature has a direct impact on the stoichiometry and composition of the ZnO structure as it determines the formation of intrinsic defects and presence of impurities. The optimal deposition temperature range for a given precursor reaction is termed the 'ALD Window'. For ZnO, this window has been established to be between $100 - 200\ ^{o}C$ for the DEZ and H_2O thermal ALD process employed in this work with an average growth rate of around 2 Å per cycle.[85] Nevertheless, even the temperature range within the ALD window has been shown to have a significant effect on the stoichiometry and composition of defects and impurities of the ZnO materials produced, which in turn

have a significant effect on the electrical and optical properties of the materials.[76,82,85] For the DEZ and H_2O reaction formation of ZnO, electron concentrations in the as deposited materials have been reported in the range of $10^{16} - 10^{20}\ cm^{-3}$ by simply varying the deposition temperature within the ZnO ALD window.[28,76] This large variation is due to the tuneability of intrinsic defects and impurities *via* deposition temperature variation. Previous studies into the formation of intrinsic native point defects in ALD ZnO revealed that O rich deposition conditions were achieved at low temperatures within the ALD window, whereas Zinc rich conditions dominated at the higher temperatures. The energy and probability of formation of native point defects in ZnO varies depending on whether the deposition is O or Zn rich, therefore different native point defects are expected to form depending on the deposition temperature chosen. All of which has a large impact on the properties of the thin film deposited. Moreover, both hydrogen and carbon impurities due to the precursors used containing large amount of hydrocarbon and hydroxyl groups cannot be overlooked in ALD ZnO films and their concentration is also dependant on the deposition temperature.[76] Investigations into the effect of deposition temperature on the electrical properties of the as grown ZnO thin films was therefore investigated in this work.

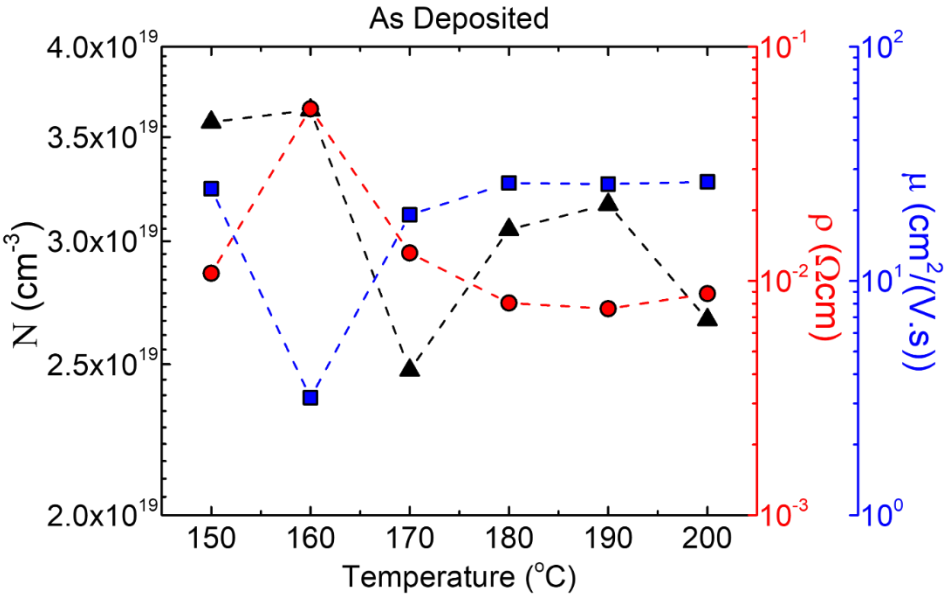

Figure 4.01 *Van der Pauw and Hall Effect measurement results for the as grown samples across the temperature range between* $150 - 200\ ^oC$ *under standard purge conditions (6 s for DEZ pulse, 7 s* H_2O *pulse), where the black symbols and left-hand axis relate to the carrier concentration,* N*, the red symbols and first right-hand axis is the resistivity,* ρ*, and the blue symbols and outermost right-hand axis is the carrier mobility,* μ*, for all samples. Results shown are the average of three consecutive measurements on the same probed contact region, where error bars are obscured by the symbols.*

To minimise the contribution of structural changes and eliminate their effect on the electrical properties for the investigation, the temperature range $150 - 200\ ^oC$ was investigated where ALD ZnO films

have been shown to produce structures with <100> preferred orientation.[319] The Van der Pauw and Hall Effect measurement results for the as grown samples across the temperature range between $150 - 200\ ^oC$ under standard purge conditions (6 s for DEZ pulse, 7 s H_2O pulse) are shown in ***Figure 4.01***. The results shown are the average of three consecutive measurements on the same probed contact region, where error bars are obscured by the symbols. From the results, all samples were found to be n-type materials with electron dominated conduction. The highest carrier concentration, N, was achieved for samples deposited at $150 - 160\ ^oC$ and has been experimentally verified across repeat samples. For the highest N sample ($160\ ^oC$) an accompanied increase in resistivity and reduction in carrier mobility is observed. This less favourable reduction in carrier transport properties for the $160\ ^oC$ film may be assigned to the higher level of ionised impurity scattering events or due to the type of defects formed in the $160\ ^oC$ film.[103] A large reduction in N occurs for the sample deposited at $170\ ^oC$, possibly signalling a change in the dominant defect type or concentration of certain defects present in the film. A further increase in N is then observed for the $180 - 190\ ^oC$ followed by a reduction for the $200\ ^oC$ sample, all of which have similar resistivity and mobility values to the $170\ ^oC$ sample despite the reduced N. It is therefore apparent that the deposition temperature plays a key role in dictating the electrical characteristics of ALD ZnO films produced in this work. This temperature dependence is assigned to the tuning of a combination of the intrinsic native point defects and impurities within the films due to the heat defined precursor reactions at the surface during the ALD process. From the literature, the ALD ZnO films produced at the lower end of the ALD temperature window ($100 - 200\ ^oC$) tend to be O rich where native point defects such as O_i and V_{Zn}, are readily formed, whereas the higher temperatures produce zinc rich films where defects such as V_O and Zn_i, are the dominant defects present.[32,76,102,148,320–323] Therefore, in the ALD range investigated in this work of $150 - 200\ ^oC$, the ZnO films are expected to go from a stoichiometric film at $150\ ^oC$ moving to a more Zn rich film at the higher temperatures where Zn_i and V_O may be more prevalent. The ALD as-deposited ZnO films in this study exhibit high n-type carrier concentration in the order of $10^{19} - 10^{20} cm^{-3}$, with low resistivity $\sim 10^{-3} \Omega cm$. ZnO is an intrinsically n-type semiconductor, but the origin of this conductivity is still not fully understood by the research community. Intrinsic defects such as V_O and Zn_i, have often been used to explain the intrinsic n-type nature, but studies suggest both defects have high formation energies in n-type ZnO, forming deep level donor states and thus do not contribute free electrons to the conduction band.[32,41,320] The standard low growth temperature of $150\ ^oC$ was chosen as it has been reported that lower growth temperatures lead to a more O rich thin film, minimising the amount of V_O present in the lattice which are expected to compensate for any acceptor type doping.[29,38,41,148] Therefore, at lower deposition temperatures, taking V_O as the predominant donor, the ZnO films should exhibit lower carrier concentrations due to the higher level of O expected in these films. However, this study shows that lower temperatures produce materials with the highest carrier concentrations. One of the most promising theories to explain the conductivity in

nominally undoped ZnO is background impurity hydrogen.[118,120] Hydrogen interstitials (H_i) have been found to behave as shallow donors in ZnO, and have been shown to prefer interstitial lattice sites where they can bond to O to form $O-H_i$ complexes.[32] Aside from H_i, hydrogen may also be incorporated as the O antisite H_O, that has also been shown to be a shallow donor in ZnO existing in the positively charged state.[118] The ALD ZnO understudy was deposited using Diethylzinc and water vapour as the metallic precursor and counteractant respectively. There is therefore a high level of hydrogen involved in the deposition process which could be readily incorporated into lattice sites in the ZnO layers during growth due to its high mobility and small atomic radius.[41,54] At higher deposition temperatures, the hydrogen atoms in the material will be more energetic and may readily diffuse out of the film to reduce the background H content, or may be promoted into H_O sites. Whereas at lower deposition temperatures the light element H_i would be more stable, thus leading to the higher carrier concentration observed for the materials deposited at $150-160\ ^oC$ in this work.[324] The high level of conductivity in the as grown ALD ZnO film is therefore proposed to arise from background impurity hydrogen. Interestingly, Vohs *et al* reported on the significant adsorption of DEZ molecules in ZnO deposited at temperatures lower than $180\ ^oC$, and detected both $Zn-C$ and $C-H$ bonds *via* X-ray photoelectron spectroscopy (XPS).[104] As mentioned, a switching point in electrical behaviour is observed for the films in this work at a deposition temperature around $170\ ^oC$. This may corroborate with the findings of Vohs *et al* and suggest that hydrogen impurities incorporated at the $C-H$ sites play a crucial role in the conduction properties of the ALD ZnO materials deposited at lower temperatures in this work. The minimal changes in carrier mobility across the majority of samples suggests minimal changes in the crystallinity between the films deposited at different temperatures, further supporting the claim that the origin of the high-level conductivity is due to the stable hydrogen at low deposition temperatures as opposed to differences in crystal structure or quality for the various growth temperatures. The lowest carrier mobility is attained for the highest carrier concentration film, which is suggestive of reduced carrier mobility due to ionised impurity scattering from the large amount of background impurity hydrogen present.[103,325]

4.1.2 Effect of ALD Purge Process on As Deposited ZnO Materials

As mentioned previously, there are a number of important deposition parameters that can be varied to modify the surface reactions during the ALD process which in turn have an effect on the properties of the deposited material.[85] The most investigated deposition variable in the literature has been the deposition temperature, but the precursor exposure time and purge process between precursor releases also needs to be controlled. Relatively little attention has been paid to the effect of the purge process (in terms of purge time and purge gas flow rate) on the material properties and are often dismissed as non-important parameters.[100] The effects of the purge time and amount of N_2 purge gas present during the diethylzinc and water reaction on the electrical properties of the as deposited ALD ZnO are therefore investigated.

Table 4.1 *Purge times for samples 1-4 for the diethylzinc (DEZ) precursor and water reactant*

Sample	DEZ Purge (s)	H_2O Purge (s)
1	3	4
2	6	7
3	12	14
4	24	28

Figure 4.02 (a) shows a triple y-plot of the results of a series of as deposited ALD films $(1-4)$ deposited at $150\ ^oC$ with $100\ mTorr$ of N_2 purge gas flowing through the system. The 'standard purge' time adapted from the manufacturer recipe are 6 s for DEZ precursor and 7 s for H_2O reactant. Purge times were varied in the deposition according to $0.5, 1, 2$ and $4\times$ the standard purge times, resulting in purge time for the DEZ precursor being varied from $3-24\ s$ whilst the H_2O purge was varied from $4-28\ s$. Full details of the deposition parameters for samples $1-4$ are shown in ***Table 4.1***. The figure details the noticeable changes in electrical properties of the film due to variations in the precursor purge time.

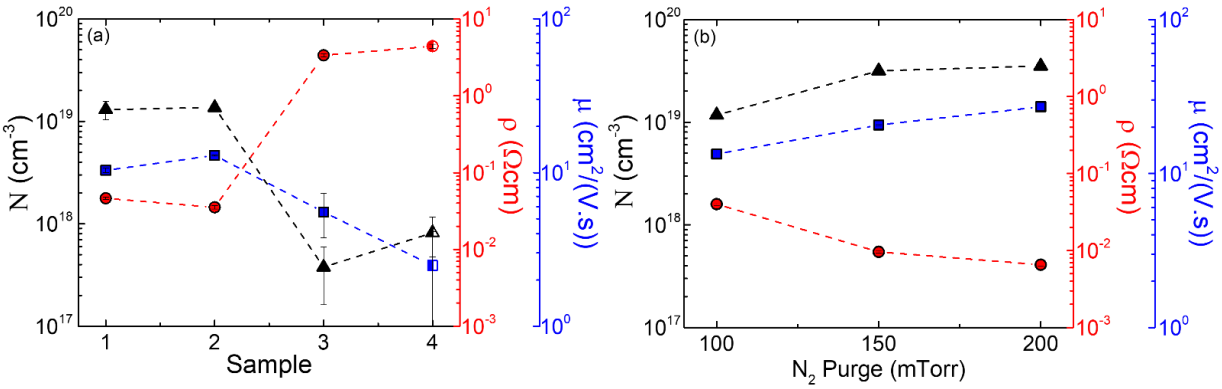

Figure 4.02 *Effect of the purge process on the as deposited electrical properties. Figure 4.02 (a) shows the electrical results of a series of as deposited ALD films* $(1-4)$ *deposited at* $150\ ^oC$ *with* $100\ mTorr$ *of* N_2 *purge flowing through the system. Full details of the deposition parameters for samples* $1-4$ *are shown in Table 4.1. Figure 4.02 (b) shows the electrical results for samples deposited at* $150\ ^oC$ *with DEZ purge of* 6 s *and* 7 s H_2O *purge, with a range of purge gas pressure between* $100-200\ mTorr$ *present in the system throughout the dynamic deposition process. Results shown are the average of three consecutive measurements on the same probed contact region, where some of the error bars are obscured by the data symbol.*

Samples with the lowest purge time produce n-type films with higher carrier concentration in the order of $10^{19}\ cm^{-3}$, with the lowest resistivity and highest carrier mobilities of the four films investigated. Of the materials, sample two was the most conductive n-type film with minor improvements in N, ρ

and μ compared to the shorter purge sample. Two orders of magnitude decrease in carrier concentration and increase in resistivity is observed for sample three alongside a reduction in mobility. Moreover, for the longest purge time sample, sample four , a further reduction in carrier mobility is observed alongside a conversion of the material from an n-type material to one that exhibits both n- and p-type behaviour according to consecutive hall effect measurements. The results show that the purge time can be precisely controlled to manipulate the electrical properties of ALD ZnO thin films. The orders of magnitude difference between the electrical properties across the four films shows a clear dependence of the electrical properties on the purge time and process. The effect of purge time on the materials properties may be understood by considering the effect the purge process has on the surface reactions during the ALD process and the removal of left-over precursor and by-products. At shorter purge times, the full surface reactions in terms of water dissociation from molecular to a hydroxyl group on the surface for the H_2O pulse followed by the ligand exchange during the DEZ pulse and subsequent removal of left-over precursor and by-products may not be fully completed before the next reaction takes place. Whereby incomplete hydroxylation of the surface or ligand removal may occur, causing hydroxyl or hydrocarbon groups to be incorporated into the thin film layers.[100,326] Such hydroxyl or hydrocarbon groups would contribute a large amount of background impurity hydrogen into the material, which acts as a donor type dopant in ZnO, leading to the increase in n-type conduction properties for the lower purge time materials. Increasing the purge time beyond a critical point would enable the full self-limiting ALD reaction to occur, minimising background impurity hydrogen inclusion, thus promoting a shift to a near stoichiometric/intrinsic film as is implied by the change in electrical behaviour between sample three to sample four. The increased purge time for sample four may also allow for other reactions to take place at the surface, including some incorporation of N in the film from the purge gas. Any inclusion of Nin the film may also act to decrease the n-type conductivity behaviour due to the contribution of nitrogen-related acceptors. These results also indicate the potential to achieve p-type ZnO materials *via* careful optimisation of the various ALD deposition parameters to produce certain acceptor type defects.[76] Further extension to the purge time may also result in the partial loss of surface hydroxyl groups which would affect the subsequent DEZ reaction.[100,326] This loss of surface hydroxyls is expected to be more prevalent at higher deposition temperatures.[324]

Another overlooked parameter in the purge process is the amount of purge carrier gas present under dynamic deposition conditions. Between reactant pulses, the ALD reactor chamber is purged with an 'inert' gas (N_2 in this work) to remove by-products and remaining precursor after the reaction. It is therefore important that enough gas (combined with an optimised purge time) is allowed to the system for the desired precursor-reactant surface reactions to occur. ***Figure 4.02 (b)*** shows the Van der Pauw and Hall Effect electrical results for samples deposited at $150\ ^oC$ with DEZ purge of $6\ s$ and $7\ s$ H_2O purge, with a range of purge gas pressure between $100 - 200\ mTorr$ present in the system throughout the dynamic deposition process. The N_2 purge flow rate is controlled using a needle valve, whereby

pressure increases from base vacuum are observed and used to set the N_2 flow through the system. The electrical results show that the film carrier concentration is doubled upon increasing the N_2 flow from $100\,mTorr$ to the $150-200\,mTorr$ range, accompanied by an increase in carrier mobility and decrease in resistivity. The observed changes in electrical properties of the films is assigned to the changes occurring in the surface reactions during the deposition process and in particular the by-product removal and surface coverage of the precursors.[76,100,326] The electrical results may be explained due to lower surface coverage of precursors ligands and faster removal of precursor or by-products with an increased purge gas flow rate. This may yield incomplete self-saturating reactions, leading to incorporation of hydroxyl or hydrocarbon impurities which results in the increased N observed for the $150-200\,mTorr$ films.[326] Faster removal of precursors may also reduce the surface coverage, in particularly of the water molecules which would alter the chemistry of the ALD reaction process, whereby water molecules may not be allowed to dissociate fully, or diethylzinc/methylene ligands may not be removed or fully reacted, leading to a change in the type of defects present and bonds formed within the material.

Investigations into the electrical properties of the as deposited ALD films presented above reveals the capability of the ALD deposition parameters to drastically tune the electrical properties of the ZnO films according to the ALD surface reactions. From the results, the highest n-type carrier concentration, with good mobility and low resistivity is achieved for the sample deposited at $150\,^{o}C$ with a DEZ purge of $6\,s$ and H_20 purge of $7\,s$ with an N_2 pressure of $200\,mTorr$ flowing through the system. This high level of n-type conductivity behaviour is assigned to the high level of background impurity hydrogen arising from $O-H$ and $C-H$ species present and stable in the films deposited at the stated deposition conditions. Moreover, work in the literature has suggested the potential of $N-H$ co-doping as a viable candidate to achieve acceptor type doping in ZnO. Therefore, the most promising seed material thought to be able to increase N solubility in ZnO through a co-doping mechanism with hydrogen *via* the CEELD process was deemed to be the $150\,^{o}C$ sample (DEZ purge: $6\,s$, H_20: $7\,s$ and N_2 pressure: $200\,mTorr$) and is carried forward as the seed as grown material for further investigations of the CEELD process unless stated otherwise.

4.2 Seed p-Type Material Development by Controlled Environment Excimer Laser Doping

The as grown ZnO material exhibits a high level of n-type conductivity and is assigned to the large amount of background hydrogen impurities residual in the film during the growth process. The n-type conducting properties are well known for ZnO and n-type material is readily available and widely used for many applications.[2,78] However, it's p-type counterpart remains elusive and the production of high quality, stable and reproducible p-type material remains a major research bottleneck in the field. As

such, the development of the highly desirable p-type ZnO material is the core focus of this work. The next sections details the results of CEELD investigations to achieve p-type doping in ZnO.

4.2.1 Electrical Properties of ZnO films after CEELD in an N_2 Environment

Nitrogen is often identified as the most suitable candidate for an acceptor dopant in ZnO due to its similar electronegativity and comparable atomic radius with that of O[38], however the solubility of N in ZnO is still low *via* conventional experimental doping methods. In this work, Controlled Environment Laser Doping (CEELD) is explored as a method to induce doping in the ALD ZnO films. The pulsed krypton fluoride $248\ nm$ excimer laser allows for precise high energy delivery across the top tens of nanometres of the surface of thin films of ZnO, inducing a controlled thermally assisted modification of the film's microstructure, defect density, crystallite size, internal strain/ film stress and introduction and activation of dopants for the associated modulation of the optical and electrical properties of the thin films. The CEELD in this work was conducted in a high pressure ($100\ psig$) N_2 environment at various laser energy density and number of laser pulses to try to introduce N into the ALD ZnO lattice *via* a laser doping method to induce stable and reproducible p-type material. The next section investigates the potential of CEELD to induce p-type doping in the ALD ZnO films *via* N doping. ***Figure 4.03*** shows Hall Effect results for the $150\ ^oC$ ALD ZnO film laser processed in high pressure, $100\ psig,\ N_2$ environment treated with $1-5$ laser pulses of varying laser energy density between $150-250\ mJcm^{-2}$. Carrier type is indicated by closed data symbols for electrons (n-type) and open data symbols for holes (p-type), whilst the half-filled symbols indicate samples that returned mixed carrier type results over consecutive HE measurements. The as grown sample is identified as the sample treated with zero pulses. The results shown are the average of three repeat measurements for each sample. The results of the laser processing studies conducted with a laser energy density of $150\ mJcm^{-2}$ reveal that all samples treated with $1-5$ pulses remain n-type with high carrier concentration, accompanied by minor changes in resistivity and carrier density which is assigned to modification of the film crystallinity at the milder laser energy density. At $200\ mJcm^{-2}$ the first indication of p-type conduction for samples processed with 1, 2 and 4 pulses, with a maximum achieved p-type carrier concentration in the order of $10^{19}\ cm^{-3}$, suggesting a high level of p-type doping. During the CEELD process, at sufficiently high laser energy density ($200\ mJcm^{-2}$) the laser irradiation is proposed to crack the N_2 in the annealing environment where it is then subsequently driven into the laser melted ZnO thin film. The high hole concentration at laser energy density of $200\ mJcm^{-2}$ in this work is hypothesised to be as a result of an increased N solubility in the ALD ZnO due to co-doping with the high-level residual hydrogen donors present in the as deposited films. [43,179] The co-doping of acceptors and donors has been proposed to both increase acceptor solubility, form shallow donor states, and restrict compensating defect formation which act as 'hole-killers'. [36][327]

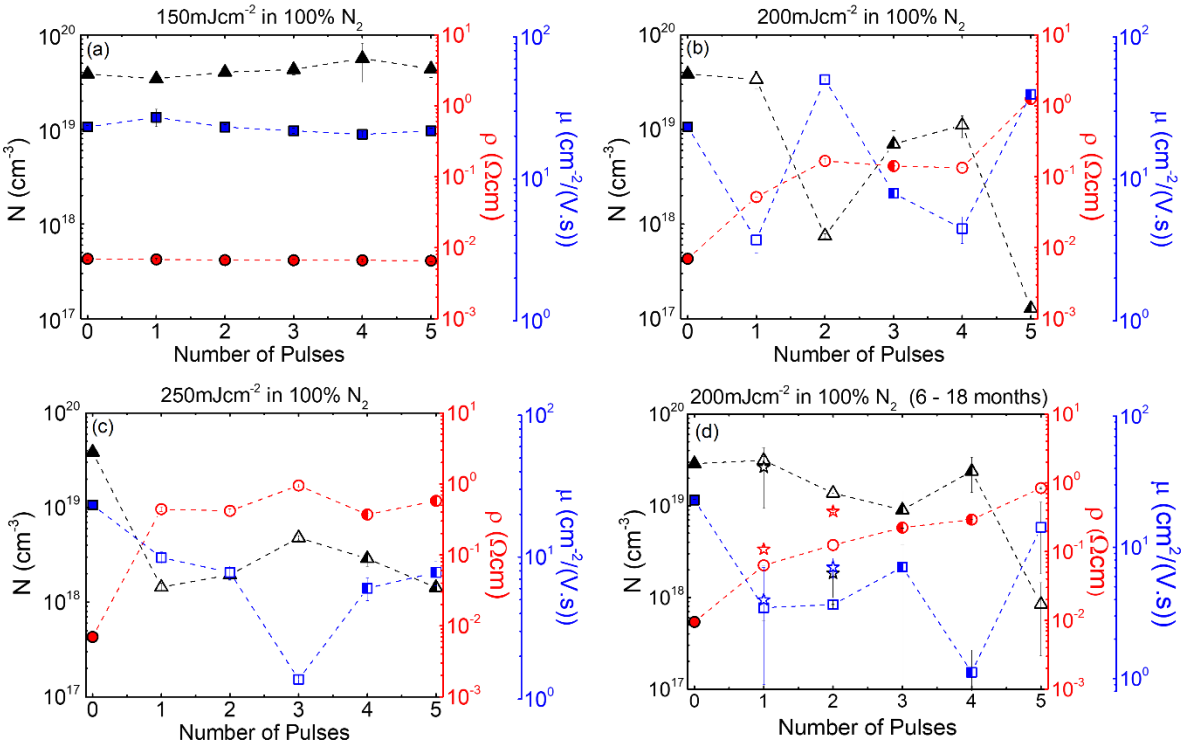

Figure 4.03 *Average Hall Effect results for the* $150\ ^{o}C$ *ALD ZnO film laser processed in high pressure* N_2 *environment treated with* $1-5$ *laser pulses at various laser energy density of (a)* $150\ mJcm^{-2}$*, (b)* $200\ mJcm^{-2}$ *and (c)* $250\ mJcm^{-2}$*. Carrier type is indicated by closed data symbols for electrons (n-type) and open data symbols for holes (p-type), whilst the half-filled symbols indicate samples that returned mixed carrier type over consecutive HE measurements. The as grown sample is identified as the sample treated with zero pulses. The stability of the electrical behaviour of the* $200\ mJcm^{-2}$ *samples over a period of* 6 *months is presented in (d), where measurements of the* 1 *and* 2 *pulse sample measured 18 months from the first measurement in (b) are also shown and indicated by the open star symbols. Some error bars are obscured by the data symbols.*

The exact position of the N and H in the lattice is unknown, but is tentatively described by the following mechanisms outlined below:

(1) N substitution in the O site in the lattice as charged N_O^- defect state, bonds to background $H_O{}^+$ in the antibond site N_O^- to form neutral defect complexes, whereby the acceptor nature of N is inadvertently passivated by the H

(2) N incorporation on O sites in the film, stabilised by interstitial hydrogen to form $N_o - H_i - N_o$ complexes. Whereby one N_o is again passivated by the H_i, whilst the other is acts as a shallow acceptor.

(3) N bonded to the H species in $O-H$ hydroxyl groups or ethyl/ methyl $C-H$ groups incorporated in the ZnO film through the high levels of $O-H$ and $C-H$ species present in the deposition process incorporated at O sites or at native point defects such as V_{Zn}

In the cases outlined above, the hydrogen increases N solubility, but also inadvertently passivates the N acceptor behaviour in ZnO. The high energy dose delivered to the samples at $200\,mJcm^{-2}$ is proposed to overcome the hydrogen passivation effect by breaking the $N-H$ bond and removing hydrogen from the film *via* thermally assisted out diffusion. The residual heat energy from the laser photon absorption during process causes the hydrogen to be mobile in the film and a thermal expansion of the upper layers of the ZnO film creates a pressure gradient that can draw the mobile hydrogen towards the surface leading to the ultimate out-diffusion of hydrogen from the film. The large number of hydrogen bonding sites available for N in the as deposited ALD ZnO films combined with the laser assisted hydrogen dissociation and diffusion activates the incorporated N as a shallow acceptor, leading to the high hole concentration observed in Figure 4.03 (b).[174] The drop in hole concentration for the samples treated at the higher fluence of $250\,mJcm^{-2}$ in Figure 4.03 (c) is possibly due to an over saturation of N_2 molecules situated at an O site which act as double donor states which act to reduce the free hole carrier concentration in the film by electron-hole recombination events. [149,328] Higher laser energy density may also induce premature or an increased rate of hydrogen out diffusion from the film before successful N incorporation can occur, thereby reducing the carrier concentration. Other non-desirable microstructural or surfaces changes for the higher laser energy of $250\,mJcm^{-2}$ may also lead to a reduction in carrier concentration through formation of trap states or non-idealities in the film. Some mixed carrier type behaviour (indicated by the half-filled symbols) is also observed for the samples processed with 3 and 5 pulses at $200\,mJcm^{-2}$ and with 4 and 5 pulses at $250\,mJcm^{-2}$. Mixed carrier type may arise due to the presence of multiple carriers in the film, or as an effect of some non-idealities during the HE measurement such as contact placement or surface/sample inhomogenieties introduced by the laser treatment.

The initial CEELD investigations show that laser annealing in a high-pressure N_2 environment can achieve a high level of p-type conductivity according to HE, which is ascribed to N-H co-doping in the non-equilibrium CEELD process. The CEELD induced p-type conduction observed for the ALD ZnO film is proposed to occur at high enough laser energy density to crack the N_2 in the annealing environment and subsequently be readily incorporated into the film during laser processing because of the large residual hydrogen concentration expected in the ALD ZnO films. The high energy supplied to the films *via* laser annealing can both break the $N-H$ bond and promote the out-diffusion of hydrogen from the film. [174] Removal of hydrogen thereby activates the remaining N as a shallow acceptor, yielding the high hole concentration observed in the HE data. The hypotheses discussed above will be investigated further in Section 4.3 *via* Time-of-flight Secondary Ion Mass Spectroscopy measurements for the identification of N related ion species.

4.2.2 Stability of the p-type Material Over Time

One of the key issues of the p-type ZnO material in the literature is the lack of stability of the p-type behaviour over time.[38] ***Figure 4.03 (d)*** (repeated below) shows the results of the samples processed with $1-5$ laser pulses at $200\,mJcm^{-2}$ 6 months after the initial measurement after storage in atmospheric conditions.

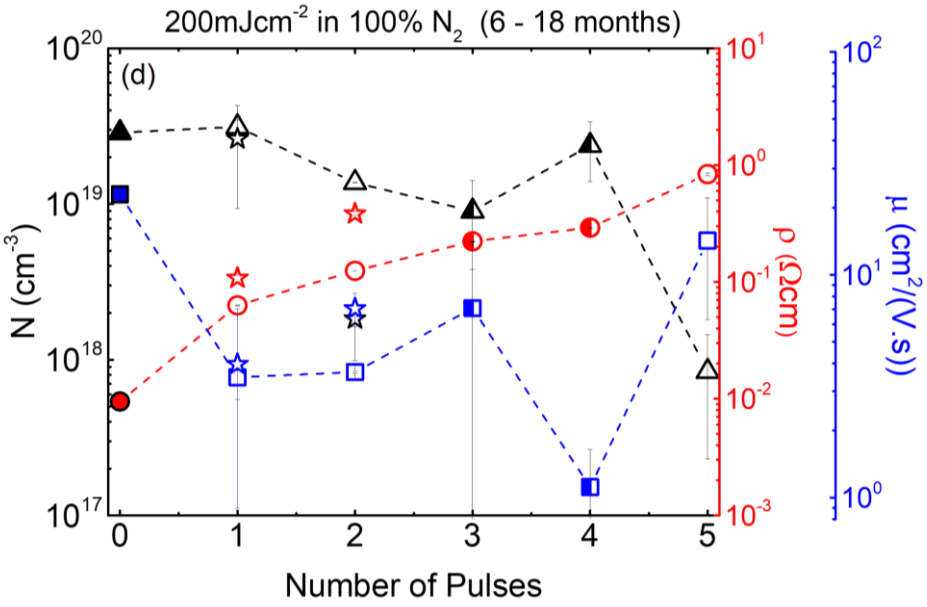

Figure 4.03 (d) *Stability in the average Hall Effect results for the* $150\,^{o}C$ *ALD ZnO film laser processed in high pressure* N_2 *environment treated with* $1-5$ *laser pulses at* $200\,mJcm^{-2}$ *samples over a period of* 6 *months including measurements of the* 1 *and* 2 *pulse sample measured 18 months from the first measurement (presented in 4.03(b) in Section 4.2.1) are also shown and indicated by the open star symbols. Carrier type is indicated by closed data symbols for electrons (n-type) and open data symbols for holes (p-type), whilst the half-filled symbols indicate samples that returned mixed carrier type over consecutive HE measurements. The as grown sample is identified as the sample treated with zero pulses.*

The results show the good stability of the p-type conductivity behaviour achieved with the 1 and 2 pulse samples. Meanwhile, the samples treated with $3-5$ pulses during the CEELD process show instability in the dominant carrier type, with a reduction in p-type character to mixed carrier type after six months for the 3 and 4 pulse samples, whilst the originally n-type 5 pulse sample has seemingly converted to p-type over time. The instability in the measurements for the $3-5$ pulse samples reduces the confidence in these materials and the HE measurements. To further verify the stability of the 1 and 2 pulse samples, the samples were re-measured around 18 months after the initial HE measurements (Figure 4.03 (b)), and the results are presented as the star shaped symbols in Figure 4.03 (d). The results of the 18-month measurements indicate the good stability of the p-type material developed by the CEELD process in high-pressure N_2 environment for the samples treated with 1 and 2 laser pulses at

$200\ mJcm^{-2}$. These laser doping conditions are therefore carried forward for the rest of the work and are referred to as the 'standard CEELD processing conditions' to achieve p-type conduction in ALD ZnO films.

4.2.3 Effect of Starting Material on the CEELD Process

CEELD studies were conducted on the full temperature range of as deposited films ($150 - 200\ ^oC$) presented in Section 4.1.1 to understand the role of the starting material during the laser doping process. The key results of samples laser treated with 1 and 2 pulses at $200 mJcm^{-2}$ in N_2 for the full temperature range set are presented in ***Figure 4.04***.

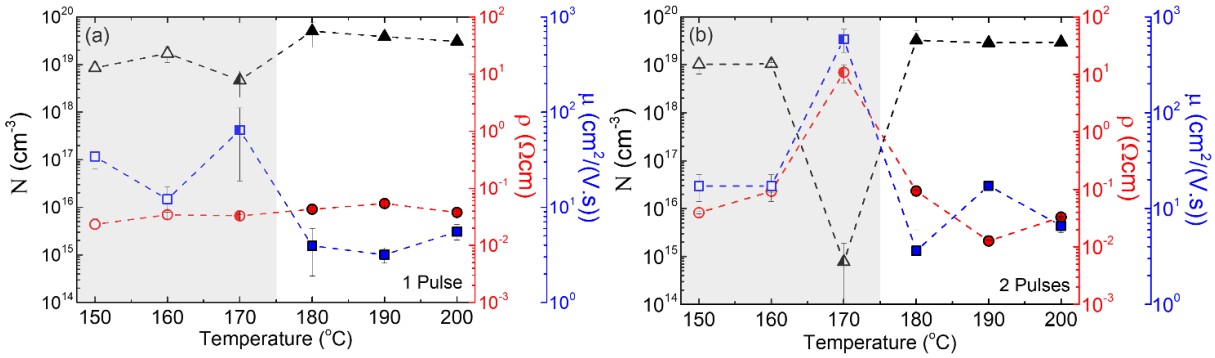

Figure 4.04. *Average Hall Effect results for the full* $150 - 200\ ^oC$ *temperature range ALD ZnO films laser processed in high pressure* N_2 *environment treated with (a)* 1 *pulse and (b) 2 pulses at a laser energy density of* $200\ mJcm^{-2}$. *Carrier type is indicated by closed data symbols for electrons (n-type) and open data symbols for holes (p-type), whilst the half-filled symbols indicate samples that returned mixed carrier type over consecutive HE measurements. The as grown sample is identified as the sample treated with zero pulses. Some error bars are obscured by the data symbols.*

The results show the conversion of the $150 - 160\ ^oC$ films to p-type, with higher carrier concentration achieved for the $160\ ^oC$ film. At $170\ ^oC$, a reduction in N is observed and HE measurements returned mixed carrier type results. Beyond $170\ ^oC$, an increase in N is observed and the samples remain n-type with no conversion to p-type unlike the lower deposition temperature films. The electrical results presented here show that the as deposited material has a significant effect on the CEELD process, leading to the difference in electrical properties presented in Figure 4.04. The Hall Effect results for the CEELD process in high-pressure N_2 environment for the various temperature deposition ALD ZnO further support to the earlier hypothesis that high level p-type conduction in the CEELD ALD ZnO films is achieved through the co-doping of H and N and is explained below.

Section 4.1.1 indicated that the residual hydrogen in the growth process is more stable within the films deposited at lower temperatures and leads to a higher level of n-type conduction in the low temperature films compared to the higher growth temperature films. At higher growth temperatures, the

hydrogen/hydroxyl groups are less stable and can readily diffuse out of the material surface with any remaining hydrogen being promoted to H_O sites due to the higher thermal energy available during growth. Moreover, higher temperature growth of ALD ZnO leads to more Zn-rich conditions, whereby the formation energy of intrinsic defects such as V_O is reduced and as such V_O may readily form under the high temperature Zn-rich ALD conditions. Whilst V_O have been shown to be deep level donors, they readily act as compensating centres in acceptor doped ZnO. Upon laser processing in a N_2 environment, results from the Hall Effect measurements show that the low temperature as grown films with the highest carrier concentration may be converted to a high level of p-type carrier concentration, whereas the high temperature films show no conversion to p-type and remain at a high level of n-type behaviour. This striking result supports both claims that (a) hydrogen complexes are the source of the residual n-type donor concentration in the low temperature films and (b) that the mechanism in which N is incorporated into the ZnO films to achieve p-type behaviour *via* the CEELD process is through co-doping with hydrogen.

The first claim is supported by the generally accepted agreement in the scientific community that high levels of intrinsic n-type dopants in ZnO such as V_O and Zn_iusually act to compensate for any acceptor doping, reducing the acceptor solubility in the film and consequently inhibit p-type conduction.[37,148,150] The opposite behaviour is observed for the low temperature samples in this work, whereby the high levels of initial n-type carrier concentration leads to higher levels of p-type doping upon laser annealing as is seen for the case of the $150-160\ ^oC$ samples versus those samples deposited between $170-200\ ^oC$. This suggests further that V_O and Zn_i cannot be the main source of the high-level n-type carrier concentration obtained in the low temperature ZnO films, thus promoting hydrogen to be the most suitable candidate. This subsequently leads to support of the second claim that high levels of N dopants are readily incorporated during the CEELD process *via* co-doping with the background impurity hydrogen present in the films. The higher concentration of hydrogen in the low temperature films means there are a greater number of hydrogen impurity sites for the N to bond to during CEELD process, leading to an increased solubility and concentration of N in the films subsequently and subsequently the highest p-type carrier concentration achieved in the low temperature deposited samples. A clear switching point in electrical characteristics is seen at the $170\ ^oC$ mark in Figure 4.04, which may be explained by the transition from the $O-H$ and $C-H$ dominated as deposited films at the low temperatures, to the V_O rich films deposited high temperatures which act as compensating centres to counteract any p-type conductivity. Moreover, the observation by Vohs *et al* that $C-H$ and $Zn-C$ species are present only for ZnO materials deposited below $180\ ^oC$ may suggest that N incorporation predominantly occurs at the $C-H$ site.[104] Such $C-H$ sites would therefore be unavailable for the N to bond to for temperatures $\geq 180\ ^oC$, which, in combination with the increased presence of compensating V_O centres, may explain why no conversion to p-type material is observed in the ZnO materials deposited at higher temperatures. The results of the CEELD experiments on various as grown

films deposited at different temperatures demonstrates that the starting material has a profound impact on the outcomes of the CEELD process.

4.2.4 Effect of CEELD environment on the electrical properties of ALD ZnO

The effect of various CEELD environments on the electrical properties of the films was also investigated. The standard laser annealing approach of 1 and 2 pulses at $200 mJcm^{-2}$ was performed in a variety of different high-pressure environments ($100\ psig$) including Ar, used as the control environment without any N; N_2 as the standard laser doping environment and NH_3 to investigate further the role of $N-H$ co-doping. Van der Pauw resistivity and Hall effect measurement results are presented in ***Figure 4.05*** for the (a) as grown, and (b) 1 and (c) 2 pulse CEELD samples processed in Ar, N_2, and NH_3 environment. Carrier type is indicated by closed data symbols for electrons (n-type) and open data symbols for holes (p-type). The as grown sample is identified as the sample treated with zero pulses, and the results shown are averages of three repeat measurements on each sample. The shaded region is added to guide the eye to the conversion between n- and p-type samples. The Hall effect results show that the Ar processed samples display similar electrical properties to the as grown films and remain n-type. An improvement in n-type behaviour is observed for the Ar processed samples versus the as grown, with increased N, reduced ρ and improved μ as a result of the CEELD process causing microstructural improvements and atomic rearrangement.[329] Upon laser processing in N_2, a conversion to p-type conductivity behaviour is achieved with electrical behaviour dominated by hole transport. Results of the N_2 processed samples show the behaviour seen previously, showcasing the repeatability of the laser doping technique to produce p-type thin films with consistently high carrier concentration with 1 and 2 pulses. The 1 pulse sample achieves the highest p-type carrier concentration of similar levels to the n-type as grown and Ar laser processed samples but is accompanied by a decrease in carrier mobility compared to the n-type films. This decrease in carrier mobility can be assigned to the presence of holes in the p-type film which are heavier than the electrons dominating the transport in the n-type materials. A reduction in overall p-type carrier concentration is obtained for the 2 pulse sample with an increased mobility compared to the 1 pulse sample. The increase in mobility may be explained due to further microstructural improvements upon the 2^{nd} laser pulse or due to a reduction in ionised impurity scattering compared to the higher carrier concentration 1 pulse film. CEELD in the NH_3 environment also causes a conversion to p-type conductivity, further indicating that the presence of N species in the annealing environment induces acceptor type doping in ZnO. Processing with 1 pulse in the NH_3 environment produces similar p-behaviour to the 2 pulse N_2 processed film, possibly signalling a catalyst present in the NH_3 CEELD environment which may arise from the presence of additional hydrogen NH_3 compared with N_2. A second pulse in NH_3 leads to a deterioration in carrier mobility and resistivity compared to the 2 pulse N_2 sample. The reduction in carrier transport properties indicates a non-favourable amendment to the stoichiometry or structural properties upon 2 pulses of

CEELD in NH_3. The HE results of the CEELD experiments in different high-pressure environments show a clear link between p-type conductivity and a N containing laser annealing environment, further indicating the ability of the laser doping technique to induce N-related acceptors in ALD ZnO.

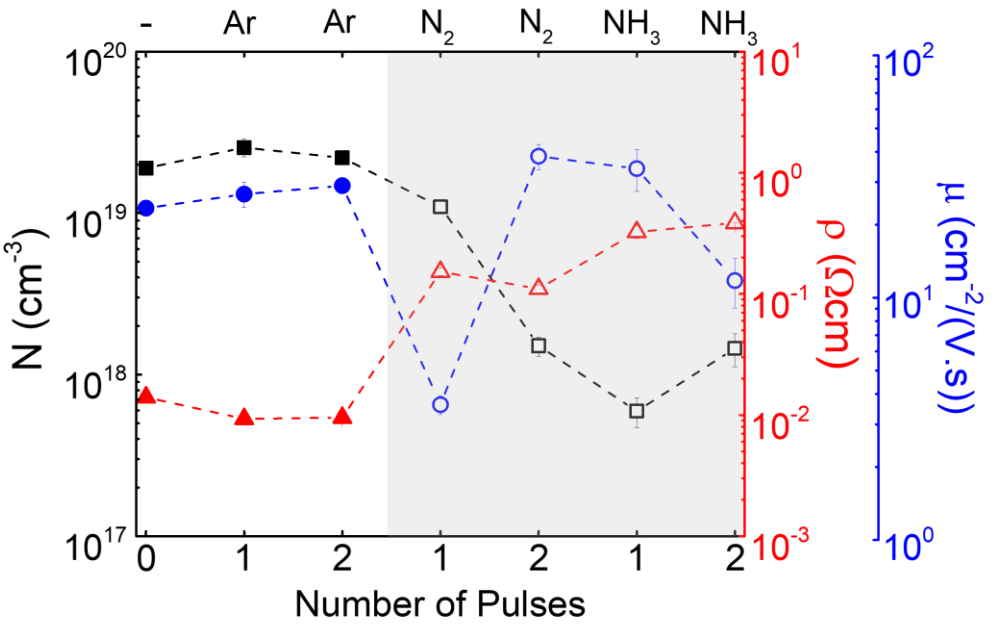

Figure 4.05 *Electrical results of the (a) Hall Carrier Concentration, (b) Van der Pauw resistivity and (c) Hall mobility for the as grown, and* 1 *and* 2 *pulse CEELD samples processed in Ar, N_2, and NH_3 environment. Carrier type is indicated by closed data symbols for electrons (n-type) and open data symbols for holes (p-type), The as grown sample is identified as the sample treated with zero pulses, and the results shown are the average of three consecutive measurements on the same probed contact region, where some error bars are obscured by the data symbols. The shaded region is added to guide the eye to the conversion between n- and p-type samples.*

The electrical results reported in this section reveal the potential of certain CEELD processing conditions in a N containing environment to induce a change toward p-type electrical behaviour in the ZnO films when compared to the as grown material and samples laser processed at low laser energy densities or in a 'control' environment such as Ar. HE measurements show the highest level of p-type carrier concentration and most stable materials are produced by performing the CEELD process in N_2 at 200 $mJcm^{-2}$ with 1 and 2 laser pulses. The mechanism with which N is incorporated into the ALD ZNO film is hypothesised to be due $N-H$ co-doping but further supporting evidence is needed to confirm the incorporation of N into the films *via* the CEELD process. The next section therefore seeks to provide further information on the doping mechanism and confirm the achievement of N incorporation in the ZnO films.

Scepticism in the literature surrounding the reliability of HE measurements to accurately report carrier type and characterise thin film materials remains a key issue. Inaccurate Hall readings may occur due to challenges associated with poor contact placement, sample inhomogeneities and surface conduction layers present in the materials being measured. The mixed carrier type returned for some of the laser processed samples in this work, reduces the confidence in the reliability of the HE measurements. A large body of work involving HE measurements was conducted before the full extent of the complications and inaccuracies of the technique were fully understood. For the films under study in this work, difficulties associated with sample inhomogeneity in the hall effect measurement due to the nature of the CEELD process as a surface treatment is a viable concern and may play a key role in the characterisation of the laser doped films. The HE measurements were therefore used as an indication of changes in electrical characteristics and are used to help to infer information on the properties of the materials developed. Due to the difficulties associated with the HE measurement, further verification of the achievement of p-type ZnO materials remains the core focus throughout the rest of **Chapter 4** and **Chapter 5** and is investigated using a variety of methods to support the claim of N-acceptor doping in ALD ZnO *via* the CEELD strategy.

4.3 Time-of-Flight Secondary Ion Mass Spectrometry Results

The next section explores further the laser doping technique by exploring the composition of the ZnO films before and after laser processing *via* ToF-SIMS. Verification of the presence of N-related ions is crucial to aid the underlying mechanisms governing the p-type conduction upon laser annealing. ToF-SIMS analysis of the 7 samples investigated in 4.2.4. (as grown, laser processed samples with 1 and 2 pulse at $200 mJcm^{-2}$ in three different high-pressure environments: Ar, N_2, NH_3) were performed to evaluate the chemical composition of the materials and to try to identify if any N species have been successfully incorporated into the materials processed in a N containing atmosphere to support the claim of successful N doping. Previous attempts to detect N in the N_2 laser processed films were undertaken by performing X-ray Photoelectron Spectroscopy (XPS) measurements at the Aristotle University of Thessaloniki, however it was concluded that the concentration of N dopants in the films developed in this work were below the 1 % XPS detection limit. Attention was therefore turned to ToF-SIMS for its high surface sensitivity and high mass resolution meaning the technique is readily capable of detecting light elements such as N and even H, which are the key elements of interest in this work. Whilst ToF-SIMS is a powerful tool for investigating relative intensities of various ions, it cannot provide absolute values of ion concentration for quantitative analysis.[330] Another important parameter to be investigated is the chemical composition profile throughout the entire ZnO thin film layers due to the surface treatment nature of the laser annealing process. It was demonstrated in Section 3.2 that the penetration depth of the $248\ nm$ laser photons is around $60\ nm$ for ZnO, meaning that for the $80\ nm$ ZnO films processed in this work, only the top $60\ nm$ of the films will be directly affected by the laser photons, whilst the remaining $20\ nm$ may only receive residual thermal treatment. Depth profile ToF-SIMS

measurements and data were acquired by Dr. Long Jiang at the University of Nottingham. ToF-SIMS measurements can identify both positive and negative secondary ions within a material.

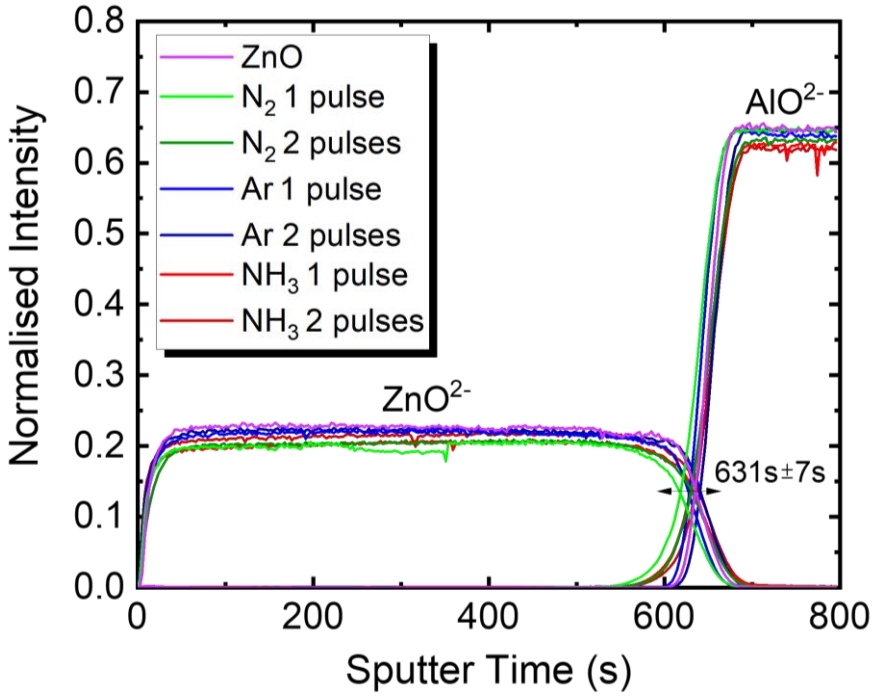

Figure 4.06 *ToF-SIMS results of the normalised intensity of* ZnO^{2-} and AlO^{2-} *ions as a function of sputter time throughout the* 80 nm *ZnO thin films, where* 0 s *is taken as the ZnO surface. Results are shown for the* 7*-sample set including the as grown film (magenta line), and the 6 samples laser processed with* 1 *and* 2 *pulses* $200 mJcm^{-2}$ *in various high-pressure environments: Ar (blue lines),* N_2 *(green lines) and* NH_3 *(red lines), where the* 1 *and* 2 *pulses samples are indicated by the light and dark line colours respectively.*

Initial investigations suggested that the negative polarity data was the most promising direction of investigation to explore N content within the ZnO thin films, whilst little useful information was obtained for the positive polarity. As such, only negative ions are reported in this work, with the most promising ions revealing the N content in the films established to be CN^-, CNO^-, NO^-, and NO_2^-. To relate the depth profile etch time to the ZnO thickness, depth profile measurements were performed until the clear interface between ZnO and the Al_2O_3 dielectric layer was reached. Figure 4.06 shows the normalised ion intensity for the ZnO^{2-} and AlO^{2-} ions as a function of sputtering (or etch) time for the as grown, and laser processed samples with 1 and 2 pulse at $200 mJcm^{-2}$ in the three different high-pressure environments: Ar, N_2, NH_3. The interface point is taken at the etch time at which there is an intensity inversion between the ZnO and Al_2O_3 ions, at which point it is assumed that the entire 80 nm ZnO layer has been etched through. The total etch time taken to reach the ZnO/Al_2O_3 interface averaged across all samples was found to be $631\ s \pm 7\ s$. From this the etch rate can be determined

and the etch time converted to ZnO layer thickness in nm. Minor deviation in the etch rate across the different samples suggest that the density of the films did not change dramatically upon laser processing, minor thickness variations may also be present throughout the sample spread which may also impact the crossing point. The average etch rate across the samples was determined to be $0.135\ nm/s \pm 0.001\ nm/s$, and all data is presented in terms of the average depth profile thickness taken across each of the 7 samples.

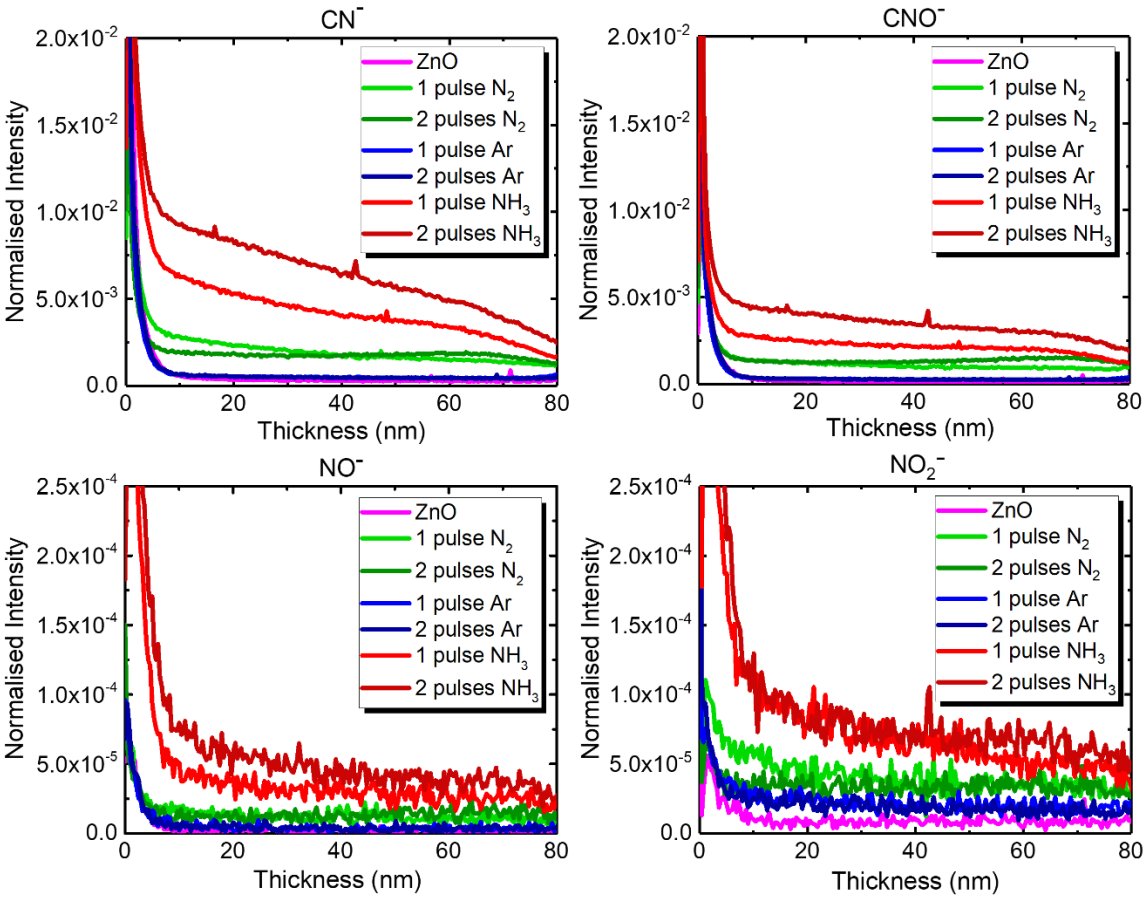

Figure 4.07 *ToF-SIMS results of the normalised intensity of (a) CN^-, (b) CNO^-, (c) NO_2^- and (d) NO^- ions as a function of depth throughout the 80 nm ZnO thin films, where 0 nm is taken as the ZnO surface. Results are shown for the 7-sample set including the as grown film (magenta line), and the 6 samples laser processed with 1 and 2 pulses $200 mJcm^{-2}$ in various high-pressure environments: Ar (blue lines), N_2 (green lines) and NH_3 (red lines), where the 1 and 2 pulses samples are indicated by the light and dark line colours respectively.*

Figure 4.07 shows the normalised intensity of (a) CN^-, (b) CNO^-, (c) NO_2^- and (d) NO^- ions obtained from the ToF-SIMS measurements as a function of depth throughout the 80 nm ZnO thin films, where 0 nm is taken as the ZnO surface. Results are shown for the 7-sample set including the as grown film (magenta line), and the 6 samples laser processed with 1 and 2 pulses $200 mJcm^{-2}$ in various high-

pressure environments: Ar (blue lines), N_2 (green lines) and NH_3 (red lines), where the 1 and 2 pulses samples are indicated by the light and dark line colours respectively. From the figure, large ion intensities are obtained in the top few nm of the ZnO films which is assigned to surface contamination due to the samples being stored in ambient conditions prior to being measured. Surface contaminant removal is indicated by the sharp decrease in intensity between $0\ nm$ to around $5-7\ nm$. For the as grown film (magenta line), minimal N associated ions are detected during the depth profile ToF-SIMS measurement (beyond the surface contamination region), which is to be expected since no intentional N doping has occurred for the as grown material. Any residual N species may arise due to the presence of N_2purge during the ALD growth process. The samples laser processed in the Ar control environment (blue lines) show similarly low levels of N ion species to the as grown material. A minor increase in N related ions can however be seen for the Ar samples possibly due to diffusion of surface contaminant C and N complexes into the film due to the laser surface treatment. Upon laser processing in the high-pressure N_2 environment (green lines), an increase in intensity for all N associated ions is obtained. For the case of the 1 pulse N_2 sample, there is a larger gradient of N-species throughout the depth of the film and is particularly evident for the CN^- and NO_2^- ions. Whilst the 2 pulse sample also achieves elevated intensities of N ions compared to the reference as grown and Ar LA samples, the intensity levels appear to remain at a more constant value throughout the entire depth of the $80\ nm$ ZnO film. This result may indicate that the larger number of laser pulses is able to drive N deeper into the thin film whilst the additional pulse and residual heating from the laser photons enables further distribution of N throughout the film. In contrast, the short 1 pulse appears to deliver the N to a more concentrated region in the top $20-40\ nm$ of the thin film as indicated by the higher intensity of CN^- and NO_2^- ions for the 1 pulse N_2 sample compared to the 2 pulse sample in the same depth region. A similar trend is observed for the CNO^- and NO^- ions but to a milder extent, which may suggest that the N related ions most responsible for acceptor type doping in the ALD ZnO films are the CN^- and NO_2^- ions. The N ion gradient implies that the 1 pulse sample may have a carrier concentration gradient across the film due to the different level of N doping. Interestingly, the second pulse in the N_2 environment does not seem to increase the nitrogen intensity, potentially indicating that the N incorporation is limited by surface saturation effects. Critically, for all cases, N incorporation seemingly occurs on sites which may be associated with residual hydrogen complexes in the film originating from the ALD growth process according to $DEZ\ \&\ H_2O \rightarrow CH_x^+\ \&\ OH^-$. This profound result offers support to the earlier hypothesis that N is more readily incorporated in the ALD ZnO films through a co-doping mechanism with the high level of impurity H within the ALD films. Whilst the prevalence of high concentrations of C related ions also supports the claim made in Section 4.2.3. that $C-H$ complexes are the dominant method of H and N incorporation in the ALD ZnO films. The $N-H$ co-doping mechanism may provide a further explanation to the lack of N incorporation increase for the 2-pulse sample compared to the 1 pulse. Upon laser processing in N_2, there may come a point where all available H sites are bonded to N, and

any further N saturation of the sample surface by processing in the high pressure N_2 environment will not lead to increased N incorporation since there are no more H sites for it to be readily incorporated. Thus, indicating that there may be an upper limit to the N doping concentration that is dependent on the H level within the film. Additionally, the laser induced sample heating may cause some out-diffusion of H from the film which will again act to decrease the N solubility. Moreover, a greater increase in N related species is observed for the 1 and 2 pulse samples processed in NH_3 (red lines), with the highest N content achieved for the 2 pulse sample. The results for the NH_3 processed samples further suggest increased N solubility in the ALD ZnO films in the presence of H due to the increased H levels in the NH_3 annealing environment compared to the pure N_2 environment. An increased presence of H may provide further bonding sites and increased probability of N incorporation in the ZnO lattice *via* H assisted co-doping. A difference in the ion intensity trends is seen for the NH_3 processed samples versus those processed in N_2, whereby the second pulse can further increase the N content in the films. One possible reason is in connection with the earlier described H limited N incorporation, which is avoided for the samples processed in NH_3 since the level of H in the ZnO films may be readily replenished by the H in the annealing environment, thus providing further sites for N incorporation. However, the higher N ion content in the NH_3 films does not yield an increased acceptor carrier concentration according to the HE results presented in ***Figure 4.05***. This may be due to an over saturation of N in the films leading to the formation of donor complexes that act to compensate and reduce the level of p-type doping in these films.[328]

A 3D representation of N ion distribution throughout the depth of the entire measurement area of the ZnO samples is shown in ***Figure 4.08***. A clear interface can be seen between the ZnO film and Al_2O_3 layer. Some columnar concentrated structures are observed that also spread into the Al_2O_3 layer, which may suggest some pinholes in the thin Al_2O_3 film. The previously explored differences in N ion concentration depending on the CEELD processing conditions are evident in the figure which displays the large concentration of N related ions at the surface and the ion distributions throughout the different films. A slight increase in the N ion concentration for the Ar processed films compared to the as grown is discernible from the 3D graphs. This is proposed to originate from the high concentration of CN^- and CNO^-ions at the surface of the as deposited material that may become mobile during the high energy laser processing which allows the diffusion of N related ions throughout the film that follows the temperature gradient induced from the surface throughout the film by the laser pulse. An alternative explanation could be due to the dissociation of any adsorbed N_2 molecules at the surface or throughout the film originating from the N_2 purge gas in the growth process, which may dissociate and bond to more preferential sites such as the N-related ions reported here because of the laser processing. Upon laser processing in N containing environment, more N species are delivered to the top surface of the film. The high energy of the laser yields a greater thermal dose to the film and as such a larger number of photons penetrate deeper in the material. The increase in photon absorption increases the depth at

which the resultant heating mechanism occurs[275], and the increased heating increases the mobility of the N species that are then driven deeper into the film.

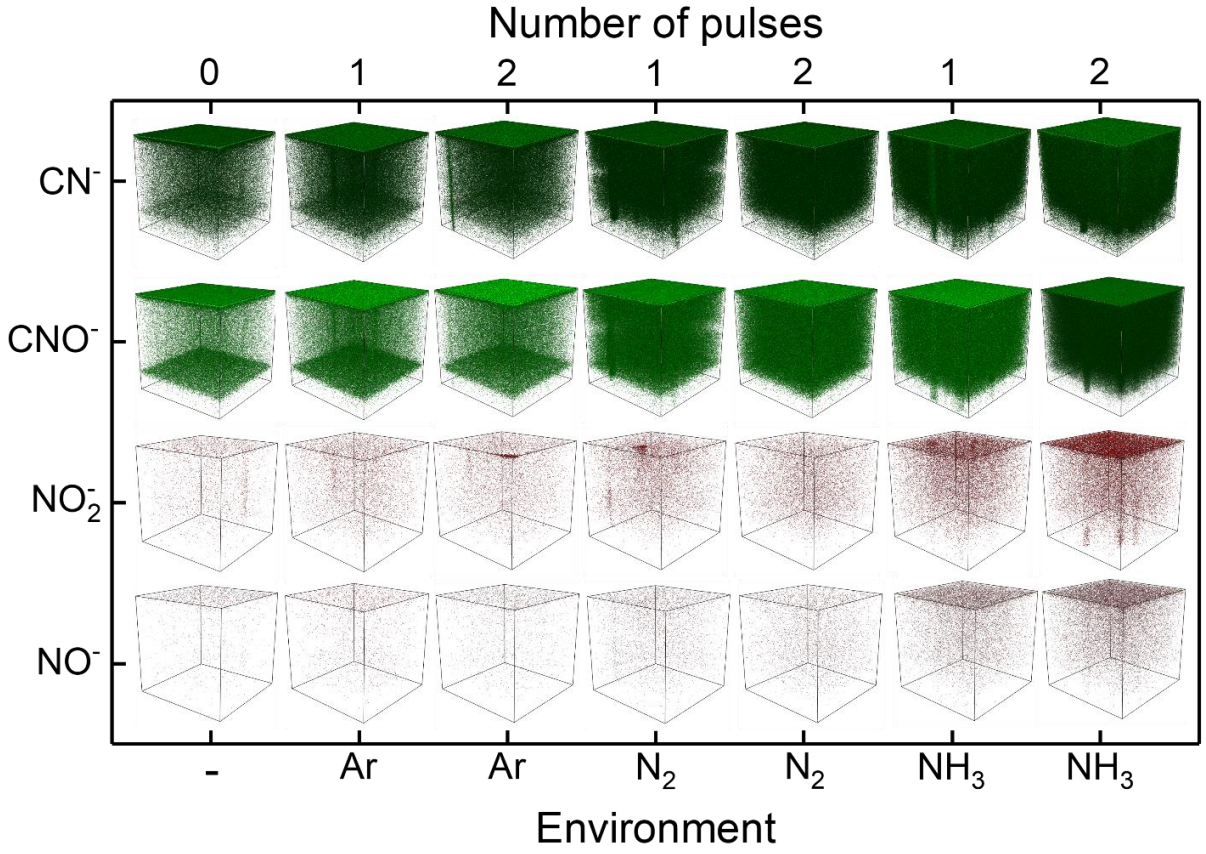

Figure 4.08 *3D representation of the ToF-SIMS measurement area results of the normalised intensity of* CN^-, CNO^-) NO_2^- *and* NO^- *ions as a function of depth throughout the* 80 nm *ZnO thin films. Results are shown for the* 7*-sample set including the as grown film (taken as the 0-pulse sample), and the 6 samples laser processed with* 1 *and* 2 *pulses* $200mJcm^{-2}$ *in various high-pressure environments: Ar,* N_2 *and* NH_3*.*

From the figure, upon delivery of a second laser pulse, a more even distribution of N ions is induced throughout the film, however the total ion content does not double upon the second pulse for the N_2 processed materials. This suggests a limit to the N solubility for those samples which assigned to the upper limit of H content in the N processed films for the N to bond to. This upper limit in N content is not observed for the NH_3 processed samples since the H levels can be increased and replenished (to compensate for the out-diffusion of thermally mobile H from the broken $N-H$ bond initially formed) within the sample as a result of the H in the laser doping environment.

For the case of the 1 pulse sample in N_2, the heat generation during the CEELD process is as a result of absorption of the 248 nm laser photons at the surface, that have a certain penetrative depth in the ALD ZnO films around 60 nm, followed by a subsequent heat diffusion process from the upper surface layer to the rest of the film.[277] There is therefore a gradient in thermal absorption and temperature which

may yield a concentration gradient of absorbed N ions. As mentioned previously, it is expected that during the CEELD process, the initial $N-H$ bond formed is then broken and the thermal and pressure gradient throughout the depth of the film induced by the laser photon penetration causes the residual hydrogen to be mobile. The now mobile hydrogen may diffuse throughout the film until it is desorbed at the surface. Upon H removal, the in-situ N is then activated as a shallow acceptor and contributes towards the p-type conduction observed in the HE measurements. However, the ultrafast laser annealing process and thermal gradient may result in incomplete dissociation and out diffusion of hydrogen, and as such not all N may be activated further away from the sample surface. A carrier concentration/ dominant carrier type gradient may therefore be formed throughout the laser doped films, resulting in only the top surface of the materials converted to a p-type conducting layer. Similar behaviour may also result in the reduced carrier concentration observed for the NH_3 samples, where the balance between out-diffusion of H for N activation versus the influx of hydrogen to the film from the laser environment maybe yield a greater number of N ions that remain passivated by the impurity H. A subsequent annealing process for the NH_3 and N_2 samples may aid in the out-diffusion of H for full activation of N-acceptors throughout the entire depth of the film.

In summary, the ToF-SIMS measurement technique is shown to be a powerful tool for the detection of ions associated with light elements and the results demonstrate the ability of the CEELD approach to nitrogen dope ALD ZnO thin films when performed in a N containing environment. Moreover, it is further shown that nitrogen is incorporated into the thin film through C, OO (and H) related complexes. Such ion complexes, alongside the dramatic increase in N ion levels upon laser processing in an NH_3 environment further supports the hypothesis that N incorporation is achieved *via* co-doping with H, and it is these complexes that lead to the p-type behaviour obtained in the earlier HE results. There is also some evidence of H limited N inclusion which further supports the co-doping theory. Nitrogen ion gradients are observed for some of the laser processed samples (beyond the surface contamination region) and must be taken into further consideration when performing electrical characterisation of these materials and their implementation into devices.

4.4 Fermi Level Shifts in Energy Band Diagrams Investigation

This section presents the results of the work undertaken to construct simple energy band diagrams (EBD) of the seed as grown ZnO material and standard laser doping approach to achieve acceptor-type doping with 1 and 2 pulses at $200\,mJcm^{-2}$ in a high-pressure N_2 environment. The aim of constructing simple EBD for these materials is to observe shifts in the Fermi level within the band gap. As explained previously, in n-type semiconducting materials, the Fermi level is expected to reside just under the conduction band. Conversely, in p-type semiconductors, the Fermi level shifts deeper in the band gap towards the valence band. Therefore, by observing shifts in the Fermi level in semiconducting materials one may ascertain further insights into the majority carrier type depending on where E_f sits

within the bandgap. EBD are therefore employed in this work to provide further support to the results of the Hall Effect measurements and the claim of achieving acceptor type doping in ZnO *via* the CEELD technique. Construction of simple EBD may be achieved by taking the results of a combination of different measurement techniques and calculating the key energy bands for a given material. In this work, results of Optical Reflectance Spectroscopy (ORS) analysis are firstly explored to obtain the optical bandgap of the materials. Valence Band X-ray Photoelectron Spectroscopy (VB XPS) results are then used to determine the position of the valence band maximum (VMB) with respect to E_f. Kelvin Probe Force Microscopy (KPFM) results measured at the ZnO surface provide information on the E_f position from vacuum (i.e., the work function). Finally, the simple EBD from the above three measurement techniques are produced using the analysis of the optical bandgap, E_g, from ORS, which, once the position of the VBM with respect to the E_f is known from VB XPS and the Fermi level energy from vacuum obtained from KPFM, the position of the conduction band minimum (CBM) can be determined from $VBM + E_g$ and as such the position of E_f within the band gap can be investigated.

4.4.1 Optical Bandgap Determination by Optical Reflectance Spectroscopy (ORS)

ORS was used to determine the optical bandgap, E_g, of ZnO materials by producing a Tauc plot using the values of the frequency dependent absorption coefficient, α, obtained from the optical constants *via* fitting of the reflectance spectra. An oscillator and geometric model was used to describe the dielectric function of each layer in the ZnO samples. The reflectance spectra and model fit for the as grown, 1 pulse and 2 pulse laser doped samples are shown in ***Figure 4.09 (a)*** whilst a schematic of the geometric and relevant oscillator models for each layer in the sample stack is shown in ***Figure 4.09 (b)***. The geometric model shows the sample stack from the Si substrate and native SiO_2 layer of known optical constants, to the Al_2O_3 spacer layer and upper ZnO thin film layer of unknown optical constants. Prior measurement of the $Al_2O_3/SiO_2/Si$ sample allowed for determination of the UV-VIS optical constants of the Al_2O_3 layer. The layer was found to be transparent in the measurement range with optical properties well described by a simple Cauchy model, of fit parameters A, B and C, alongside the film thickness d_{Al2O3}. The fit parameters and the thickness of the Al_2O_3 were then fixed for the subsequent modelling of the ZnO samples to reduce fit parameter correlation. In 4.09 (b), the grey shaded regions indicate parameters that were fixed in the modelling, whilst the parameters allowed to fit freely are indicated by the coloured shaded regions. The ZnO layer was found to be modelled well using a PSEMI-M0 oscillator model (with associated fit parameters A_{PS}, γ_{PS}, and E_{PS} to describing amplitude, broadening and energy respectively and fixed parameters $WR1_{PS}, PR1_{PS}, AR1_{PS}$ and $O2R1_{PS}$) and a single Gaussian (A_G, γ_G, and E_G) to describe the lineshape of the band gap transition which is the dominant optical feature dominating the spectrum in the measured range. For the case of the unprocessed, as deposited ZnO film, a single layer was used to describe the ZnO, whilst a dual layer

approach was used to describe the optical properties of the 1 and 2 pulse samples to account for the expected bilayer resulting from the CEELD process. For the CEELD films, the underlayer was modelled as the as grown material of unknown thickness but otherwise fixed oscillator parameters, and the upper layer was again described by PSEMI-M0 and Gaussian oscillators of unknown thickness and free fit parameters that were allowed to fit in order to derive the optical properties of the upper CEELD processed area.

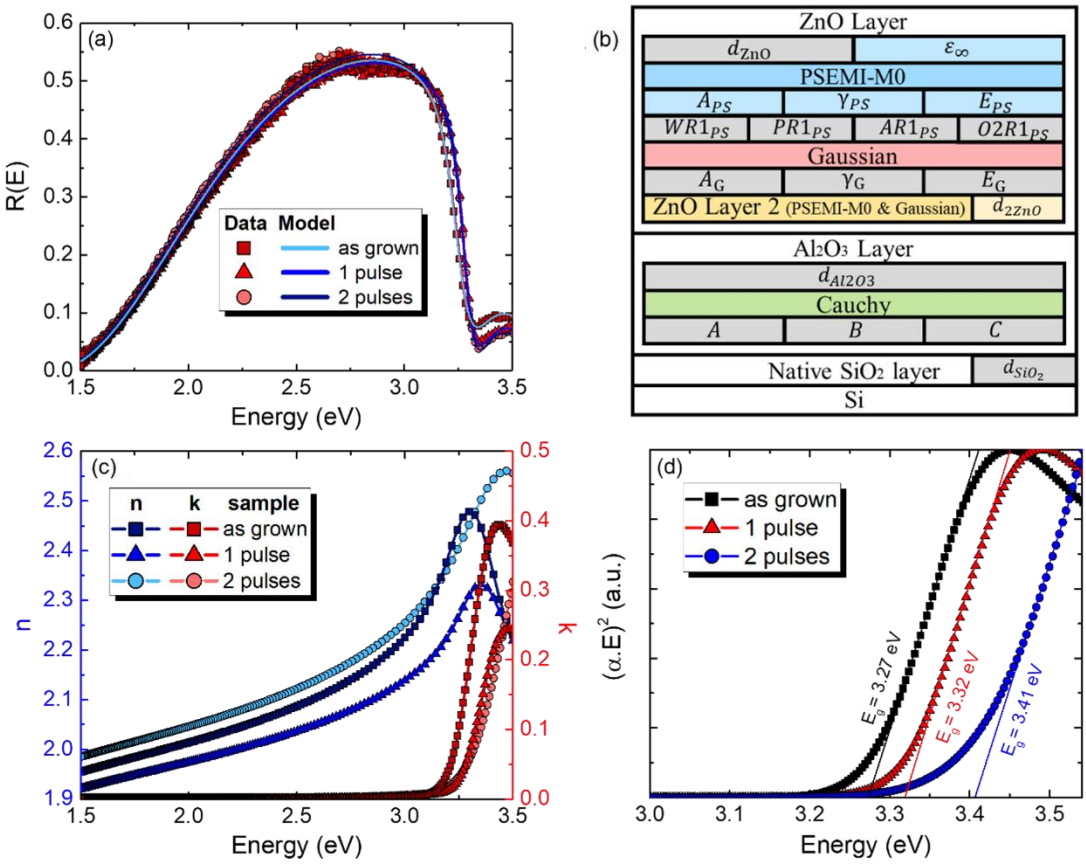

Figure 4.09 *Optical Reflectance Spectroscopy results and analysis, where figure (a) shows the reflectance spectra and model fit for the as grown, 1 pulse and 2 pulse laser doped samples, (b) details the geometric and oscillator model used for the analysis (single ZnO layer used for as grown, dual ZnO layer for the laser processed samples), (c) shows the optical constants n and k and (d) shows the* $(\alpha.E)^2$ *versus E plot and linear extrapolation to determine the optical band gap of the as grown and the* 1 *and* 2 *pulse laser doped samples.*

The resultant optical constants n and k derived from the modelling of the as grown, and 1 and 2 pulse laser annealed samples are shown in **Figure 4.09 (c)**. From n and k, α can be determined according to Eq. 3.28 (repeated below). The E_g can then be related to α through the Tauc method based on the assumption that α can be expressed as Eq. 3.30 (repeated below) for direct bandgap materials.[331,332]

$$\alpha = \frac{4\pi k}{\lambda} \tag{3.28}$$

$$\alpha(hv) = C(hv - E_g)^{1/2} \tag{3.30}$$

Tauc plots for the materials are presented in ***Figure 4.09 (d)***, alongside the linear extrapolation which was used to determine E_g at $\alpha = 0$ intercept at the energy axis. From the plots, the as grown ZnO sample has reduced E_g compared to the commonly quoted literature value of 3.34 eV. This band gap narrowing has been reported for some heavily doped ZnO materials and occurs due to the electron-electron repulsive interaction. The collective Coulomb repulsion of the electrons arises due to the Pauli exclusion principle and leads to a downward shift of the conduction band, thus narrowing E_g.[333,334] Band gap narrowing has also been reported due to the hybridisation of shallow donor impurity levels with the conduction band, leading to an apparent downward shift in the conduction band and a reduced E_g.[335] Meanwhile, a blue shift in E_g is observed for both laser annealed samples, with E_g values of around 3.3 eV, which is much closer to the expected value of E_g for ZnO.[336] The origin of the increase in E_g for the laser annealed samples may arise due to several reasons, such as the reduced carrier concentration obtained for the laser annealed films compared to the as grown. Another explanation could be based upon the hypothesis that upon laser annealing, the shallow donor hydrogen forms a neutral complex with the N introduced into the film through laser doping, and the subsequent heat energy produced during the CEELD process breaks this bond and allows the hydrogen to diffuse from the thin film. In this case, de-hybridisation of the previously postulated hybrid shallow donor impurity hydrogen band with the conduction band that resulted in the narrowed E_g in the as grown film would occur due to the removal of the hydrogen donor state, thus resulting in the widening of E_g. Moreover, hydrogen has been reported to have donor ionisation energies in ZnO between $35 - 47\ meV$ in the literature.[118,120] From ***Figure 4.09 (d)***, a 43 meV increase in E_g is obtained from the as grown to the laser annealed samples which further supports the claim of hydrogen donor level removal upon ELA. Furthermore, the E_g obtained for all materials presented here are consistent with the expected bandgap of ZnO and as such the ZnO materials developed in this work are suitable for use in short wavelength devices in the near-UV window.

4.4.2 Valence Band Maximum Determination *via* Valence Band X-Ray Photoelectron Spectroscopy (VB XPS)

XPS measurements in the low binding energy range, i.e., the valence band region, were performed at the Aristotle University of Thessaloniki to obtain the valence band maximum of the ZnO thin films. Depth profile XPS measurements were performed to obtain measurements of VBM throughout the depth of the ZnO film. ***Figure 4.10*** shows the valence band spectra in the binding energy (BE) between $-5\ to\ 5\ eV$ for the as grown, 1 and 2 pulse samples. The spectra were normalised, and binding energy calibrated to a known energy Ar peak. In the VBS measurement, once electrical contact is established between the sample and measurement system, the 0 eV BE may be taken as the Fermi level position.[337]

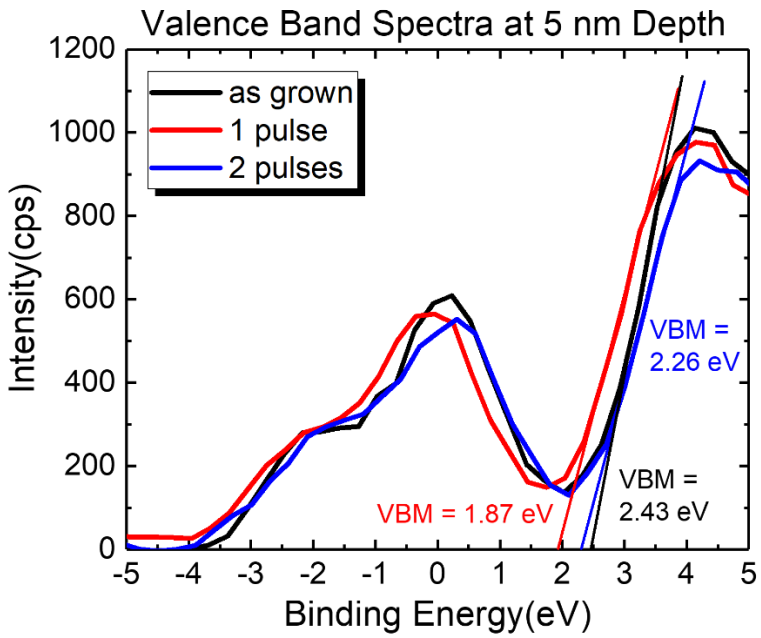

Figure 4.10 *Valence band spectra in the binding energy (BE) between* -5 *to* 5 eV *for the as grown (black-line),* 1 *(red-line) and* 2 *pulse (blue-line) laser processed samples at* $200mJcm^{-2}$*. The linear extrapolation of each spectrum to the energy axis details the valence band maximum (VBM) at* $BE = 0\ eV$.

For all samples, a peak occurs around $0\ eV$, indicating there are occupied states at the Fermi level, and as such the films may be classed as conducting. The occupation of E_f for the as grown sample may be explained by the high level of n-type carrier concentration. For the laser annealed p-type films, the occupied E_f may indicate the presence of some trapped charge states within the bandgap that are inactive/ undetectable during the dynamic Hall Effect measurements but can be detected by the static VB XPS measurements. The VBM can be determined by performing a linear extrapolation to the peak relating to the bandgap that has an apparent maximum at $4\ eV$. Results of the linear extrapolation are shown in the figure and the VBM for the as grown, 1 pulse and 2 pulse samples are positioned at $2.43\ eV$, $1.87\ eV$ and $2.26\ eV$ below the Fermi level at a depth of $5\ nm$ below the surface. These initial results suggest that there is a smaller energy gap between the VBM and Fermi level for the laser annealed samples compared to the as grown material, which indicates the increase in acceptor type doping for the laser processed films. VB XPS measurements were performed throughout the depth of the ZnO samples. As described previously, laser annealing is a surface treatment and as such may not produce an entirely uniform film, as indicated by the gradient in N related ions for the 1 pulse sample in N_2 from the ToF-SIMS results. It is therefore desirable to observe changes in the VBM throughout the sample thickness to better understand the N diffusion depth obtained during the laser doping technique and the resultant effect on the conducting properties throughout the film. ***Figure 4.11*** shows the VBM position with respect to the Fermi level at $0\ eV$ for the as grown, and 1 and 2 pulse CEELD

samples throughout the first 60 nm of the ZnO thin film. Measurements beyond 60 nm were emitted due to an increased difficulty in determining the VBM at deeper depths in the film due to poor signal to noise ratio.

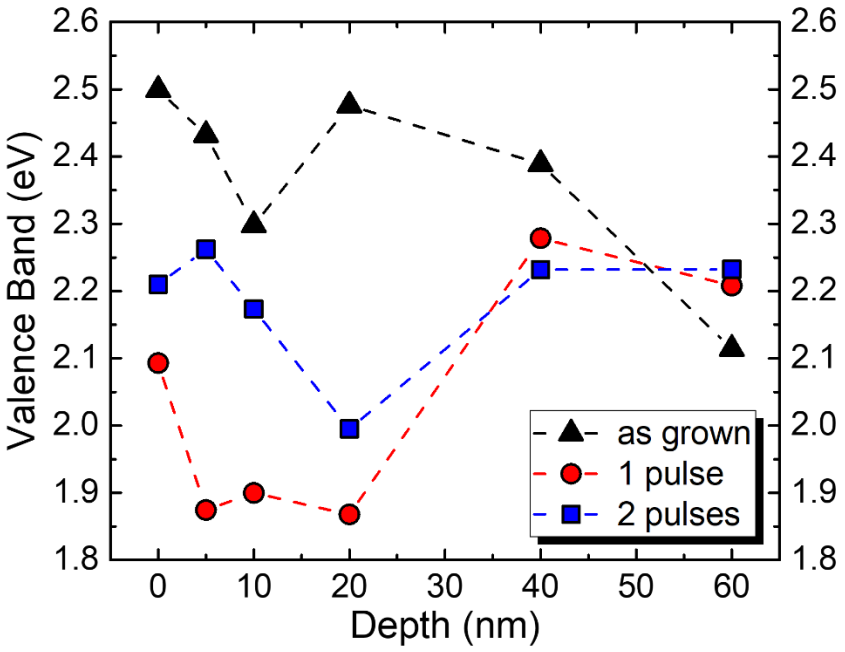

Figure 4.11 *VBM position with respect to the Fermi level at* 0 eV *as a function of depth throughout the first 60 nm of the as grown (black symbols), and laser processed ZnO films with 1 pulse (red symbols) and 2 pulse (blue symbols) at* $200mJcm^{-2}$.

Generally higher VBM (with respect to E_f) are found for throughout the depth of the as deposited ZnO, which is to be expected due to the high level of n-type doping pushing the Fermi level upwards in the bandgap towards the conduction band. A reduction of VBM is observed for the 1 and 2 pulse samples with the 1 pulse material achieving the smallest energy gap between VBM and E_f. Interestingly, a sharp increase in VBM is observed between the $20-40$ nm measurement for the 1 pulse sample, whereby the VBM reaches a maximum value at 40 nm that is similar in magnitude to the n-type as grown material. This indicates that the depth limit of the acceptor type doping for the 1 pulse film is somewhere between $20-40$ nm. This result further supports the behaviour observed for the 1 pulse N_2 sample in the ToF-SIMS measurements, where a gradient in N related ions is observed in the top 40 nm of the film and crosses the 2 pulse ion intensity line between $20-40$ nm. The results for the VBM throughout the 1 pulse sample further supports the idea that laser doping is a surface limited technique and produces a N diffusion gradient in the ZnO thin film, whilst the remaining thickness of the film has valence properties similar to the as grown film. A more consistent VBM is observed for the 2 pulse sample which supports the more consistent N ion level in the ToF-SIMS results. However, despite the reduction in energy gap between the VBM and E_f for the laser annealed samples, the VBM

energy values place the E_f above the middle of the bandgap for the ZnO ($\sim 3.3\ eV$). Whilst this suggests a reduction in the n-type character through acceptor doping, the E_f remains further from the VBM than is expected for p-type materials. The co-doping strategy of doping a material with both n- and p-type dopants to increase acceptor solubility as followed in this work may lead to Fermi levels away from the VBM and close to the middle of the bandgap.[32] An E_f close to the middle of E_g is preferential as it lowers the formation energy of acceptor type dopants (thus increasing solubility) whilst increasing the formation energy of compensating native donor-type defects in the film. Upon removal of the n-type dopant (hydrogen in this work) however, the E_f should shift towards the VBM. The formation of surface defects during the depth profile etch process may induce donor-type defects that would act to compensate the as fabricated p-type behaviour of the film, resulting in an upward shift of the E_f away from the VBM. The effects of storage and sample aging cannot be discounted from the results of the film as the VB XPS measurements were performed outside of NTU sometime after the last Hall effect verification of p-behaviour. As such, repeat measurements on a fresh sample set would be highly desirable to improve confidence in the results. An alternate method to investigate the valence band of semiconductors materials is through UV Photoelectron Spectroscopy (UPS), which is the preferred method of measuring valence electrons due to the low penetration depth of the radiation used that can only ionise the electrons in the outermost electronic level (i.e., the valence electrons). Moreover, UPS can also provide information on the work function of a material. Measurements of VBM and work function in unison would be highly desirable to improve confidence in the energy band diagram investigations.

4.4.3 Surface Work Function Investigation *via* Kelvin Probe Force Microscopy (KPFM)

KPFM measurements were performed at the King Abdullah University of Science and Technology to investigate the work function of the materials. The first set of measurements were performed on the as received samples sometime after the samples were sent to be measured, and a freshly exfoliated piece of highly ordered pyrolytic graphite (HOPG) was used as the reference material to calibrate the measured work function to real values. The contact potential difference formed between the Kelvin Probe tip and sample is not only affected by the real surface work function of the material but is also affected by any surface defects or adsorbates and oxide layers, all of which would affect the measured values of work function causing it to deviate from the real work function of the material. A second measurement was therefore performed after a mild thermal anneal at $80\ ^oC$ overnight in an N_2 filled glovebox to try and 'clean' the sample surface to remove any additional defects that may have formed at the surface due to storage in air over an extended period. Results of the first and second KPFM measurements are shown in ***Figure 4.12*** for the as grown, 1 pulse and 2 pulse films. Results from the first measurement show opposite behaviour to what is expected for n- and p-type materials. For n-type

materials, the work function is expected to be close to the conduction band and therefore shallower within the bandgap, whereas for p-type samples the work function is expected to be close to the valence band and at deeper energies within the bandgap, but the opposite is observed in the first measurements of the material work functions.

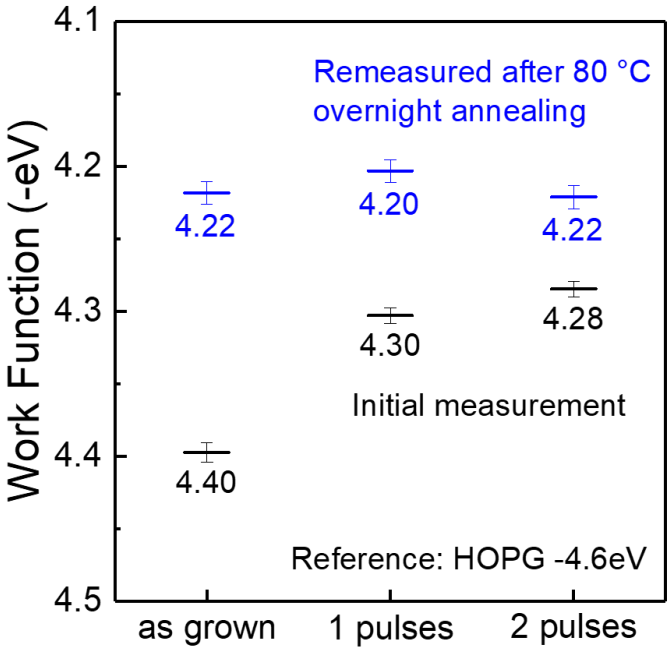

Figure 4.12 *Results of the work function for the as grown,* 1 *pulse and* 2 *pulse CEELD samples processed in high pressure* N_2 *at* 200 $mJcm^{-2}$ *as determined by Kelvin Force Probe Microscopy at KAUST.*

After the gentle anneal, a reduction in the work function value for all samples was observed. This may be an effect of the HOPG reference sample measurement which the overall magnitude of the ZnO samples are dependent on. However, a change in the relative difference between the samples is observed for the 'surface cleaned' samples, with the values of the work function now being very close together. The origin of the change in behaviour in terms of either an effect of the mild annealing or simply the extended storage time and surface defect layer was unclear. Remeasurements on freshly prepared samples or by alternate means such as UPS would be desirable to improve confidence in the results.

4.4.4 Energy Band Diagram (EBD) Construction

Energy band diagrams (EBD) are useful tools to further understand a material and its properties. In this work, EBDs are constructed to observe changes in the Fermi level, E_f, within the material bandgap, E_g, to further asses the n-or p-type character of the ZnO films developed in this research. The results of the three experimental techniques outlined above (VB XPS, ORS and KPFM) allow for the reconstruction of simple EBD for the ZnO films. From KPFM the position of the Fermi level from vacuum (the work

function) was determined for the ZnO surface. Analysis of ORS data gave the optical bandgap of the materials, which once the position of the VBM with respect to the E_f is known from VB XPS and in relation to the Fermi level energy obtained from KPFM, the position of the conduction band minimum (CBM) can be determined from $VBM + E_g$. ***Figure 4.13 (a-c)*** show the simple EBD for the as grown, 1 pulse and 2 pulse samples, where VBM, CBM, E_f, E_g and the vacuum level are labelled in the figure.

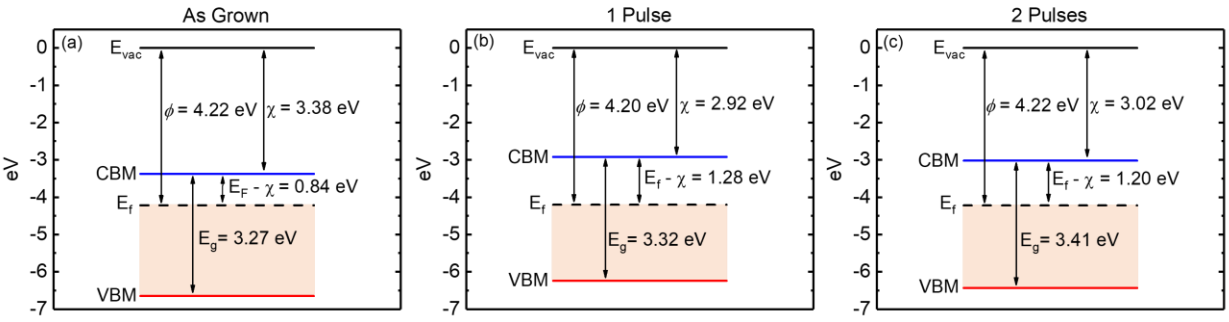

Figure 4.13 *Simple Energy Band Diagrams (EBD) for the (a) as grown (b) 1 pulse and (c) 2 pulse standard laser processed samples in high-pressure* N_2*, where the positions of the VBM, CBM,* E_f *with respect to the vacuum level,* E_{vac}*, are labelled in the figure. Values of* E_g*,* φ*,* χ*, and* $E_f - \chi$ *are also presented in the figure.*

A clear downward shift in the Fermi level is observed for the laser processed samples which is indicative of a reduced n-type behaviour due to an increased acceptor type doping as a result of N acceptor complexes being incorporated into the films. However, as discussed previously, the E_f position remains above the middle of the bandgap for the Hall effect determined p-type samples and so full support of p-type conduction cannot be claimed from these initial EBD results. Non-ideal measurement technique may play a role in the results. Non-idealities include the fact that the measurements were performed on three different sample sets, which would result inconsistency across the measurements. Despite the p-behaviour of samples being confirmed before sending them for measurements, the sample sets were of different ages and the effect of aging and extended storage time may also have influenced the results, with some samples more than 2 years old by the time of measurement (where p-character was indicated at 18 months *via* HE measurements). A more robust experimental procedure by repeating measurements using the same sample set for all measurement techniques at shorter time intervals or alternative methods such as UPS measurements could be employed to more reliably investigate both the VBM, and work function simultaneously to help improve confidence and reliability of the results.

In summary, a method was presented to construct simple energy band diagrams for semiconducting films. An increase in bandgap energy between the as grown and laser annealed samples of around 43 meV was observed which is proposed to be due to the removal of the shallow hydrogen donor

impurity state underneath the conduction band after laser processing, which further supports the hypothesis of $N-H$ co-doping and hydrogen removal. A deepening of E_f within the bandgap is also observed for the laser doped samples which indicates an increase in acceptor type doping that acts to reduce the n-type conductivity of the as grown material. However, the position of E_f does not go below the mid-gap point and as such does not support p-type semiconductor theory. Challenges in accurately determining the Fermi level of the materials by KPFM may arise due to surface contamination or the effect of sample storage and aging and inconsistencies across the three measurement techniques due to the different samples sets used. A more robust experimental procedure including either repeating measurements on a consistent sample set in a short time window for all three measurement techniques or by using UPS to measure both the Fermi level and VBM which is the preferred method for investigating valence electrons that may be performed throughout the depth of the material should be considered for future work.

4.5 Carrier Type Determination *via* Infrared Spectroscopic Ellipsometry

Due to ambiguity in the literature on the very existence of p-type ZnO, it is important to enhance reliability of results by supporting with alternate measurement techniques to determine free carrier properties in thin films. Conventional electrical measurements used to investigate free charge carrier type such as HE can yield noisy and unreliable measurements due to poor Ohmic contacts of the probes to the sample and inaccurate carrier type determination due to the tendency of electrical measurements to probe surface charge accumulation layers or trapped charged states which do not represent the bulk properties of the thin films.[233] Other factors also effect the reliability of HE measurements including the resistance and mobility of the samples, stratified layers of different electrical characteristics in the sample being measured, and Fermi level pinning all contribute to inaccuracies in the HE measurement.[338,339] As such, accurate electrical characterisation of semiconducting thin films remains a challenge by conventional methods. Infrared Spectroscopic Ellipsometry (IRSE) is an optical measurement technique strongly affected by lattice and free carrier excitations and therefore could be used to probe free charge carrier information (such as carrier type, concentration (N) and effective mass ($m*$)) in semiconducting films. The development of a robust IRSE method is highly desirable as it would offer several benefits to traditional electrical characterisation techniques since the IR photons can penetrate the entire sample stack to probe the bulk properties of the semiconducting thin film beyond the surface charge layers for full sample characterisation, mitigating the often erroneous results obtain by HE.[340]

Schöche *et al*[340,341] proposed the potential of IRSE as a method for carrier type determination by employing the Kukharskii oscillator model (KM) (Eq. 3.42 which is repeated below) to describe the dielectric function of semiconducting thin films. The KM was developed to describe the anharmonic coupling of longitudinal optical (LO) phonon modes with free carrier plasmon excitations to form hybrid

LO phonon-plasmon (LPP) modes in polar semiconductors, and can therefore provide insights into the free carriers within a semiconducting film.[315]

$$\varepsilon_{||,\perp}(\omega) = \varepsilon_{||,\perp;\infty} \frac{\left(\omega^2 + i\gamma_{LPP^-_{:||,\perp}}\omega - \omega^2_{LPP^-_{:||,\perp}}\right)\cdot\left(\omega^2 + i\gamma_{LPP^+_{:||,\perp}}\omega - \omega^2_{LPP^+_{:||,\perp}}\right)}{\omega\left(\omega + i\gamma_{p;||,\perp}\right)\cdot\left(\omega^2 + i\gamma_{TO;||,\perp}\omega - \omega^2_{TO;||,\perp}\right)} \tag{3.42}$$

The coupling between an LO phonon mode and plasmon to form the hybrid LPP modes is expected to differ depending on the free charge carrier type, due to the difference in carrier mass and mobility between electrons and holes. Typically, holes exhibit heavier mass and lower mobilities compared to electrons. The different coupling behaviours are proposed to manifest in different broadening values of the $LPP^{+(upper)/-(lower)}$ modes described by the KM, which are independent to the m^* of the free carriers and therefore exempt from any inaccurate assumptions.[313,341] Therefore, careful analysis of IRSE data and the KM parameters alongside correlation with electrical measurements could allow for the development of IRSE as a contactless, non-destructive technique for determining carrier type in ZnO and other polar semiconductors.

This section presents the method and results of IRSE analysis and investigates the Kukharskii model parameters of the laser processed materials developed in this work that returned purely n- and p-type results and some mixed carrier type results with consecutive repeat Hall Effect measurements.

4.5.1 Optical Modelling of as grown and LA ALD ZnO Materials

The fitting process of SE data is non-trivial, and various oscillator models in combination with a geometric model can be employed to describe the dielectric function of thin film materials.[24,307,342,343] This section details the process followed to fit IRSE measurements in the IR spectral range between $0.03 - 0.3\ eV$ (where the phonon and plasmon absorptions dominate the spectra) to extract the complex permittivity according to $\tilde{\varepsilon}(E) = \varepsilon_1(E) + i\varepsilon_2(E)$ and the LPP properties of the ZnO thin films. The ZnO thin films under investigation in terms of their fabrication conditions, IRSE determined plasma energy and Hall Carrier concentration are shown in **Table 4.2**. For all cases, the thin film thickness was determined by fitting a simple Cauchy model[343] (Equation 4.1) in the spectral range or $0.4 - 0.8\ eV$ which is the transparent region.

$$n(\lambda) = A + \frac{B}{\lambda^2} + \frac{C}{\lambda^4} \tag{4.1}$$

Where A, B and C in the Cauchy model are unitless fitting parameters related to the refractive index and dispersion. The resultant film thickness was then fixed for each individual sample during the Kukharskii model analysis. To unveil the physical mechanisms that govern the light-matter interactions of the ZnO materials in the spectral range $0.03 - 0.3\ eV$, an oscillator model must be used to describe $\tilde{\varepsilon}$ as a summation of different oscillators.

Table 4.2 *ZnO thin films under investigation in terms of their IRSE determined plasma energy, ω_p, laser processing conditions and Hall carrier concentration, N_{Hall}.*

Sample ω_p (eV)	**Number of LA pulses**	**Laser Energy Density ($mJcm^{-2}$)**	**Laser Doping Environment**	**N_{Hall} (cm^{-3})**
0.13	1	150	N_2	-3.43×10^{19}
0.14415	2	150	N_2	-4.03×10^{19}
0.14473	3	150	N_2	-4.30×10^{19}
0.13507	4	150	N_2	-5.64×10^{19}
0.14083	5	150	N_2	-4.36×10^{19}
0.17732	1	200	N_2	$+3.39\times10^{19}$
0.18618	2	200	N_2	$+7.50\times10^{17}$
0.18311	3	200	N_2	$+/-6.99\times10^{18}$
0.15306	4	200	N_2	$+1.11\times10^{19}$
0.1542	5	200	N_2	$+/-1.28\times10^{18}$
0.14153	1	250	N_2	$+1.44\times10^{18}$
0.14277	2	250	N_2	$+1.94\times10^{18}$
0.13618	3	250	N_2	$+4.80\times10^{18}$
0.14871	4	250	N_2	$+/-2.89\times10^{18}$
0.12661	5	250	N_2	$+/-1.43\times10^{18}$
0.17713	1	200	N_2	$+1.10\times10^{19}$
0.20324	2	200	N_2	$+1.51\times10^{18}$
0.19863	1	200	NH_3	$+5.94\times10^{17}$
0.19689	2	200	NH_3	$+1.45\times10^{18}$
0.155	2	150	N_2	-3.76×10^{19}
0.223	3	150	N_2	-4.09×10^{19}

Various oscillator models were attempted to describe the IRSE spectra including a Drude oscillator to account for the absorptions due to free carrier plasmons and a series of Gaussian and/or Lorentzian

oscillators to describe the absorptions due to the IR active phonons in the polar ZnO. However, it was found that a summed, isotropic model was not capable of describing the lineshape of the IRSE spectra fully, in particular, the dip feature due to a loss of reflectivity in the spectra at around $0.07\ eV$ could not be captured whilst maintaining the physicality of the model. Further investigation revealed that the dip structure manifested from the coupling between the LO phonon mode in the polar ZnO crystal structure and the free carrier plasmon excitations in the ZnO thin films.[340] A factorised model to describe the anharmonic coupling between phonons and plasmons in polar semiconductors was developed in 1963 by Kukharskii[315] and was found, when used in an anisotropic model, to capture the dip feature well, improving the realness of the model and reducing the mean squared error (MSE) of the fit (which is the main parameter describing the goodness of fit). The KM specifies the imaginary permittivity, ε_2, whilst the real permittivity, ε_1, is calculated from ε_2 by using the Kramers-Kronig (KK) relations. The KK relations ensure real physicality of the fitting, maintaining $\varepsilon_2 > 0$ which is required to report a real and physical permittivity of a thin film material. No further non-idealities were accounted for in the model, such as surface roughness, as a less than 25% MSE reduction was achieved. Any additional non-idealities were therefore considered unnecessary complications that may lead to 'over-fitting' of the data. As such, an anisotropic form of the KM was determined to be the best candidate to describe the IRSE lineshape and was used to model all ZnO films in this work. A schematic of the geometric model describing the sample architecture and the general oscillator models for each layer alongside the main fit parameters are shown in **Figure 4.14 (a)**. Shaded areas in light blue indicate parameters that were fitted associated with the KM model for the ZnO layer, whereas grey shaded regions indicate parameters that were fixed during the fitting. The main KM LPP parameters were coupled to ω_p, ω_{TO} and ω_{LO} through Equation 3.43.

$$\omega_{\mathrm{LPP}^{\pm}} = \sqrt{\frac{1}{2}\left[\omega_{\mathrm{p}}^2 + \omega_{\mathrm{LO}}^2 \pm \sqrt{(\omega_{\mathrm{p}}^2 + \omega_{\mathrm{LO}}^2)^2 - 4\omega_{\mathrm{p}}^2\omega_{\mathrm{TO}}^2}\right]} \tag{3.43}$$

Figure 4.14 (b) presents the experimental Ψ (blue-lines) and Δ (red-lines) and best-matched Kukharskii model calculated Ψ and Δ data (green-lines) taken at 70^{o} angle of incidence for the Mid-IR spectral range $(0.03 - 0.3$ eV) for an n-type (1 pulse at $150 mJcm^{-2}$ in N_2) and p-type (2 pulses at $200 mJcm^{-2}$ in N_2) laser processed sample (according to HE measurement results). The resultant calculated real, ε', and imaginary, ε'', permittivity for the ordinary (ε' =black line, ε'' = red line) and extraordinary ((ε' =blue line, ε'' = green line)) axis are shown in **Figure 4.14 (c)** for ε' and **(d)** for ε''. The dip in the ψ spectra at $\sim 0.12\ eV$ arises from the Al_2O_3 substrate layer. IRSE measurements of the Al_2O_3 on Si were performed prior to ZnO layer deposition, and the thickness and dielectric function of the Al_2O_3 layer was determined using a general oscillator model consisting of a single Gaussian oscillator which was fixed during the ZnO layer analysis. The peak $\sim 0.05\ eV$ originates from the ZnO TO phonon mode, and the dip structure $\sim 0.07\ eV$ manifests from the coupling between the LO phonon

mode and plasmon excitations in the ZnO thin film. This coupling effect has been observed in other semiconductors such as GaN[344], InN [340] and GaAs[315]. The observation of phonon-plasmon coupling in the ALD ZnO films suggests their potential as a plasphonic material for applications in the technologically important IR regime[345]. The implication of phonon-plasmon coupling on the dielectric function of ZnO is explored further in **Chapter 6** and is therefore not reported here.

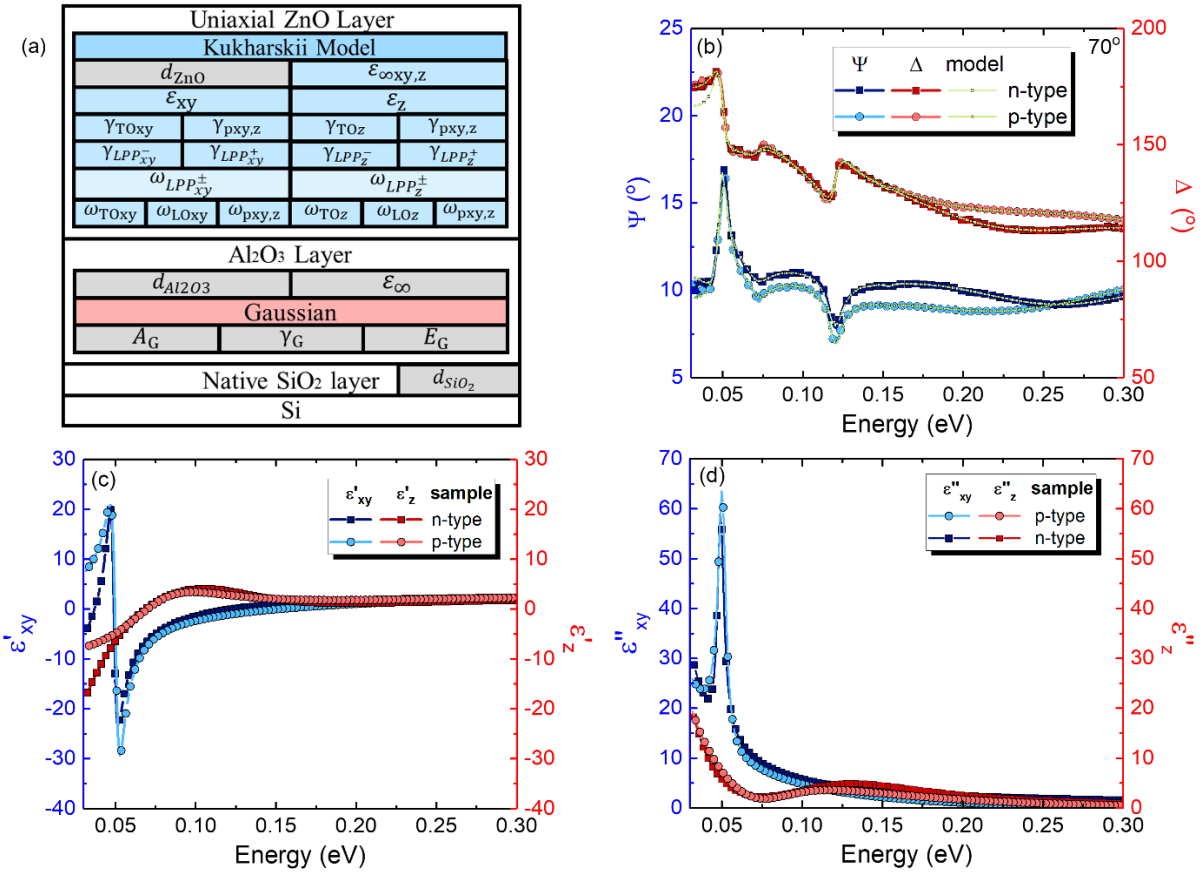

Figure 4.14 *IR Spectroscopic Ellipsometry results and analysis, where figure (a) shows the experimental Ψ (blue-lines) and Δ (red-lines) and best-matched Kukharskii model calculated Ψ and Δ data (green-lines) taken at 70^{o} angle of incidence for the Mid-IR spectral range $(0.03 - 0.3\ eV)$ for both an n-type (1 pulse, $150 mJcm^{-2}$) and p-type (2 pulses, $200 mJcm^{-2}$) (according to HE) laser processed samples, (b) details the geometric and oscillator model used for the analysis, (c) shows the real part of the permittivity for both the ordinary, xy, and extraordinary, z, axes and (d) shows the imaginary part of the permittivity for both the ordinary, xy, and extraordinary, z, axes.*

4.5.2 Phonon-Plasmon Broadening Behaviour Investigation

The above fitting procedure was followed for a series of CEELD films with $1 - 5$ pulses in a fluence range between $150 - 250\ mJcm^{-2}$ in 100 $psig$ high purity N_2 or NH_3 environment. The electrical properties of all films were determined *via* HE measurements and were explored in Section 4.2.1. and across several consecutive repeat HE measurements, a selection of different carrier type response for

the films were obtained: n-type, p-type and mixed carrier type and are highlighted, alongside the carrier concentration for each sample in ***Table 4.1***.

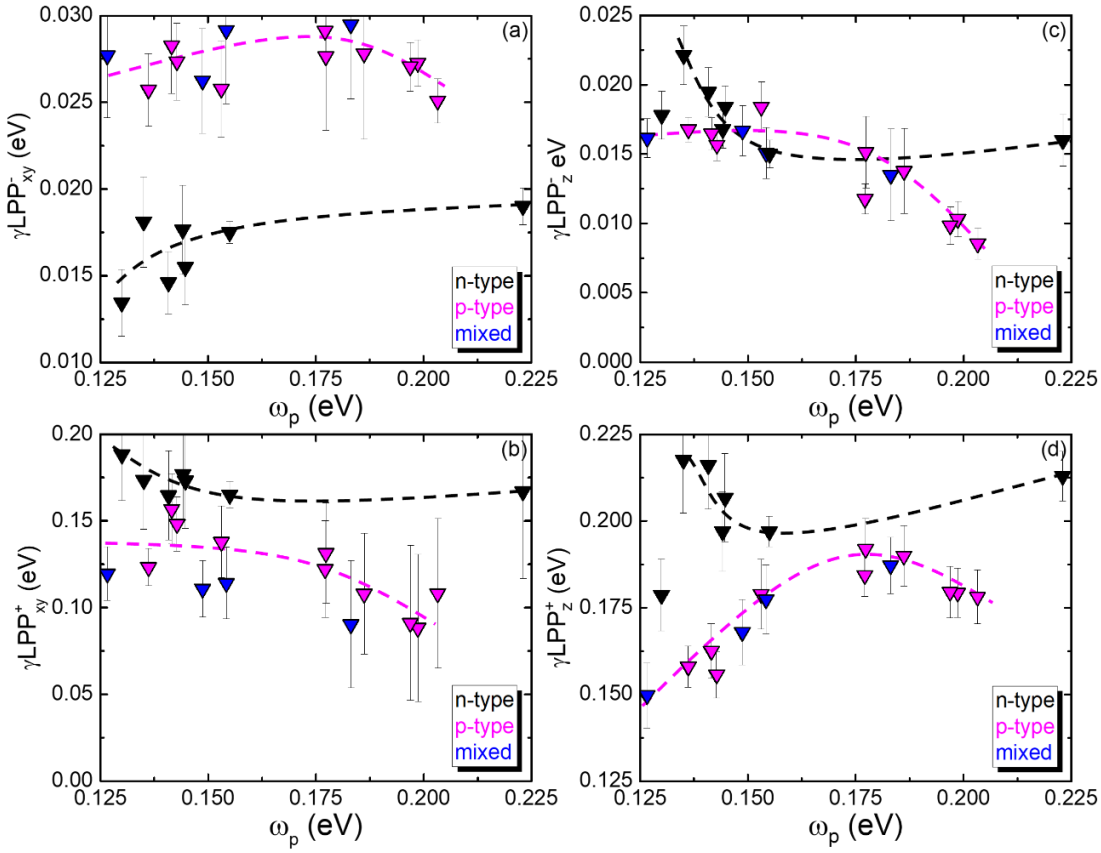

Figure 4.15 *Broadening behaviour values of the upper and lower LPP branches for both ordinary and extraordinary axes in terms of the sample plasma energy extracted from the Kukharskii model fit parameters: (a) LPP_{xy}^{-}, (b) LPP_{xy}^{+}, (a) LPP_{z}^{-}, (a) LPP_{z}^{+}. Variations in the symbol colour indicate samples of n-type (black), p-type (magenta) and mixed (blue) carrier type as determined by HE measurements. Dashed lines have been added to guide the eye.*

The KM fit parameters relating to the polariton broadening were extracted for each sample to observe any trends in broadening behaviour between the films of different carrier type, according to the theory outlined at the start of this section that different charge carriers may exhibit different broadening due to the difference in charge carrier mass and mobility.[340] ***Figure 4.15*** shows the broadening behaviour values of the upper and lower *LPP* branches for both ordinary and extraordinary axes in terms of the sample plasma energy. Variations in the symbol colour indicate samples of n-type (black), p-type (magenta) and mixed (blue) carrier type as determined by HE measurements. Dashed lines have been added to guide the eye. The broadening parameters for the lower branch *LPP* modes are lower in energy compared with the upper branches, which is expected due to the higher energy values of the upper *LPP* modes.[340] For the LPP_{xy}^{-} mode, a sudden change in broadening parameters is observed for the p-type and mixed carrier type films compared to the n-type materials, with a clear, observable increase in

broadening. As such, the n-type ZnO samples can clearly be distinguished from the p-type materials of similar plasma frequencies by the strong increase in LPP_{xy}^{-} broadening. Conversely, a decrease in broadening is observed between the n- and p-type/mixed materials for the LPP_{xy}^{+} mode. In the extraordinary plane, at lower ω_p range samples, broadening parameters of both n- and p-type materials are generally similar in magnitude, whereas a decrease in broadening is observed for the higher ω_p films, which is consistent with the expected phonon-like behaviour of the lower branch mode at higher ω_p. Minor differences in broadening behaviours between the carrier types can also be seen for the LPP_{z}^{+} mode. Overall, changes in broadening behaviour trends are observed for the p-type samples compared with the n-type materials, suggesting IRSE may be used as an indicative method to distinguish between n- and p-type ZnO materials. ***Figure 4.16*** displays the plasma broadening parameter values, γ_p, for the samples. Previously, γ_p has been overlooked due to its relation to the ω_p and therefore the effective mass.[340,341] However, this work shows a clear difference in γ_p behaviour between the n-type and p-type/mixed samples, with an increase in γ_p values for the p-type/mixed samples.

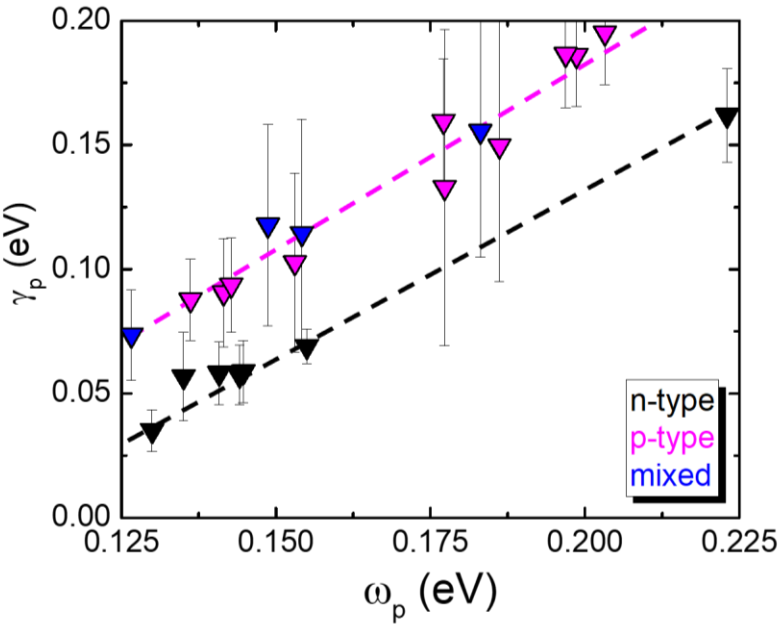

Figure 4.16 *Plasmon broadening behaviour in terms of the sample plasma energy extracted from the Kukharskii model fit parameters. Variations in the symbol colour indicate samples of n-type (black), p-type (magenta) and mixed (blue) carrier type as determined by HE measurements. Dashed lines have been added to guide the eye.*

This difference in broadening behaviour may be explained due to the presence of heavy holes with low mobility that increases the broadening parameters of the free carrier plasmons. It is therefore argued that γ_p is a key parameter that should not be overlooked, and its direct relation to the free carrier plasmons renders it a more suitable parameter to investigate and is more indicative of the changes in

carrier type than most of the coupled modes. From the results presented here, it is proposed that the $\gamma_{LPP_{xy}^{-}}$ and γ_p are the most promising broadening parameters to investigate and indicate the carrier type in the ALD ZnO thin films developed in this work. Obvious changes in the broadening behaviour is observed for these parameters between the different carrier types indicated by HE measurements. Moreover, clear changes in the broadening behaviours for samples of opposite carrier type but in the same ω_p range provide the most support for IRSE as a potential contactless method to indirectly indicate changes in the dominant carrier type of ZnO thin films. The results of this work therefore provide further evidence of the potential of IRSE as a complementary technique to conventional methods such as Hall Effect to detect changes in dominant carrier type of semiconductor thin films by examining both the coupled LPP and plasma broadening parameters extracted from the Kukharskii model.

4.6 Chapter Summary

Chapter 4 was devoted to reporting on the development of the seed n-type ALD ZnO materials and the investigations into the potential of controlled environment excimer laser annealing in a N containing environment to induce N acceptor-type in ZnO materials. ALD of ZnO thin films onto Al_2O_3 on Si substrates were performed for a range of deposition conditions including the deposition temperature, precursor purge time, and pressure of purge gas flowing through the system during the dynamic deposition process. Electrical characterisation of the as deposited materials revealed that the above deposition parameters can be precisely controlled to viably manipulate the electrical properties of the ZnO thin films. ZnO materials with high n-type carrier concentration were obtained with hydrogen identified as the most probable shallow n-type dopant arising for the $O-H$ and $C-H$ groups present during the growth process, where the hydrogen is more stable at lower growth temperatures. The chapter then explored the potential of controlled environment excimer laser annealing to achieve N-acceptor doping in ZnO. Results from Hall Effect measurements revealed that laser processing the seed n-type ZnO material in a high-pressure N_2 containing environment at $200\,mJcm^{-2}$ with 1 and 2 pulses yielded the most promising p-type results, with a high level of p-type carrier concentration achieved that remained stable over an extended period. The dependence of the CEELD process on the starting material and laser environment were also found to have an impact on the CEELD process. Verification of the N incorporation into the ZnO films *via* the CEELD process was achieved via ToF-SIMS measurements that revealed N incorporation mainly through CN^{-}, CNO^{-}, NO^{-}, and NO_2^{-} ions. ToF-SIMS results therefore seem to support the hypothesis that N is readily incorporated into the ZnO thin films through co-doping with H, which is present in the films at the $O-H$ and $C-H$ sites. Upon laser processing, the N is incorporated at the sample surface and diffuses throughout the film bonding to the H sites. Residual energy from the laser processing is then able to break the $N-H$ bond and the H diffuses out of the film to activate the N as a shallow acceptor. Further support to the $N-H$ co-doping

hypothesis is achieved *via* laser processing in an NH_3 environment, which induces a higher level of N-related ions in the film which is assigned to the replenishment of H into the film due to the presence of H in the annealing atmosphere. The ToF-SIMS results also suggest some N gradient throughout the films because of the surface limited CEELD process. Further verification of acceptor type doping was then sought through the development of simple energy band diagrams using the results of ORS, VB XPS and KPFM measurements. Results from ORS suggested an optical bandgap range between $3.27 - 3.41\ eV$ for the seed n-type and p-type materials, suggesting the potential of the ZnO materials for near-UV applications. A method was then presented for the construction of simple EBD, whereby shifts in the Fermi level were observed and used to infer information on the doping in the ZnO materials. Whilst the results showed a shift towards the valence band for the CEELD films which is indicative of acceptor-type doping, the Fermi level remains above the mid-gap point. An improved measurement procedure is proposed involving UPS for both VBM and work function and ORS for E_g to be measured across the same sample sets and should be considered for future work to improve the reliability of the EBD investigation. Finally, IRSE was presented as an indicative method to distinguish between different carrier type films in ZnO. The CEELD process is therefore presented as method to induce N-acceptor type doping in ALD ZnO. However, the scepticism surrounding the reliability of the Hall Effect measurement technique and concerns arising from the E_f EBD investigation imply the need for further confirmation of p-type conduction, which will be investigated in the next chapter through implementation of the seed n- and p-type materials into simple devices.

5. ZnO Based Devices

This chapter employs the seed n- and p-type ZnO materials developed in Chapter 4 into a variety of electronic devices for further verification of p-type material through basic device physics. The chapter starts by exploring the investigations into developing Ohmic contacts to both n- and p-type materials that are the prerequisite for the further device studies. The chapter then continues to go on to explore the electrical behaviour of fabricated p-n junctions of both laterally and vertical design, and an initial study into the photo-response of the p-n junctions is also presented. Finally, the results of ZnO based TFT investigations are shown, alongside initial attempts to increase the depth of N incorporation into the ZnO materials. Overall, further proof of p-type conductivity achieved *via* the CEELD technique is exposed through simple device physics, and a perspective of the CEELD technique as a one-step fabrication method to achieve both laterally and vertically printed p-n homojunction devices is revealed.

5.1. Metal Contacts Introduction

This section presents the research efforts into developing Ohmic contacts with low contact resistance to both the n- and p-type ZnO materials developed in this work. Good Ohmic metal contacts with low contact resistance in ZnO semiconductors are crucial for both accurate device and material characterization and device performance.[234] For this research, it is important to develop metallisation schemes and Ohmic contact materials for both n- and p-type ZnO for accurate material characterization and improved device performance. Thermally evaporated aluminium contacts and magnetron sputtered gold and platinum contacts were deposited through a $1\ mm$ circular shadow mask with $5\ mm$ spacings. Full details of the Ohmic contact fabrication method can be found in Chapter 3. Initially, the I-V characteristics of the as deposited metal contacts to the as grown and N_2 CEELD thin films were investigated. These initial investigations showed that all three metals could make good Ohmic contact to the n-type as grown material, but only non-linear contacts were formed to the p-type laser annealed material. The next phase of the investigation was to thermally anneal the metal contacts, which is a common fabrication step in many Ohmic contact metallisation schemes. Annealing at high temperature can either cause the deposited metal to alloy with a semiconductor or to help reduce the barrier height at the interface.[234] Initially thermal annealing was performed in atmosphere at $300 - 400\ ^oC$. Results showed non-preferential contact behaviour was achieved after annealing at such high temperatures in an oxidising environment. The next approach was to thermally anneal samples under vacuum in the ALD chamber at lower temperatures between $200 - 300\ ^oC$ for varying times between $0.5 - 10$ minutes. Previous reports in the literature indicate minimum contact resistance generally occurs for post deposition annealing temperatures of between $200 - 300\ ^oC$ on doped samples which must be treated to further increase the near surface carrier concentration.[234] It was found that $1\ minute$ of annealing at $200\ ^oC$ under vacuum yielded the most promising Ohmic contact results. Both the non-annealed contact investigation results and the optimised thermal annealing I-V characteristics of the

metal contacts developed are presented in the following section. The identified optimum Ohmic contact fabrication was then successfully applied to the various devices explored later in the chapter.

5.1.1. Non-Annealed Metal Contact Investigations

Figure 5.01 shows the I-V characteristics of the non-annealed Al, Au and Pt metal contacts on (a) n-type as grown and p-type laser doped films processed with (b) 1 and (c) 2 pulses at $200mJcm^{-2}$ in 100 $psig$ high purity N_2. The nomenclature adopted 'nn' and 'pp' is indicative of measurements taken across two contacts to the n-type material and two contacts to the p-type material respectively. As can be seen in Figure 3.0, the non-annealed metal contacts to the n-type film show linear I-V relationships and are therefore considered to be Ohmic.

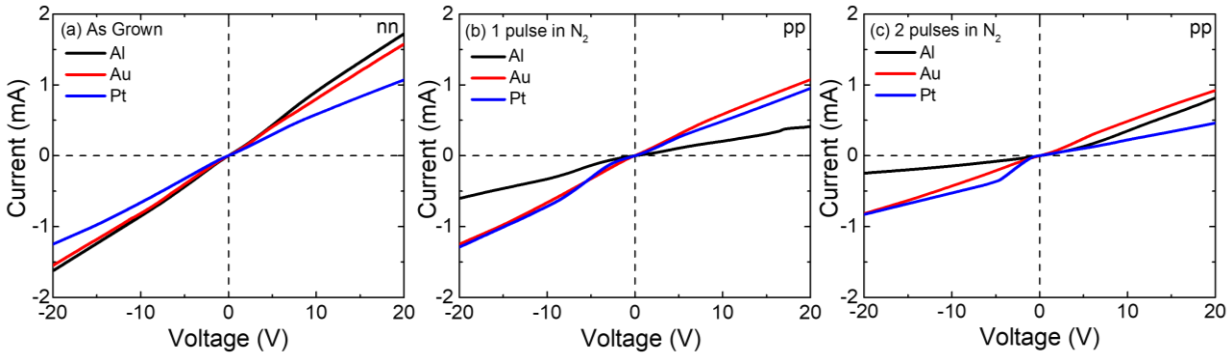

Figure 5.01 *The I-V characteristics of the non-annealed Al (black-line), Au (red-line) and Pt (blue-line) metal contacts on (a) n-type as grown and p-type laser annealed films processed with (b)* 1 *and (c)* 2 *pulses at* $200mJcm^{-2}$ *in* 100 $psig$ *high purity* N_2. *The nomenclature adopted 'nn' and 'pp' is indicative of measurements taken across two contacts to the n-type material and two contacts to the p-type material respectively.*

The Al contact presents the steepest gradient and thus has the lowest contact resistance. This is to be expected since Ohmic contact formation to n-type semiconductors requires $\Phi_m \leq \chi_{sc}$. The χ_{sc} of ZnO is around 4.35 eV whilst Φ_{Al} is around 4.20 eV and so obeys the relationship, conversely the work function of the other two metals investigated are much larger with $\Phi_{Au} \approx 5.1\ eV$ and $\Phi_{Pt} \approx 6.35\ eV$ and so should produce contacts with higher contact resistances as is shown by the decreasing gradients in the figure in accordance to the magnitude of the metals work function. Theoretically, metals with high work functions such as Au and Pt should form a junction with a high potential barrier such that a Schottky contact is formed to the n-type ZnO material.[230,231,233] However, more often, defects within the film and at the metal-semiconductor (M-S)interface may act as trap sites and offer an alternative route of conduction which allows for a tunnel current to flow across the M-S junction. For example, it has been reported that Au may form Ohmic contact to n-ZnO if the ZnO surface is Zn rich.[346] This trap

aided tunnel current alongside the high carrier density of the as deposited ZnO thin films may explain why Ohmic contacts are formed for all three metals.

The contact investigation results presented in Figure 5.0 (b) and (c) for the p-type laser annealed samples do not show such linear behaviour as obtained for the non-annealed metal contacts to the n-type material. However, the I-V characteristics do not exhibit rectifying behaviour and so the contacts formed may be considered near-Ohmic with a combination of thermionic emission and tunnelling contributing to the current flow across the junction. To achieve the desirable linear Ohmic contact behaviour, an enhancement in surface carrier concentration of the semiconductor and/or an improved interface between the metal and semiconductor is required. This may be achieved via a subsequent thermal annealing step and is often performed in Ohmic contact metallisation schemes.[238] The key results of the contact thermal annealing investigations are presented in the next section.

5.1.2. Annealed Metal Contact Investigations

Figure 5.02 shows the I-V characteristic results for the Al, Au and Pt metal contacts on both n- and p-type materials after a 1-minute vacuum thermal anneal at $200\,^{o}C$ in the ALD chamber. For the case of the n-type as grown film, the linear Ohmic behaviour was maintained for all three metals after the thermal annealing treatment, with an order of magnitude increase in current through the devices alongside a reduction in contact resistance. The improvement of Ohmic performance of the metal contacts after annealing could be due to improvements at the M-S interface after annealing and heat assisted alloying between the metal and semiconductor.

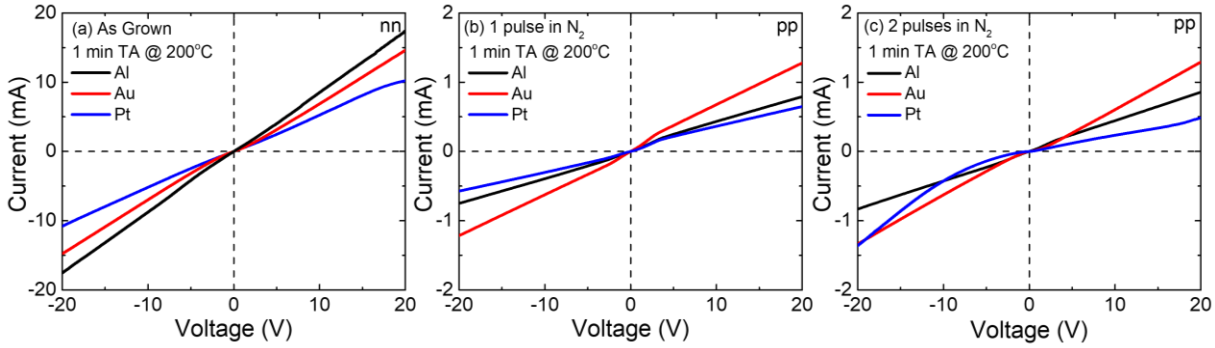

Figure 5.02 *shows the I-V characteristic results for the Al (black-line), Au (red-line) and Pt (blue-line) metal contacts to the (a) n-type as grown and the p-type laser annealed films processed with (b)* 1 *and (c)* 2 *pulses at* $200 mJcm^{-2}$ *in* $100\,psig$ *high purity* N_2 *after a 1-minute vacuum thermal anneal at* $200\,^{o}C$**.** *The nomenclature adopted 'nn' and 'pp' is indicative of measurements taken across two contacts to the n-type material and two contacts to the p-type material respectively.*

For the case of the Al contact, some Al may diffuse into the ZnO surface *via* thermal assistance. Aluminium is a well-known n-type dopant in ZnO and so such Al diffusion may form a thin layer of

highly conductive aluminium-doped ZnO (AZO) with increased carrier concentration compared to the non-annealed semiconductor surface.[143] This increase in surface carrier density would reduce the potential barrier width, increasing the probability of tunnelling events and thus decreasing the contact resistivity and in turn improve the Ohmic contact. This results in the Al remaining as the best metallisation scheme after thermal treatment to the as grown ZnO film, however Ohmic contacts with enhanced performance are still achieved for the thermally treated Au and Pt contacts. The improvement of the Au and Pt contact performance may be assigned to better alloying between the M-S and/or increase in the surface conductivity *via* formation of O defect complexes that may form O at the ZnO surface at elevated temperatures.[347,348] For the annealed metal contacts to the proposed p-type ZnO thin films shown in Figure 5.02 (b) 1 pulse and (c) 2 pulses, an improvement in linearity and Ohmic behaviour for all three metals can be observed. The Au contact shows the lowest contact resistance and largest allowed current through the device versus the other two metals. The improved Ohmic behaviour for the Au contact may be assigned to better alloying of the metal to the material after annealing leading to an increased adhesive force, and by interfacial reactions at the M-S interface resulting in a surface carrier concentration enhancement due to Au acceptor doping in the ZnO with subsequent associated potential barrier height reduction. An increase in surface conductivity has also been reported upon thermal annealing due to out-diffusion of Zn from the film surface upon to form acceptor-like Zn-vacancy complexes.[240] Ohmic contact was also found to be achieved with the annealed Al contact, which may be due to Al diffusion into the ZnO film to form Al-N complexes which act as co-dopants that may lead to an increase in surface carrier concentration and thus improved Ohmic performance.[349–352] For the annealed Pt contact, linear Ohmic behaviour is achieved for the 1 pulse sample, whilst near Ohmic I-V characteristics are obtained for the second pulse sample. This reduced Ohmic behaviour compared to the other metals may be due to the much higher work function of Pt and the lower hole carrier concentration of the $2-$pulse sample (according to Hall Effect measurements) which may increase the barrier height and reduce the tunnelling probability across the junction.

From the results of the contact investigation, it was concluded that Au metal contacts annealed in vacuum for $1-$minute at $200\,^{o}C$ was the best Ohmic contact metallisation scheme to the p-type material. Whilst Al achieved the lowest contact resistance to the n-type material. Despite Al forming the better Ohmic contact to n-ZnO, the annealed Au contact also achieved good Ohmic behaviour. Thus, it was concluded that the annealed Au metallisation scheme was suitable to be carried forward throughout the subsequent device fabrication and testing to both n- and p-type materials.

5.2. ZnO Homojunction Investigations Introduction

In this section, the electrical characterisation of the ZnO homojunctions developed in this work are reported using the Ohmic contacts established in the previous section. By implementing the n-type and proposed p-type materials developed in this research into simple p-n homojunction devices, we seek to

further support the claim of the development of p-type material by obtaining characteristic p-n junction diode I-V characteristic outputs. Initially, 'lateral' junctions are investigated, followed by a comparison between lateral and vertical junction devices fabricated by the novel one-step CEELD technique. Finally, a preliminary investigation into the photoconductivity of the devices is presented.

5.2.1. Lateral P-N Junction Investigations

Lateral p-n junctions were formed by taking $16 \times 8\ mm$ sections of an as deposited $80\ nm$ ALD ZnO (on $40\ nm$ Al_2O_3 on Si) sample and using the standard 1 and 2 pulse laser processing at $200 mJcm^{-2}$ in high purity N_2 approach to anneal and selectively dope half of the sample ($8 \times 8\ mm$ spot) p-type, thus producing a lateral p-n junction. Ohmic contacts were formed and verified using the previously established metallisation scheme, with a pair of $1\ mm$ circular Au contacts deposited on both the n-side and p-side of the junction to aid electrical characterisation. I-V electrical characterisation was then performed under dark and light conditions. Measurements were taken across the n-type and p-type contacts (nn and pp) to verify Ohmic contact, and across the junction (pn) to investigated electrical transport across the junction.

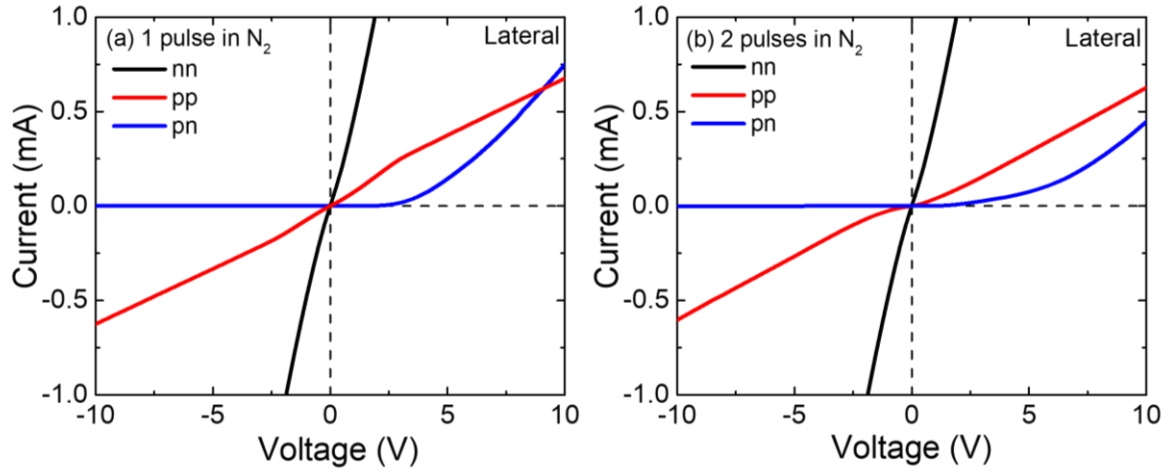

Figure 5.03 *displays the I-V characteristics across the metal contacts nn (black-line) and pp (red-line) and across the proposed pn junction (blue-line) for the two different samples half laser processed with (a)* 1 *pulse and (b)* 2 *pulses.*

Figure 5.03 displays the I-V characteristics across the metal contacts nn and pp and across the proposed pn junction for the two different samples half laser processed with (a) 1 pulse and (b) 2 pulses. In both Figure 5.03 (a) and (b), at low voltages, there is a clear difference in I-V character for the three different measurements. Linear and thus Ohmic behaviour is obtained for the contact measurements, with a clear difference in resistance between the n- and p-type materials shown by the different linear gradients. More crucially, there is an obvious difference between the contact measurements and measurement across the p-n junction at low voltages, signifying that the I-V behaviour of the pn

measurement is dominated by carrier transport at the junction and not arising from transport at the metal contacts. Moreover, the I-V characteristics across the junction display the typical rectification behaviour expected of a diode-like response, which further supports the claim that a p-n junction is formed between the laser processed and non-processed ZnO film.

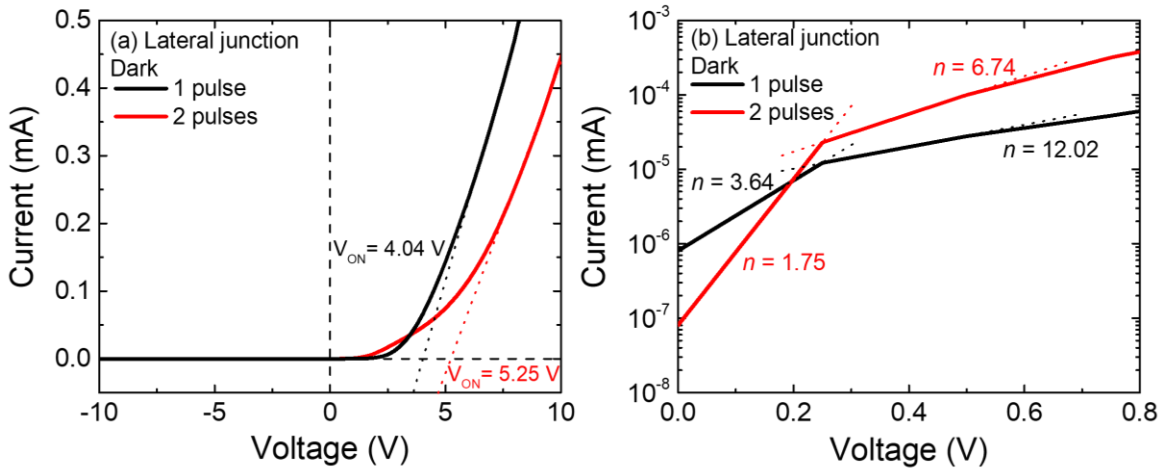

Figure 5.04 *Dark I-V characteristics of the lateral p-n junctions. Where (a) shows a comparison of the two lateral p-n junctions with p-regions produced by the standard CEELD in high pressure* N_2 *environment with* 1 *(black-line) and* 2 *pulses (red-line) at* $200 mJcm^{-2}$*, and (b) explores the ideality factor of the two diodes and shows the semi-log plot of I-V curves measured under dark conditions for the p-n junctions with p-material developed with* 1 *(black-line) and* 2 *(red-line) laser pulses in the low voltage range.*

Figure 5.04 (a) shows a comparison of the two lateral p-n junctions with p-regions produced by the standard CEELD approach in high pressure N_2 environment with 1 and 2 pulses at $200 mJcm^{-2}$. The figure shows the rectification behaviour of both junctions, indicating the diode-like behaviour. No breakdown current is observed by either Zener breakdown (through tunnelling mechanisms in heavily doped p-n junctions) or Avalanche breakdown (*via* carrier collision mechanisms) when the applied reverse bias is $-10\ V$.[245] By extrapolating the linear region of the I-V curves, the on voltage, V_{ON}, for the diode can be determined, which should scale with or be greater than the band gap energy of the semiconductor materials making up the junction, E_g.[113] This condition is upheld for both the 1 and 2 pulse p-material junctions, where $V_{ON,1\ pulse} = 4.04\ V$ and $V_{ON,2\ pulses} = 5.25\ V$ both of which satisfy the condition $V_{ON} > E_{g,ZnO \approx 3.34eV}$. There are reports in the literature that some proposed ZnO p-n homojunctions have $V_{ON} < E_{g,ZnO}$ which is atypical compared to other wide bandgap materials such as GaN and ZnSe.[353] However, such small values of V_{ON} may suggest the rectifying behaviour obtain in the I-V curves may not originate from a p-n junction, and therefore contribute to the scepticism in the literature surrounding the claims of p-type ZnO development.[40] For the p-n junctions developed in this

work, larger V_{ON} values are obtained compared to the band gap energy of ZnO, which is in line with other wide-gap materials. Shifts in V_{ON} beyond $E_{g,ZnO}$ may originate from any series resistance in the devices which would reduce the voltage across the diode leading to a necessary increase in the turn on voltage.[354] A shift in V_{ON} is also observed between the 1 and 2 pulse devices, which may be assigned to the difference in carrier concentration between the 1 and 2 pulse p-materials and larger contact resistances associated with the 2 pulse sample. The turn-on voltage is proportional to the concentration of dopants, where higher concentration will result in lower turn-on voltages. The difference in carrier concentration between the two p-materials is also evident by the difference in maximum current achieved in both devices, whereby higher currents are achieved for the device consisting of the more highly conductive 1 pulse p-region.

Figure 5.04 (b) explores the ideality factor of the two diodes and shows the semi-log plot of I-V curves measured under dark conditions for the p-n junctions with p-material developed with 1 and 2 laser pulses in the low voltage range. Short linear regions are observed in the semi-log plot at low voltages. By fitting the linear regions, the ideality factor, η, can be extracted from the gradient which is equal to $e/\eta k_B T$ according to the Shockley diode equation in Equation 2.10 repeated below.

$$I = I_0 \left[exp\left(\frac{qV}{nk_B T}\right) - 1 \right] \tag{2.10}$$

The ideal diode equation describes the I-V characteristics by thermionic emission of conduction electrons theory and is dependent on the dominating carrier recombination mechanism.[113] For an ideal diode, $\eta = 1$ when the I-V behaviour is dominated by an ideal minority carrier diffusion current, whereas $\eta = 2$ when recombination occurs in the space charge layer, forming a recombination current that is limited by both majority and minority carriers. High ideality factors ($\eta > 2$) indicate the diode is non-linear and that the I-V characteristics are not only limited by thermionic emission or recombination currents but by other dominant transport mechanisms as well. These diode non-linearities may be attributed to a combination of tunnelling currents in highly doped semiconducting materials more often through deep level defects, defects associated with interface inhomogenieties forming charge/complex traps causing barrier height nonuniformity at the interface, and/or the presence of electron-hole generation and recombination in the SCL.[355] Two different linear regions for both 1 and 2 pulse p-n junctions can be seen in the low voltage semi-log I-V plots in Figure 5.04 (b). The gradients of the linear regions (dashed lines) were fitted separately and the ideality factor for each region was determined, and the values are displayed in the figure. The first linear regime for the 2-pulse junction shows near-ideal behaviour with $\eta \approx 1.75$, which indicates both minority carrier diffusion and recombination currents are the key carrier transport mechanisms at such low voltages. Meanwhile, all other regions for both the 1 and 2 pulse samples show deviations from ideality with $\eta > 2$. Such high values of $\eta (> 2)$ are often reported for wide band gap materials such as GaN and ZnO and

suggests the diodes are non-linear. The larger values of η for the 1 pulse device may be assigned to an increase in tunnelling currents at the junction. According to HE results, the 1 pulse device contains more highly doped p- (and n-) regions than the 2 pulse device. This high density of carriers in the 1 pulse device increases the probability of tunnelling events occurring at the junction, therefore leading to an increased value of η. Other transport mechanisms resulting in the large η may arise due to the imperfections and non-smooth junction formed by the laser doping method, which would also contribute the non-linearity of the device.[356] As explored previously, some carrier concentration gradient may occur in the laser doped p-side of the junction due to a N-related defect gradient as observed in the ToF-SIMS results. A gradient in material properties and defects at the p-n junction interface may cause barrier height nonuniformity resulting in multiple transport mechanisms to occur across the junction. All of which cause deviation from the thermionic emission model of the ideal diode. The presence of any electron-hole pair (EHP) generation and recombination in the SCL will also increase the value of η.[357,358] Rates of EHP generation and recombination may be increased in ZnO due to persistent photoconductivity reported for ZnO materials.[125] Previous reports of ZnO homojunctions indicate a range of η values achieved between $2.28 - 25$ and therefore the junctions developed in this work have ideality factors that sit at the lower end of values reported in the literature.[184,185,357,359–363]

The lateral p-n junction I-V results demonstrate p-n junction diode-like behaviour and offer further support to the claim of developing p-type ZnO *via* the novel CEELD technique developed in this work and presents the laser doping as a potential one-step method for lateral p-n junction fabrication. From VBS and ToF-SIMS, there is some indication that the selective laser doping only produces a p-type layer between $20 - 40\ nm$ thick when processing an $80\ nm$ thick ZnO thin film. This indicates the potential of the laser doping technique to not only produce lateral p-n junctions but also vertical p-n junctions when processing as grown ZnO materials that are more than $40\ nm$ thick. Upon laser processing, the top $20 - 40\ nm$ will be converted to p-type, whilst the remaining thickness of material underneath retains n-type behaviour due to insufficient N diffusion to such depths into the film, therefore creating a vertical p-n junction. Similar demonstrations of laser induced doping for p-n junction formation have been reported for Si, SiC, diamond, CdTe, WSe_2 and GaAs, but at the time of writing has not yet been reported for ZnO.[204,212,222,226–229] The next section investigates the I-V characteristics of the proposed vertical p-n junctions.

5.2.2. Vertical P-N Junction Diode Investigations

Vertical p-n junction devices were fabricated using an $80\ nm$ ZnO thin film, whose surface (to a depth of around $20 - 40\ nm$) has been treated with the proprietary laser doping technique delivering 1 and 2 laser pulses at an energy density of $200 mJcm^{-2}$ in high pressure N_2 to form a thin p-type layer. The $80\ nm$ ZnO film is stacked on to the standard $40\ nm$ Al_2O_3 dielectric layer on Si substrate, whilst the

Ohmic contact metallisation scheme outlined above was used to form Au metal contacts to the top p-layer of the ZnO surface and to the underlying n-type material *via* an Au back contact deposited onto the back surface of the Si wafer. The device architecture is shown in **Figure 5.05**. As demonstrated in Figure 5.4, the CEELD approach is capable of inducing doping in highly selective and controlled areas, and as such may offer an industry viable solution to both lateral and laterally printed vertical ZnO based p-n homojunction devices for advanced device micropatterning.

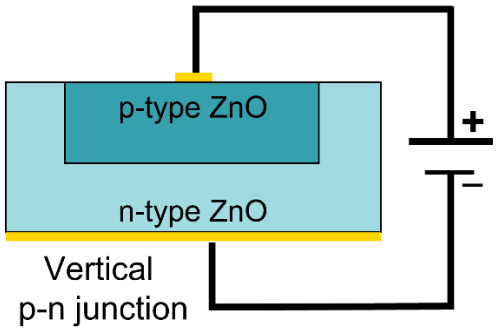

Figure 5.05 *Schematic of vertical p-n junction diode architecture fabricated by excimer laser doping.*

Figure 5.06 (a) shows the I-V characteristics of two vertical p-n junction devices with p-regions developed using 1 and 2 laser pulses. Typical rectification behaviour is observed suggesting diode-like behaviour, whilst no breakdown is observed up to a reverse bias of $-10\ V$. Much larger currents are achieved for both vertical devices compared to the lateral devices, and this is assigned to the larger surface area of the metal contacts, and thus increased area of the p-n junction involved in the characterisation of the vertical device. The device turn-on voltages are extracted from the linear fits as before and determined to be $V_{ON,1\ pulse} = 2.75\ V$ and $V_{ON,2\ pulses} = 2.94\ V$. The values of V_{ON} for the vertical devices are therefore more similar in magnitude and are more comparable to the ZnO band gap energy of 3.34 eV compared to the lateral devices. This reduction in V_{ON} for the vertical devices may be assigned to reduced series resistance, a different n-material involved in the junction compared to the pure as grown material or may be associated with the type of p-n junction formed for the vertical devices which may differ to that of the lateral devices. The reduced V_{ON} compared to $E_{g,ZnO}$ has been reported for other proposed ZnO p-n junctions (although those reported previously are more often much less than $E_{g,ZnO}$)[364–366] and is considered to achieve long operation times without serious Ohmic heating at the contact.[353] Deviation from the ideal diode is observed for 1 and 2 pulse junctions in the low voltage regime as shown in the semi-log I-V plot in **Figure 5.06 (b)**. However, a reduced range in η is obtained for the vertical devices between $3\ V < \eta < 6\ V$ versus $2\ V < \eta < 12\ V$ for the lateral devices. The reduction in η may further suggest differences in the junction formed between n- and p-type materials between the two types of directional diode or may be because of reduced tunnelling events due to a lower dopant concentration in the underlying n-material in the vertical device versus the as grown n-type material involved in the junction for the lateral devices. Changes to the n-type material involved

in the vertical junctions may be expected due to the effect of residual heating during the laser processing despite not being directly affected by the N doping and/or laser photons. Further information into the type of junctions formed in the lateral and vertical p-n junction devices may be obtained by performing capacitance-voltage measurements and should be considered for future work. The I-V results demonstrated for the vertical p-n junction devices suggest the laser doping technique is capable of fabricating both lateral and vertical rectifying diodes based on a ZnO p-n homojunction.

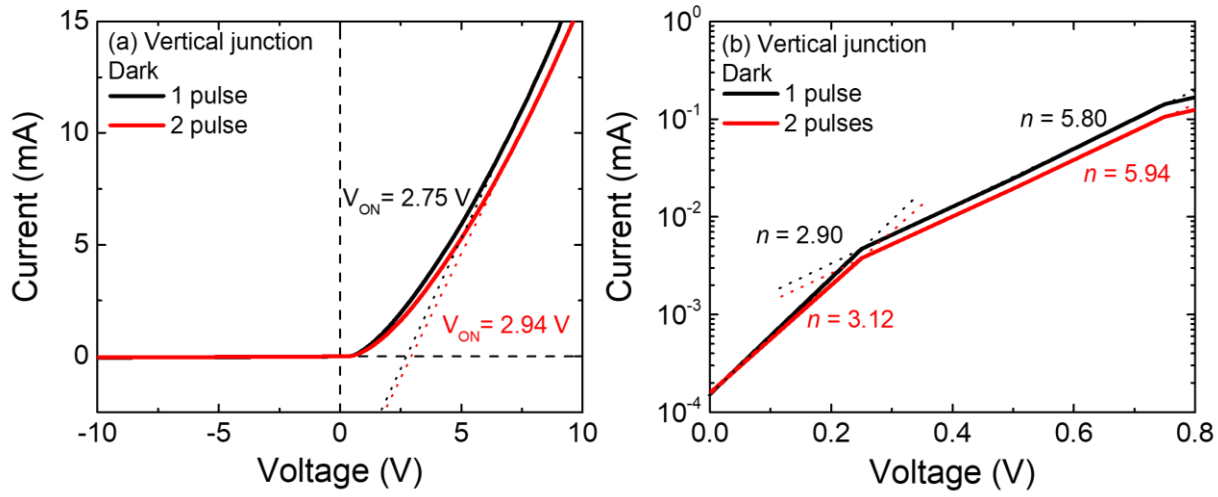

Figure 5.06 *Dark I-V characteristics of the vertical p-n junctions. Where (a) shows a comparison of the two vertical p-n junctions with p-regions produced by the standard CEELD in high pressure* N_2 *environment with* 1 *(black-line) and* 2 *pulses (red-line) at* $200 mJ cm^{-2}$*, and (b) explores the ideality factor of the two diodes and shows the semi-log plot of I-V curves measured under dark conditions for the p-n junctions with p-material developed with* 1 *(black-line) and* 2 *(red-line) laser pulses in the low voltage range.*

For both the lateral and vertical p-n junction devices, no obvious photoemission was observed from the p-n junction. Various factors may affect the potential of a p-n junction to produce electroluminescence including: defects at the p-n junction interface and surface which may form mid-bandgap trap sites causing interface and surface recombination events[367], deep-level defects within the band-gap of the semiconductor generated by imperfections in the crystal structure such as impurity atoms, dislocations, and interstitial or vacancy related defects which act to capture electrons and holes and function as Shockley-Read-Hall recombination centres[368–370], or by phonon-assisted recombination events *via* the Auger process[371], all of which cause non-favourable recombination events before the desirable radiative recombination can occur. Unoptimized device architectures, such as the simple devices produced in this work, also limit the efficiency of a device to emit light. Various optimisations to the device design may improve the internal and extraction efficiencies of an LED structure. The internal quantum efficiency (IQE) of an LED device may be improved by minimising defects and dislocations

within the materials, the use of a structured active layer by employing band gap engineered materials as quantum wells and barrier layers cladding the active region, or by harnessing plasmonic effects to increase the density of states and improve the rate of spontaneous emission according to the Purcell effect.[16,34,39,372–376] Such device heterostructures allow for efficient carrier and optical confinement to high quality material regions, shifts in the electroluminescent response and enhancements of the emission intensity. Meanwhile enhancements to the light extraction efficiency (LEE) can be achieved through a variety of methods, with one of the simplest and most effective ways being surface roughening or structuring. Difficulties in light extraction arise from the large difference in refractive index between the device and the surrounding medium (air). The surface of wafers typically employed in devices are smooth and so only a fraction of light can be extracted from the surface into the light cone, the remaining light is totally internally reflected (TIR) and the energy is lost through thermal dissipation. One way to avoid the effect of TIR is to roughen the wafer surfaces. This increased surface roughness increases the effective surface area, which allows for more scattering events for the efficient outcoupling of light, greatly improving the extraction of generated light out of the device. Other mechanisms to reduce the TIR in devices have also been reported alongside structured metallic surface layers to increase the outcoupling of light *via* plasmonic effects [12,377–380] Therefore, future work for the development of UV LEDs based on the ZnO homojunctions developed in this work should focus on trying to implement methods to improve the IQE and LEE of the diodes.

5.2.3. Photodiode Investigations

Initial I-V characterisation investigations suggested the lateral p-n junctions fabricated in this work exhibit photoconductive properties when the junction is measured as a diode under white light illumination. The fast photoconductivity in ZnO materials has often been reported and has been assigned to a variety of mechanisms including interband, exciton and phonon-assisted photoelectron generation.[381] Photocurrents may also arise in certain p-n junction devices – the photodiode – operated under reverse bias, when the junction is illuminated by an optical signal. The I-V behaviour of a photodiode under illumination yields an increase in negative current under reverse bias, caused by the photocurrent generation across the SCL of the p-n junction.[113] Several ZnO based photodiodes have been reported in the literature.[187,192,382–386] I-V characterisation of both the lateral and vertical p-n junctions were therefore performed under dark and light conditions to investigate the observed photodiode response and provide further evidence of the presence of a p-n junction. **Figure 5.07** shows the semi-log I-V characteristics for the (a) lateral 1 pulse p-region (b) lateral 2 pulse p-region (c) vertical 1 pulse p-region and (d) vertical 2 pulse p-region p-n junction devices under dark (black line) and light (red line) conditions. White light illumination was provided by the built-in bulb of the microscope on the Semiprobe SMU probing station.

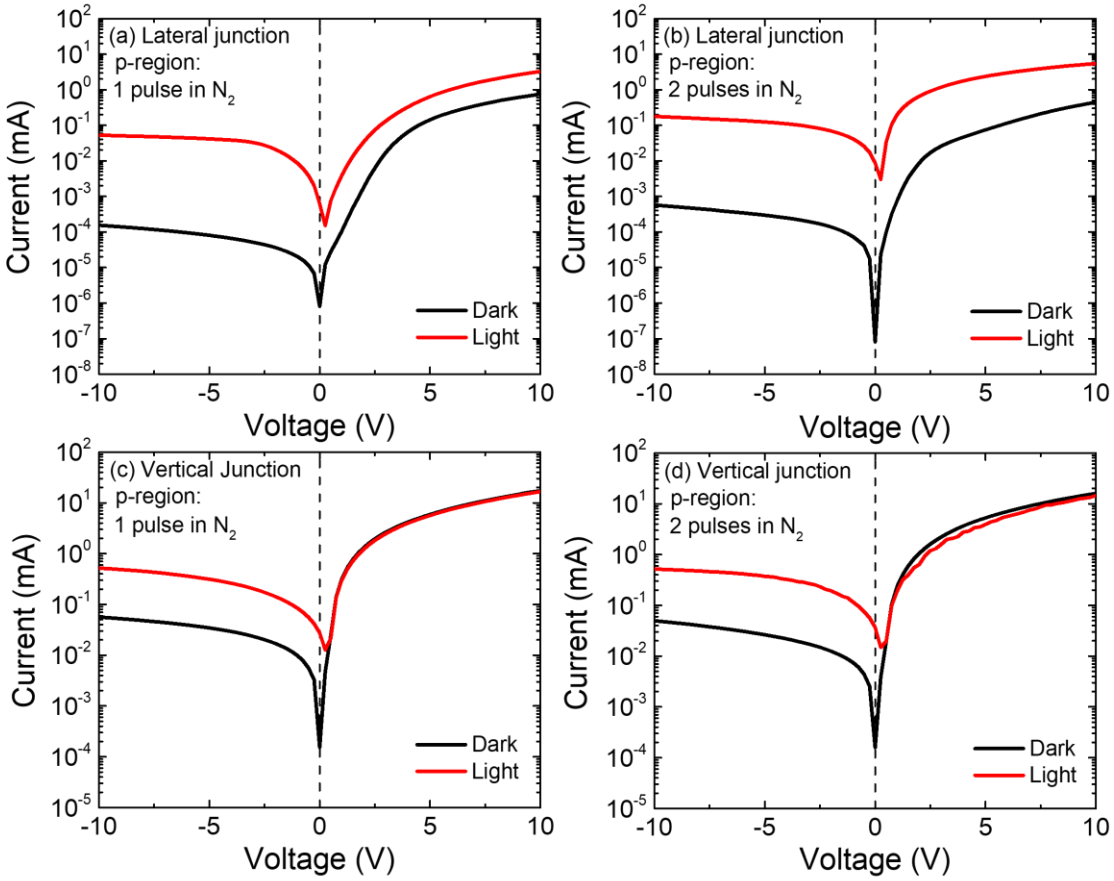

Figure 5.07 *shows the semi-log I-V characteristics for the (a) lateral 1 pulse p-region (b) lateral 2 pulse p-region (c) vertical 1 pulse p-region and (d) vertical 2 pulse p-region p-n junction devices under dark (black line) and light (red line) conditions.*

The photocurrent, I_{Ph}, and diode sensitivity, S, are calculated using values of dark and light current (I_{dark} and I_{light}) at $-10\ V$ (reverse bias) for each sample according to:

$$I_{Ph} = I_{light} - I_{dark} \tag{5.1}$$

$$S = \frac{I_{light} - I_{dark}}{I_{dark}} \tag{5.2}$$

Whilst the rectification ratio is determined by taking the ratio of the maximum current achieved between forward and reverse bias at $10\ V$ for dark and light measurements separately. The electrical parameters for the fabricated photodiodes are shown in **Table 5.1**.

Table 5.1 *Electrical Parameters of the p-n junction diodes*

Sample (p-region)	p-n junction	$V_{ON_{dark}}$ (V)	Rectification Ratio	η_{dark} (range)	Sensitivity, S	I_{Ph} (mA)
1 pulse in N_2	Lateral	4.04	4830	$3.64 - 6.74$	339	340
2 pulses in N_2	Lateral	5.25	776	$1.75 - 12.02$	311	312
1 pulse in N_2	Vertical	2.75	322	$2.90 - 5.80$	9.46	10.5
2 pulses in N_2	Vertical	2.94	307	$3.12 - 5.94$	8.21	9.21

Under reverse bias at $10\,V$, the reverse current for the lateral 1 and 2 pulse p-n junction devices increases from dark current values of $1\,pulse = 1.56 \times 10^{-4}\,mA$ and $2\,pulse = 5.73 \times 10^{-4}\,mA$ to $1\,pulse = 5.26 \times 10^{-2}\,mA$ and $2\,pulse = 1.79 \times 10^{-1}\,mA$ upon illumination, whilst the reverse current for the vertical devices at $10\,V$ increases from $1\,pulse = 4.96 \times 10^{-2}\,mA$ and $2\,pulse = 5.63 \times 10^{-2}\,mA$ to $5.19 \times 10^{-1}\,mA$ for both the 1 and 2 pulse lateral devices upon light exposure. This increase in reverse bias current after illumination accompanied with the upward shift in current at $0\,V$ is due to the generation of excess charge carriers due to the incident photons across the p-n junction and is the characteristic reverse bias behaviour expected of a photodiode. Moreover, a three-fold increase in photocurrent generation is observed for the lateral devices compared to the vertical diodes, which is once again assigned to the direct p-n junction illumination that occurs for the lateral device.

The photocurrent generation in reverse bias after an optical signal is delivered to the device, alongside the enhanced magnitude of photocurrent generated in the lateral device upon direct p-n junction illumination compared to the vertical device, further supports the claim of achieving p-type ZnO material and the formation of the elusive ZnO p-n homojunction. These preliminary photodiode tests indicate the potential of the p-n junction devices in photodiode applications such as light detectors. The generation of p-n homojunction based photodiodes is highly desirable to overcome the challenges associated with large barrier heights associated with Schottky junction and band discontinuity in heterojunction-based photodiodes.[192] Future work should focus on investigating the wavelength specificity of the photocurrent generation by performing spectrally resolved measurements, alongside investigations into the photovoltaic power generation and efficiencies of the photodiode devices produced in this work to fully assess their potential for photodiode applications. Further verification that the origin of the photocurrent is due to the p-n junction may be achieved *via* scanning photocurrent microscopy to obtain a spatial map of the photo-response of the device.[387]

5.3. ZnO Based Thin Film Transistors

This section presents the work undertaken to investigate the fabrication of ZnO thin film transistors (TFTs) based on the materials developed in this work fabricate *via* ALD and followed by performing

CEELD in a high pressure N_2 environment. The electrical performance of oxide based TFTs is affected by a wide range of fabrication parameters based on the materials used and geometry of the sample, including the semiconducting active layer intrinsic characteristics, the electrodes used, gate dielectric and the TFT geometry. In particular, the dominating carrier type in the semiconducting active layer has a clear effect on the TFT transfer characteristics, whereby the polarity of the voltage when the device is switched on is dependent on the dominating free charge carrier in the layer i.e., the device is switched on in positive gate voltages for electrons in an n-type material, whereas for a hole dominated p-type material the device is switched on with negative gate voltages.[47,248,251,252,388] As such, the overall target in this research is to examine the polarity of the ON voltages of TFT transfer curves to further verify the majority carrier type of the ZnO layers developed in this work and further support the claim of achieving p-type ZnO.

The first phase of the investigation was to examine TFT transfers of the $80\ nm$ as grown ZnO active layer TFT devices versus TFTs employing the standard 'p-type' ZnO developed by CEELD processing conditions with 1 and 2 pulses at $200 mJcm^{-2}$ in a $100\ psig$ high purity N_2 environment as the active layers. The next phase of investigations focussed on the early research efforts into trying to drive deeper the nitrogen doping into the ZnO thin films to increase the p-layer thickness and see how these films act as an active layer in TFTs. A method was tested to increase the nitrogen diffusion depth in the $80\ nm$ ZnO thin films namely, a post CEELD thermal annealing step with the intention of increasing N diffusion throughout the entire thickness of the thin film. The final stage of TFT investigations investigated thinner as grown and laser annealed ZnO active layers of $20\ nm$ with the hopes of full conversion of the entire $20\ nm$ film to a p-type active layer.

5.3.1. TFT Device Fabrication and CEELD Treatment Investigation

Bottom-gate-staggered TFT devices with ALD ZnO active layers were fabricated. Whilst bottom-gate designs are typically associated with TFT stability issues due to exposure of the active layer to air, this structure was adopted to mitigate uncertainties in the laser annealed ZnO film properties under investigation by maintaining the sample architecture used throughout the entire work so far. The CEELD technique is highly sensitive to the sample architecture and so any changes to the standard laser annealing method performed so far in this work would significantly alter the resultant thin film material properties. Moreover, the main aim of the TFT investigations was not to produce TFTs fit for industrial purposes, but to utilise TFT device physics to infer further, undisputable information about the majority cartier type in the ZnO films developed in this work. The structure of the TFT devices developed in this work is shown for the CEELD case in **Figure 5.08**, whilst the TFT fabrication process is outlined below:

1. $40\ nm$ Al_2O_3 gate dielectric deposited onto Si substrates *via* ALD
2. A 20 or $80\ nm$ ZnO active layer is deposited by ALD onto Al_2O_3 gate dielectric

3. The substrates were then diced into $8 \times 8\ mm$ square pieces *via* a laser dicing method
4. The ZnO active layers were then laser processed in a $100\ psig$ N_2 environment with varying number of laser pulses $(1 - 2)$ and laser energy density $(50 - 200 mJcm^{-2})$. The laser optics were adjusted to achieve an $8 \times 8\ mm$ square laser spot to treat the entire surface of the ZnO samples. (Note different samples were used for each device)
5. Gold back gate and top source and drain electrodes were deposited by sputter deposition, using a T-bar shadow mask for the source and drain electrodes. The contacts were then annealed in vacuum for 1 minute at $200\ ^oC$ according to the Ohmic contact investigations described previously.
6. Finally, the I-V characteristics of the TFT devices were measured using the Kiethley 4200-SCS Parameter Analyser

All device fabrication and measurements were undertaken at Nottingham Trent University.

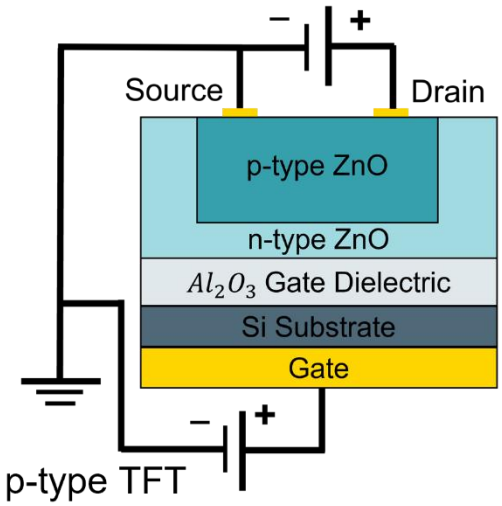

Figure 5.08 *Architecture of the CEELD case ZnO TFT devices fabricated in this research.*

5.3.2. ZnO TFT Results & Discussion

In the previous chapter it was demonstrated that the most promising laser processing conditions to achieve p-type doping in the ALD ZnO in this work were those processed with 1 and 2 pulses at $200 mJcm^{-2}$ in a $100\ psig$ high purity N_2 environment. However, Hall Effect results have been met with some scepticism in the literature since there are a variety of sample features that may induce uncertainties in the measurements and the misinterpretation of results. It is therefore of significant importance to find alternative means of determining the carrier type in thin films. As described previously, by investigating the transfer electrical characteristics of TFTs, information on majority charge carrier type in the semiconducting active layer may be obtained. This approach is adopted to

further investigate the n-type as grown and N_2 doped laser processed thin films. In this section, to mitigate complexities associated with fabrication and laser processing, standard 80 nm ZnO active layers with various deposition and post processing conditions were adopted as the active layers in the TFTs under investigation, following the process flow outlined in the previous section.

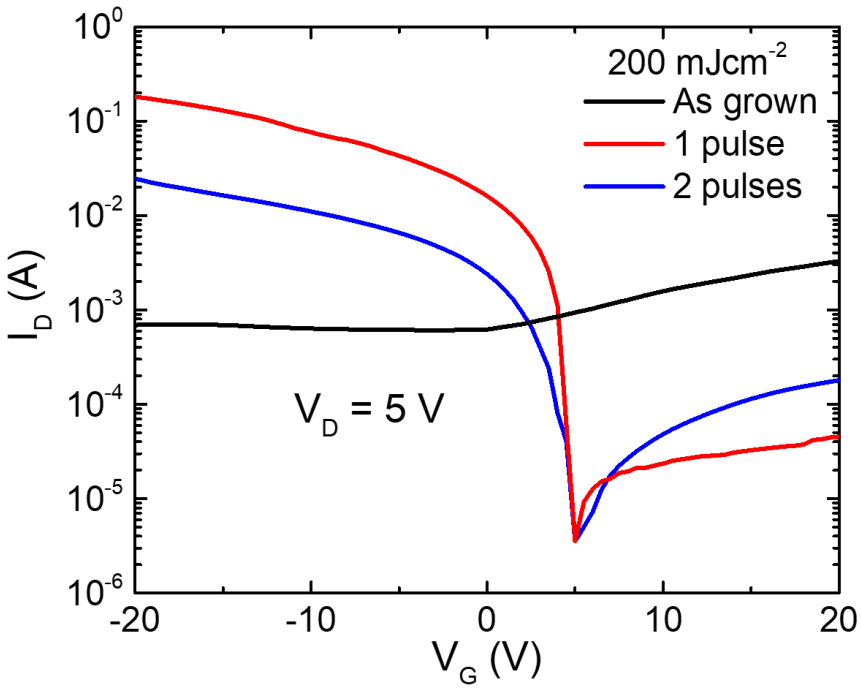

Figure 5.09 *Comparison of the transfer characteristic curves at V_D = 5 V for the 80 nm as grown (black line) and the samples processed with the standard CEELD in high pressure N_2 environment with* 1 *(red-line) and* 2 *pulses (blue-line) at* $200 mJcm^{-2}$

Figure 5.09 compares the transfer characteristic curves at a drain voltage, V_D, of 5 V for the 80 nm as grown and the two standard laser processed samples. The TFT with the as grown ZnO active layer (black line) does not exhibit the typical switching expected of the TFT, i.e., it is always in the ON state independent of the gate voltage bias. The lack of conductivity modulation of the as grown active layer according to the gate voltage field effect is because of the high carrier density associated with the as grown film as explored previously due to the high level of impurity level hydrogen content within the as grown ZnO thin films. High carrier concentration results in poor channel conductivity modulation *via* the gate voltage, where the free carriers cannot be fully depleted from the channel layer – gate dielectric interface, regardless of applied voltage (i.e., a conductive channel layer connects or shorts the source and drain electrodes).[94,248,249,251] Another parameter known to affect the switching behaviour of TFT devices is a semiconducting active layer thickness. For the case of high thickness active layers, there may remain an area of semiconductor with high carrier concentration that cannot be depleted without using a large negative (for the case of n-type active layers) gate voltage that would cause dielectric breakdown and destroy the device.[251,389] Those devices with high thickness active layers are

unable to be fully switched off. For the case of the 80 nm as grown ZnO film, high carrier concentration and high film thickness contribute to the minimal switching behaviour observed. Nevertheless, minor switching is observed with an order of magnitude increase in drain current for positive gate voltages. An increase in I_D along with positive V_G is indicative of an n-type or electron dominant active layer. Conversely, for the case of the laser processed samples, opposite switching behaviour is observed, whereby the ON-state is achieved with negative V_G bias, which is characteristic of a hole dominant active layer, i.e., a p-channel TFT is formed. The reverse in polarity of the ON V_G for the laser processed thin films indicates a switch in dominant carrier type from electrons in the as grown films to holes in the laser processed samples. This profound result supports the claim of achieving p-type doping in the CEELD ALD ZnO thin films produced in this work *via* laser induced N doping.

Moreover, a significant improvement in TFT performance is obtained for the laser processed TFTs. When treated with 1 pulse under standard laser processing conditions, the ON-state I_D is increased by almost two orders of magnitude, alongside a reduction in the off-state current. This preferential increase in ON/OFF ratio for the 1 pulse device could be assigned to several reasons including those outlined below:

1. The slightly reduced conductivity of the 1 pulse sample compared to the as grown meaning it can be better modulated by the gate voltage, resulting in the improved switching.

2. Reduced number of defects after laser processing improving the semiconductor/insulator interface.

3. The potential p-n bilayer proposed to be induced by the laser annealing process. It has been reported that dual active layers with differing conductivities may help to drastically improve the TFT behaviour and produce high performance TFTs, whereby defects in the channel and at the interface can be effectively passivated by the high electron concentration in the n-layer and as such a higher current can be achieved due to a decrease in offset resistance due to defect passivation. Reports also discuss the possibility of a thin layer of alternate carrier type than the bulk material between the gate and active layer may promote hole injection due to band bending through the tunnelling effect, in turn increasing the ON-state current. Thus, the thickness of the bilayer and relative conductivities may play a key role in the TFT transfer characteristics and should be investigated further in future work.[389–395] Other reports have also documented how charge carrier traps filled by immobile electrons may improve the ON-current in a similar manor.[396] From the VBS measurements analysed previously, the large bump in energy around the Fermi energy was assigned to screened trapped electron states within the band gap, possibly originating from the n-type underlayer in the laser annealed samples.

The larger ON-current for the 1 pulse sample compared to the 2-pulse sample may predominantly be due to a combination of the larger carrier concentration in the 1 pulse film according to HE measurements and the presence of a bilayer that is more obvious for the 1 pulse film versus the 2-pulse film according to ToF-SIMS and VBS results. Any additional series resistance in the 2-pulse device may cause a lowering of the generated I_D for the same applied gate voltage due to a voltage drop across any additional resistance across the semiconductor channel. The slow transfer between ON/OFF ratio for the 2 pulse sample further indicates the presence of an increased resistance between gate-bias back contact and the source and drain electrodes.[93]

The off-state current in TFT devices is typically associated with the active layer conductivity and the semiconductor-dielectric interface.[248] Novel negative off-state current phenomenon is observed for the laser annealed samples, which has recently been reported by Huo *et al*.[397] The I_D polarity switching is clearly indicated by the minimum in the absolute I_D at $V_G \approx 5\ V$, with increasing negative I_D for $V_G > 5\ V$, and increasing positive I_D for $V_G < 5\ V$. This negative current has been assigned to capacitor discharging during the gate voltage sweeping which leads to negative current generation. Huo *et al* developed a dynamic model (Eq. 5.3)[397] to explore the mechanism behind the novel negative OFF current that considers non-idealities associated with the source and drain series contact resistances, R_S and R_D, and for gate insulator leakage due to gate-drain and gate-source resistances, R_{GD} and R_{GS}:

$$i_D(t) = \frac{(V_D - v_G(0) - At)}{R_{GD}} - AC_{GD} \times \left(1 - exp\left(\frac{1}{R_D C_{GD}} t\right)\right) \tag{5.3}$$

Where $i_D(t)$ is the dynamic drain current at time, t, V_D is the drain voltage, $v_G(0)$ is the starting sweep gate voltage, C_{GD} is the capacitance between source and drain and A is the sweep rate. The model suggests that dynamic drain current is more likely to turn negative with larger R_{GD}, C_{GD}, and A values, and with smaller R_D, V_D and $v_G(0)$ values. Larger R_{GD} and C_{GD} would indicate better insulation and fewer dielectric-channel interface defects, while smaller R_D indicates better contact between the drain and channel, therefore better TFT parameters are more likely to cause the negative OFF-state I_D associated with the capacitor discharging phenomenon. The link between negative OFF state I_D and preferential device characteristics further suggests that superior TFTs are obtained for the laser annealed devices.[397] However, this negative current adds complexity to the determination of the ON/OFF ratio of the devices, and so is defined in this work as the ratio in absolute values of I_D at $V_G = +10\ V$ and $V_G = -10\ V$. In Figure 3.7, a one order and two orders of magnitude decrease in total off-state current can be seen between the as grown and the 2 pulse and 1 pulse laser annealed samples respectively. The increase in ON/OFF ratio for the laser annealed samples is most probably due to the reduction in conductivity from n-channel to p-channel TFTs, resulting in easier depletion of carriers in the active layer for the annealed samples. Another potential explanation could be due to a reduction in active layer thickness. Depending on where the channel is being formed in the dual p- and n-layer structure, it is

possible that it is confined to the thinner p-layer and so the issue regarding a potential nondepleted region of high carrier concentration in thick active layer TFT devices may be avoided.[389,395]

The clear change in the ON-state V_G polarity between the as grown and laser annealed TFT devices provides undisputable support to the claim of achieving p-type doping in ZnO *via* the laser doping technique developed in this work. However, questions remain as to the depth of the acceptor doping within the 80 nm thin films. Whilst the laser assisted one-step p-n homojunction fabrication method is attractive; it is also desirable to be able to control the thickness of the n- and p-layers for both device applications and to ease material characterisation.

5.3.3. Thermally Annealed **80 *nm*** TFTs

Preliminary efforts were made to try to increase the p-layer thickness N *via* a post laser doping thermal anneal at relatively low temperatures to simultaneously try to promote N diffusion within the film and removal of excess H that may act to passivate the N complexes as acceptor type dopants.

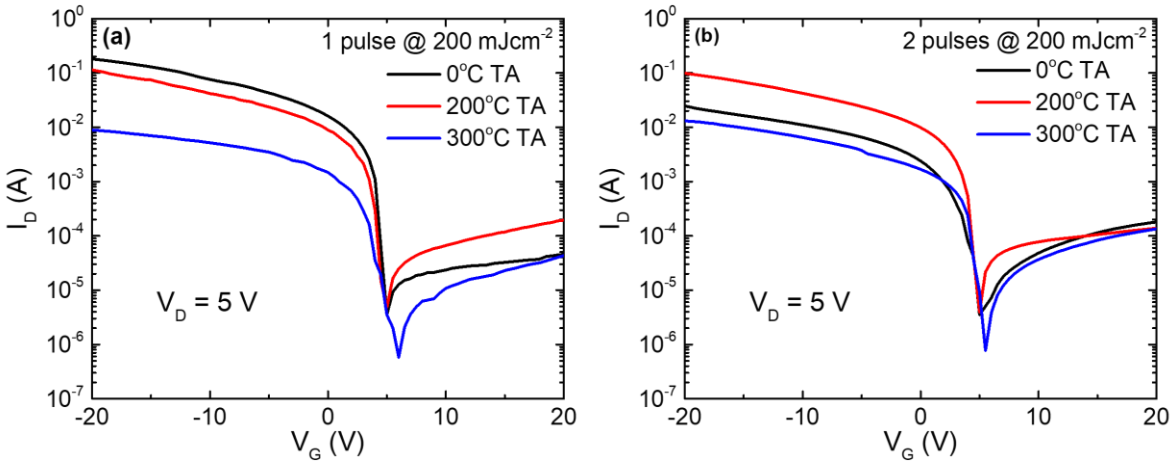

Figure 5.10 *The transfer results presented at* $V_D = 5\ V$*, for the as laser processed nonthermally treated,* $0\ ^oC$ *sample, and the results for the thermally annealed samples at* $200\ ^oC$ *and* $300\ ^oC$ *for both the (a)* 1 *pulse and (b)* 2 *pulse laser processed samples.*

We first consider the post CEELD thermal annealing treatment on the samples processed with 1 and 2 pulses at $200 mJcm^{-2}$ in a 100 $psig$ high purity N_2 environment. The samples were treated with a mild thermal anneal (TA) for 1 hour at $200\ ^oC$ and $300\ ^oC$ under vacuum after laser processing. **Figure 5.10** (a) and (b) show the transfer results presented at $V_D = 5\ V$, for the as laser processed nonthermally treated, $0\ ^oC$ sample, and the results for the thermally annealed samples for both the 1 and 2 pulse laser processed samples. For the 1 pulse sample thermally treated at $200\ ^oC$, ON-state is once again achieved with negative V_G, and thus the p-type character is maintained after TA. The magnitude of the ON current decreases slightly after the annealing treatment at $200\ ^oC$, suggesting the potential

reduction in carrier density due to the thermal diffusion of dopants throughout the film and an alteration to the dual active layer proposed previously. From the ToF-SIMS investigations, it was concluded that the level of N doping throughout the film was surface saturation limited. Upon the $200\ ^oC$ anneal, no additional H or N was introduced into the system, and so the total p-type carrier concentration achieved in the thermally annealed device is limited to the total N available at the surface and so a reduced overall p-type carrier density is achieved for the thermally annealed active layer due to N diffusion throughout the film. An increase in absolute magnitude of the off-current is also observed, i.e., a more negative current occurs. The increase in negative current compared to the as processed TFT may indicate an increase in R_{GD} and C_{GD},[397] possibly due to a reduction of defects at the channel interface due to the thermal treatment, which may improve the density of defects *via* atomic rearrangement[398] or due to a complete conversion of the entire 80 nm active layer such that the channel forms at the semiconductor dielectric interface rather than at the p-n interface. After TA treatment at $300\ ^oC$, an order of magnitude decrease in ON current is observed for the 1 pulse sample, accompanied by a positive shift in the ON voltage, V_{ON}, and a slowing of the transfer between the ON and OFF states of the device. The further decrease in the ON current indicates a reduction in carrier density possibly due to further out diffusion of H and N from the thin film at the elevated temperature. A further reduction in carrier concentration may significantly increase the contact resistance of the source and drain electrodes which may explain the slow transfer for this device[93], and the positive shift in V_{ON} may be assigned to carrier crowding due to the higher contact resistance.[94,180,252,399] The instability in the measurement of the TFTs annealed at $300\ ^oC$ may originate from the formation of defects and traps at the surface after the higher temperature anneal which may also hinder the contact made at the source and drain electrodes. Moreover, the noisy measurement may further suggest current crowding at the metal contacts.[400] For the sample processed with 2 pulses, upon thermal annealing at $200\ ^oC$, almost an order of magnitude increase in ON-state current is achieved, which contrasts with the behaviour of the 1 pulse sample. From the ToF-SIMS results in Section 4.3, it was shown that the N ion concentration had a reduced gradient throughout the depth of the ZnO thin film compared to the 1 pulse sample. The 1 hour annealing at $200\ ^oC$ may therefore contribute to crystal structure improvements as opposed to the diffusion of N and may suggest that improved carrier mobility is the cause of the increase in ON current for the 2 pulse sample. A decrease in ON current and slight increase in V_{ON} is observed for the sample annealed at $300\ ^oC$ once again due to a decrease in carrier concentration from out-diffusion of nitrogen and N species from the film. This effect was more pronounced for the 1 pulse film due to the higher concentration of N species at the surface which are more readily removed from the material upon high temperature thermal annealing.

The $80\ nm$ TFT devices exhibit different switching behaviours between the n-type as grown ALD semiconductor active layer and the proposed p-type laser annealed semiconducting active layers. There is some evidence to suggest that for the as processed films, the channel formed is at the p-n interface as

a result of the laser surface treatment. From the results we tentatively suggest that upon thermal annealing N is able to diffuse deeper into the thin films for the 1-pulse sample at $200\ ^oC$, whilst annealing at $300\ ^oC$ is detrimental to the sample and causes out-diffusion of important species that play a key role in the electrical properties of the semiconducting films. Further support from ToF-SIMS measurements would be able to verify the underlying mechanisms governing the TFT behaviour of the thermally treated ZnO samples.

5.3.4. 20 nm ZnO TFTs

In the previous section, a post thermal annealing methodology was investigated to try to deepen the N diffusion within the ZnO thin films with the goal of achieving full conversion of the 80nm thin films one uniformly doped p-type film. An alternative approach is presented in this section, whereby the ZnO starting material is reduced to $20\ nm$ thickness. As presented previously, according to VBS, it appears the acceptor type doping is achieved to a depth between $20 - 40\ nm$. Therefore, by reducing the ZnO thickness to $20\ nm$, it is likely that N diffusion has occurred throughout the $20\ nm$ and thus the entire film should be converted to p-type after laser doping to form uniform p-channel TFTs. However, as mentioned previously, the outcomes of the laser doping experiment depend heavily on the sample structure being processed. By reducing the standard $80\ nm$ ZnO film investigated so far in this study to $20\ nm$, it is reasonable to assume the standard recipe of $1 - 2$ pulses at $200\ mJcm^{-2}$ may not achieve the same p-type behaviour. A large range of laser fluences from $50 - 200\ mJcm^{-2}$ was therefore investigated to try to induce p-type doping throughout the entire $20\ nm$ film. The resultant TFTs under investigation consisted of a $20\ nm$ ZnO active layer on top of the standard $40\ nm$ Al_2O_3 dielectric layer on Si substrate with Au source, drain and gates electrodes, with the same TFT fabrication process flow being followed as described in section 5.3.1. **Figure 5.11** compares the transfer characteristic curves of the $20\ nm$ as grown TFTs alongside the $20\ nm$ CEELD ZnO TFTs processed with 1 and 2 pulses in a fluence range of $50 - 200 mJcm^{-2}$ with $5\ V$ bias applied to the drain. For the as grown films, an increase in I_D with positive V_G is indicative of the expected n-type nature of the as grown material. Two minima are observed in the transfer of the as grown TFT, one at $V_G = 5\ V$ which signifies the ON-switching of the device, and a second minima at $V_G = 0\ V$. Unlike the TFTs explored so far, this second minimum does not arise from a change in polarity of I_D as no negative current is achieved in this device. As such, the relatively large OFF-current for this device is assigned to the high carrier concentration of the as grown thin film, resulting in minimal switching behaviour between the ON/OFF states. Better switching is however achieved for the $20\ nm$ film when compared to the transfer characteristics of the $80\ nm$ TFTs. This is assigned to the reduced thickness of the $20\ nm$ thin film, whereby the entire 20 nm layer may contribute to the channel, unlike the $80\ nm$ film where we expect that some part of the highly conductive bulk material may remain outside of the channel layer resulting in a larger OFF current. Conversely, all TFTs featuring a laser annealed active layer exhibit increasing

I_D with increasingly negative V_G which is the typical switching behaviour expected of a p-channel TFT. For all cases, improved switching behaviour is observed with increased ON/OFF ratios compared to the as grown film. These improved TFT transfer characteristics for the laser annealed films is a result of reduced conductivity of the active layers in these films which leads to improved TFT performance. Instability in the measurements of the CEELD TFTs is observed and is most likely due to laser induced surface damage or deformation of the thin $20\ nm$ film leading to defects or trapping sites at the interface between the semiconductor surface and the source and drain electrodes.

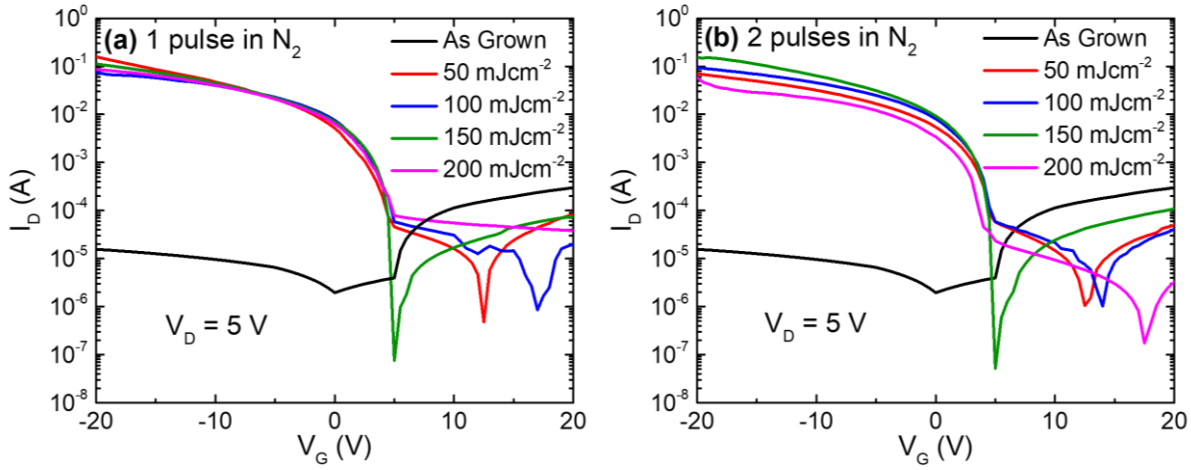

Figure 5.11 *The transfer results for the as grown (black-line) and laser processed* $20\ nm$ *semiconductor layer TFTs presented at* $V_D = 5\ V$*, for the (a) 1 pulse and (b) 2 pulse samples laser processed with* $50\ mJcm^{-2}$ *(red-line),* $100\ mJcm^{-2}$ *(blue-line),* $150\ mJcm^{-2}$ *(green-line) and* $200\ mJcm^{-2}$ *(magenta-line) laser energy density.*

For all CEELD cases, a minimum is observed around $V_G = 5\ V$, which indicates the ON-switching of the devices. For the samples treated with $50 - 100 mJcm^{-2}$, a second minimum relating to the I_D polarity switching occurs at varying values of V_G for samples treated with 1 and 2 pulses. Conversely, only one minimum exists for the 1 and 2 pulse samples at $150 mJcm^{-2}$, which indicates both the ON-switching and change in polarity around $V_G = 5\ V$. The transfer characteristics of the $20\ nm$ films processed at $150\ mJcm^{-2}$ are akin to those of the $80\ nm$ films processed with the same number of pulses at $200\ mJcm^{-2}$ which may indicate the transferable laser processing conditions required to achieve the same active layer for the thinner ZnO devices as the $80\ nm$ devices. Meanwhile, the samples treated with $200 mJcm^{-2}$ show a disparity in transfer behaviour between the 1 and 2 pulse samples, with only the 2-pulse sample showing both minima within the measurement range. The change in V_G at which negative $I_D$occurs is related to the capacitor discharging phenomenon, and so related to the transistor capacitance, whereby an increase V_G for which I_D becomes negative suggests greater

transistor capacitance. Capacitance-voltage measurements of these TFT devices may reveal further insight into the TFT operation and should therefore be considered for future work.

5.4. Chapter Summary

This chapter presented the work on implementing the materials developed in Chapter 4 into working devices, starting from the development of Ohmic contacts to both n- and p-type materials using a metallisation scheme involving the sputter deposition of gold metal contacts followed by a 1 minute thermal anneal at $200\,^{o}C$ under vacuum. The p- and n-materials and metallic contacts were then implemented into TFT and p-n junction devices to try and elucidate further the dominant charge carrier types within the thin films and provide further support to the claim of achieving p-type ZnO *via* the CEELD process in a high-pressure N_2 environment. The TFT devices showed a clear difference in transfer behaviour between the n-type as grown and p-type laser processed samples displaying the exact opposite ON-switching behaviour. Furthermore, both lateral and vertical p-n junction devices were fabricated using the selective excimer laser doping technique developed in this work. The two different p-n junction device architectures showed clear rectifying behaviour, indicating diode-like behaviour. Moreover, upon comparison with the I-V results across the p-n junction versus the metal contacts for the n- and p-type materials, clear differences could be observed in the low voltage regime, and it was therefore concluded the I-V behaviour was dominated by transport at the p-n junction and not at the contacts. Simple photodiode tests also confirmed the presence of a p-n junction by achieving characteristic photodiode I-V behaviour under reverse bias, and therefore showed the potential of the p-n junction devices developed in this work as photodetectors. Future work should focus on capacitance-voltage measurements of both the TFTs and p-n junctions to reveal further information about the dopant defects and the type of p-n junction formed, alongside more thorough photodiode investigations to test the full potential of the devices developed. The work in this chapter has demonstrated that the best way to verify the dominant carrier type in semiconducting thin films is by implementing the materials into simple devices and observing the different device behaviour according to device physics theory for opposing dominant charge carriers: electrons and holes. The work performed in this chapter supports the claim of achieving p-type doping in ZnO and presents the potential of controlled environment excimer laser doping as a highly selective, ultrafast, low thermal budget and highly controllable doping method as a one-step ZnO based ultra-shallow p-n homojunction fabrication method for both lateral devices and laterally printed vertical devices.

6. Infrared Optical Properties of ZnO

6.1. Introduction

The following section is devoted to investigating the infrared (IR) optical properties of ZnO *via* spectroscopic ellipsometry (SE). Focus into the IR optical properties of ZnO was brought about due to the restrictions imposed by the Covid-19 pandemic lockdowns and limited access to the laboratory. This chapter is based on the work underway for the publication "On the phonon plasmon coupling and manipulation of the natural hyperbolic behaviour in ZnO" (J. M. West *et al*., Nanomaterials MDPI). The chapter builds upon the work in Chapter 4, starting with the theory and motivation of the work (Section 6.2), followed by exploring the experimental methods and SE data sets of samples with a broad range of carrier concentrations to investigate the tailoring of the real permittivity with increasing plasma energy (Section 6.3-6.4) and identify the potential of ZnO as a natural hyperbolic material (NHM). The phonon and plasmon properties of the sample set is then investigated (Section 6.5) and three different material regimes are identified, namely: phonon-like, the phonon-plasmon strong coupling region, and plasmon-like. The following sections then explore the: effect of these material regimes on the hyperbolic bandwidth (Section 6.6) and the hyperbolic ratio (Section 6.7). Section 6.8 then investigations the hyperbolic field distributions of ZnO *via* finite-difference-time-domain simulations.

6.2. Motivation and Theory

Optical metamaterials (OMMs)[401] are artificially nano-structured media which have been engineered to extend material properties far beyond those capable in nature. Such unconventional properties enable OMMs to support unique bulk electromagnetic states facilitating superior control over light-matter interactions at the nanoscale. The field of MMs has therefore unlocked a wide range of exotic and useful functionalities with applications across all materials science.

Recently, the field of OMMs has been extended to include an attractive new class of extremely anisotropic ($\varepsilon'_{x,y}\varepsilon'_{z} < 0$), active and tuneable materials which support indefinite[402] or hyperbolic dispersion. These are entitled Hyperbolic Metamaterials (HMMs) and can display dielectric properties ($\varepsilon' > 0$) in one or two of the orthogonal components while exhibiting metal-like properties ($\varepsilon' < 0$) in the other component(s) of the real part of the dielectric permittivity. The hyperbolic name is so derived from the topology of the isofrequency surface, which governs the electromagnetic (EM) wave propagation and light-matter interactions of a material.[403] For conventional materials such as dielectrics and those that observe standard anisotropy, the isofrequency surfaces are closed and spherical or ellipsoidal respectively. For HMMs exhibiting the extreme anisotropy in their dielectric tensor described above, the isofrequency surface opens into a hyperboloid causing EM waves to propagate with hyperbolic dispersion in such materials.[402] This open surface allows for waves with infinitely large wavevectors to propagate in the material. In conventional media, such fields would be

evanescent and decay exponentially, and so it is the unique property of high wave vector wave propagation that makes HMMs such a fascinating class of materials. In non-magnetic media, there are generally two types of hyperbolic dispersion: Type 1 is described by the condition $\varepsilon'_{x,y} > 0, \varepsilon'_z < 0$, whilst Type 2 is defined by $\varepsilon'_{x,y} < 0, \varepsilon'_z > 0$.[404] The shape of the isofrequency surfaces for Type 1 and Type 2 hyperbolic dispersion are shown in **Figure 6.01(a) and (b)**. Such HMMs support unique bulk electromagnetic states which facilitate superior control over light-matter interactions at the nanoscale. [405]

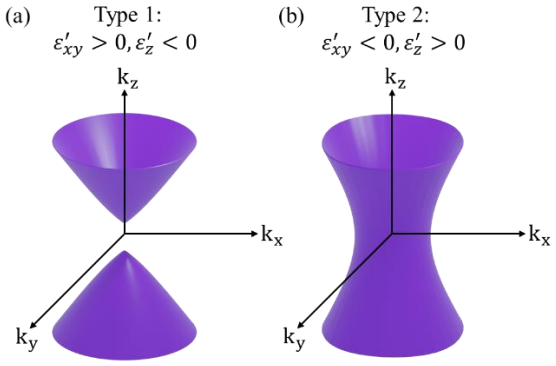

Figure 6.01. *Isofrequency Surface Contours for (a) Type 1 and (b) Type 2 hyperbolic dispersion.*

In recent years, HMMs and their extraordinary properties have spurred interest into a wide range of practically important topics[5, 6] such as non-linear effects,[7, 8] negative refraction,[9-11] as well as enhancement and engineering of spontaneous[412] and thermal emission[13,14]. They offer exciting experimental effects in broadband Purcell factor,[15, 16, 17] photonic spin Hall effect,[18, 19] super-Planckian heat transfer[420] and Cherenkov radiation.[21, 22] Finally, they provide a promising plethora of applications in far-field subwavelength imaging,[23,24] sub-diffraction focussing,[425] high-speed, high efficiency light sources,[426] sensing and detection,[427–432] single photon sources,[32–34] and subwavelength waveguides.[435]

The hyperbolic requirement, $\varepsilon'_{x,y}\varepsilon'_z < 0$, dictates the need for both metal-like (negative real permittivity) and dielectric (positive real permittivity) components. Initial efforts into achieving such hyperbolic dispersion in materials were focussed into using artificial nanostructures fabricated using either metal-dielectric multilayers[436] or metallic nanostructures embedded in a dielectric medium,[437] since it was believed that single materials with such extreme anisotropy did not readily occur in nature. Such artificial HMMs can support hyperbolic dispersion across the optical spectrum through careful optimisation of the materials and architectures used. The key material requirements to be considered when choosing suitable materials for artificial HMMs are the spectral range of interest, hyperbolic dispersion bandwidth, material losses (ideally to be minimised), and impedance matching between the dielectric and metal components (whereby the absolute magnitude of the permittivity of both

components needs to be similar in order to support hyperbolic dispersion modes).[407] Suitable materials for artificial HMMs across the whole spectral range have been evaluated in detail elsewhere.[438–440]

However, the ability to take full advantage of the hyperbolic phenomena in artificial HMMs is made difficult since their hyperbolic behaviour is governed by the choice of constituent materials and the geometry of the hybrid structure, leading to a fixed hyperbolic response in a finite spectral range, with only either Type 1 or Type 2 hyperbolicity being achieved. As well as the fixed nature of artificial HMMs, their manufacture remains technically challenging, with fabrication limitations leading to impedance mismatch, high material losses, surface and interface scattering and an upper limit on the available high-k states dictated by the unit cell dimension limit of such artificial nanostructures.[440] It is therefore important to search for alternatives to artificial HMMs if the full potential promised by hyperbolic media is to be realised.

In the past decade it has been observed that some natural materials can achieve hyperbolic dispersion.[441–443] Uniaxial polar dielectrics are single-phase materials that have negative real dielectric permittivity ($\varepsilon' < 0$) in their Reststrahlen bands[444] i.e. the energy range between the Transverse Optical (TO) and Longitudinal Optical (LO) phonon energies.[443] Some of these uniaxial materials can display extreme anisotropy[445] in their optical phonon properties, with such natural anisotropy leading to the fulfilment of the hyperbolic requirement $\varepsilon'_{x,y}\varepsilon'_{z} < 0$. Therefore, such natural materials can exhibit phonon polariton (PhP) enabled hyperbolic dispersion. These natural hyperbolic materials (NHMs) can overcome many of the challenges faced by artificial HMMs, demonstrating much reduced losses than their plasmonic based counterparts in the IR range, have nanoscale dimensions allowing propagation of higher momentum states, and also negate the need for complex fabrication processes.[446] They also experience no internal wave scattering since they are single phase materials, unlike HMMs where wave scattering due to poor impedance matching between the dielectric and metallic material is a problem. Such natural materials are also capable of harnessing both types of hyperbolic response, however, whilst the ability of a single material to support both types of hyperbolicity is attractive, the relatively narrow Reststrahlen region of most phonon-resonant materials leads to a much narrower spectral band in which hyperbolic modes can be supported. This contrasts with artificial HMMs where the metallic component can exhibit negative permittivity over the entire Mid-IR range, and provided that a suitable nominally dispersive dielectric is chosen, a very broad hyperbolic region can be achieved. The relatively fixed response of natural materials dictated by their intrinsic properties and fixed optical phonons yields a fundamental disadvantage of NHMs compared to HMMs. As such, research has shifted in recent years to try to manipulate the spectral region in which hyperbolicity can be supported in natural materials. Promising advancements in the tunability of NHM properties have been achieved through doping,[447] thermal treatment,[448] pressure,[440] or electron addressability.[45,46] More recently, the field of natural hyperbolic materials has been extended to include materials that can support a variety of hyperbolic polaritons including: phonon polaritons [451–453], plasmon polaritons[454,455], exciton

polaritons[456], ghost polaritons[457] and shear polaritons[458]. It has also been reported that 2D materials (such as black phosphorus) can support hyperbolic plasmons,[455] as opposed to the hyperbolic phonons supported in other NHMs.

Of the NHMs identified so far,[440][459] hexagonal Boron Nitride (h-BN) has gained heightened interest as it can support highly dispersive phonon polariton modes in two separate Reststrahlen bands enabling h-BN to support both types of hyperbolicity. [451,460–464] What really sets h-BN apart however is the unparalleled high degree of TO phonon energy anisotropy which results in a much broader bandwidth in which hyperbolic modes are available.[465] However, whilst h-BN remains a highly attractive material due to its unique physicochemical properties,[464,466] the synthesis of large area, high quality material using cost effective methods remains a crucial issue. Subsequently, the high cost and challenging fabrication associated with h-BN is a significant bottleneck in the development and commercialisation of natural hyperbolic media in the nanophotonic industry.[466]

To this end, this work seeks to shine a light on ZnO as a potential low cost, tuneable NHM in the Mid-IR regime. ZnO is a well-established multifunctional polar semiconductor[32] with uniaxially anisotropic optical properties that has been previously overlooked as a suitable NHM candidate due to the small degree of anisotropy between its optical phonons along the ordinary (in-plane) and extraordinary (out-of-plane) axis in its single crystal form.[312] Such a small degree of anisotropy results in a narrow bandwidth in which ZnO can support only Type 2 hyperbolic behaviour, limiting its suitability as a potential NHM. However, in this work, it is demonstrated that by appropriate doping, the carrier concentration (and thus the plasma energy) can be tuned in ALD ZnO, which subsequently leads to a considerable variation in the line shape of the real part of the permittivity (both the ordinary, $\varepsilon'_{x,y}$, and extraordinary, ε'_{z}) of the materials. As a result, the hyperbolic bandwidths of the ZnO materials, which would otherwise be fixed, can be tuned and extended. Principally, the phonon-plasmon coupling phenomena and the resultant tailoring of the real permittivity, ε', are investigated. The potential to tune and extend the bandwidths of different types of hyperbolic response across three fundamental material regimes: phonon-like; phonon-plasmon strong coupling; and plasmon-like regime is then presented. It is shown that through phonon-plasmon coupling and by increasing the plasma energy in ZnO, both types of hyperbolic dispersion can be obtained as well as large extensions to the energy range in which such hyperbolic modes could be supported. An experimental observation of an elusive optical topological transition between the two types of hyperbolic behaviour by increasing the plasma energy is also reported. Moreover, ZnO is already a well-established technological material, characterised by its low cost, earth abundance, high temperature stability, CMOS compatibility and ease of fabrication in high quality *via* ALD. Combined with the above-mentioned hyperbolic properties, ZnO is presented as a potentially viable candidate as an alternative NHM candidate for nanophotonic applications in the mid IR regime.

6.3. Experimental Details

A series of ~80 nm ZnO thin films with varying carrier concentrations were deposited onto Si or Al_2O_3/ Si substrates by ALD[82] using the Anric Technologies AT-400 ALD system plus ATOZONE generator.

Table 6.1 Sample Fabrication Methodology

Sample ω_p [eV]	**Substrate**	**Deposition Temperature [°C]**	**Reactant**	**Number of LA pulses**
0.0187	Si	150	NH_3, H_2O	0
0.0337	Si	150	NH_3, H_2O	0
0.0773	Si	180	Ozone	0
0.0899	Al_2O_3/Si	180	H_2O	0
0.112	Al_2O_3/Si	170	H_2O	0
0.121	Al_2O_3/Si	150	H_2O	0
0.134	Al_2O_3/Si	150	H_2O	0
0.155	Al_2O_3/Si	150	H_2O	2
0.161	Si	150	H_2O	0
0.173	Si	145	H_2O	0
0.223	Al_2O_3/Si	150	H_2O	4
0.239	Al_2O_3/Si	150	H_2O	3
0.256	Si	165	H_2O	0

The Al_2O_3 dielectric layer was incorporated into the sample architecture to facilitate electrical measurements not presented in this chapter. The range of carrier concentrations in the ZnO samples were achieved by varying the ALD deposition parameters such as deposition temperature (between $145 - 180$ ℃) and ALD reactant (H_2O / O_3 / NH_3), or by post laser processing of the ALD samples in 100 psi N_2 environment with $0 - 4$ laser pulses at $150\ \mathrm{mJcm^{-2}}$ (where 0 pulses indicate no laser annealing has been performed on that sample). IRSE measurements were then performed on all samples according to Chapter 3 Section. **Table 6.1** shows the full details of the thin film fabrication and post processing details of the films under investigation in this Chapter according to their ascending plasma energy.

6.4. IRSE Data and Model Dielectric Function

To investigate the hyperbolic phenomena observed in ZnO, the IR dielectric function attained from the complex modelling of IR ellipsometric data (as described in detail in **Chapter 3**) is evaluated. In this section the IRSE measured Ψ and Δ data and the Kukharskii modelled dielectric function of a series of n-type ZnO thin film samples with a broad range of carrier concentrations are explored. (Note that ω_p varies according to the square root of the carrier concentration, as shown in Equation 3.38, as such the two are proportional and will be used interchangeably in the text.) The range of carrier concentrations in the ZnO samples were achieved by varying the ALD deposition parameters as described in Section 6.3. **Figure 6.02** presents the experimental Ψ (red-line) and Δ (green-line) and best-matched Kukharskii model calculated Ψ and Δ data (black lines) taken at 70 ° angle of incidence for the Mid-IR spectral range ($0.03 - 0.3$ eV) of all ALD samples investigated in this chapter each labelled with their respective plasma energy in a range of $0.0187\ eV \leq \omega_p \leq 0.256\ eV$. Samples with a large range in ω_p were chosen to observe the changes induced to the Kukharskii model permittivity upon increasing the free carrier concentration (and in turn ω_p). For all samples in Figure 6.2, the position of the uncoupled phonon energies ($TO - LO$) and the coupled Longitudinal Phonon-Plasmon (LPP) modes, for both ordinary (x, y) and extraordinary (z) axes as determined from the Kukharskii model are shown. The black brackets mark the TO and LO phonon energies, whereas the blue brackets mark the lower LPP^- and upper LPP^+ branch energies. Note, the LPP^- branch energies for the low ω_p samples and the TO_z, LO_z and LPP_z^+ modes of the $\omega_p = 0.0773\ eV$ sample are beyond the presented measured range and so are not indicated in Figure 6.02. The dip feature dominating some of the Ψ and Δ spectra at ~0.12 eV is due to a loss of reflectivity from the 40 nm Al_2O_3 dielectric interlayer (between the ZnO film and the Si substrate). In all cases, the ZnO $TO_{x,y}$ mode strongly influences the Ψ and Δ spectra manifesting as a sharp peak in Ψ at the $TO_{x,y}$ phonon mode energy. A loss of reflectivity manifesting as a dip-like feature in the Ψ spectra can also be seen for all samples at around 0.0731 eV, which originates from the coupling between the LO phonon mode and plasmon excitations in the ZnO thin film. This LPP mode appears shifted from the uncoupled LO mode due to the hybridisation of the LO mode with the free carriers present in the samples. For the ZnO films with low ω_p (ω_p= 0.0187-0.0337 eV), the dip-like structure is sharp and similar in magnitude to the TO mode. In this plasma energy region, the value of ω_p is below that of the phonon modes therefore there is no significant interaction between the two modes and as a result, the Ψ and Δ show a predominantly phononic line-shape.

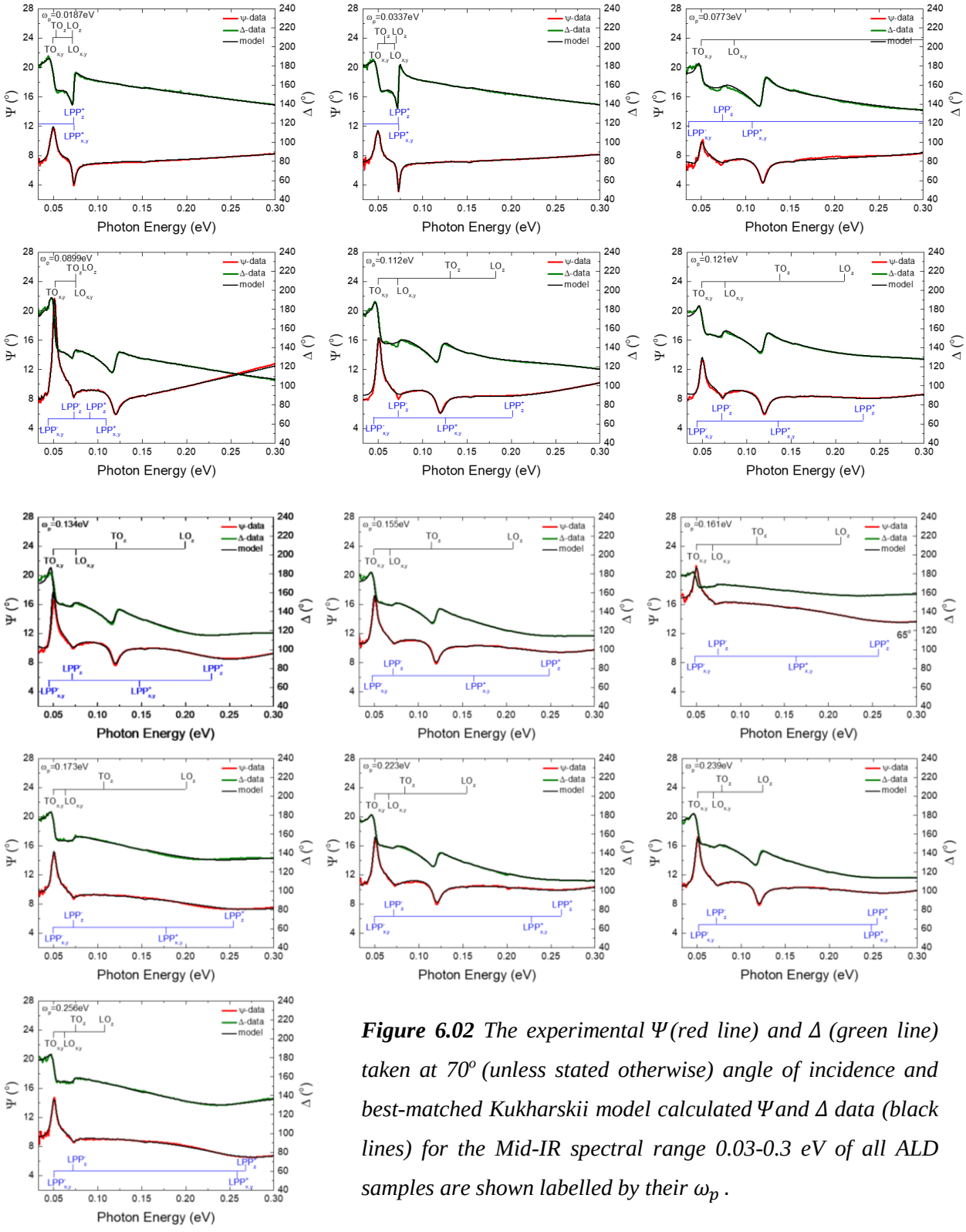

Figure 6.02 *The experimental Ψ (red line) and Δ (green line) taken at 70° (unless stated otherwise) angle of incidence and best-matched Kukharskii model calculated Ψ and Δ data (black lines) for the Mid-IR spectral range 0.03-0.3 eV of all ALD samples are shown labelled by their* ω_p .

As ω_p approaches and increases beyond the phonon energies, the dip-like structure becomes less sharp and smaller in magnitude due to the result of coupling between the plasmons and phonons in the thin films, and at higher ω_p , the dip structure appears reduced in magnitude due to a screening effect from the higher number of free electrons in those samples. In all cases, the dip structure is well described by the Kukharskii model. Similar coupling effects have been observed in other semiconductors such as

GaN,[344] InN[340] and GaAs[315] , AZO[467] and ZnO nanorods[468], but to the best of our knowledge has not yet been studied in terms of ellipsometry spectra for ALD grown ZnO. This striking observation introduces ZnO as a potential plasphonic[345] material for applications in the technologically important IR regime.

Figure 6.03 shows the resultant calculated real, ε', and imaginary, ε'', permittivity for the ordinary (ε' =black line, ε'' = red line) and extraordinary ((ε' =blue line, ε'' = green line)) axis for all samples labelled by their plasma energy in the mid-IR range as determined by the Kukharskii model. In polar semiconductors, the real permittivity becomes negative in the Reststrahlen band. However, for the case of the ZnO films in this work, it is observed that the real permittivity becomes negative in an extended region beyond the Reststrahlen band limits upon the addition of free carriers. The engineering of the Reststrahlen region *via* doping is well documented for many material systems.[469] For the case of the low ω_p ZnO samples (ω_p= 0.0187-0.0337 eV) in this work, there is a narrow region where $\varepsilon'_{x,y} < 0$ between the $TO_{x,y}$ mode and the coupled $LPP^{+}_{x,y}$ mode, whilst in the extraordinary axis a second extremely narrow negative real permittivity region occurs between the TO_z mode and the coupled LPP^{+}_{z} mode. As the ω_p is increased to values greater than $0.0337\ eV$, an almost monotonous increase to the extension of the Reststrahlen band in the $\varepsilon'_{x,y}$ with ω_p can be seen between the $TO_{x,y}$ mode and the screened plasma energy (which is red shifted from the real value of ω_p due to the deviation of ε_∞ from unity to a higher average value of around 3.55 for these films). Along the extraordinary axis, the value of real permittivity becomes negative at the LPP^{-}_{z} mode and extends deeper into the IR, beyond the measurement range. Thus, the otherwise narrow negative real permittivity region between the TO and LO modes for undoped ZnO can be significantly engineered and extended through the addition of free carriers mediated by phonon-plasmon coupling. Such an extension to the negative real permittivity regions broadens the spectral range in which the ZnO could be used as a plasphonic[345] material. Upon comparison of the ε' spectra for each optical axis Figure 6.03 for all samples, a striking observation can be made that there are two regions with extreme anisotropy, whereby ε' has opposite signs in the two axes (ordinary and extraordinary). This allows for the fulfilment of the hyperbolic criterion, $\varepsilon'_{x,y}\varepsilon'_{z} < 0$, and thus hyperbolic modes could be supported in those spectral ranges. The regions in which $\varepsilon'_{x,y} > 0$ and $\varepsilon'_{z} < 0$ are highlighted by the blue shaded regions indicating the bandwidths in which Type 1 hyperbolic dispersion can be supported, whilst Type 2 behaviour, $\varepsilon'_{x,y} < 0$ and $\varepsilon'_{z} > 0$, is indicated by the grey shaded regions. Similar behaviour has been reported in h-BN which is capable of supporting both Type 1 and Type 2 hyperbolic behaviour in two different spectral regions,[460] but to the best of our knowledge has not yet been reported for ZnO thin films. Interestingly, for the low ω_p samples (ω_p= 0.0187-0.0337 eV) two narrow regions of Type 2 behaviour can be observed.

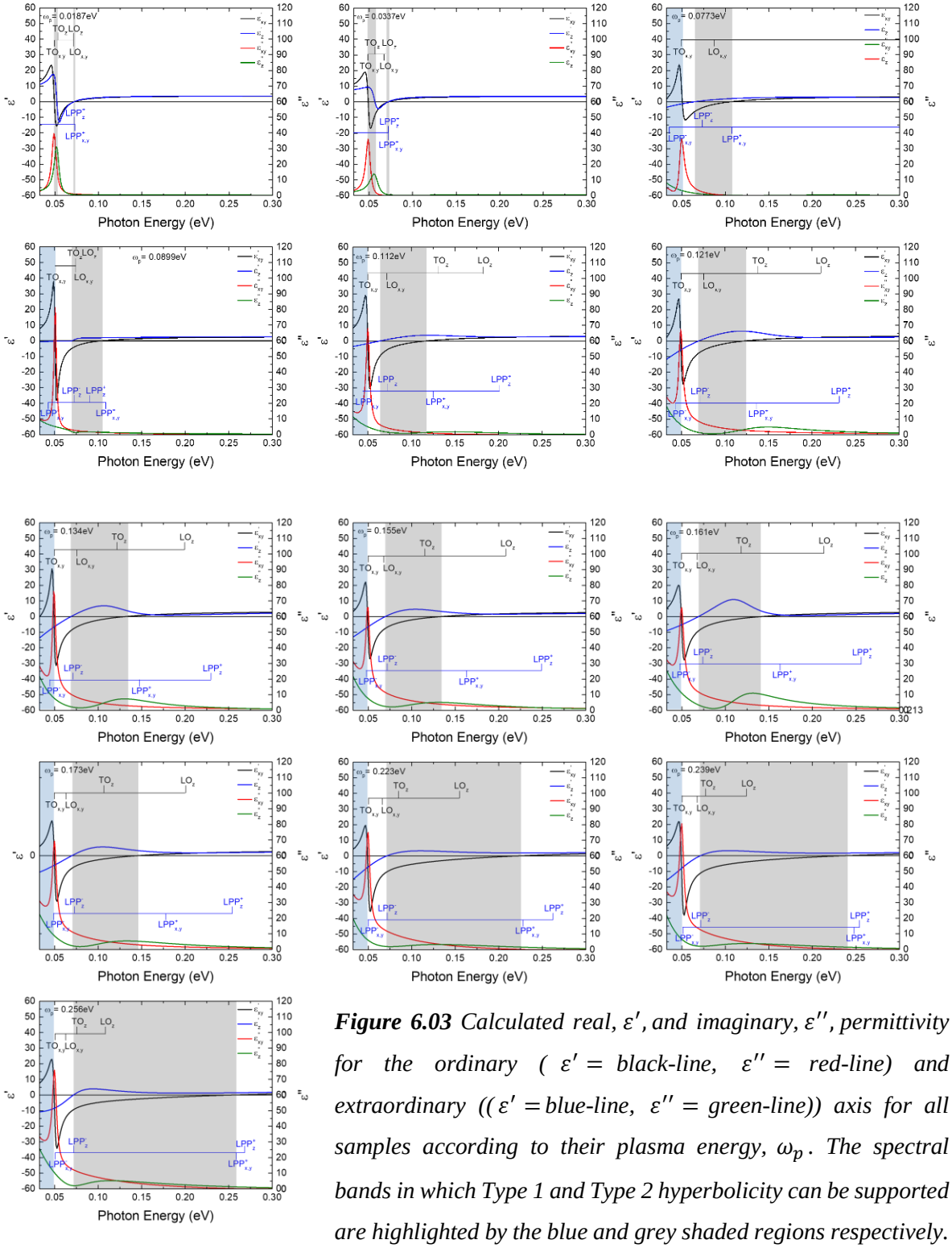

Figure 6.03 *Calculated real, ε', and imaginary, ε'', permittivity for the ordinary ($\varepsilon' =$ black-line, $\varepsilon'' =$ red-line) and extraordinary (($\varepsilon' =$ blue-line, $\varepsilon'' =$ green-line)) axis for all samples according to their plasma energy, ω_p. The spectral bands in which Type 1 and Type 2 hyperbolicity can be supported are highlighted by the blue and grey shaded regions respectively.*

Upon higher doping, for samples with $\omega_p \geq 0.0773\ eV$, both Type 1 and Type 2 hyperbolic behaviour can be supported. The hyperbolic region at the lower energies has undergone a complete inversion from Type 2 to Type 1 over an extended spectral range compared to the Type 2 behaviour, observed for the two low ω_p samples, which is referred to as an optical topological transition that is discussed further in

Section 6.5 below.[470] The second hyperbolic region at higher photon energies (grey shaded region) remains Type 2 for all samples, with increasing bandwidth as ω_p increases. Interestingly, as ω_p increases from 0.0337 eV to 0.0773 eV (which is close to the phonon energies in ZnO), a large broadening of this second hyperbolic mode is observed. Increasing the ω_p further to 0.0899 eV, however, appears to show a slight reduction in this Type 2 region bandwidth, before once again increasing as $\omega_p \geq 0.112\ eV$. The trend in the hyperbolic bandwidth as ω_p increases is explored further in Section 6.5.

6.5. Phonon-Plasmon Coupling in ZnO

To further explain the behaviour of the IR dielectric function for the ZnO films investigated in Section 6.3, the phononic and plasmonic properties of the series of ZnO thin films are evaluated. The coupling between bulk plasmons and phonon vibrational resonances gives rise to a set of two new hybrid phonon-plasmon eigenmodes (Equation 3.43) with distinct anti-crossing behaviour in the strong coupling regime.[69, 70]

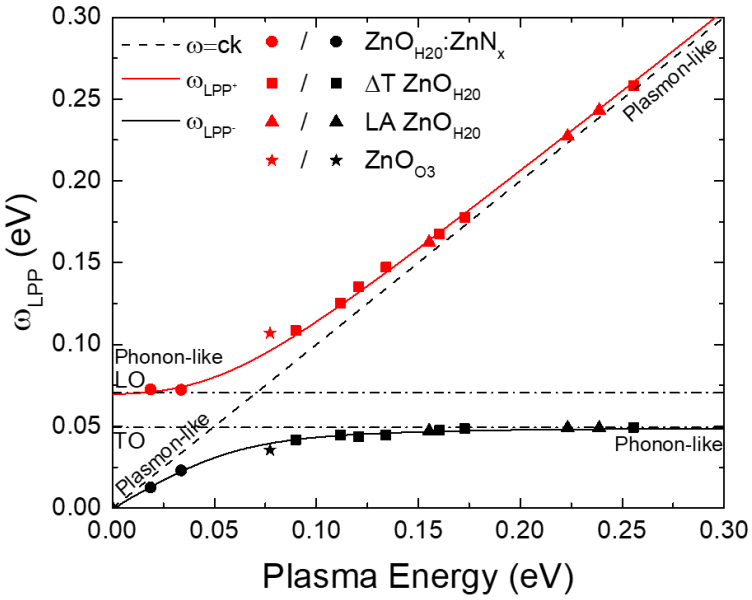

Figure 6.04. *Results of the upper and lower coupled phonon-plasmon mode energies obtained from the Kukharskii dielectric function model for the x,y axis in dependence of sample plasma energy. The position of the LPP+/- mode energies are indicated by individual symbols for each sample in accordance with its plasma energy, along the upper (red line) and lower (black line) branch dispersion curves, whereby the upper and lower mode energies can be distinguished using red and black symbols respectively. The uncoupled LO and TO phonon energies are shown by the two-horizontal dot-dashed lines.*

Such hybridisation between the phonon and plasmon modes can be described by an electromagnetically coupled oscillator model whereby the local polarisation fields generated by the lattice vibrations of

phonons and the plasmon resonances can cause the two modes to couple through near field interactions. When such coupling becomes sufficiently strong, the energies and lifetimes of the two uncoupled modes can be significantly modified with the result of the coupling being the two hybrid LPP modes. **Figure 6.04** shows the upper and lower coupled phonon-plasmon mode energies with ZnO plasma energy, obtained from the Kukharskii model fit for the ordinary axis dielectric function. The calculated $LPP_{x,y}^{+/-}$ branch dispersion in dependence of the plasma energy are shown by the red (upper branch) and black (lower branch) lines. The position of the $LPP_{x,y}^{+/-}$mode energies of each sample as obtained from the model analysis are indicated by individual symbols along the dispersion curves. Four different shaped symbols have been used to highlight the various sample preparation methods: squares for films deposited at different temperatures; dots for those films deposited using both H_2O and NH_3 reactants; triangles for those films' that were post-fabrication laser annealed; and star for the film deposited using O_3 as the reactant. The LPP^+ and LPP^- mode energies can be distinguished using red and black colours respectively. The uncoupled LO and TO phonon energies averaged across all samples are also show in Figure 6.04 by the two-horizontal dot-dashed lines, whilst the plasmon line is shown as the dashed diagonal line. The dispersion relations of the two hybridised branches shown in Figure 6.04 observe a pronounced anti-crossing known as Rabi energy splitting of the dispersion curve[473] separated by a distinct forbidden energy gap which can be related to the phonon Reststrahlen band and the coupling strength between the phonons and plasmons. The signature of such strong coupling can be observed around $\omega_p = 0.07\ eV$ which could be exploited for the many benefits of a hybridised strongly coupled phonon-plasmon system.[474–477]

6.6. ZnO as a NHM: Hyperbolic Bandwidth

The hyperbolic bandwidth is defined as the spectral range of photon energies for which the hyperbolic criterion, $\varepsilon'_{x,y}\varepsilon'_z < 0$, is fulfilled. The hyperbolic bandwidths were determined by taking the difference between the photon energies where the hyperbolic criterion is fulfilled according to the real permittivity's shown previously in Figure 6.03. A data selector tool was used to identify the photon energies in which the relation $\varepsilon'_{x,y}\varepsilon'_z < 0$ is true for each sample by focussing on those restricted photon energy regions. For all cases, an average of two photon energies taken around the crossing point (positive and negative values of the real permittivity around 0) to identify the exact energy at which the dispersion becomes hyperbolic.

The relationship between hyperbolic bandwidth and the level of doping (in terms of plasma energy) in the ZnO films is shown in **Figure 6.05**, whereby calculated hyperbolic bandwidths of each film for (a) Type 1 and (b) Type 2 hyperbolic regions are shown against ω_p. The different symbols have been used to highlight the various sample preparation methods as described in Figure 6.04. The uncoupled $LO_{x,y}$ phonon energy averaged across all samples is also shown in the figure by the solid-vertical line at

$0.0706\ eV$. Three distinct regions have been identified according to the dominant behaviour in three different plasma energy ranges of the films. These three regions have been informed by the upper LPP branch in Figure 6.04 and are as follows:

(i) Phonon-like: films with low plasma energy ($\omega_p < \omega_{LO_{x,y}}$), are indicated by black symbols whose behaviour is dominated by a phonon-like response.

(ii) Phonon-plasmon Strong Coupling Region (SCR): indicated by red symbols for films with hybridised behaviour. As ω_p approaches the energy of the LO phonon mode, the resonance matching regime is entered where the mixed phonon-plasmon strong coupling interaction is dominant (grey shaded region) and the films have hybridised phonon-plasmon behaviour. This region is informed by Figure 2 in the ω_p region at which the upper and lower branches of the coupled modes tend away from the uncoupled phonon and plasmon lines to form the hybridised modes.

(iii) Plasmon-like: For films with higher ω_p, blue symbols are used, representing films whose properties are dominated by a plasmon-like response as ω_p moves from the SC resonance matching region and the LPP mode branches return to follow the phonon and plasmon-light line.

In Figure 6.05 (a) the behaviour of the Type 1 ($\varepsilon'_{x,y} > 0, \varepsilon'_z < 0$) hyperbolic bandwidth of the ZnO thin films with increasing ω_p is reported, noting (e.g. by inspection of Figure 6.03) that it is restricted to photon energies $\omega < \omega_{TO_{x,y}}$ and so is dielectric-like (according to its behaviour in the x,y plane).[478] It is important to note that the lower end of the IRSE measurement spectrum ends at 0.03 eV, so the maximum Type 1 bandwidth for which hyperbolic modes can be supported may be wider, stretching further into the IR (below 0.03 eV). For further insights into this region, THz ellipsometry[479] could be useful. The two samples with $\omega_p \ll \omega_{LO_{x,y}}$ do not exhibit any Type 1 behaviour, however the zero data points for these samples are included to demonstrate the engineering of Type 1 behaviour across the full plasma energy range. As the ω_p approaches $\omega_{LO_{x,y}}$, the Type 1 hyperbolic bandwidth reaches a maximum for the sample where $\omega_p \approx \omega_{LO_{x,y}}$ (presented with the star symbol in Figure 6.5(a)). Therefore, it can be surmised that it is the splitting of the LPP branches in the strong coupling regime that induces the high level of anisotropy in the real permittivity of ZnO and extends the bandwidth of available exotic hyperbolic modes further into the IR regime and across a broader spectrum than available in other natural hyperbolic metamaterials such as h-BN.[440] As the ZnO ω_p moves away from the strong coupling point, the hyperbolic bandwidth decreases slightly as the extreme anisotropy inducing effects of the strong coupling diminishes, until a minimum value of hyperbolic bandwidth is reached at the edge of the grey SCR region. As ω_p increases further, the hyperbolic bandwidth extends

slightly as another material regime is entered, namely the plasmon-like region. The hyperbolic bandwidth appears to reach a plateau in this plasmon-like region to a value of around 0.017 eV which is expected to be due to the low photon energy measurement limit of 0.03 eV. The slight bandwidth broadening in the plasmon-like region is due to the increasing contribution of the Drude term to the lineshape of the real permittivity.

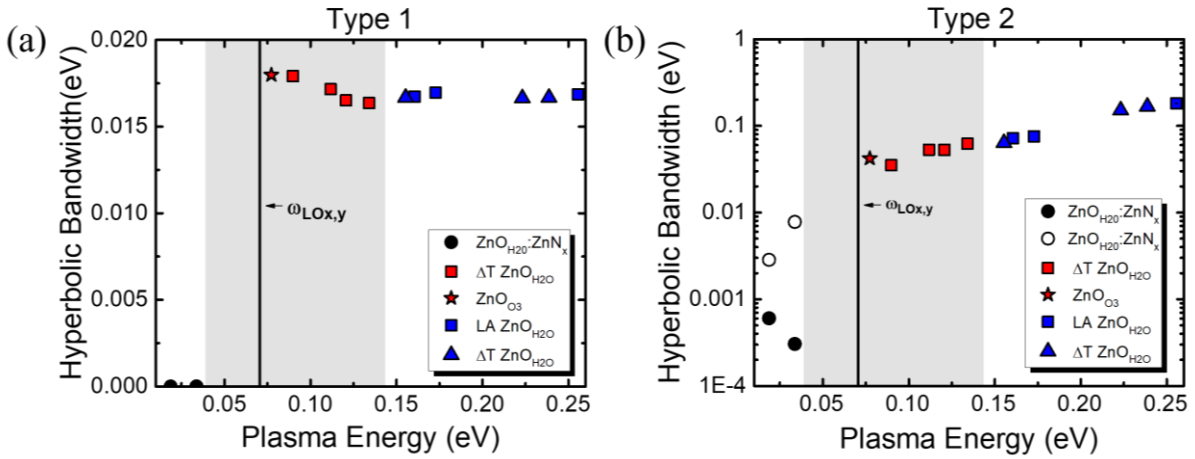

Figure 6.05*. Values of the calculated (a) Type 1 and (b) Type 2 hyperbolic bandwidths in the ALD ZnO thin films with increasing plasma energy. Four different shaped symbols have been used to highlight the various sample preparation methods. The uncoupled $LO_{x,y}$ phonon energy averaged across all samples is indicated by the solid-vertical line at 0.074 eV. Three distinct regions have been identified different symbol colours have been used according to the dominant behaviour in three different plasma energy ranges of the films: (i) phonon-like: black symbols, (ii) phonon-plasmon SCR: red symbols, (iii) plasmon-like: blue symbols. The grey shaded region has been used to identify samples with plasma energy around the resonance matching condition.*

In Figure 6.05 (b) the effect of increasing ω_p on the Type 2 hyperbolic bandwidth ($\varepsilon'_{x,y} < 0, \varepsilon'_z > 0$) hyperbolicity is investigated. For $\omega_p < \omega_{LO_{x,y}}$, it can be observed that there are two narrow Type 2 hyperbolic bands for each $\omega_{p.}$. The first of these is present only for films with $\omega_p < \omega_{TO_{x,y}}$ (shown by the open dot symbols at low plasma energies) and as ω_p approaches $\omega_{LO_{x,y}}$ this Type 2 response inverts to Type 1. The experimental observation of such a transition between two topologically different hyperbolic phases (Type 1 and 2) by varying the carrier concentration in ZnO is a striking result. The transition between Type 2 and Type 1 occurs between the phonon-like regime and the phonon-plasmon SCR, making this an area of interest for research into such a unique optical topological transition (OTT). The OTT observed here could be due to changes in intrinsic loss between the two material phases or changes in the magnetic permeability.[480] Therefore, as the ω_p is increased from the phonon-like region through to the SCR, there must be a critical point, ω_c , at which the Type 2 hyperboloid evolves into the Type 1 hyperboloid.[481] Such a topological singularity at ω_c allows for zero refractive index and may

lead to conical refraction[482] which has many exciting applications.[483] Recent work has shown that controlling the carrier density provides an efficient means to trigger phase transitions and modulate the optical properties in natural materials.[484] Thus, by increasing the plasma energy from the phonon-like to SCR, a topological transition in the optical response of the photonic system can be induced. Recent works have investigated OTTs in graphene—h-BN/ α-MoO_3 systems whereby a transition from elliptical to hyperbolic isofrequency surface is achieved *via* phonon-plasmon coupling,[484–486] whilst other works have investigated similar OTTs from elliptic to hyperbolic *via* interface engineering in biaxial crystal such as α-MoO_3.[487,488] However, the dielectric functions investigated in this work show that not only transitions from both elliptic to hyperbolic surfaces can be achieved by varying the carrier concentration, but also transitions from one type of hyperbolic response to another, which to the best of our knowledge has not previously been reported. This remarkable transition occurs as ω_p approaches the phonon energies in ZnO and it is therefore surmised that this change occurs due to the phase change resulting from the phonon-plasmon coupling in the ZnO under investigation here. Such control of the isofrequency surface in this ZnO material could find many applications in tuneable radiative heat flow control for radiative cooling or tuneable super-Planckian near field thermal emission,[420,486,489–491] programmable polaritonics, energy transfer and neuromorphic photonics.[488] The remaining Type 2 behaviour in Figure 6.5 (b) then continues to monotonically increase in hyperbolic bandwidth as ω_p increases, and different rates of increase associated with the different regimes are observed. Type 2 behaviour ($\varepsilon'_{x,y} < 0, \varepsilon'_z > 0$) has two negative components and this 'metallic' behaviour results in a dispersion that is much more sensitive to changes in the plasma energy than its Type 1 counterpart. Consequently, there is a large extension to the Type 2 hyperbolic bandwidth in the plasmon-like region due to the increasing contribution of the Drude term to the real permittivity lineshape. The data trend in Figure 6.5 (b) in the plasmon-like regime shows no saturation of the hyperbolic bandwidth with increasing plasma energy within the spectral range of these measurements. Therefore, by increasing the free carrier concentration in ALD ZnO, it is possible to achieve hyperbolic behaviour over a much-extended spectral range in the IR regime.

6.7. Hyperbolic Ratio

In order to compare ZnO, fabricated in this work, with the leading NHM h-BN, the ratio between $\varepsilon'_{x,y}$ and ε'_z across the IRSE spectral range is presented in a colour coded global map in **Figure 6.06** for h-BN, and three indicative ZnO samples with varying carrier concentrations that fall within the three distinct regimes: phonon-like (referred to as $ZnO_{Ph\text{-}like,}$ $\omega_p = 0.0187$ eV), phonon-plasmon SCR ($ZnO_{SCR,}$ $\omega_p = 0.0773$ eV), or plasmon-like ($ZnO_{Pl\text{-}like,}$ $\omega_p = 0.256$ eV). By investigating the hyperbolic ratio $\varepsilon'_{x,y}/\varepsilon'_z$, both the hyperbolic spectral region, i.e., the range of energies for which $\varepsilon'_{x,y}/\varepsilon'_z < 0$, and the magnitude of the ratio between $\varepsilon'_{x,y}$ and ε'_z which is important when considering potential practical applications can be observed.[440] In Figure 6.06, the value of the hyperbolic ratio is

colour coded such that regions in which there is no hyperbolic behaviour, i.e., $\varepsilon'_{x,y}/\varepsilon'_z > 0$ are shown as white, whilst the regions in which hyperbolic dispersion can be supported ($\varepsilon'_{x,y}/\varepsilon'_z < 0$) are indicated using a limited colour map to explore the magnitude of the hyperbolic ratio, whereby the bright red coloured region shows the energies at which the absolute magnitudes of $\varepsilon'_{x,y}$ and ε'_z are equal (i.e. a ratio value close to or equal to -1). Note that all hyperbolic ratio values less than or equal to -2 are coloured black. The anisotropic dielectric constants of h-BN were taken from ref [460] whilst the hyperbolic bandwidth was determined using the same method as for the ZnO samples.

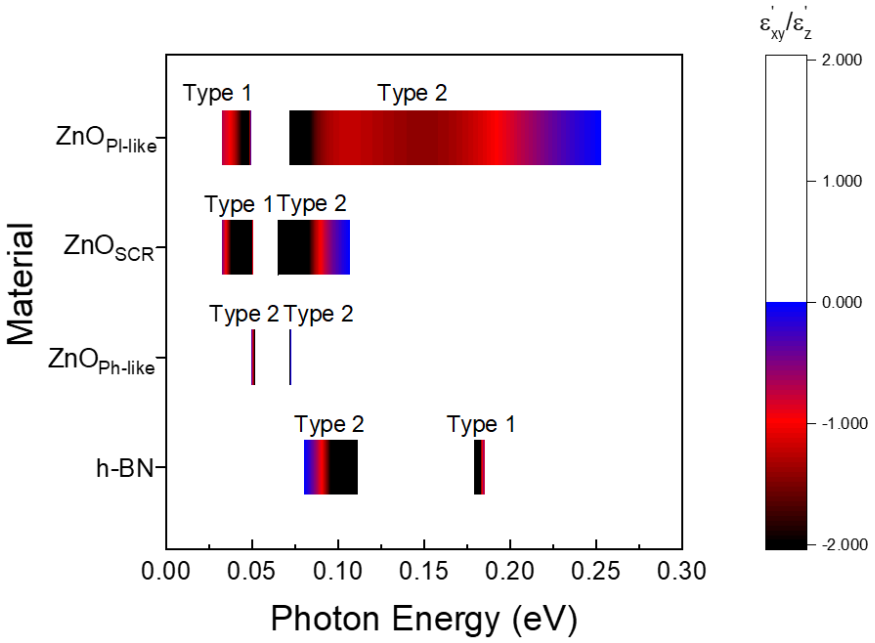

Figure 6.06 *Global map of the values of the hyperbolic ratio $\varepsilon'_{x,y}/\varepsilon'_z$ across the measurement spectral range in photon energy (eV) for h-BN [460], and three of the ZnO samples according to phonon-like ($ZnO_{Ph\text{-}like}$, $\omega_p = 0.0187\ eV$), phonon-plasmon SCR (ZnO_{SCR}, $\omega_p = 0.0773\ eV$), and plasmon-like ($ZnO_{Pl\text{-}like}$, $\omega_p = 0.256\ eV$) behaviour. Within the graph, Type 1 and Type 2 hyperbolic behaviour have been labelled for each sample.*

As shown in Figure 6.06, Type 1 hyperbolic bandwidth supported by h-BN lies in a higher spectral range in the IR with a much narrower bandwidth than the Type 1 modes presented for ZnO. The broad bandwidth of Type 1 modes in ZnO promotes it as an excellent candidate material for hyperbolic applications deeper into the IR range, where material options are scarce. Whilst beneficial in terms of losses, the all-dielectric nature of h-BN and other NHMs results in a lower optical density of states than their plasmonic counterparts in artificial HMMs. The strong coupling and hybrid nature of the Type 1 hyperbolic phonon-plasmon modes in ZnO is predicted to yield a much higher optical density of states available when compared to traditional NHM systems such as h-BN. The above mentioned hyperbolic

properties could promote ZnO as an NHM candidate for applications requiring high speed operation, super-resolution, and propagation over short distances in deeply subwavelength volumes.[492]

The bandwidth for Type 2 behaviour of h-BN lies between that of the $ZnO_{Ph\text{-}like}$ and ZnO_{SCR} samples respectively. However, the Type 2 bandwidth for the plasmon-like film encompasses the full spectral range of the h-BN Type 2 modes and extends even wider across the IR range. Thus, ZnO, through appropriate doping, is capable of supporting Type 2 hyperbolic modes over a much-increased, tuneable, spectral range than the current leading h-BN whose hyperbolic dispersion can only be tuned through the difficult fabrication of h-BN and graphene structures,[450] negating the benefit of having a single-phase material which can itself support hyperbolic dispersion over a broad spectral range. The Type 2 hyperbolic dispersion in ZnO also takes advantage of the larger number of high-k propagation modes due to the enhanced density of states resulting from the plasmon contribution to the hyperbolic dispersion.[493]

The hyperbolic ratio, $\varepsilon'_{x,y}/\varepsilon'_{z}$, is of interest when considering potential NHMs as changes in the ratio (and therefore changes in the magnitudes of $\varepsilon'_{x,y}$ and ε'_{z}) strongly modifies the shape of the hyperbolic dispersion and thus the propagative properties of electromagnetic waves in the material.[494] For investigations into the hyperbolic ratio between the magnitudes of the dielectric-like and metal-like permittivity for hyperbolic modes, the global colour map shows broad red regions for which the hyperbolic modes supported in the ZnO films have hyperbolic ratio values of close or equal to unity. In particular, the $ZnO_{Pl\text{-}like}$ film promises an extremely broad region in which it can support hyperbolic modes whereby the absolute magnitudes of the real permittivity in both optical axes are equal, which may be important for practical hyperbolic material applications. Such hyperbolic modes exhibited by the ZnO films span across much broader spectral regions compared to the same modes in h-BN, and thus promote ZnO to be a potential candidate as an NHM in the mid-IR to THz range. Figure 6.06 also indicates regions in which there are large disparities between the magnitudes of $\varepsilon'_{x,y}$ and ε'_{z} which may be of benefit to certain applications.[440] It is therefore shown that by varying the carrier concentration in ZnO, not only can the spectral range in which the hyperbolic behaviour is supported be modified, but also the hyperbolic ratio and thus shape of the hyperbolic dispersion.

6.8. Theoretical Demonstration of Hyperbolic Modes

To further investigate the potential of ZnO as a NHM material and the effect of phonon-plasmon coupling, hyperbolic field distributions for the ZnO materials developed in this work were simulated using full-vector finite-difference time-domain (FDTD). The FDTD simulations were performed by collaborators at the University of Ioannina. As a benchmark, the dielectric function of a perfect, undoped ZnO crystal with extremely sharp TO phonon absorptions (associated with minimal losses) is obtained from the literature for comparison of the hyperbolic behaviour supported in single crystal ZnO compared to the ZnO materials developed in this work.[495] **Figure 6.07** shows the real, ε', and

imaginary, ε'', permittivity for the ordinary (ε' = black line, ε'' = red line) and extraordinary ((ε' =blue line, ε'' = green line)) axis for the single crystal ZnO material presented in ref[495] used as the literature clean ZnO sample for comparison to the ALD & RFMS samples produced in this work. The permittivity show extremely sharp features due to the well-ordered, sharp, and low loss phonon modes in the undoped, single crystal ZnO material. Two extremely narrow hyperbolic regions are indicated by the blue (Type 1) and grey (Type 2) shaded regions.

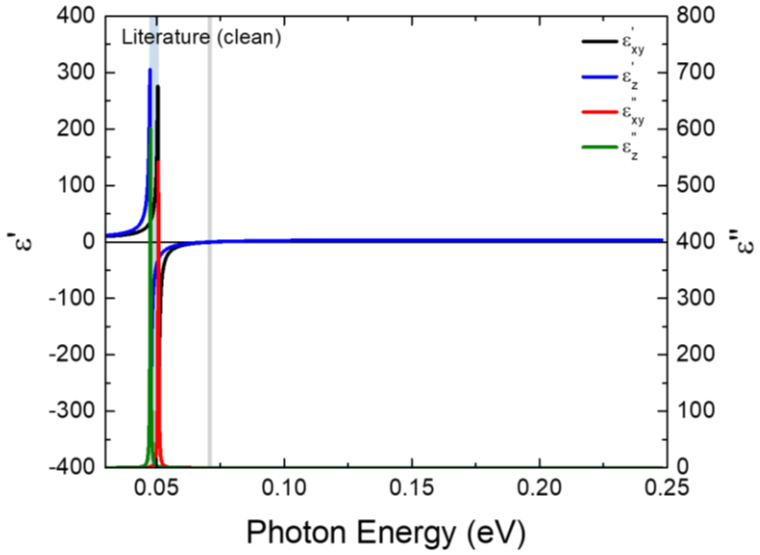

Figure 6.07. *Calculated real, ε', and imaginary, ε'', permittivity for the ordinary (ε' =black-line, ε'' = red-line) and extraordinary ((ε' =blue-line, ε'' = green-line)) axis for the clean single crystal literature ZnO material.*[495] *Type 1 and Type 2 hyperbolic regions are highlighted by the blue and grey shaded regions respectively.*

Principally, three indicative ALD ZnO samples with varying carrier concentrations that fall within the three distinct regimes: phonon-like ($\omega_p = 0.0187$ eV), phonon-plasmon SCR ($\omega_p = 0.0773$ eV), and plasmon-like ($\omega_p = 0.256$ eV) are chosen to compare to the benchmark ZnO from the literature. Attention is focussed on comparing the E-field enhancement and behaviour of the pristine undoped literature ZnO[495] compared to the three ALD ZnO films described above. For each case, two simulations are performed using the FDTD method in a $180 \times 65\ \mu m^2$ computational cell with perfectly matched layer (PML) conditions and a 2 nm/grid resolution in both directions (in-plane and out-of-plane). The light source is a TM-polarized Gaussian beam with a $30\ \mu m$ waist radius and a wavelength range from $13\ to\ 30\ \mu m$. In the first simulation, a suspended $20\ nm$ thick ZnO layer is irradiated, and the field intensity $|Eb|^2$ at the bottom ZnO/Air interface is calculated. In the second simulation, a $10 \times 20\ nm^2$ Au nanorod is placed on top of the ZnO layer to launch propagating modes. The $|En|^2$ is again calculated at the bottom ZnO/Air interface. The electric field enhancement $|En|^2/|Eb|^2$ is recorded for each case and presented in **Figure 6.08**. For the pristine, undoped literature

sample in Figure 6.08(a), three distinct spectral regions can be clearly identified showcasing varying optical behaviours. The first one appears at $17 - 17.4\ \mu m$ where hyperbolic phonon polariton (HPhP) modes are launched with Type 2 behaviour where $\varepsilon_{xy} < 0\ and\ \varepsilon_z > 0$. The second one appears above $17.4\ \mu m$, where surface plasmon emerge since in this spectral range, both the in-plane and the out-of-plane real part of the permittivity is negative $(\varepsilon_{xy} < 0\ and\ \varepsilon_z < 0)$. A third regime manifests at $24.3 - 26.6\ \mu m$ where HPhP modes are launched with Type 1 behaviour where $\varepsilon_{xy} > 0\ and\ \varepsilon_z < 0$. The benchmark sample achieves a maximum field enhancement of 100%, attributed to the well-defined phonon absorption which dominates its optical properties.

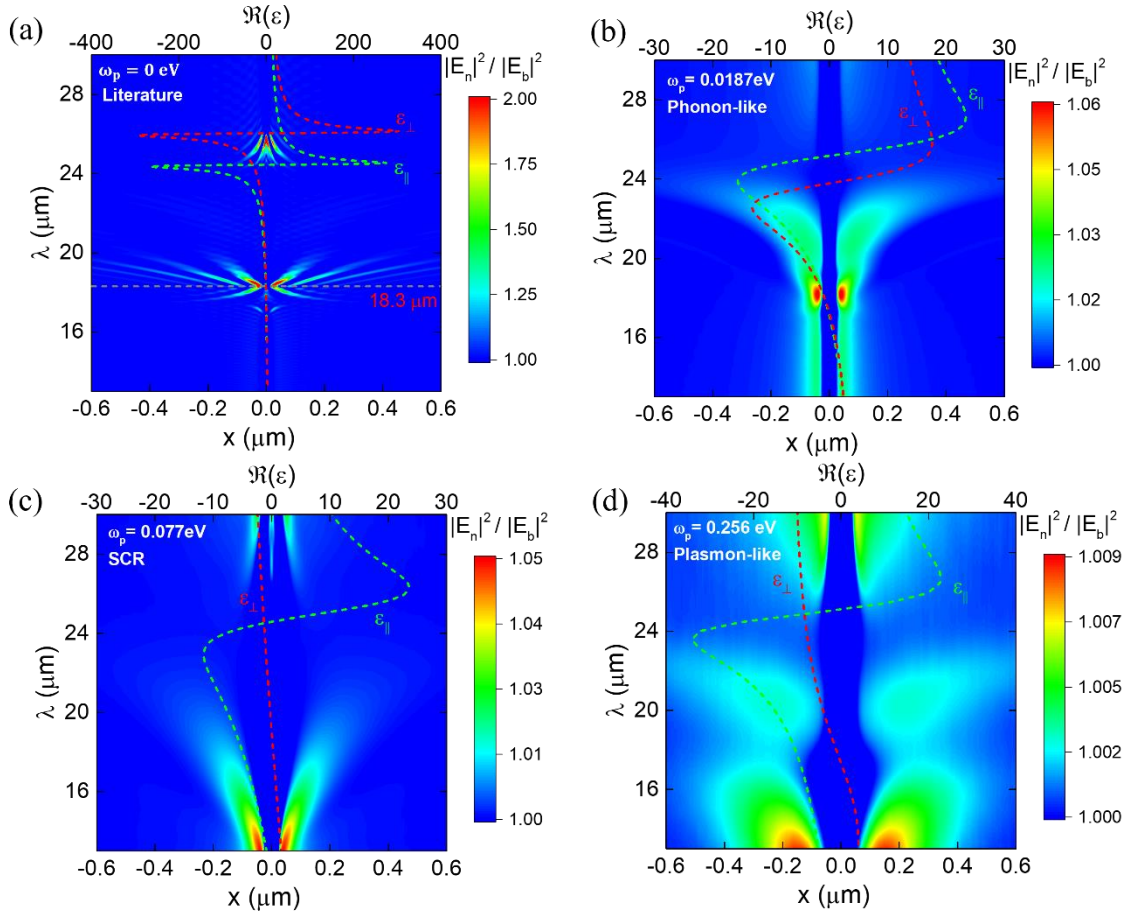

Figure 6.08. *The intensity enhancement at the bottom of the ZnO/Air interface is shown as a function of x-position and wavelength for the (a) pristine literature ZnO, (b) phonon-like, (c), SCR, and (d) plasmon-like ALD ZnO films. The dashed lines represent the real in-plane (green) and real out-of-plane (red) parts of the respective ZnOs permittivity.*

In comparison, for all ALD materials, the higher energy HPhP and plasmonic excitations cannot be distinguished between easily. Additionally, for the lowest ω_p phonon-like ALD material, the lower energy Type 2 hyperbolic modes around $24\ \mu m$ are lost and are unable to propagate due to the low mismatch between the ordinary and extraordinary modes. For the higher ω_p samples in (c) and (d), the

Type 1 hyperbolic modes are recovered and can propagate within the material. Meanwhile, for the sample with $\omega_p = 0.0773$ eV, a large extension to the Type 2 hyperbolic region from $12 - 17.4\ \mu m$ is achieved compared to the pure literature ZnO layer. Whilst good extension to the hyperbolic bandwidth can be achieve through phonon-plasmon coupling with increased doping, maximum field enhancements of ~5 % are achieved for the ALD materials, in comparison to the 100% enhancement for the literature single crystal material. The low field enhancement and broad, ill-defined polaritonic features originate from the high losses associated with the ALD materials. Suppression of these losses should be the focus of future work so that the benefits of the highly tuneable ALD ZnO material can be exploited for NHM applications. Whilst the hyperbolic behaviour demonstrated by the ALD ZnO is seemingly unfavourable compared to the pristine sample, at the time of writing, the FDTD simulations performed for this work were restricted to a reduced wavelength range compared to the full spectrum obtained in the IRSE data. In particular, key information on the long wavelength hyperbolic behaviour may be lost by this restricted simulation range and will be the subject of further exploration.

From the experimental findings above, it was found that the materials presented in the sections above suffered from extremely high material losses, according to the large full width half maximum (FWHM) of the peaks in the $\varepsilon''_{x,y}/\varepsilon''_{z}$ spectra presented in Figure 6.03.A great experimental effort was therefore conducted to try and reduce the losses in the ZnO materials by trying to both improve the crystallinity (to reduce phonon associated losses) and reduce the carrier concentration (to minimise plasmonic losses). A variety of avenues were researched, including the use of Radio Frequency Magnetron Sputtering (RFMS) as an alternate ZnO deposition method, variations in the ALD deposition parameters with focus on purge times to reduce the carrier concentration (as explored in Section 4.1.2), and post growth or post laser processing thermal annealing performed at high temperatures in a conventional furnace oven. From the investigations, two home grown case materials were chosen to be used for the FDTD simulations. The first case was a RFMS ZnO sample with $\omega_p = 0\ eV$ considered to have good crystallinity and little to no free carrier plasmons. IRSE analysis revealed little to no free carriers present in the film and so the material was modelled with a simple TOLO model according to Equation 3.39.

$$\tilde{\varepsilon}_{TOLO}(\omega) = \varepsilon_\infty \left(\frac{\omega_{LO}^2 - \omega_{TO}^2}{\omega_{TO}^2 - \omega^2 - i\gamma\omega} \right) \tag{3.39}$$

The second material was also a RFMS ZnO film thermally annealed for 1 hour at 800 ℃ to try and induce crystallographic improvements for the reduction of losses which gave $\omega_p = 0.0384\ eV$ according to IRSE Kukharskii model fit. The fit parameter results and associated errors from the IRSE model dielectric function fit for each sample are presented in **Table 6.2**. The experimental Ψ (red-line) and Δ (green-line) and best-matched IRSE model calculated Ψ and Δ data (black lines) taken at 70 ° angle of incidence for the Mid-IR spectral range $(0.03 - 0.3$ eV) for the two RFMS samples are shown in **Figure 6.09** (a) $\omega_p = 0\ eV$ and (c) $\omega_p = 0.0384\ eV$. The calculated real, ε', and imaginary, ε'',

permittivity for the ordinary (ε' =black line, ε'' = red line) and extraordinary ((ε' =blue line, ε'' = green line)) axis for both samples are shown in **Figure 6.09** (b) $\omega_p = 0\ eV$ and (d) $\omega_p = 0.0384\ eV$**.**

Table 6.2 IRSE fit parameters for the RFMS samples

ω_p [eV]	0
t [nm]	171.49 ± 2.474
$\varepsilon_{\infty,xy}$	3.561 ± 0.039
$\omega_{TO,xy}$ [eV]	0.0508 ± 0.0006
$\omega_{LO,xy}$ [eV]	0.0722 ± 0.0036
$\gamma_{TO,xy}$ [eV]	0.0039 ± 0.0003
$\gamma_{LO,xy}$ [eV]	0.000 ± 0.008
$\varepsilon_{\infty,xy}$	3.459 ± 0.150
$\omega_{TO,z}$ [eV]	0.0494 ± 0.0054
$\omega_{LO,z}$ [eV]	0.0715 ± 0.005
$\gamma_{TO,z}$ [eV]	0.0034 ± 0.0068
$\gamma_{LO,z}$ [eV]	0.0037 ± 0.0010

ω_p [eV]	0.0384 ± 0.00789
t [nm]	59.17 ± 4.788
ε_{∞}	3.673 ± 0.207
$\omega_{TO,xy}$ [eV]	0.0504 ± 0.0002
$\omega_{LO,xy}$ [eV]	0.0731 ± 0.0003
$\gamma_{TO,xy}$ [eV]	0.00192 ± 0.0003
$\omega_{TO,z}$ [eV]	0.0460 ± 0.0364
$\omega_{LO,z}$ [eV]	0.0645 ± 0.0510
$\gamma_{TO,z}$ [eV]	0.0119 ± 0.162
$\omega_{LPP_{xy}^{-}}$ [eV]	0.02458
$\omega_{LPP_{xy}^{+}}$ [eV]	0.07880
$\gamma_{LPP_{xy}^{-}}$ [eV]	0.0122 ± 0.0405
$\gamma_{LPP_{xy}^{+}}$ [eV]	0.00861 ± 0.05319
$\omega_{LPP_{z}^{-}}$ [eV]	0.03058
$\omega_{LPP_{z}^{+}}$ [eV]	0.07086
$\gamma_{LPP_{z}^{-}}$ [eV]	0.0306 ± 0.187
$\gamma_{LPP_{z}^{+}}$ [eV]	0.00545 ± 0.0007
γ_p [eV]	0.00865 ± 0.102

Upon comparison of the dielectric function, the $\omega_p = 0.0384\ eV$ film was found to have sharper TO phonon absorption with reduced bandwidth compared to the $\omega_p = 0\ eV$ sample suggesting better crystallinity was achieved after the high temperature thermal anneal. Meanwhile, the benchmark literature ZnO sample is a perfect crystal with extremely sharp TO phonon absorptions associated with minimal losses. Thus, the literature ZnO has the lowest losses of all three samples, whilst $\omega_p = 0.0384\ eV$ suffers intermediate losses, and $\omega_p = 0\ eV$ is associated with the largest losses of the three cases according to the absorption peaks in the dielectric function spectra.

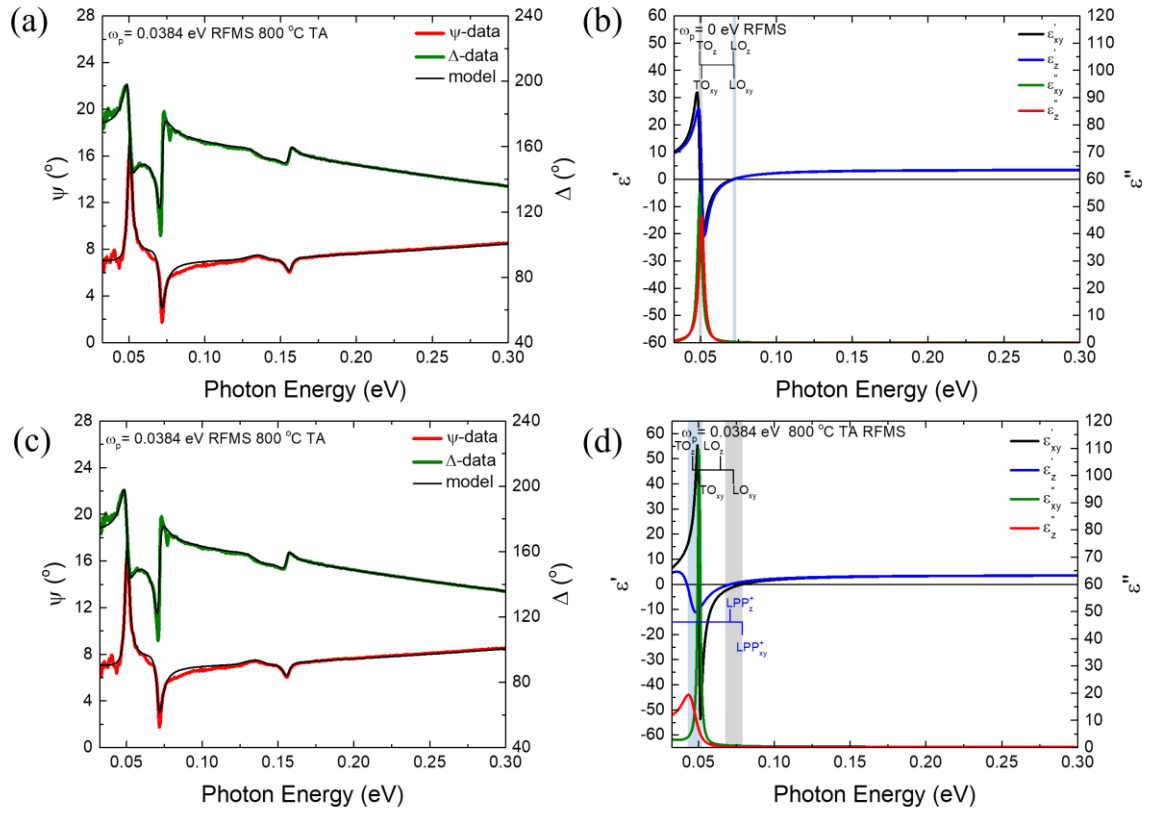

Figure 6.09. *IRSE measurement and analysis for two RFMS ZnO samples. Experimental (red line) and best-matched model calculated (black line) Ψ-data for the: (a) as grown $\omega_p = 0\ eV$ sample and (b) thermally annealed sample with $\omega_p = 0.0384\ eV$ sample. The calculated real permittivity for the ordinary (black-line) and extraordinary (blue-line) axis: (c) as grown $\omega_p = 0\ eV$ sample and (b) thermally annealed sample with $\omega_p = 0.0384\ eV$. The spectral bands in which Type 1 and Type 2 hyperbolicity can be supported are highlighted by the blue and grey shaded regions respectively.*

To explore the optical behaviour and hyperbolic character of the ALD grown ZnO films, full-vector finite-difference time-domain (FDTD) simulations are employed assuming a TM-polarized plane wave source and a thin layer of ZnO material of variable thickness (**Figure 6.10**). At first, attention is focussed on the absorption as the thickness of a suspended ZnO layer is increased. All three types of ZnO achieve

maximum single-pass absorption of 50% (maximum single-pass absorption of a thin absorbing layer in air) at different thicknesses. This is achieved due to resonant excitation of the in-plane TO ZnO phonon, as evident from the absorption peaks' spectral position, which matches the ω_0 resonant frequency of the TO phonon at ~ 24 μm (~0.05 eV).

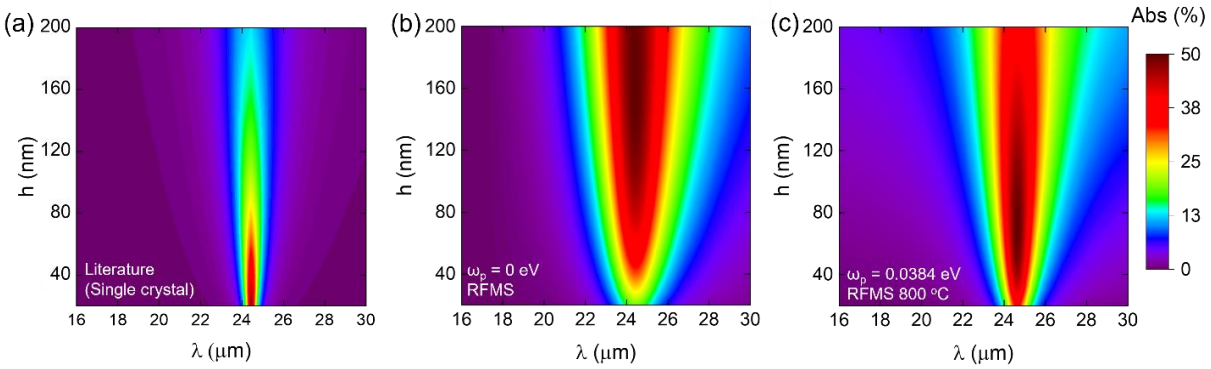

Figure 6.10 *Absorption of (a) suspended literature (b) as grown RFMS $\omega_p = 0$ eV and (c) thermally annealed RFMS $\omega_p = 0.0384$ eV ZnO thin films as a function of wavelength and thin film thickness h.*

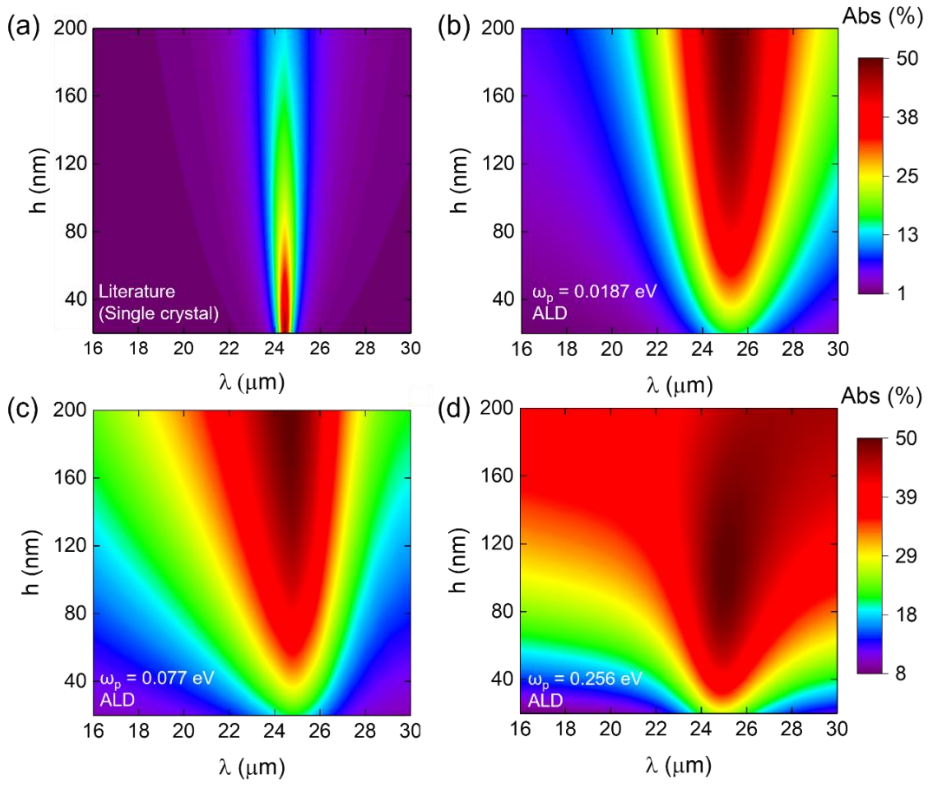

Figure 6.11 *Absorption of (a) suspended literature (b) ALD phonon-like $\omega_p = 0.0187$ eV (c) ALD SCR $\omega_p = 0.077$ eV and (d) ALD plasmon-like $\omega_p = 0.256$ eV ZnO thin films as a function of wavelength and thin film thickness h.*

The FWHM of the absorption spectra and the thickness (h) of the ZnO layer, where the maximum absorption is achieved, are directly linked with the phonon resonance Q-factor as depicted in the in-

plane ($\varepsilon||$) part of the ZnO permittivity. Indeed, resonators with higher *Q*-factor have higher absorption at much smaller critical thickness.[460] A reduction in the critical thickness for the annealed RFMS material versus the as grown RFMS film indicates the reduced loss and improved quality induced by the annealing process. For comparison, the absorption as the thickness of a suspended ZnO layer is increased is presented in **Figure 6.11** for the ALD materials presented in Figure 6.6 above. For all cases, the ZnO achieve maximum single-pass absorption of 50%. The phonon absorptions show increased bandwidths compared to the clean literature sample due to the high losses associated with the phononic and plasmonic absorptions in the ALD materials. All ALD materials show increased critical thickness compared to the literature sample indicating the reduced Q-factor of the phonon resonance I these materials. Whilst a minor reduction in critical thickness is observed for the $\omega_p = 0.256\ eV$ sample, it is accompanied by an increased bandwidth and therefore is still associated with high material losses. The high losses in the ALD materials explain the reduced E-field enhancement achieved for these materials versus the literature material.

To further explore this optical behaviour of the RFMS ZnO layers, attention is turned to comparing the E-field enhancement and behaviour of the pristine undoped literature ZnO[495] and the $\omega_p = 0\ eV$ and $\omega_p = 0.0384\ eV$ samples developed in this work. For each case, two simulations are performed using the FDTD method in a $180 \times 65\ \mu m^2$ computational cell with perfectly matched layer (PML) conditions and a 2 nm/grid resolution in both directions (in-plane and out-of-plane). The light source is a TM-polarized Gaussian beam with a $30\ \mu m$ waist radius and a wavelength range from $13\ to\ 30\ \mu m$. In the first simulation, a suspended $20\ nm$ thick ZnO layer is irradiated, and the field intensity $|Eb|^2$ at the bottom ZnO/Air interface is calculated. In the second simulation, a $10 \times 20\ nm^2$ Au nanorod is placed on top of the ZnO layer to launch propagating modes. The $|En|^2$ is again calculated at the bottom ZnO/Air interface. The electric field enhancement $|En|^2/|Eb|^2$ is recorded for each case and presented in **Figure 6.12**. The E-field behaviour of the literature sample is discussed in the main manuscript. For the two RFMS samples, different E-field enhancement behaviour is observed between the two cases. For the as grown RFMS sample with $\omega_p = 0\ eV$, only one clear field enhancement region can be identified around the plasmonic region at $17.9 - 20.1\ \mu m$, regions in which the dielectric function suggest hyperbolic modes should exist do not appear for the as grown RFMS sample. This may be understood due to the small mismatch in magnitude between ordinary and extraordinary modes and moderate material losses which do not allow for hyperbolic mode propagation in this material. For the annealed case, all three spectral regions are recovered for the $\omega_p = 0.0384\ eV$ sample. The first one appears at $15.6 - 17.6\ \mu m$ where hyperbolic phonon polariton (HPhP) modes are launched with $\varepsilon|| < 0\ and\ \varepsilon\perp > 0$. The second one appears above $17.6\ \mu m$, where surface plasmon modes are excited as in this spectral range, both the in-plane and the out-of-plane real part of the permittivity is negative ($\varepsilon|| < 0\ and\ \varepsilon\perp < 0$). The third one manifests at $24.5 - 28.8\ \mu m$ where HPhP modes are launched

with $\varepsilon|| > 0\ and\ \varepsilon\perp < 0$. Compared to the best ALD sample case at the strong coupling resonance condition with $\omega_p = 0.077\ eV$, the spectral region at which highest field enhancement occurs is larger for the annealed RFMS material occurring in both the hyperbolic regions and plasmonic region.

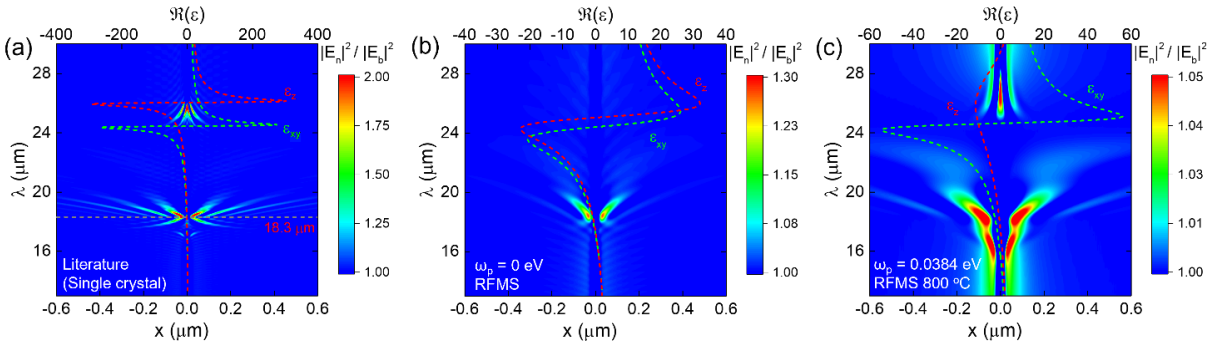

Figure 6.12. *The intensity enhancement at the bottom of the ZnO/Air interface is shown as a function of x-position and wavelength for the (a) pristine literature ZnO, (b) as grown RFMS $\omega_p = 0\ eV$ and (c) thermally annealed RFMS $\omega_p = 0.0384\ eV$, SCR, and (d) plasmon-like ALD ZnO films. The dashed lines represent the real in-plane (green) and real out-of-plane (red) parts of the respective ZnO permittivity.*

The annealed RFMS sample also shows enhanced epsilon near zero (ENZ) behaviour which may be of interest for future work. Overall, the annealed RFMS sample displays enhanced hyperbolic behaviour compared to the ALD films and should be considered for future investigations.

6.9. Chapter Summary

This chapter presented the results of investigations into the IR optical properties of some of the ALD ZnO films developed in this work. The anisotropic Kukharskii model was found to provide a suitable model to accurately describe the lineshape of IRSE measurement spectra in the mid-IR range between 0.03-0.3 eV, and the resultant real and imaginary parts of the permittivity were investigated. It was shown that the ZnO materials investigated in this chapter had two distinct spectral regions in which the hyperbolic criterion was upheld. Moreover, it was shown how the Mid-IR hyperbolic bandwidth in ZnO can be tuned and extended across three different material regimes according to their plasma energy: phonon-like, phonon-plasmon strong coupling, and plasmon-like, where variations in ω_p achieved *via* modifying the carrier concentration of ALD ZnO films *via* various deposition parameters or post processing. Thus, three different hyperbolic polaritons may exist in ZnO across the three different material regimes. Investigations into the hyperbolic bands revealed that ZnO can harness both Type 1 and Type 2 hyperbolic behaviour in separate spectral bandwidths spanning a broad range of energies in the mid-IR, potentially extending to even lower energies beyond the measurement range possible in this work, opening further opportunities to explore the hyperbolic phenomena and its applications deeper into the IR range. An interesting topological transition from Type 2 to Type 1 hyperbolic behaviour was

observed for the lower spectrum hyperbolic band when the materials plasma energy was tuned from the phonon-like regime into the SCR regime. To investigate the potential of ZnO materials to support hyperbolic modes, the hyperbolic field distributions were explored. The E-field enhancement of the hyperbolic and plasmonic modes in the ALD ZnO materials were explored and compared to a clean, single crystal ZnO material. Whilst the extension to the hyperbolic regions is evident in the ALD materials, maximum field enhancements of only ~ 5 % can be achieved for the ALD materials due to the high level of losses associated with the broad phonon modes and metallic losses from the plasmonic excitations. An initial study with focus on reducing the losses in the ALD materials or by investigating alternate ZnO deposition routes such as RFMS was presented, demonstrating beneficial improvements to the hyperbolic character for the RFMS ZnO materials. These initial studies into reducing the losses in the ZnO material revealed a promising direction for future work. Indeed, once the material losses are addressed, the competitive hyperbolic properties of ZnO presented in this research, alongside many other desirable qualities associated with ZnO as a well-established technological material could bring ZnO to the forefront of research into NHMs in the IR-THz regime, their fundamentals, and their practical realisation in a wide range of nanophotonic applications.

7. Conclusions and Future Perspectives

7.1. Conclusions

The main conclusion of this research is that performing laser annealing in a controlled high pressure N_2 environment can induce N related acceptor type doping in ALD ZnO. Moreover, the controlled environment excimer laser doping (CEELD) approach has been proven to be an effective ultra-fast, low thermal budget and highly selective one-step fabrication route to ultra-shallow doping and p-n junction formation ($< 100\ nm$) in ZnO, capable of laser printing both lateral and laterally printed vertical p-n junctions for a new approach to device printing in ZnO.

In Chapter 4, the development of the seed n-type and p-type ALD ZnO materials was presented. Initially the effect of ALD growth parameters on the electrical properties of the as deposited seed n-type ZnO materials was investigated. Chiefly, the deposition temperature, precursor purge time, and pressure of purge gas flowing through the system during the dynamic deposition process were all found to influence the ALD surface reactions which induced changes to the properties of the ZnO materials. Electrical characterisation of the as deposited materials revealed that the above deposition parameters can be precisely controlled to viably manipulate the electrical properties of the ZnO thin films. ZnO materials with high n-type carrier concentration were obtained and hydrogen was identified as the most probable shallow n-type dopant in the ZnO materials. The high level of background impurity hydrogen was proposed to arise from the high concentration of $O-H$ and $C-H$ groups present during the growth process originating from the DEZ and H_2O precursors. It was proposed that at low temperatures, interstitial hydrogen, H_i, is more stable at lower growth temperatures of around $150-160$ ℃, contributing to a high electron concentration and reduced resistivity. At higher deposition temperatures, it was proposed that hydrogen becomes more mobile during the growth process and is either promoted to substitutional O sites, H_O, which may be misinterpreted for V_OO, or more H_i is proposed to diffuse out of the films at the higher temperatures, reducing the n-type carrier concentration. The chapter then explored the potential of a novel CEELD process to achieve N-acceptor doping in ZnO. Results from Hall Effect measurements revealed that conversion to p-type material occurs after laser processing the seed n-ZnO material with 1 and 2 laser pulses delivered at a laser fluence of $200\ mJcm^{-2}$ performed in a high-pressure N_2 containing environment. This CEELD process was able to induce a high level of p-type carrier concentration in ZnO that remained stable over an extended period. The dependence of the CEELD process on the starting material and laser environment were also found to have an impact on the CEELD process. Verification of the N incorporation into the ZnO films *via* the CEELD process was achieved *via* ToF-SIMS measurements that revealed N incorporation mainly through CN^-, CNO^-, NO^-, and NO_2^- ions. The results from the ToF-SIMS investigation supported the earlier hypothesis that N may be readily incorporated into the ALD ZnO thin films through co-doping with high level of background impurity H present in the seed n-ZnO material. The

H was proposed to be incorporated at interstitial sites in $O-H$ and $C-H$ bonds, which is supported by the N-related ions identified by ToF-SIMS that shows N incorporation at sites where H may have existed. Upon laser processing, the N in the processing environment is proposed to photo-dissociate *via* the high energy laser photons, where it is then incorporated at the sample surface and subsequently diffuses throughout the ZnO film where it may readily bond to the H sites. Residual energy from the laser processing is then able to break the $N-H$ bond in the film and the H is then able to thermally diffuse out of the film to activate the N as a shallow acceptor. Further support to the $N-H$ co-doping hypothesis is achieved *via* laser processing in an NH_3 environment, that induces a higher level of N-related ions in the film which is assigned to the replenishment of H into the film due to the presence of H in the annealing atmosphere. The ToF-SIMS results also suggest some N gradient throughout the films. This was proposed to be because of the surface limited CEELD process. Further verification of acceptor type doping beyond the Hall Effect was then sought through the development of simple electronic energy band diagrams using the results of ORS, VB XPS and KPFM measurements. Results from ORS suggested an optical bandgap range between $3.27-3.41\ eV$ for the seed n-type and p-type materials, indicating the potential of the ZnO materials for near-UV applications. The position of the valence band maximum with respect to the Fermi level was found to vary throughout the depth of the laser processed films, with a clear change in VBM position between a depth of $20-40\ nm$ in the films. This supports the N gradient observed for the 1 pulse CEELD sample which may induce the change in acceptor concentration throughout the depth of the film. A change in VBM was also observed at the same depth for the 2 pulse CEELD sample, despite little observable gradient in N ion concentration in ToF-SIMS. It was suggested that the depth of acceptor type doping is also dependent on the out diffusion of H from the film, that would be greater at the upper layers of the CEELD samples, and therefore only the top surface N acceptors are activated for p-type conduction through reduction of H passivation. Results investigating the position of the Fermi level within the bandgap showed the indicative downward shift of the E_f towards the valence band for acceptor doping. However, the E_f was found to reside above the mid-gap point, possibly due to passivation effects of contamination (H) over the extended storage period. An improved measurement set is proposed involving UPS for both VBM and work function and ORS for E_g to be measured across the same sample sets and should be considered for future work to improve the reliability of the EBD investigation. Finally, it was found that IRSE could be used as an indicative method to distinguish between different carrier type films in ZnO through observing changes in the broadening behaviour of the phonon-plasmon coupled modes and the plasma broadening parameter, according to the different mass and mobility of the electron versus hole plasmons. The CEELD process was therefore presented as method to induce N-acceptor type doping in ALD ZnO. However, the scepticism surrounding the reliability of the Hall Effect measurement technique and concerns arising from the E_f EBD investigation implied the need for further confirmation of p-type conduction.

Chapter 5 presented the results of the implementation of the seed n- and p-type ZnO materials into simple devices. Initially, the development of Ohmic contacts to both n- and p-type materials was investigated. It was found that using a metallisation scheme involving the sputter deposition of gold metallic contacts subsequently treated with a 1 minute thermal anneal at 200^oC under vacuum produced Ohmic contact to both n- and p-type materials. The Ohmic contact metallisation scheme was then incorporated into fabrication of simple p-n homojunction devices. Initially, lateral devices were investigated, followed by an investigation into the ability of the CEELD process to induce an ultra-shallow vertical p-n homojunction due to the expected $20 - 40\ nm$ depth of p-type material out of an entire ZnO depth of $80\ nm$. The two different p-n junction device architectures showed clear rectifying I-V characteristics, indicating diode-like behaviour. Moreover, upon comparison with the I-V results across the p-n junction versus the metal contacts for the n- and p-type materials, clear differences could be observed in the low voltage regime, and it was therefore concluded the I-V behaviour was dominated by transport at the p-n junction and not at the contacts, thus verifying the existence of the p-material. Simple photodiode tests also confirmed the presence of a p-n junction by achieving characteristic photodiode I-V behaviour under reverse bias, and therefore showed the potential of the p-n junction devices developed in this work for photovoltaic applications. The seed materials and metallic contacts were then used to fabricate TFT devices. The clear difference in on-switching polarity in the transfer behaviour was shown between the n-type and p-type seed materials, further indicating the change in dominant carrier type between the materials. The work in this chapter therefore supported the claim that performing CEELD in N_2 ambient could induce p-type doping in ZnO. Moreover, the ability of CEELD to fabricate ultra-shallow vertical p-n ZnO homojunctions that can be laterally printed was demonstrated. Thus, CEELD is presented as an effective, ultra-fast, low thermal budget and highly selective technique to both induce N-related p-type doping in ZnO to depths less than $40\ nm$, and fabricate ultra-shallow p-n junctions that can be vertically and laterally printed in a novel one-step method that is viable for industrial applications.

Chapter 6 built upon the work undertaken in Chapter 4 concerning the analysis of IRSE spectra to investigate the phononic and plasmonic properties of ZnO. The chapter presented the results of investigations into the IR optical properties of some of the n-type ALD ZnO films developed in this work whose plasma energy (n-type dopant concentration) was tuned over a broad range between $0.0187\ eV \leq \omega_p \leq 0.256\ eV$ *via* variations in the sample deposition and post processing parameters. The anisotropic Kukharskii model was found to provide a suitable model to accurately describe the lineshape of IRSE measurement spectra in the mid-IR range between $0.03 - 0.3\ eV$, and the resultant real and imaginary parts of the permittivity were investigated. It was shown that the ZnO materials investigated in Chapter 6 could uphold the hyperbolic criterion, $\varepsilon'_{x,y}\varepsilon'_z < 0$, in two distinct spectral regions. Moreover, it was shown how the Mid-IR hyperbolic bandwidth in ZnO can be tuned and extended across three different material regimes according to their plasma energy: phonon-like,

phonon-plasmon strong coupling, and plasmon-like. Thus, the potential existence of three different hyperbolic polaritons across the three different material regimes were proposed. Investigations into the hyperbolic bands revealed that ZnO can harness both Type 1 and Type 2 hyperbolic behaviour in separate spectral bandwidths spanning a broad range of energies in the mid-IR. In some cases, the hyperbolic bandwidth was limited at the low energy limits of the spectral range possible in this work, as such the hyperbolic behaviour is expected to extend to even lower energies, opening further opportunities to explore the hyperbolic phenomena and its applications deeper into the IR. An interesting topological transition from Type 2 to Type 1 hyperbolic behaviour was observed for the lower spectrum hyperbolic band when the materials plasma energy was tuned from the phonon-like regime into the SCR regime. To investigate the potential of ZnO materials to support hyperbolic modes, the hyperbolic field distributions were explored by FDTD. It was found that, whilst beneficial in terms of bandwidth tuneability, the plasmonic losses associated with the phonon-plasmon modes were unfavourable to support hyperbolic dispersion, and future work should focus on trying to minimise these plasmonic losses whilst maintaining an element of tuneability before ALD ZnO can be presented as viable low-cost NHM candidate with tuneable hyperbolic character for nanophotonic applications in the mid-IR regime.

7.2. Future Perspectives

The research undertaken in this Ph.D. program, like many other Ph.D. programs before, has led to further new research questions, experiments, and potential avenues for future investigations. Some perspectives for future work are outlined below.

1. Further extrinsic doping of N acceptors may be performed during the ALD process by incorporating pulses of a N containing gas such as NH_3 during the growth process. The delta doping achieved by introducing a secondary ALD cycle may introduce complications in the growth process due to changes in the surface states available for the ideal surface reactions. This may result in less than one-monolayer of growth per cycle, inhomogeneous doping/ ineffective doping, or the formation of a ‘multi-layer’ structure. Various ALD experimental parameters should be investigated to optimise the growth of such N doped films. A post processing step such as excimer laser annealing may be performed to improve the distribution of dopants by the addition of thermal energy for atomic rearrangement. Moreover, the probe of defects or introduction of further O or N to the film may be achieved by performing the CEELD process in various environments for defect engineering.
2. As mentioned in section 2.2.4, Na is a potential acceptor type dopant in ZnO that upon efficient incorporation should substitute on Zn sites in the lattice to induce acceptor type doping. Reports of Na doping in the literature report low solubilities and ineffective incorporation. Previous studies of excimer laser annealing to promote donor dopants such as Al onto preferential substitutions lattice sites in ZnO and increase effective incorporation may also be a transferable technique to activate

group I acceptors onto the Zn site for acceptor doping in ZnO. Na may be introduced during the ALD growth process by an aqueous Na solution and then activated into preferential substitutional sites upon laser annealing. The Na acceptor may also benefit from a co-doping mechanism with the background impurity hydrogen in the ALD films for enhanced solubility. Note the incorporation of a Na precursor pulse during the deposition would pose the same potential issues reported in point (1.) above.

3. Band gap engineering through alloying. An attractive quality of ZnO is its ability to undergo band gap engineering for targeting various device applications (including full spectrum UV LEDs) by alloying with materials such as MgO ($E_g = 7.8eV$), BeO ($E_g = 10.6eV$) or CdO ($E_g = 2.2eV$). The ALD deposition methods can produce alloyed, ternary, or quaternary materials which would provide a route to alloying the ZnO materials developed in this work. Moreover, following the alloying process, post deposition laser annealing could be performed to improve the alloyed material properties by proving thermal energy for atomic rearrangement. Furthermore, investigations into the CEELD approach for acceptor type doping in the alloyed materials for p-type doping in even wider band gap materials would be of increase interest for the development of p-n junction-based devices operating deeper into the UV spectrum.
4. Extra expertise and evaluation/ analysis of XPS data with particular focus on the Zn and O peaks (since XPS results of the materials in this work were not sensitive to the low N concentration) to observe any changes in the deconvoluted peak energies to assess changes in the types of Zn and O bonds formed for the as grown and 1 and 2 pulse at $200\ mJcm^{-2}$ lasered samples. Further analysis of these XPS peaks may therefore reveal the presence of H or C related bonds to Zn and O, or any potential $Zn-N$/ $O-N$ bonds or bonds involving C and H (for supporting information to the ToF-SIMS results) to further understand the defect chemistry in the films studied in this work. Further XPS studies would also be desirable for the ammonia laser doped samples which ToF-SIMS revealed a much higher concentration of N ions.
5. Improved investigations into the construction of energy band diagrams to observe shifts in the Fermi level are also highly desirable. The first attempts included several inconsistencies including measurements on three different sample sets of different ages and non-controlled storage conditions. All of which may have influenced the results of the measurement and reduce the confidence in the results. Furthermore, repeat measurements on the full 7 sample set including the as grown and 1 and 2 pulse at $200\ mJcm^{-2}$ samples processed in Ar, N_2 and NH_3, and using Ultraviolet Photoelectron Spectroscopy for both measurement of the valence band and material work function, plus ORS on the same set of materials, would provide a clearer picture by a more robust and reliable method.
6. Further investigations into the N diffusion depth/ acceptor activation depth and further laser processing parameters investigations to try and tune the depth which is converted to p-type would

also be of interest and benefit for the tailoring of the material for various applications which may require different dimensions/depth of p-type material.

7. ALD and CEELD approach on nanostructured devices. One of the many benefits of ALD is its high conformality for producing high quality material layers on more complex geometries/ substrate topographies. The ever-growing need for more complex device geometries and the many advantages offered by nanostructured devices make applying the ALD ZnO plus CEELD process on nanostructured substrates an attractive route for investigation. Complications may arise during the laser photon absorption from a shadowing effect on more complicated surfaces depending on the scale of the nanostructure dimensions.
8. Implementation of the CEELD approach to ZnO materials deposited by techniques other than ALD. Of interest may be investigations into the dual laser induced action of photo-conversion of sol-gel ZnO organometallic precursors in thin films performed in a N ambient to induce N acceptors into the film during the conversion process for efficient incorporation. Investigating the CEELD process for the doping of other materials (potentially requiring different gaseous environments than those investigated in this work depending on the material to be processed and its relevant dopant atoms) would help to further cement the CEELD process in the field and support its development for use in industry.
9. Cryogenic photoluminescent measurements to assess the exciton bound states and help to identify donor/ acceptor species/ bound excitons alongside defect states in the materials.
10. Low temperature Hall Effect measurements to assess how the doping changes with temperature and identification of defect dominant conduction. Other device architectures for improved Hall Effect measurement reliability may also be considered including cross/ clover shapes.
11. Investigation of the ZnO diodes developed in this work for high power electronics. The p-n junction devices presented in this thesis were pushed to the equipment power limits, supplying in excess of $\pm 150\ V$ without observation of device failure/ breakdown, suggesting the potential of these devices for high power devices. Future work should further these initial investigations to present the potential of the CEELD produced p-n junction devices for high power electronic applications to rival SiC and GaN. Combined with the ultrafast, low thermal budget and ultra-shallow doping of the CEELD homojunction fabrication method could promote ZnO and the CEELD process as a new advantageous material system for laterally printed power devices below $100\ nm$.
12. The results of the electrical characterisation of the p-n junctions fabricated in this work were shown exhibit photoconductive properties when the junction is measured as a diode under white light illumination. The below outlined experiments are proposed to explore and expand upon the results presented in this thesis to further investigate the photoconductivity of the ZnO based devices and their potential for photodiode applications. The following experiments were informed by the work done by Baugher *et al* in 'Optoelectronic devices based on electrically tuneable p-n diodes in a monolayer dichalcogenide'. [496]

- The first proposed experiment is based upon 'scanning photocurrent microscopy', whereby the current is measured as a laser spot is scanned over the sample (photons impinging on the junction create electron-hole pairs, which are separated to opposite contacts by the electric field at the junction, generating a photocurrent. The beam is scanned over the sample measuring the current at $0\ V$ bias, yielding a spatial map of the photoresponse of the device. If upon analysis, the photocurrent generated is centred around the expected junction, it will demonstrate that the photoresponse is dominated by the p-n junction and not any Schottky barriers formed at the contacts. Propose to use broad spectrum white light focussed to a smaller spot and scan across the lateral p-n junction devices investigated in this work. Measured light reflected from the sample maybe of interest also.
- To obtain spectrally resolved photocurrent, the current can be measured as a function of excitation wavelength at constant light intensity. Any peaks observed in the spectrally resolved photocurrent should match well with photoluminescence, differential reflectance, and optical absorption spectroscopy results. From this exercise, the efficiency of light conversion into current can be quantified by extracting the external quantum efficiency, EQE, at a constant laser power as a function of wavelength by $EQE = \left(\frac{I}{P_{light}}\right)\left(\frac{hc}{e\lambda}\right)$, where P_{light} is the power of the laser and all other symbols have their usual meanings.
- To test the photovoltaic power generation capability of the devices in this work, the current as a function of applied voltage at various laser powers/ light intensities (at a filtered wavelength informed by the spectrally resolved photocurrent experiment above) can be investigated. Baugher *et al* use various laser powers from a supercontinuum white light source bandpass filtered at a certain fixed wavelength.[496] The photocurrent $I_{ph} = I_{light} - I_{dark}$, at certain voltage plotted for each laser power can be linearly fit, from which the slope gives the responsivity of the device in AW^{-1}, which could then be compared to literature values of other reported devices.

Results of the above three outlined experiments will provide further verification of the presence of a p-n junction (and thus p-material) and its potential for use in photovoltaic applications.

13. Capacitance-Voltage profiling of the p-n junctions produced in this work to probe a variety of internal characteristics of the p-n and the constituent materials. The measurements would rely upon and exploit the capacitor-like behaviour of the p-n junction depletion region to perform a variety of Capacitance measurements including C-V, Capacitance-frequency, and forward bias C-V measurements to reveal information on the doping profile and active defect states and density as well as categorising the type of junction formed (linear, abrupt, graded) by varying the depletion width of the junction. Such measurements would provide further details on the CEELD doping mechanism/acceptor diffusion and the defects formed, as well as the type of junction formed by the CEELD process.

14. Optimisation LED emission and investigations

    Whilst no visible electroluminescence was observed for the p-n junctions in this work, it would be desirable for future work to undertake an electroluminescence study on a variety of the CEELD materials developed, including the optimisation of certain devices characteristics/ design for improved internal/ extraction efficiencies. Methods for improving the electroluminescent properties were discussed in Chapter 5, Section 5.2.2, and are important for the implementation of the materials for UV LED applications.

15. Optimised TFT investigations. The TFTs developed in this work were not optimised in terms of device architecture in order to reduce the uncertainties that may arise by changing the device structure for the laser doping process. However, to fully test the potential of the materials developed in this work for TFT applications, better optimisation of the device structure should be made including the thickness of the dielectric layer and the metallic contacts.

16. Optimisation of ZnO thin film properties to reduce losses for improved NHM performance. Upon comparison with the NHMs in the literature, the ZnO materials in this work suffer high losses (as indicated by the imaginary permittivity) which may indicate inferior NHM behaviour due to too large absorptions in the material. Therefore, efforts into trying to reduce the phonon-plasmon associated losses should be undertaken, potentially by further annealing studies or optimisation of the deposition process to produce highly crystalline films. However, such optimisation may ultimately lead to a reduction in free carrier plasmons and so the superior tuning properties of the hyperbolic bandwidth *via* phonon-plasmon coupling in ZnO may be lost.

17. Further investigations into the development of IRSE as an indicative method for carrier type determination in the ZnO materials developed in this work should be performed using multilayer analysis to address the potential inhomogeneity throughout the depth of the laser processed films. Whilst initial model analysis suggested limited Mean Squared Error improvement by adding inhomogeneities into the model, a more accurate picture may be developed by modelling the material as a double layer structure. This would add extra complications to the Kukharskii model developed and used in this work for IRSE analysis which would need to be investigated to reduce correlation in the model. Moreover, to gain a more physical representation of each film via the IRSE geometric model, further characterisation of all the films developed would be needed to assess the potential bilayers, since it is expected that for films processed with more laser pulses/ at higher fluence may produce more uniform doping throughout the depth of the film which would need to be taken into consideration for the model.

8. References

[1] M. Grundmann, F. Klüpfel, R. Karsthof, P. Schlupp, F. L. Schein, D. Splith, C. Yang, S. Bitter, H. Von Wenckstern, *J. Phys. D. Appl. Phys.* **2016**, *49*, DOI: 10.1088/0022-3727/49/21/213001.

[2] M. Ozgür, D. Hofstetter, H. Morkoç, *Proc. IEEE* **2010**, *98*, 1255.

[3] D. K. Hwang, M. S. Oh, J. H. Lim, S. J. Park, *J. Phys. D. Appl. Phys.* **2007**, *40*, DOI: 10.1088/0022-3727/40/22/R01.

[4] Y. S. Choi, J. W. Kang, D. K. Hwang, S. J. Park, *IEEE Trans. Electron Devices* **2010**, *57*, 26.

[5] F. Rahman, *Opt. Eng.* **2019**, *58*, 1.

[6] T. D. Moustakas, R. Paiella, **2017**.

[7] D. W. Runton, B. Trabert, **2013**, 82.

[8] S. Nakamura, M. R. Krames, *Proc. IEEE* **2013**, *101*, 2211.

[9] A. Liu, P. Tu, C. Langpoklakpam, Y. Huang, Y. Chang, A. Tzou, L. Hsu, C. Lin, H. Kuo, E. Y. Chang, **2021**.

[10] D. K. Sharma, S. Shukla, K. K. Sharma, V. Kumar, *Mater. Today Proc.* **2020**, *49*, 3028.

[11] Y. Ryu, T. S. Lee, J. A. Lubguban, H. W. White, B. J. Kim, Y. S. Park, C. J. Youn, *Appl. Phys. Lett.* **2006**, *88*, 86.

[12] J. Cho, J. H. Park, J. K. Kim, E. F. Schubert, *Laser Photonics Rev.* **2017**, *11*, DOI: 10.1002/lpor.201600147.

[13] A. Baltakesmez, **2011**, *054502*, DOI: 10.1063/1.3627247.

[14] J. Zhang, W. Guo, B. Xie, X. Yu, X. Luo, T. Zhang, Z. Yu, H. Wang, X. Jin, *Opt. Laser Technol.* **2017**, *94*, 193.

[15] K. Song, M. Mohseni, F. Taghipour, *Water Res.* **2016**, *94*, 341.

[16] Y. Nagasawa, A. Hirano, *Appl. Sci.* **2018**, *8*, 1264.

[17] G. Tamulaitis, **2011**, *51*, 177.

[18] M. S. Shur, R. Gaska, *IEEE Trans. Electron Devices* **2010**, *57*, 12.

[19] R. Gaska, M. S. Shur, J. Zhang, *ICSICT-2006 2006 8th Int. Conf. Solid-State Integr. Circuit Technol. Proc.* **2007**, 842.

[20] J. Han, H. Amano, L. Schowalter, *Semicond. Sci. Technol.* **2014**, *29*, 32.

[21] M. Nakamura, Shuji; Mukai, Takashi; Senoh, *Jpn. J. Appl. Phys.* **1991**, *30*, 1998.

[22] T. D. Moustakas, R. J. Molnar, *MRS Proc.* **1992**, *281*, 753.

[23] J. C. Fan, S. L. Chang, Z. Xie, **2013**, DOI: 10.5772/51181.

[24] M. Benhaliliba, *Optik (Stuttg).* **2021**, *241*, 167197.

[25] P. Sharma, M. Rahil, N. Kumar, A. Bishoyi, J. Narang, *Sensors Int.* **2023**, *3*, 100182.

[26] T. Hanada, **2009**, 1.

[27] F. Rahman, **2023**, *58*, DOI: 10.1117/1.OE.58.1.010901.

[28] Ü. Özgür, Y. I. Alivov, C. Liu, A. Teke, M. A. Reshchikov, S. Doğan, V. Avrutin, S.-J. Cho, H. Morkoç, C. V Avrutin, *J. Appl. Phys.* **2005**, *98*, DOI: 10.1063/1.1992666.

[29] J. C. Fan, K. M. Sreekanth, Z. Xie, S. L. Chang, K. V. Rao, *Prog. Mater. Sci.* **2013**, *58*, 874.

[30] T. Zhang, M. Li, J. Chen, Y. Wang, L. Miao, Y. Lu, Y. He, *Mater. Sci. Eng. R Reports* **2022**, *147*, 100661.

[31] K. Ellmer, A. Bikowski, *J. Phys. D. Appl. Phys.* **2016**, *49*, DOI: 10.1088/0022-3727/49/41/413002.

[32] A. Janotti, C. G. Van De Walle, *Reports Prog. Phys.* **2009**, *72*, DOI: 10.1088/0034-4885/72/12/126501.

[33] Y. Liu, Y. Li, H. Zeng, *J. Nanomater.* **2013**, *2013*, DOI: 10.1155/2013/196521.

[34] C. List, O. F. Authors, S. Ahmad, M. A. Raushan, M. J. Siddiqui, I. Ashraf, **2018**, 42016.

[35] X. H. Xie, B. H. Li, Z. Z. Zhang, L. Liu, K. W. Liu, C. X. Shan, D. Z. Shen, *Wuli Xuebao/Acta Phys. Sin.* **2019**, *68*, DOI: 10.7498/aps.68.20191043.

[36] S. B. Zhang, S. H. Wei, A. Zunger, *Phys. Rev. B - Condens. Matter Mater. Phys.* **2001**, *63*, DOI: 10.1103/PhysRevB.63.075205.

[37] K. Tang, S. L. Gu, J. D. Ye, S. M. Zhu, R. Zhang, Y. D. Zheng, *Chinese Phys. B* **2017**, *26*, DOI: 10.1088/1674-1056/26/4/047702.

[38] J. G. Reynolds, C. L. Reynolds, *Adv. Condens. Matter Phys.* **2014**, *2014*, DOI: 10.1155/2014/457058.

[39] Y. Ryu, T. S. Lee, J. A. Lubguban, H. W. White, B. J. Kim, Y. S. Park, C. J. Youn, *Appl. Phys. Lett.* **2006**, *88*, 1.

[40] N. Izyumskaya, V. Avrutin, Ü. Özgür, Y. I. Alivov, H. Morkoç, *Phys. Status Solidi Basic Res.* **2007**, *244*, 1439.

[41] D. C. Look, B. Claflin, *Phys. Status Solidi Basic Res.* **2004**, *241*, 624.

[42] J. L. Lyons, A. Janotti, C. G. Van De Walle, *Appl. Phys. Lett.* **2009**, *95*, 1.

[43] T. Yamamoto, **2002**, *421*, 100.

[44] T. Yamamoto, H. Katayama-yoshida, **2000**, *215*, 552.

[45] Z. Ye, H. He, L. Jiang, *Nano Energy* **2018**, *52*, 527.

[46] J. Zhang, K. Tse, M. Wong, Y. Zhang, J. Zhu, *Front. Phys.* **2016**, *11*, DOI: 10.1007/s11467-016-0577-2.

[47] Z. Wang, P. K. Nayak, J. A. Caraveo-Frescas, H. N. Alshareef, *Adv. Mater.* **2016**, *28*, 3831.

[48] R. W. Johnson, A. Hultqvist, S. F. Bent, *Mater. Today* **2014**, *17*, 236.

[49] H. Kim, H. Lee, W. Maeng, *Thin Solid Films* **2009**, *517*, 2563.

[50] D. J. Hagen, M. E. Pemble, M. Karppinen, **2021**, *041309*, DOI: 10.1063/1.5087759.

[51] M. Hamalainen, Jani, Ritala, M. Leskela, **2014**.

[52] B. Macco, W. M. M. E. Kessels, **2022**, *041313*, DOI: 10.1063/5.0116732.

[53] J. S. Ponraj, G. Attolini, M. Bosi, J. S. Ponraj, G. Attolini, M. Bosi, **2013**, *8436*, DOI: 10.1080/10408436.2012.736886.

[54] F. A. Review, X. Meng, Y. Byun, H. S. Kim, J. S. Lee, A. T. Lucero, L. Cheng, J. Kim, **2016**, DOI: 10.3390/ma9121007.

[55] N. P. Dasgupta, X. Meng, A. B. F. Martinson, **2015**, DOI: 10.1021/ar500360d.

[56] Z. Zhang, Y. Zhao, Z. Zhao, G. Huang, Y. Mei, **2020**, DOI: 10.1021/acs.chemmater.9b04414.

[57] L. Henderick, A. Dhara, A. Werbrouck, J. Dendooven, C. Detavernier, **2022**, *011310*, DOI: 10.1063/5.0069647.

[58] A. J. M. Mackus, J. R. Schneider, C. Macisaac, J. G. Baker, S. F. Bent, *Chem. Mater.* **2019**, *31*, 1142.

[59] B. R. L. Puurunen, **2014**, 332.

[60] H. Kim, D. Kim, Y. Kim, M. Kim, J. Park, **n.d.**

[61] W. Jeon, **2019**, DOI: 10.1557/jmr.2019.335.

[62] S. Sinha, D. K. Nandi, P. S. Pawar, S. Kim, J. Heo, *Sol. Energy* **2020**, *209*, 515.

[63] Y. W. Yeh, S. H. Lin, T. C. Hsu, S. Lai, P. T. Lee, S. Y. Lien, D. S. Wuu, *Nanoscale Res. Lett.* **2021**, DOI: 10.1186/s11671-021-03623-x.

[64] J. R. Bakke, K. L. Pickrahn, T. P. Brennan, S. F. Bent, **2011**, DOI: 10.1039/c1nr10349k.

[65] Z. Zhao, G. Huang, Y. Kong, J. Cui, A. A. Solovev, X. Li, Y. Mei, *Atomic Layer Deposition for Electrochemical Energy : From Design to Industrialization*, Springer Nature Singapore, **2022**.

[66] L. Han, C. Hsieh, B. C. Mallick, J. Li, Y. A. Gandomi, **2021**, 2728.

[67] D. Go, J. Woo, S. Seunghyeon, L. Jaehyeong, L. Byung, C. Yang, Y. Won, *Int. J. Precis. Eng. Manuf. Technol.* **2023**, *10*, 851.

[68] Y. Koshtyal, D. Olkhovskii, A. Rumyantsev, M. Maximov, **2022**.

[69] Z. Li, J. Su, X. Wang, *Carbon N. Y.* **2021**, *179*, 299.

[70] Z. Zhao, Y. Kong, Z. Zhang, G. Huang, Y. Mei, **2019**, DOI: 10.1557/jmr.2019.329.

[71] X. Liu, Y. Su, R. Chen, **n.d.**

[72] Z. Gao, P. Banerjee, *J. Vac. Sci. Technol. A* **2019**, *37*, 050802.

[73] V. Miikkulainen, M. Leskelä, M. Ritala, R. L. Puurunen, *J. Appl. Phys.* **2013**, *113*, DOI: 10.1063/1.4757907.

[74] F. Zaera, *Coord. Chem. Rev.* **2013**, *257*, 3177.

[75] P. Y. Lin, J. R. Gong, P. C. Li, T. Y. Lin, D. Y. Lyu, D. Y. Lin, H. J. Lin, T. C. Li, K. J. Chang, W. J. Lin, *J. Cryst. Growth* **2008**, *310*, 3024.

[76] E. Guziewicz, T. A. Krajewski, E. Przezdziecka, K. P. Korona, N. Czechowski, L. Klopotowski, P. Terziyska, *Phys. Status Solidi Basic Res.* **2020**, *257*, 1.

[77] R. Triboulet, *Prog. Cryst. Growth Charact. Mater.* **2014**, *60*, 1.

[78] A. Kolodziejczak-Radzimska, T. Jesionowski, *Materials (Basel).* **2014**, *7*, 2833.

[79] C. Otalora, M. A. Botero, G. Ordon, **2021**, 15538.

[80] J. A. Oke, T. Chien, *Int. J. Adv. Manuf. Technol.* **2023**, DOI: 10.1007/s00170-023-11478-y.

[81] W. Hao, C. Marichy, C. Journet, *2D Mater.* **2019**, *6*, DOI: 10.1088/2053-1583/aad94f.

[82] T. Tynell, M. Karppinen, *Semicond. Sci. Technol.* **2014**, *29*, DOI: 10.1088/0268-1242/29/4/043001.

[83] J. Cai, Z. Ma, U. Wejinya, M. Zou, Y. Liu, H. Zhou, *J. Mater. Sci.* **2019**, *54*, 5236.

[84] F. Zaera, *J. Phys. Chem. Lett.* **2012**, *3*, 1301.

[85] C. H. Burgess, *Mater. Sci. Technol. (United Kingdom)* **2017**, *33*, 809.

[86] M. J. Chen, J. R. Yang, M. Shiojiri, *Semicond. Sci. Technol.* **2012**, *27*, DOI: 10.1088/0268-1242/27/7/074005.

[87] S. Chen, H. Syu, C. Liao, Y. Chang, C. Huang, **2013**, *34*, 972.

[88] M.-C. Bi, Wu-Liang, Lee, Wei-Hao, Yeh, Hsin-Hao, Wu, *Jounral Vac. Sci. Technol. B* **2020**, *38*.

[89] P. Caban, R. Pietruszka, K. Kopalko, B. S. Witkowski, K. Gwozdz, *Opt. - Int. J. Light Electron Opt.* **2018**, *157*, 743.

[90] H. A. Gatz, D. Koushik, J. K. Rath, W. M. M. Kessels, R. E. I. Schropp, *Energy Procedia* **2016**, *92*, 624.

[91] V. Kumar, W. Lee, Y. Chung, J. Kim, *Mater. Sci. Semicond. Process.* **2021**, *121*, 105406.

[92] H. Jo, J. K. Kim, J. Kim, T. Seong, H. J. Son, J. Jeong, H. Yu, **2021**, DOI: 10.1021/acsaem.1c02511.

[93] H. Li, D. Han, L. Liu, J. Dong, G. Cui, S. Zhang, X. Zhang, Y. Wang, *Nanoscale Res. Lett.* **2017**, *12*, 4.

[94] S. J. Lim, J.-M. Kim, D. Kim, S. Kwon, J.-S. Park, H. Kim, *J. Electrochem. Soc.* **2010**, *157*, H214.

[95] S. I. Boyadjiev, V. Georgieva, R. Yordanov, Z. Raicheva, I. M. Szilágyi, *Appl. Surf. Sci.* **2016**, *387*, 1230.

[96] Y. Lu, C. Hsieh, G. Su, **2019**.

[97] H. Riascos, **2020**, DOI: 10.1088/1742-6596/1492/1/012052.

[98] D. Yun, G. Seo, W. Lee, S. Yoon, *IEEE Trans. Electron Devices* **2017**, *64*, 2350.

[99] T. Stapi, B. Swatowska, W. Powro, H. Czternastek, G. Lewi, **2021**.

[100] H. K. Park, B. S. Yang, S. Park, M. S. Kim, J. C. Shin, J. Heo, *J. Alloys Compd.* **2014**, *605*, 124.

[101] G. J. Klingshirn, C.F., Waag, A., Hoffman, A., *Zinc Oxide Zinc Oxide From Fundamental Properties Towards Novel Applications*, **2013**.

[102] A. Janotti, C. G. Van de Walle, *Phys. Rev. B, Condens. matter Mater. physics.* **2007**, *76*, 165202.

[103] B. Macco, H. C. M. Knoops, M. A. Verheijen, W. Beyer, M. Creatore, W. M. M. Kessels, *Sol. Energy Mater. Sol. Cells* **2017**, *173*, 111.

[104] J.M. Vohs, M.A. Barteau, *J. Electron Spectros. Relat. Phenomena* **1989**, *49*, 87.

[105] B. Xia, J. J. Ganem, E. Briand, S. Steydli, H. Tancrez, I. Vickridge, B. Xia, J. J. Ganem, E. Briand, S. Steydli, H. Tancrez, **2021**.

[106] T. Singh, T. Lehnen, T. Leuning, D. Sahu, S. Mathur, *Appl. Surf. Sci.* **2014**, *289*, 27.

[107] A. Adhikari, E. Przezdziecka, S. Mishra, P. Sybilski, J. Sajkowski, E. Guziewicz, **2021**, *2000669*, 1.

[108] V. N. Jafarova, G. S. Orudzhev, U. Hubbard, *Solid State Commun.* **2021**, *325*, 114166.

[109] P. S. Xu, **2003**, *199*, 286.

[110] S. H. I. C. A. I, X. U. Faqiang, P. A. N. Haibin, **2000**, *44*.

[111] S. Mi, Y., Odaka, H., Iwata, *Jpn. J. Appl. Phys.* **1999**.

[112] A. Neamen, Donald, *Semiconductor Physics and Devices: Basic Principles*, **2012**.

[113] S. O. Kasap, *Principals of Electronic Materials and Devices.*, **2018**.

[114] J. Kaupužs, A. Medvids, P. Onufrijevs, H. Mimura, *Opt. Laser Technol.* **2019**, *111*, 121.

[115] A. Janotti, C. G. Van De Walle, *J. Cryst. Growth* **2006**, *287*, 58.

[116] L. Liu, Z. Mei, A. Tang, A. Azarov, A. Kuznetsov, Q. Xue, X. Du, **2016**, *235305*, 1.

[117] A. Janotti, C. G. Van De Walle, *J. Cryst. Growth* **2006**, DOI: 10.1016/j.jcrysgro.2005.10.043.

[118] E. V. Lavrov, *Phys. B Condens. Matter* **2009**, *404*, 5075.

[119] C. G. Van De Walle, *Phys. Rev. Lett.* **2000**, *85*, 1012.

[120] D. M. Hofmann, A. Hofstaetter, F. Leiter, H. Zhou, F. Henecker, B. K. Meyer, S. B. Orlinskii, J. Schmidt, P. G. Baranov, **2002**, 1.

[121] T. Minami, T. Miyata, Y. Ohtani, *Phys. Status Solidi Appl. Mater. Sci.* **2007**, *204*, 3145.

[122] A. Kaschner, U. Haboeck, M. Strassburg, M. Strassburg, G. Kaczmarczyk, A. Hoffmann, C. Thomsen, A. Zeuner, H. R. Alves, D. M. Hofmann, B. K. Meyer, *Appl. Phys. Lett.* **2002**, *80*, 1909.

[123] R. Hutson, A., *Phys. Rev. B* **1957**, 222.

[124] C. G. Van De Walle, *J. Alloys Compd.* **2007**.

[125] H. H. Nahm, C. H. Park, Y. S. Kim, *Sci. Rep.* **2014**, *4*, 1.

[126] D. Gaspar, L. Pereira, K. Gehrke, B. Galler, E. Fortunato, R. Martins, *Sol. Energy Mater. Sol. Cells* **2017**, *163*, 255.

[127] J. Park, T. Jung, J. Lee, H. Kim, J. Park, *Ceram. Int.* **2015**, *41*, 1839.

[128] W. Mtangi, F. D. Auret, W. E. Meyer, M. J. Legodi, **2014**, DOI: 10.1063/1.4709728.

[129] K. Ellmer, A. Bikowski, **2016**, DOI: 10.1088/0022-3727/49/41/413002.

[130] S. D. Ponja, S. Sathasivam, I. P. Parkin, C. J. Carmalt, *Sci. Rep.* **2020**, *10*, 1.

[131] S. Khan, E. Stamate, *Nanomaterials* **2022**, *12*, DOI: 10.3390/nano12091539.

[132] Nagarani, S. Jayachandran, M., Chinnapanadar, S., *Mater. Sci. Forum* **2011**, *671*.

[133] S. O. El Hamali, W. M. Cranton, N. Kalfagiannis, X. Hou, R. Ranson, D. C. Koutsogeorgis, *Opt. Lasers Eng.* **2016**, *80*, 45.

[134] D. N. Papadimitriou, *Micromachines* **2022**, *13*, DOI: 10.3390/mi13111966.

[135] W. Li, Y. Li, G. Du, N. Chen, S. Liu, S. Wang, H. Huang, C. Lu, X. Niu, *Ceram. Int.* **2016**, *42*, 1361.

[136] A. Mallick, D. Basak, *Prog. Mater. Sci.* **2018**, *96*, 86.

[137] M. Singh, F. Scotognella, *Micromachines* **2023**, *14*, 536.

[138] Z. Chen, K. Saito, T. Tanaka, M. Nishio, Q. Guo, *J. Mater. Sci. Mater. Electron.* **2016**, *27*, 9291.

[139] Z. Wang, C. Chen, K. Wu, H. Chong, H. Ye, **2019**, *1700794*, 1.

[140] H. Hosono, H. Ohta, M. Orita, K. Ueda, M. Hirano, **2002**, *66*, 419.

[141] H. Liu, V. Avrutin, N. Izyumskaya, Ü. Özgr, H. Morkoç, *Superlattices Microstruct.* **2010**, *48*, 458.

[142] F. U. Hamelmann, *J. Phys. Conf. Ser.* **2014**, *559*, DOI: 10.1088/1742-6596/559/1/012016.

[143] T. Minami, *Semicond. Sci. Technol.* **2005**, *20*, DOI: 10.1088/0268-1242/20/4/004.

[144] Y. Jiangang, Ma., Dong, Lin., Peng, Li., Guochun, *Chinese Sci. Bull.* **2020**, *65*.

[145] S.-H. Yan, Yanfa, Wei, *Phys. Status Solidi* **2008**, *652*, 641.

[146] J. Robertson, Z. Zhang, *MRS Bull.* **2021**, *46*, 1037.

[147] S. B. Zhang, S. Wei, A. Zunger, **1999**, *274*, 976.

[148] Y. Tsur, I. Riess, *Phys. Rev. B - Condens. Matter Mater. Phys.* **1999**, *60*, 8138.

[149] X. Li, B. Keyes, S. Asher, S. B. Zhang, S. H. Wei, T. J. Coutts, S. Limpijumnong, C. G. Van De Walle, *Appl. Phys. Lett.* **2005**, *86*, 1.

[150] T. Jannane, M. Manoua, N. Fazouan, A. El Hichou, A. Almaggoussi, A. Liba, *Superlattices Microstruct.* **2020**, *147*, 106689.

[151] S. B. Zhang, S. H. Wei, A. Zunger, *Phys. B Condens. Matter* **1999**, *273–274*, 976.

[152] J. D. Chadi, *Japanese J. Appl. Physics, Part 1 Regul. Pap. Short Notes Rev. Pap.* **1999**, *38*, 2617.

[153] K. Tang, S. L. Gu, J. D. Ye, S. M. Zhu, R. Zhang, Y. D. Zheng, *Chinese Phys. B* **2017**, *26*, DOI: 10.1088/1674-1056/26/4/047702.

[154] E. Kami??ska, A. Piotrowska, J. Kossut, R. Butkute, W. Dobrowolski, R. Lukasiewicz, A. Barcz, R. Jakie??a, E. Dynowska, E. Prze??dziecka, M. Aleszkiewicz, P. Wojnar, E. Kowalczyk, *Phys. Status Solidi C Conf.* **2005**, *2*, 1119.

[155] S. Limpijumnong, S. B. Zhang, S. Wei, C. H. Park, *Phys Rev Lett.* **2004**, DOI: 10.1103/PhysRevLett.92.155504.

[156] M. C. Tarun; M. Zafar Iqbal; M. D. McCluskey, *AIP Adv.* **2017**, *022105*, DOI: 10.1063/1.3582819.

[157] G. . C. . Tuomisto , F .; Saarinen , K .; Look , D . C .; Farlow, **2005**, *72*, 1.

[158] J. E. Stehr, K. M. Johansen, T. S. Bjørheim, L. Vines, B. G. Svensson, W. M. Chen, I. A. Buyanova, **2014**, DOI: 10.1103/PhysRevApplied.2.021001.

[159] Z. Yao, K. Tang, Z. Xu, J. Ye, S. Zhu, S. Gu, *Nanoscale Res. Lett.* **2016**, DOI: 10.1186/s11671-016-1736-7.

[160] Z. H. H. Uang, H. A. R. Uan, H. O. N. G. Z. Hang, D. Ongping, S. Hi, W. L. I. Anjun, G. U. Q. In, F. W. U. Ang, L. I. F. Ang, C. H. K. Ong, *Opt. Mater. Express* **2019**, *9*, 3098.

[161] M. N. Amini, R. Saniz, D. Lamoen, B. Partoens, *Phys.Chem.Chem.Phys* **2020**, *17*, 5485.

[162] Junhyeok Bang; Youg-Sung Kim; C. H. Park; F. Gao; S. B. Zhang, *Appl. Phys. Lett.* **2014**, *104*.

[163] B. and D. D. M. Puchala, *Phys. Rev. B* **2012**, *85*.

[164] S. D. Liu L, Xu J, Wang D, Jiang M, Wang S, Li B, Zhang Z, Zhao D, Shan CX, Yao B, *Phys Rev Lett.* **2012**, *108(21):21*.

[165] N. S. Parmar, J. Choi, L. A. Boatner, M. D. Mccluskey, K. G. Lynn, *J. Alloys Compd.* **2017**, *729*, 1031.

[166] J. G. Lu, Z. Z. Ye, F. Zhuge, Y. J. Zeng, B. H. Zhao, L. P. Zhu, *Appl. Phys. Lett.* **2004**, *85*, 3134.

[167] J. Ding, J. Yan, Y. Jin, Y. Cao, H. Chen, *Int. J. Quantum Chem.* **2022**, *122*, 1.

[168] Q.-Y. Hou, L.-F. Qu, C.-W. Zhao, *Wuli Xuebao/Acta Phys. Sin.* **2016**, *65*, DOI: 10.7498/aps.65.057401.

[169] A. Ismail, M. J. Abdullah, M. A. Qaeed, M. A. Khamis, B. Ali AL-Asbahi, S. M. Qaid, W. A. Farooq, *J. King Saud Univ. - Sci.* **2021**, *33*, 101229.

[170] B. Saravanakumar, R. Mohan, S.-J. Kim, *J. Korean Phys. Soc.* **2012**, *61*, 1737.

[171] D. Snigurenko, E. Guziewicz, T. A. Krajewski, R. Jakiela, Y. Syryanyy, K. Kopalko, W. Paszkowicz, *Mater. Res. Express* **2016**, *3*, DOI: 10.1088/2053-1591/3/12/125907.

[172] M. Li, L. Wang, Y. Liu, *IAENG Int. J. Comput. Sci.* **2017**, *44*, 105.

[173] S. J. Jokela, M. D. McCluskey, *J. Appl. Phys.* **2010**, *107*, 1.

[174] J. G. Lu, S. Fujita, *Phys. Status Solidi Appl. Mater. Sci.* **2008**, *205*, 1975.

[175] S. Eisermann, A. Kronenberger, M. Dietrich, S. Petznick, A. Laufer, A. Polity, B. K. Meyer, *Thin Solid Films* **2009**, *518*, 1099.

[176] A. Gregorovič, T. Apih, V. Žagar, J. Seliger, *Phys. Chem. Chem. Phys.* **2019**, *21*, 306.

[177] J. Villafuerte, O. Chaix-pluchery, J. Kioseoglou, F. Donatini, E. Sarigiannidou, J. Pernot, V. Consonni, J. Villafuerte, O. Chaix-pluchery, J. Kioseoglou, F. Donatini, E. Sarigiannidou, J. Villafuerte, O. Chaix-pluchery, J. Kioseoglou, F. Donatini, **2021**.

[178] R. Mannam, E. S. Kumar, N. DasGupta, M. S. Ramachandra Rao, *Appl. Surf. Sci.* **2017**, *400*, 312.

[179] A. Boonchun, W. R. L. Lambrecht, J. T-thienprasert, S. Limpijumnong, **2012**, DOI: 10.1557/opl.2012.246.

[180] A. Abliz, X. Xue, X. Liu, G. Li, L. Tang, *Appl. Phys. Lett.* **2021**, *118*, 0.

[181] T. A. Krajewski, K. Kopalko, D. Snigurenko, E. Guziewicz, R. Jakiela, *Semicond. Sci. Technol.* **2014**, *30*, 015001.

[182] M. Liu, M. Jiang, Q. Zhao, K. Tang, S. Sha, B. Li, C. Kan, D. N. Shi, *ACS Appl. Mater. Interfaces* **2022**, DOI: 10.1021/acsami.2c19806.

[183] Y. Zhao, H. Yang, Y. Xiao, P. Yang, *Sol. Energy* **2022**, *231*, 889.

[184] A. C. Saritha, M. R. Shijeesh, L. S. Vikas, R. R. Prabhu, M. K. Jayaraj, *J. Phys. D. Appl. Phys.* **2016**, *49*, DOI: 10.1088/0022-3727/49/29/295105.

[185] H. D. Cho, A. S. Zakirov, S. U. Yuldashev, C. W. Ahn, Y. K. Yeo, T. W. Kang, *Nanotechnology* **2012**, *23*, 1.

[186] L. Qi, Z. Chai, H. Yang, M. B. Shahzad, Y. Qi, *J. Alloys Compd.* **2019**, *793*, 295.

[187] et al Wang, Guoping, Chu, Sheng, Zhan, Ning, **2011**, *041107*, 1.

[188] F. Cao, X. Ji, *J. Mater. Sci. Mater. Electron.* **2018**, *29*, 6594.

[189] I. Mohammad, R. Deep, J. Lin, T. Yoshida, Y. Fujita, **2022**, *2100556*, 1.

[190] T. Zhang, X. Zhang, B. Ding, J. Shen, Y. Hu, H. Gu, *Appl. Opt.* **2020**, *59*, 2498.

[191] R. Nasser, J. M. Song, H. Elhouichet, *Superlattices Microstruct.* **2021**, *155*, 106908.

[192] L. Agarwal, K. S. Rao, R. P. Dwivedi, *J. Nano- Electron. Phys.* **2022**, *14*, 1.

[193] C. Cao, B. Zhang, S. Lin, *APL Mater.* **2022**, *10*, DOI: 10.1063/5.0083753.

[194] Y. H. Kwon, D. H. Kim, H. K. Kim, J. Nah, *Nano Energy* **2015**, *18*, 126.

[195] I. Y. Y. Bu, *J. Mater. Sci. Mater. Electron.* **2014**, *25*, 5277.

[196] R. G. Elliman, J. S. Williams, *Curr. Opin. Solid State Mater. Sci.* **2015**, *19*, 49.

[197] B. J. Sealy, *Mater. Sci. Technol. (United Kingdom)* **1988**, *46*.

[198] L. Ye, M. P. De Jong, T. Kudernac, W. G. Van Der Wiel, J. Huskens, **2017**, *62*, 128.

[199] K. Huet, F. Mazzamuto, T. Tabata, I. Toqué-tresonne, Y. Mori, *Mater. Sci. Semicond. Process.* **2017**, *62*, 92.

[200] E. Yarali, C. Koutsiaki, H. Faber, K. Tetzner, E. Yengel, P. Patsalas, N. Kalfagiannis, D. C. Koutsogeorgis, T. D. Anthopoulos, **2020**, *1906022*, 1.

[201] J.-N. G. J.-Y. D. M. Meunier, Appl., *Appl. Phys. Lett* **2005**, *222104*, DOI: 10.1063/1.1927275.

[202] H. Fu, K. Fu, C. Yang, H. Liu, K. A. Hatch, D. H. Mudiyanselage, B. Li, T. Kim, R. Shanthan, P. Su, D. C. Messina, X. Deng, C. Cheng, V. Meidanshahi, X. Huang, H. Chen, T. Yang, A. M. Armstrong, A. A. Allerman, E. T. Yu, J. Han, S. M. Goodnick, D. J. Smith, R. J. Nemanich, F. A. Ponce, Y. Zhao, **2021**, *xxx*, 1.

[203] M. S. Brown, C. B. Arnold, **n.d.**, 91.

[204] O. I. V. and S. N. L. V. A. Gnatyuk, T. Aoki, *IEEE Nucl. Sci. Symp. Conf. Rec.* **20011**.

[205] H. Kawahara, T. Shimogaki, *Appl. Phys. B* **2015**, 463.

[206] Akihiro Ikeda; Koji Nishi; Hiroshi Ikenoue; ... et. al, *Appl. Phys. Lett.* **2013**, *052104*, DOI: 10.1063/1.4790621.

[207] A. Ikeda, D. Marui, H. Ikenoue, T. Asano, *Jpn. J. Appl. Phys* **2015**, 20.

[208] S. Y. Lee, E. S. Shim, H. S. Kang, S. S. Pang, J. S. Kang, *Thin Solid Films* **2005**, *473*, 31.

[209] k and A. D. Eniko, Gyorgy, Angel Perez del Pino, Costantin Logofatu, Cristina Cazan, *J. Am. Ceram. Soc.* **2014**, *2724*, 2718.

[210] Y. Hatanaka, M. Niraula, A. Nakamura, T. Aoki, *Appl. Surf. Sci.* **2001**, *175–176*, 462.

[211] B. Deul, N. Han, M. Han, S. Chandramohan, Y. Jae, K. Bok, J. Bae, T. Viet, C. Hong, *Mater. Lett.* **2014**, *116*, 412.

[212] J. Narayan; R. T. Young; R. F. Wood; W. H. Christie, *Appl. Phys. Lett.* **1978**, *33*.

[213] R. et al. Slaoui, A., Foulon, F., Stuck, *Appl. Phys. A* **1990**, *50*.

[214] M. Sugioka, K. ; Toyoda, K. ; Tachi, K. ; Otsuka, *Appl. Phys. A Solids Surfaces* **1989**, *49*.

[215] H. Sugioka, Koji ; Toyoda, Koichi ; Jyumonji, Masayuki ; Takai, *Proc. SPIE* **1996**, *2703*.

[216] G. Kerrien, T. Sarnet, D. Debarre, J. Boulmer, M. Hernandez, C. Laviron, *Thin Solid Films* **2004**, *454*, 106.

[217] K. Ohara, T. Seino, A. Nakamura, T. Aoki, H. Kominami, *Appl. Surf. Sci.* **2005**, *244*, 369.

[218] D. P. Norton, H. S. Kim, J. M. Erie, S. J. Pearton, Y. L. Wang, F. Ren, *Proc. SPIE* **2008**, *6895*, 68950W.

[219] W. Lin, X. Ma, *Appl. Surf. Sci.* **2004**, *230*, 44.

[220] K.-Josef Kramer; Somit Talwar; Isabella T. Lewis; John E. Davison; Kenneth A. Williams; Keith A. Benton; Kurt H. Weiner, *Appl. Phys. Lett.* **1996**, *68*.

[221] F. Roccaforte, P. Fiorenza, M. Vivona, G. Greco, F. Giannazzo, **2021**.

[222] P. Gundel, D. Suwito, U. Jäger, F. D. Heinz, W. Warta, M. C. Schubert, *IEEE Trans. Electron Devices* **2011**, *58*, 2874.

[223] K. Kramer, S. Talwar, A. M. Mccarthy, K. H. Weiner, *IEEE ELECTRON DEVICE Lett.* **1996**, *17*, 15.

[224] T. Sarnet, G. Kerrien, N. Yaakoubi, A. Bosseboeuf, E. Dufour-gergam, D. De, J. Boulmer, K. Kakushima, C. Laviron, *Appl. Surf. Sci.* **2005**, *247*, 537.

[225] S. Heo, E. S. Lett, S. Heo, S. Baek, D. Lee, M. Hasan, *Electrochem. Solid-State Lett.* **2006**, 3.

[226] D. Bouchier, A. Grouillet, D. Lenoble, *Appl. Surf. Sci.* **2002**, *186*, 45.

[227] C. Lee, J. Kim, *J. Mater. Chem. C* **2020**, *8*, DOI: 10.1039/d0tc01790f.

[228] E. Paneerselvam, S. H. Choutapalli, H. G. P. Kumar, N. J. Vasa, D. Nakamura, M. S. R. Rao, H. Ikenoue, T. Thomas, *J. Micromanufacturing* **2022**, DOI: 10.1177/25165984211016281.

[229] E. Abubakr, S. Ohmagari, A. Zkria, H. Ikenoue, *Mater. Res. Lett. ISSN* **2022**, DOI: 10.1080/21663831.2022.2083457.

[230] S. M. Sze, K. K. Ng, *Physics of Semiconductor Devices: Third Edition*, **2006**.

[231] B. G. S. and S. K. Banerjee, *Solid State Electronic Devices Seventh Edition*, **2016**.

[232] N. K. Reddy, Q. Ahsanulhaq, J. H. Kim, M. Devika, Y. B. Hahn, *Nanotechnology* **2007**, *18*, DOI: 10.1088/0957-4484/18/44/445710.

[233] L. J. Brillson, Y. Lu, *J. Appl. Phys.* **2011**, *109*, DOI: 10.1063/1.3581173.

[234] K. Ip, G. T. Thaler, H. Yang, S. Youn, Y. Li, D. P. Norton, S. J. Pearton, S. Jang, F. Ren, **2006**, *287*, 149.

[235] S. Vallisree, R. Thangavel, T. R. Lenka, **2019**.

[236] W. Zhang, N. Tang, **2020**.

[237] J. A. Phys, **2022**, *175302*, DOI: 10.1063/5.0087044.

[238] S. J. Ikhmayies, N. M. Abu El-Haija, R. N. Ahmad-Bitar, *J. Semicond.* **2015**, *36*, DOI: 10.1088/1674-4926/36/3/033005.

[239] Y. F. Lu, Z. Z. Ye, Y. J. Zeng, L. P. Zhu, B. H. Zhao, *Electrochem. Solid-State Lett.* **2008**, *11*, DOI: 10.1149/1.2911917.

[240] L. J. Mandalapu, Z. Yang, J. L. Liu, *Appl. Phys. Lett.* **2007**, *90*, 3.

[241] E. S. Kumar, J. Chaterjee, S. Singh, N. Dasgupta, M. S. R. Rao, N. Functional, M. Technology, M. Science, **2010**, 995.

[242] S. J. Ikhmayies, N. M. Abu El-Haija, R. N. Ahmad-Bitar, *J. Semicond.* **2015**, *36*, DOI: 10.1088/1674-4926/36/3/033005.

[243] F. Zhuge, **2005**, *092103*, 85.

[244] P. Hofmann, *Solid State Physics: An Introduction*, Wiley, **2015**.

[245] N. Gupta, K. M., Gupta, in *Semicond. Mater. Their Prop. Appl. Recent Adv.*, Springer, **2015**.

[246] E. Fortunato, P. Barquinha, R. Martins, *Adv. Mater.* **2012**, *24*, 2945.

[247] A. C. Tickle, *Thin-Film Transistors - A New Approach to Microelec- Tronics*, Wiley, New York, **1969**.

[248] S. D. Brotherton, *Introduction to Thin Film Transistors: Physics and Technology of TFTs*, **2013**.

[249] Y. Kuo, *Electrochem. Soc. Interface* **2013**, *22*, 55.

[250] P. Kagan, C. R., Andry, *Thin Film Transistors-A Historical Perspective*, **2009**.

[251] R. L. Hoffman, B. J. Norris, J. F. Wager, *Appl. Phys. Lett.* **2003**, *82*, 733.

[252] Z. Ouyang, W. Wang, M. Dai, B. Zhang, J. Gong, M. Li, L. Qin, H. Sun, **2022**.

[253] O. O. Abegunde, E. T. Akinlabi, O. P. Oladijo, **2019**, *6*, 174.

[254] S. O. Mbam, S. E. Nwonu, O. A. Orelaja, *Mater. Res. Express* **2019**.

[255] J. E. Greene, **2018**, *204*, 0.

[256] S. L. Pyshkin, J. M. Ballato, *ADVANCED MATERIALS AND DEVICES Edited by Sergei L . Pyshkin*, **2013**.

[257] P. S. Patil, **1999**, *59*.

[258] Y. Diao, L. Shaw, S. C. B. Mannsfeld, **2014**, 2145.

[259] J. H. Mostafavi, H. A., Mishra, K., A, Kim, M. Ulbricht, F. Coclite, Anna Maria, Hosseini, S., S., Gallucci, **2023**, 1.

[260] S. Rahemi, A. Sabour, R. Aghdam, M. Nazari, A. Bayat, *J. Anal. Appl. Pyrolysis* **2019**, *141*, 104631.

[261] C. Glynn, C. O. Dwyer, **2017**, DOI: 10.1002/admi.201600610.

[262] S. K. Chaluvadi, **n.d.**

[263] A. J. Haider, T. Alawsi, M. J. Haider, B. A. Taha, H. A. Marhoon, *Opt. Quantum Electron.* **2022**, 1.

[264] U. Helmersson, M. Lattemann, J. Bohlmark, A. P. Ehiasarian, J. Tomas, **2006**, *513*, 1.

[265] W. Nunn, T. K. Truttmann, B. Jalan, *J. Mater. Res.* **2021**, *36*, 4847.

[266] E. Alfonso, J. Olaya, G. Cubillos, **2011**.

[267] H. Pedersen, S. T. Barry, J. Sundqvist, **2021**, DOI: 10.1116/6.0001125.

[268] J. A. Oke, T. C. Jen, *J. Mater. Res. Technol.* **2022**, *21*, 2481.

[269] M. Suzuki, *Introduction to Thin Film Deposition*, **2014**.

[270] M. Weber, N. Boysen, O. Graniel, A. Sekkat, C. Dussarrat, P. Wiff, A. Devi, D. Mun, **2023**, DOI: 10.1021/acsmaterialsau.3c00002.

[271] C. Cabral, C. Lavoie, C. Murray, A. Pyzyna, K. Rodbell, **2020**, DOI: 10.1116/6.0000230.

[272] T. S. Tripathi, M. Karppinen, *Adv. Mater. Interfaces* **2017**, *4*, 1.

[273] O. Graniel, J. Puigmartí-luis, D. Muñoz-rojas, **2021**, *50*, DOI: 10.1039/d1dt00232e.

[274] K. Suguro, *MRS Adv.* **2022**, *7*, 1241.

[275] J. A. Hillier, **2021**.

[276] J. Bonami, G., *Heat Treatment: Theory, Techniques and Applications*, **2011**.

[277] S. O. Elhamali, **2016**, 216.

[278] Y. Gong, Z. Gong, **2023**, *2200949*, 1.

[279] X. Du, *J. Phys. Conf. Ser.* **2007**, 5.

[280] R. Journal, **2015**, 1.

[281] C. Charpentier, R. Boukhicha, P. Prod, T. Emeraud, J. Lerat, *Sol. Energy Mater. Sol. Cells* **2014**, *125*, 223.

[282] G. Basting, D., Marowsky, *Excimer Laser Technology*, **2005**.

[283] N. Kalfagiannis, **n.d.**

[284] L. J. van der Pauw, *Philips Res. Reports 13* **1958**, 1.

[285] S. H. N. Lim, D. R. McKenzie, M. M. M. Bilek, *Rev. Sci. Instrum.* **2009**, *80*, DOI: 10.1063/1.3183503.

[286] D. W. Koon, *Rev. Sci. Instrum.* **1989**, *60*, 271.

[287] D. S. Perloff, *Solid State Electron.* **1977**, *20*, 681.

[288] M. Cornils, M. Doelle, O. Paul, *October* **2007**, *54*, 2756.

[289] L. J. Van der Pauw, *Philips Tech. Rev.* **1958**, *20*.

[290] D. W. Koon, A. A. Bahl, E. O. Duncan, *Rev. Sci. Instrum.* **1989**, *60*, 275.

[291] E. H. Hall, **1879**, *2*, 287.

[292] R. Green, *White Pap.* **2011**, 1.

[293] D. K. Schroder, *Semiconductor Material and Device Characterization: Third Edition*, **2005**.

[294] S. Fearn, *An Introduction to Time-of-Flight Secondary Ion Mass Spectrometry (ToF-SIMS) and Its Application to Materials Science*, Morgan & Claypool, **2015**.

[295] P. Malmberg, E. Jennische, D. Nilsson, **2011**, 2711.

[296] V. Converso, **n.d.**

[297] T. Stephan, **2001**, *49*, 859.

[298] A. Benninghoven, *Angew. Chemie Int. Ed.* **1994**.

[299] S. Sims, **n.d.**, 1.

[300] Bubert, H, Riviere, J., C., Werner, W., S., M., *X-Ray Photoelectron Spectroscopy (XPS)," in Surface and Thin Film Analysis: A Compendium of Principles, Instrumentation, and*

Applications, Wiley-VCH Verlag GmbH & Co., **2011**.

[301] J. Watts, J., F., Wolstenholm, *An Introduction to Surface Analysis by XPS and AES*, John Wiley & Sons, Ltd, **2003**.

[302] D. N. G. Krishna, J. Philip, *Appl. Surf. Sci. Adv.* **2022**, *12*, 100332.

[303] P. Patsalas, M. Handrea, S. Logothetidis, M. Gioti, S. Kennou, W. Kautek, **2001**, 960.

[304] Nonnenmacher, M., O'Boyle, M., P., Wickramasinghe, H., K., *Appl. Phys. Lett.* **1991**, 2921.

[305] W. Melitz, J. Shen, A. C. Kummel, S. Lee, *Surf. Sci. Rep.* **2011**, *66*, 1.

[306] W. N. Hansen, G. J. Hansen, **2001**, *481*, 172.

[307] H. Fujiwara, *Spectroscopic Ellipsometry*, John Wiley & Sons, Ltd, **2007**.

[308] E. Born, M, Wolf, E, Hecht, *Phys. Today* **2000**.

[309] N. F. Mott, E. A. Davis, C. P. Oxford, **n.d.**

[310] J. Tauc, **1972**, *10*, 569.

[311] H. Fujiwara, *Spectrosc. Ellipsom. Princ. Appl.* **2007**, 1.

[312] M. Schubert, T. Tiwald, *Phys. Rev. B - Condens. Matter Mater. Phys.* **2000**, *61*, 8187.

[313] S. Schöche, T. Hofmann, V. Darakchieva, N. Ben Sedrine, X. Wang, A. Yoshikawa, M. Schubert, *J. Appl. Phys.* **2013**, *113*, DOI: 10.1063/1.4772625.

[314] H. P. Gavin, *Duke Univ.* **2019**, 1.

[315] A. A. Kukharskii, *Solid State Commun.* **1973**, *13*, 1761.

[316] S. Zollner, P. P. Paradis, F. Abadizaman, N. S. Samarasingha, *J. Vac. Sci. Technol. B* **2019**, *37*, 012904.

[317] D. W. Berreman, F. C. Unterwald, **1968**, *174*.

[318] F. Gervais, J. F. Baumard, *Solid State Commun.* **1977**, *21*, 861.

[319] T. Weckman, K. Laasonen, *J. Phys. Chem. C* **2016**, *120*, 21460.

[320] M. D. Mccluskey, S. J. Jokela, **2016**, DOI: 10.1063/1.3216464.

[321] S. Dutta, S. Chattopadhyay, A. Sarkar, M. Chakrabarti, D. Sanyal, D. Jana, *Prog. Mater. Sci.* **2009**, *54*, 89.

[322] K. Tang, S. Gu, J. Ye, S. Zhu, R. Zhang, Y. Zheng, *J. Semicond.* **2016**, *37*, DOI: 10.1088/1674-4926/37/3/031001.

[323] C. G. Van De Walle, *Phys. B Condens. Matter* **2001**, *308–310*, 899.

[324] J. Bang, K. J. Chang, *Appl. Phys. Lett.* **2008**, *92*, 1.

[325] D. Gaspar, L. Pereira, K. Gehrke, B. Galler, E. Fortunato, R. Martins, *Sol. Energy Mater. Sol. Cells* **2017**, *163*, 255.

[326] T. Weckman, K. Laasonen, *J. Phys. Chem. C* **2016**, *120*, 21460.

[327] J. A. Phys, J. Hu, H. Y. He, B. C. Pan, **2009**, *113706*, DOI: 10.1063/1.2939257.

[328] N. Temahuki, F. Jomard, A. Lusson, I. Stenger, S. Hassani, J. Chevallier, J. M. Chauveau, C. Morhain, J. Barjon, *Appl. Phys. Lett.* **2021**, *118*, DOI: 10.1063/5.0044373.

[329] S. O. El, W. M. Cranton, N. Kalfagiannis, X. Hou, R. Ranson, D. C. Koutsogeorgis, *Opt. Lasers Eng.* **2016**, *80*, 45.

[330] K. Kumar, P. Casey, G. Hughes, **n.d.**, 16.

[331] P. Makuła, M. Pacia, W. Macyk, *J. Phys. Chem. Lett.* **2018**, *9*, 6814.

[332] J. Tauc, *Mater. Res. Bull.* **1968**.

[333] J. G. Lu, S. Fujita, T. Kawaharamura, H. Nishinaka, Y. Kamada, T. Ohshima, Z. Z. Ye, Y. J. Zeng, Y. Z. Zhang, L. P. Zhu, H. P. He, B. H. Zhao, *J. Appl. Phys.* **2007**, *101*, DOI: 10.1063/1.2721374.

[334] C. Guillén, J. Herrero, *Thin Solid Films* **2016**, *605*, 136.

[335] H. P. He, F. Zhuge, Z. Z. Ye, L. P. Zhu, F. Z. Wang, B. H. Zhao, J. Y. Huang, *J. Appl. Phys.* **2006**, *99*, DOI: 10.1063/1.2161419.

[336] V. Srikant, D. R. Clarke, *J. Appl. Phys.* **1998**, *83*, 5447.

[337] C. Green, J., *Annu. Rev. Phys. Chem.* **1977**, *28*, 161.

[338] D. C. Look, *J. Electrochem. Soc.* **1990**, *137*, 260.

[339] F. Werner, *J. Appl. Phys.* **2017**, *122*, DOI: 10.1063/1.4990470.

[340] S. Schöche, T. Hofmann, V. Darakchieva, N. Ben Sedrine, X. Wang, A. Yoshikawa, M. Schubert, *J. Appl. Phys.* **2013**, *113*, DOI: 10.1063/1.4772625.

[341] S. Schöche, T. Hofmann, V. Darakchieva, X. Wang, A. Yoshikawa, K. Wang, T. Araki, Y. Nanishi, M. Schubert, *Thin Solid Films* **2014**, *571*, 384.

[342] J. A. Hillier, S. Camelio, W. Cranton, A. V. Nabok, C. J. Mellor, D. C. Koutsogeorgis, N. Kalfagiannis, *ACS Photonics* **2020**, *7*, 2692.

[343] H. G. Tompkins, J. N. Hilfiker, *Spectroscopic Ellipsometry: Practical Application to Thin Film Characterization*, **2015**.

[344] A. Kasic, M. Schubert, S. Einfeldt, D. Hommel, T. E. Tiwald, *Phys. Rev. B* **2000**, *62*, 7365.

[345] R. Marty, A. Mlayah, A. Arbouet, C. Girard, S. Tripathy, *Opt. Express* **2013**, *21*, 4551.

[346] N. Sakagami, M. Yamashita, T. Sekiguchi, S. Miyashita, K. Obara, T. Shishido, *J. Cryst. Growth* **2001**, *229*, 98.

[347] J. H. Kim, J. Y. Moon, H. S. Lee, W. S. Han, H. K. Cho, J. Y. Lee, H. S. Kim, *Mater. Sci. Eng. B Solid-State Mater. Adv. Technol.* **2009**, *165*, 77.

[348] L. J. Brillson, H. L. Mosbacker, Y. M. Strzhemechny, B. D. White, **2011**, *012102*, DOI: 10.1063/1.1984089.

[349] Y. Zeng, Z. Ye, J. Lu, L. Zhu, D. Li, B. Zhao, J. Huang, **2005**, *249*, 203.

[350] L. Z. Peredo, I. M. Velis, A. Martínez, J. H. Torres, L. G. González, L. D. Lvova, N. F. Ramírez, S. V. García, G. S. Rodríguez, *Rev. Mater.* **2018**, *23*, DOI: 10.1590/S1517-707620180002.0454.

[351] Q. Y. Zhu, Z. Z. Ye, G. D. Yuan, J. Y. Huang, L. P. Zhu, B. H. Zhao, J. G. Lu, **2006**, *253*, 1903.

[352] Z. Ye, F. Zhu-ge, J. Lu, Z. Zhang, L. Zhu, B. Zhao, J. Huang, **2004**, *265*, 127.

[353] J. G. Lu, **2006**, *053501*, 87.

[354] Y. R. Ryu, **2003**, *4032*, DOI: 10.1063/1.1625787.

[355] H. Chiu, Y. Chang, W. Wu, J. Wu, **2014**.

[356] Y. Yang, X. W. Sun, B. K. Tay, G. F. You, S. T. Tan, K. L. Teo, *Appl. Phys. Lett.* **2008**, *93*, DOI: 10.1063/1.3054639.

[357] S. S. Lin, **2008**, DOI: 10.1088/0022-3727/41/15/155114.

[358] Y. Cao, L. Miao, S. Tanemura, M. Tanemura, Y. Kuno, Y. Hayashi, *Appl. Phys. Lett.* **2006**, *88*, 1.

[359] W. Ryu. Y.R., Lee, T-S., Leem, J., H., White, H., *Appl. Phys. Lett.* **2003**, *83*.

[360] C. Kumari, A. Pandey, A. Dixit, *Superlattices Microstruct.* **2019**, *132*, 106154.

[361] K. S. Ahn, T. Deutsch, Y. Yan, C. S. Jiang, C. L. Perkins, J. Turner, M. Al-Jassim, *J. Appl. Phys.* **2007**, *102*, 1.

[362] V. I. Kolkovsky, D. Snigurenko, R. Jakiela, E. Guziewicz, *Semicond. Sci. Technol.* **2014**, *29*, DOI: 10.1088/0268-1242/29/8/085006.

[363] P. J. Li, Z. M. Liao, X. Z. Zhang, X. J. Zhang, H. C. Zhu, J. Y. Gao, K. Laurent, Y. Leprince-Wang, N. Wang, D. P. Yu, *Nano Lett.* **2009**, *9*, 2513.

[364] X. Guo, J. C. Hoi, H. T. Abata, T. K. Awai, **2001**, *40*, 177.

[365] Y. W. Heo, Y. W. Kwon, Y. Li, **2005**, *3474*, 1.

[366] T. Aoki, Y. Hatanaka, D. C. Look, *Appl. Phys. Lett.* **2000**, *76*, 3257.

[367] K. Viswanath, in *Handb. Surfaces Interfaces Mater.* (Ed.: H.S. Nalwa), Academic Press, **2001**.

[368] R. N. Hall, **n.d.**, 6.

[369] W. Shockley, W. T. Read, **n.d.**

[370] J. Yang, L. Shi, L. Wang, S. Wei, *Nat. Publ. Gr.* **2016**, 1.

[371] K. Hyeon-deuk, **2014**.

[372] S. Materials, S. Materials, M. Science, **2015**, *40*, 3639.

[373] J. Lu, Z. Shi, Y. Wang, Y. Lin, Q. Zhu, Z. Tian, J. Dai, S. Wang, C. Xu, *Sci. Rep.* **2016**, *6*, 1.

[374] C. Y. Cho, M. K. Kwon, S. J. Lee, S. H. Han, J. W. Kang, S. E. Kang, D. Y. Lee, S. J. Park, *Nanotechnology* **2010**, *21*, DOI: 10.1088/0957-4484/21/20/205201.

[375] H. Guo, X. Huang, *J. Alloys Compd.* **2018**, *764*, 809.

[376] K. Okamoto, M. Funato, Y. Kawakami, K. Tamada, *J. Photochem. Photobiol. C Photochem. Rev.* **2017**, *32*, 58.

[377] A. I. Zhmakin, *Phys. Rep.* **2011**, *498*, 189.

[378] R. Liang, J. Dai, L. Xu, J. He, S. Wang, Y. Peng, H. Wang, L. Ye, C. Chen, *IEEE Trans. Electron Devices* **2018**, *65*, 2498.

[379] W.-Y. Chang, Y. Kuo, Y.-F. Yao, C. C. Yang, Y.-R. Wu, Y.-W. Kiang, *Opt. Express* **2018**, *26*, 8340.

[380] X. Liu, Y. Mou, H. Wang, R. Liang, X. Wang, Y. Peng, M. Chen, *Appl. Opt.* **2018**, *57*, 7325.

[381] T. C. Litton, Cole W., Reynolds, Donald C., Collins, *Zinc Oxide Materials for Electronic and Optoelectronic Device Applications*, Wiley, **2011**.

[382] Y. R. Ryu, **2006**, *153504*, 1.

[383] A. Rasool, M. C. S. Kumar, C. G. R. Amiruddin, *J. Mater. Sci. Mater. Electron.* **2020**, *31*, 7100.

[384] T. Asar, T. Yavuz, B. Coşkun, *J. Mater. Sci. Mater. Electron.* **2020**, *31*, 6059.

[385] Z. Chen, Q. Yan, Y. Zhao, M. Cao, J. Wang, L. Wang, *J. Sol-Gel Sci. Technol.* **2019**, 101.

[386] J. Huang, L. Wang, R. Xu, K. Tang, W. Shi, Y. Xia, **2009**, DOI: 10.1088/0268-1242/24/7/075025.

[387] B. W. H. Baugher, H. O. H. Churchill, Y. Yang, P. Jarillo-Herrero, *Nat. Nanotechnol.* **2014**, *9*, 262.

[388] Z. W. Shang, H. H. Hsu, Z. W. Zheng, C. H. Cheng, *Nanotechnol. Rev.* **2019**, *8*, 422.

[389] W. Huo, Z. Mei, Y. Lu, Z. Han, R. Zhu, T. Wang, Y. Sui, H. Liang, X. Du, *Chinese Phys. B* **2019**, *28*, DOI: 10.1088/1674-1056/28/8/087302.

[390] A. Kuo, T. K. Won, J. Kanicki, *IEEE Trans. Electron Devices* **2008**, *55*, 1621.

[391] J. C. Park, S. Kim, S. Kim, C. Kim, I. Song, Y. Park, U. I. Jung, D. H. Kim, J. S. Lee, *Adv. Mater.* **2010**, *22*, 5512.

[392] Z. Chen, D. Han, N. Zhao, J. Wu, Y. Cong, J. Dong, F. Zhao, S. Zhang, X. Zhang, Y. Wang, L. Liu, *Jpn. J. Appl. Phys.* **2015**, *54*, DOI: 10.7567/JJAP.54.04DF03.

[393] E. Broderick, W. Huo, H. Liang, Y. Lu, Z. Han, R. Zhu, Y. Sui, **2021**.

[394] Y. R. Liu, G. W. Zhao, P. T. Lai, R. H. Yao, *Chinese Phys. B* **2016**, *25*, DOI: 10.1088/1674-1056/25/8/088503.

[395] S. J. Li, X. He, D. D. Han, Y. Wang, L. Sun, S. D. Zhang, *ICSICT 2012 - 2012 IEEE 11th Int. Conf. Solid-State Integr. Circuit Technol. Proc.* **2012**, 14.

[396] A. Gangwar, B. Mazhari, *IEEE Trans. Electron Devices* **2016**, *63*, 4776.

[397] W. Huo, R. Zhu, Z. Mei, Z. Han, T. Wang, Y. Sui, H. Liang, X. Du, *IEEE Trans. Electron Devices* **2019**, *66*, 5162.

[398] S. O. Elhamali, **2016**.

[399] MURRMANN H, WIDMANN D, **1969**, 162.

[400] P. Karnatak, T. P. Sai, S. Goswami, S. Ghatak, S. Kaushal, A. Ghosh, *Nat. Commun.* **2016**, *7*, 1.

[401] W. C. And, V. Shalaev, *Optical Metamaterials: Fundamentals and Applications*, Springer, **2009**.

[402] D. R. Smith, D. Schurig, **2003**, 5.

[403] Z. L. Liao, W. M. Deng, Z. L. Xiang, W. J. Chen, J. W. Dong, *Front. Phys.* **2022**, *10*, 1.

[404] A. Poddubny, I. Iorsh, P. Belov, Y. Kivshar, **2013**, *7*, DOI: 10.1038/nphoton.2013.243.

[405] P. Shekhar, J. Atkinson, Z. Jacob, *Nano Converg.* **2014**, *1*, 1.

[406] J. S. T. Smalley, F. Vallini, X. Zhang, Y. Fainman, *Adv. Opt. Photonics* **2018**, *10*, 354.

[407] L. Lu, R. E. Simpson, S. K. Valiyaveedu, *J. Opt. (United Kingdom)* **2018**, *20*, DOI: 10.1088/2040-8986/aade68.

[408] A. V. Zayats, *8th Int. Congr. Adv. Electromagn. Mater. Microwaves Opt. METAMATERIALS 2014* **2014**, *111*, 431.

[409] C. Argyropoulos, N. M. Estakhri, F. Monticone, A. Alù, *Opt. Express* **2013**, *21*, 15037.

[410] A. J. Hoffman, L. Alekseyev, S. S. Howard, K. J. Franz, D. Wasserman, V. A. Podolskiy, E. E. Narimanov, D. L. Sivco, C. Gmachl, *Nat. Mater.* **2007**, *6*, 946.

[411] A. Fang, T. Koschny, C. M. Soukoulis, *Phys. Rev. B - Condens. Matter Mater. Phys.* **2009**, *79*, 1.

[412] T. Galfsky, H. N. S. Krishnamoorthy, W. Newman, E. E. Narimanov, Z. Jacob, V. M. Menon, *Optica* **2015**, *2*, 62.

[413] Y. Guo, Z. Jacob, *Opt. Express* **2013**, *21*, 15014.

[414] J. Song, Q. Cheng, L. Lu, B. Li, K. Zhou, B. Zhang, Z. Luo, X. Zhou, *Phys. Rev. Appl.* **2020**, *13*, 1.

[415] Z. Jacob, I. I. Smolyaninov, E. E. Narimanov, *Appl. Phys. Lett.* **2012**, *100*, DOI: 10.1063/1.4710548.

[416] A. N. Poddubny, P. A. Belov, P. Ginzburg, A. V. Zayats, Y. S. Kivshar, *Phys. Rev. B - Condens. Matter Mater. Phys.* **2012**, *86*, 1.

[417] B. Romeira, A. Fiore, *IEEE J. Quantum Electron.* **2018**, *54*, 1.

[418] P. V. Kapitanova, P. Ginzburg, F. J. Rodríguez-Fortuño, D. S. Filonov, P. M. Voroshilov, P. A. Belov, A. N. Poddubny, Y. S. Kivshar, G. A. Wurtz, A. V. Zayats, *Nat. Commun.* **2014**, *5*, DOI: 10.1038/ncomms4226.

[419] Y. Liu, Y. Ke, H. Luo, S. Wen, *Nanophotonics* **2017**, *6*, 51.

[420] Y. Guo, C. L. Cortes, S. Molesky, Z. Jacob, *Appl. Phys. Lett.* **2012**, *101*, DOI: 10.1063/1.4754616.

[421] S. Xi, H. Chen, T. Jiang, L. Ran, J. Huangfu, B. I. Wu, J. A. Kong, M. Chen, *Phys. Rev. Lett.* **2009**, *103*, DOI: 10.1103/PhysRevLett.103.194801.

[422] H. Hu, X. Lin, D. Liu, P. Genevet, B. Zhang, Y. Luo, *2019 Photonics Electromagn. Res. Symp. - Fall, PIERS - Fall 2019 - Proc.* **2019**, 318.

[423] Z. Jacob, L. V. Alekseyev, E. Narimanov, *Conf. Quantum Electron. Laser Sci. - Tech. Dig. Ser.* **2007**, *14*, 8247.

[424] Z. Liu, H. Lee, Y. Xiong, C. Sun, X. Zhang, *Science (80-.).* **2007**, *315*, 1686.

[425] M. Kim, S. So, K. Yao, Y. Liu, J. Rho, *Sci. Rep.* **2016**, *6*, 1.

[426] J. J. D. McKendry, R. P. Green, A. E. Kelly, Z. Gong, B. Guilhabert, D. Massoubre, E. Gu, M. D. Dawson, *IEEE Photonics Technol. Lett.* **2010**, *22*, 1346.

[427] K. V. Sreekanth, Y. Alapan, M. ElKabbash, A. M. Wen, E. Ilker, M. Hinczewski, U. A. Gurkan, N. F. Steinmetz, G. Strangi, *Adv. Opt. Mater.* **2016**, *4*, 1767.

[428] K. V. Sreekanth, P. Mahalakshmi, S. Han, M. S. Mani Rajan, P. K. Choudhury, R. Singh, *Adv. Opt. Mater.* **2019**, *7*, 1.

[429] F. Ghodsi, H. Dashti, J. Ahmadi-Shokouh, *Opt. Quantum Electron.* **2020**, *52*, DOI: 10.1007/s11082-020-02431-4.

[430] S. Castilla, I. Vangelidis, V. V. Pusapati, J. Goldstein, M. Autore, T. Slipchenko, K. Rajendran, S. Kim, K. Watanabe, T. Taniguchi, L. Martín-Moreno, D. Englund, K. J.

Tielrooij, R. Hillenbrand, E. Lidorikis, F. H. L. Koppens, *Nat. Commun.* **2020**, *11*, 1.

[431] S. Cynthia, R. Ahmed, S. Islam, K. Ali, M. Hossain, *RSC Adv.* **2021**, *11*, 7938.

[432] C. L. Cortes, W. Newman, S. Molesky, Z. Jacob, *J. Opt. (United Kingdom)* **2014**, *16*, DOI: 10.1088/2040-8978/16/12/129501.

[433] M. Imran, H. Wang, Y. Jiang, Z. Xu, L. Shen, *Opt. Express* **2019**, *27*, 16461.

[434] F. Chen, Q. Li, M. Li, H. Zhang, F. Huang, J. Zhang, *Proc. Int. Conf. Numer. Simul. Optoelectron. Devices, NUSOD* **2017**, 99.

[435] J. S. T. Smalley, F. Vallini, B. Kanté, Y. Fainman, *Opt. Express* **2014**, *22*, 21088.

[436] Y. Xiong, Z. Liu, C. Sun, X. Zhang, *Nano Lett.* **2007**, *7*, 3360.

[437] J. Yao, Z. Liu, Y. Liu, Y. Wang, C. Sun, G. Bartal, A. M. Stacy, X. Zhang, *Science (80-.).* **2008**, *321*, 930.

[438] C. L. Cortes, W. Newman, S. Molesky, Z. Jacob, *J. Opt. (United Kingdom)* **2012**, *14*, DOI: 10.1088/2040-8978/14/6/063001.

[439] P. Huo, S. Zhang, Y. Liang, Y. Lu, T. Xu, *Adv. Opt. Mater.* **2019**, *7*, 1.

[440] K. Korzeb, M. Gajc, D. A. Pawlak, *Opt. Express* **2015**, *23*, 25406.

[441] R. Wang, J. Sun, J. Zhou, *Appl. Phys. Lett.* **2010**, *97*, 12.

[442] L. V. Alekseyev, V. A. Podolskiy, E. E. Narimanov, *Adv. Optoelectron.* **2012**, *2012*, DOI: 10.1155/2012/267564.

[443] J. D. Caldwell, L. Lindsay, V. Giannini, I. Vurgaftman, T. L. Reinecke, S. A. Maier, O. J. Glembocki, *Nanophotonics* **2015**, *4*, 44.

[444] J. D. Caldwell, L. Lindsay, V. Giannini, I. Vurgaftman, T. L. Reinecke, S. A. Maier, O. J. Glembocki, **2014**, 1.

[445] G. Shvets, Y. A. Ur, *OSA Trends Opt. Photonics Ser.* **2004**, *97*, 775.

[446] E. E. Narimanov, A. V. Kildishev, *Nat. Photonics* **2015**, *9*, 214.

[447] M. Desouky, A. M. Mahmoud, M. A. Swillam, *Sci. Rep.* **2017**, *7*, 1.

[448] H. N. S. Krishnamoorthy, Y. Zhou, S. Ramanathan, E. Narimanov, V. M. Menon, *Appl. Phys. Lett.* **2014**, *104*, DOI: 10.1063/1.4869297.

[449] I. V. Iorsh, I. S. Mukhin, I. V. Shadrivov, P. A. Belov, Y. S. Kivshar, *Phys. Rev. B - Condens. Matter Mater. Phys.* **2013**, *87*, DOI: 10.1103/PhysRevB.87.075416.

[450] S. Dai, Q. Ma, M. K. Liu, T. Andersen, Z. Fei, M. D. Goldflam, M. Wagner, K. Watanabe, T. Taniguchi, M. Thiemens, F. Keilmann, G. C. A. M. Janssen, S. E. Zhu, P. Jarillo-Herrero, M. M. Fogler, D. N. Basov, *Nat. Nanotechnol.* **2015**, *10*, 682.

[451] C. Ciano, V. Giliberti, M. Ortolani, L. Baldassarre, *Appl. Phys. Lett.* **2018**, *112*, DOI: 10.1063/1.5024518.

[452] W. Ma, P. Alonso-González, S. Li, A. Y. Nikitin, J. Yuan, J. Martín-Sánchez, J. Taboada-Gutiérrez, I. Amenabar, P. Li, S. Vélez, C. Tollan, Z. Dai, Y. Zhang, S. Sriram, K. Kalantar-Zadeh, S. T. Lee, R. Hillenbrand, Q. Bao, *Nature* **2018**, *562*, 557.

[453] J. Taboada-Gutiérrez, G. Álvarez-Pérez, J. Duan, W. Ma, K. Crowley, I. Prieto, A. Bylinkin, M. Autore, H. Volkova, K. Kimura, T. Kimura, M. H. Berger, S. Li, Q. Bao, X. P. A. Gao, I. Errea, A. Y. Nikitin, R. Hillenbrand, J. Martín-Sánchez, P. Alonso-González, *Nat. Mater.*

2020, *19*, 964.

[454] C. Wang, S. Huang, Q. Xing, Y. Xie, C. Song, F. Wang, H. Yan, *Nat. Commun.* **2020**, *11*, 1.

[455] C. Wang, G. Zhang, S. Huang, Y. Xie, H. Yan, *Adv. Opt. Mater.* **2020**, *8*, 1.

[456] A. J. Sternbach, S. H. Chae, S. Latini, A. A. Rikhter, Y. Shao, B. Li, D. Rhodes, B. Kim, P. J. Schuck, X. Xu, X. Y. Zhu, R. D. Averitt, J. Hone, M. M. Fogler, A. Rubio, D. N. Basov, *Science (80-.).* **2021**, *371*, 617.

[457] W. Ma, G. Hu, D. Hu, R. Chen, T. Sun, X. Zhang, Q. Dai, Y. Zeng, A. Alù, C. W. Qiu, P. Li, *Nature* **2021**, *596*, 362.

[458] N. C. Passler, X. Ni, G. Hu, J. R. Matson, G. Carini, M. Wolf, M. Schubert, A. Alù, J. D. Caldwell, T. G. Folland, A. Paarmann, *Nature* **2022**, *602*, 595.

[459] Z. Dai, G. Hu, Q. Ou, L. Zhang, F. Xia, F. J. Garcia-Vidal, C. W. Qiu, Q. Bao, *Chem. Rev.* **2020**, *120*, 6197.

[460] J. D. Caldwell, A. V. Kretinin, Y. Chen, V. Giannini, M. M. Fogler, Y. Francescato, C. T. Ellis, J. G. Tischler, C. R. Woods, A. J. Giles, M. Hong, K. Watanabe, T. Taniguchi, S. A. Maier, K. S. Novoselov, *Nat. Commun.* **2014**, *5*, 1.

[461] X. G. Xu, B. G. Ghamsari, J. H. Jiang, L. Gilburd, G. O. Andreev, C. Zhi, Y. Bando, D. Golberg, P. Berini, G. C. Walker, *Nat. Commun.* **2014**, *5*, 1.

[462] S. Dai, J. Quan, G. Hu, C. W. Qiu, T. H. Tao, X. Li, A. Alù, *Nano Lett.* **2019**, *19*, 1009.

[463] J. D. Caldwell, I. Aharonovich, G. Cassabois, J. H. Edgar, B. Gil, D. N. Basov, *Nat. Rev. Mater.* **2019**, *4*, 552.

[464] Q. Weng, X. Wang, X. Wang, Y. Bando, D. Golberg, *Chem. Soc. Rev.* **2016**, *45*, 3989.

[465] S. Foteinopoulou, G. C. R. Devarapu, G. S. Subramania, S. Krishna, D. Wasserman, *Phonon-Polaritonics: Enabling Powerful Capabilities for Infrared Photonics*, **2019**.

[466] J. Yin, L. Jidong, Y. Hang, Y. Jin, G. Tai, L. Xuemei, Z. Zhang, W. Guo, *Small* **2016**, *12*, 2942.

[467] K. Ding, Q. C. Hu, W. W. Lin, J. K. Huang, F. Huang, *Appl. Phys. Lett.* **2012**, *101*, 3.

[468] A. J. Cheng, Y. Tzeng, H. Xu, S. Alur, Y. Wang, M. Park, T. H. Wu, C. Shannon, D. J. Kim, D. Wang, *J. Appl. Phys.* **2009**, *105*, DOI: 10.1063/1.3093877.

[469] S. Foteinopoulou, G. C. R. Devarapu, G. S. Subramania, S. Krishna, D. Wasserman, *Phonon-Polaritonics: Enabling Powerful Capabilities for Infrared Photonics*, **2019**.

[470] P. Sohr, D. Wei, Z. Wang, S. Law, *Nano Lett.* **2021**, *21*, 9951.

[471] A. Mooradian, B. Wright, **1966**, *16*, 999.

[472] B. B. Varga, **1965**, *8*, 1896.

[473] X. Yu, Y. Yuan, J. Xu, K. T. Yong, J. Qu, J. Song, *Laser Photonics Rev.* **2018**, *13*, 1.

[474] W. Wan, X. Yang, J. Gao, **2016**, *24*, 1367.

[475] J. Flick, N. Rivera, P. Narang, **2018**, *7*, 1479.

[476] D. J. Shelton, I. Brener, J. C. Ginn, M. B. Sinclair, D. W. Peters, G. D. Boreman, **2011**, 2104.

[477] A. F. Kockum, A. Miranowicz, **2018**, 0.

[478] L. Ferrari, C. Wu, D. Lepage, X. Zhang, Z. Liu, *Prog. Quantum Electron.* **2015**, *40*, 1.

[479] T. Hofmann, C. M. Herzinger, J. L. Tedesco, D. K. Gaskill, J. A. Woollam, M. Schubert, *Thin Solid Films* **2011**, *519*, 2593.

[480] Z. Guo, H. Jiang, H. Chen, *J. Appl. Phys.* **2020**, *127*, DOI: 10.1063/1.5128679.

[481] S. Ishii, E. Narimanov, *Sci. Rep.* **2015**, *5*, 1.

[482] I. Fedorin, O. Vdovychenko, *2020 IEEE Ukr. Microw. Week, UkrMW 2020 - Proc.* **2020**, 546.

[483] A. Turpin, Y. V. Loiko, T. K. Kalkandjiev, J. Mompart, *Laser Photonics Rev.* **2016**, *10*, 750.

[484] H. Hu, N. Chen, H. Teng, R. Yu, Y. Qu, J. Sun, M. Xue, D. Hu, B. Wu, C. Li, J. Chen, M. Liu, Z. Sun, Y. Liu, P. Li, S. Fan, F. J. Garcí A De Abajo, Q. Dai, **n.d.**

[485] G. Álvarez-Pérez, A. González-Morán, N. Capote-Robayna, K. V. Voronin, J. Duan, V. S. Volkov, P. Alonso-González, A. Y. Nikitin, *ACS Photonics* **2022**, *9*, 383.

[486] A. Bapat, S. Dixit, Y. Gupta, T. Low, A. Kumar, *Nanophotonics* **2022**, *11*, 2329.

[487] G. Hu, Q. Ou, G. Si, Y. Wu, J. Wu, Z. Dai, A. Krasnok, Y. Mazor, Q. Zhang, Q. Bao, C.-W. Qiu, A. Alù, **2020**.

[488] Y. Zeng, Q. Ou, L. Liu, C. Zheng, Z. Wang, Y. Gong, X. Liang, Y. Zhang, G. Hu, Z. Yang, C. W. Qiu, Q. Bao, H. Chen, Z. Dai, *Nano Lett.* **2022**, DOI: 10.1021/acs.nanolett.2c00399.

[489] Y. Guo, Z. Jacob, *Opt. Express* **2013**, *21*, 15014.

[490] X. Wang, R. Starko-Bowes, C. Khandekar, Z. Jacob, *Annu. Rev. Heat Transf.* **2020**, *23*, 355.

[491] X. Wu, R. Liu, *ES Energy Environ.* **2020**, DOI: 10.30919/esee8c939.

[492] K. Liu, S. Sun, A. Majumdar, V. J. Sorger, *Sci. Rep.* **2016**, *6*, 1.

[493] H. Hajian, A. Ghobadi, S. A. Dereshgi, B. Butun, E. Ozbay, *J. Opt. Soc. Am. B* **2017**, *34*, D29.

[494] Z. Guo, H. Jiang, H. Chen, *J. Appl. Phys.* **2020**, *127*, 1.

[495] M. Ge, Yin, Jun, Yuan, Wei, Juang, Jianfei, Zhu, Yungui, *Chinese Phys. B* **2016**.

[496] B. W. H. Baugher, H. O. H. Churchill, Y. Yang, P. Jarillo-Herrero, *Nat. Nanotechnol.* **2014**, *9*, 262.